Review of Climate Change and Hygrothermal Performance of Wood Frame Wall Systems under Climate Change in Marine Climate of Vancouver

Mehretab Kidanu

A Thesis
In
The Graduate Program
Of
Building Science/ Building Engineering

The School of Construction and the Environment

Presented in Partial Fulfilment of the Requirements
for the Degree of Master of Applied Science at
British Columbia Institute of Technology
Burnaby, British Columbia, Canada

April 2020

Burnaby, British Columbia, Canada

Abstract

Buildings have a long life span which in most circumstances ranges from 50 to 100 years, throughout these service years buildings are most likely to encounter unprecedented weather conditions. Nowadays, both scientific research and physical evidences show a changing climate conditions. An increased accumulation of Green Houses Gases (GHG) on the atmosphere believed to be the leading cause. In the building sector, climate change has posed various challenges. Some of the major problems include a shift in energy demand, premature buildings enclosure damage by heavy wind-driven rain, flood and storm, increase in structural load due to strong wind, and reduced air quality caused by wildfires and biodiversity losses. Using a hygrothermal model developed in COMSOL Multiphysics Software Package, the presented research has addressed the potential impacts of climate change on wood frame walls durability for residential houses located in Vancouver. Hourly current and future weather data suitable to use in building performance analysis developed using an absolute and relative approach based on CanESM2 with CanRCM4 LE and HadCM3 with time series adjustment. Then hygrothermal simulations are conducted using current and future weather data for various wall assemblies, modeling factors, orientations, and indoor environmental conditions. Finally, the durability of the walls examined primarily based on hygrothermal model outputs with associated mold growth and deterioration effect.

Acknowledgment

First, my acknowledgment goes to my supervisor Dr. Fitsum Tariku for his assistance and guidance at every step of the research process. Second, I would like to express special thanks to my family, who always has been by my side when I need strength to succeed over challenges. Last but not least, my gratitude goes to BCIT's staff members and every individual who directly and indirectly contributes to the completion of the research.

Table of Contents

List of Figures

List of Tables

1 Introduction

Buildings and climate cannot be separated in various aspects, as one has a direct effect on the other. For instance, buildings to offer a comfortable living and working environment consumes around a third of total energy use. On the other hand, the generation of such amount of energy comes at the cost of releasing 30% of global annual greenhouse gases emissions (IPCC, 2007). Zhai et al. (2019) pointed out that between 1971 and 2004, the annual rate of carbon emission has grown by 2.5% and 1.7 % for commercial and residential buildings, respectively. Also, many of the potential effects of climate change on the building sector are not well studied. Therefore, climate change could have a significant impact on the design and operations of the built environment.

Climate change, principally caused by greenhouse gases emission (GHG), is one of the most crucial global environmental problems that our world is facing today. This challenge has widely recognized as having a significant impact to seriously affect the integrity of ecosystems and human welfare (Guan, 2009). Nik et al. (2012) pointed due to climate change building's current energy requirement can be altered, and climate change has a direct influence on the durability of building enclosure. Adding that increased structural load from heavy wind could affect building structure. Recently both scientific research and physical evidences show a change in climate patterns as well as extreme weather events

Study and prediction of climate change have been a focus to assess the potential impact in human life, such as the related effect in agriculture, ecology, hydrology, social and economic life (Crawford et al., 2019; Shen et al., 2018). Climate change direct effect can have two forms (Wu et al., 2020). Long term change in climate variables characterize one way. Short term effects determined by extreme weather events such as floods, droughts, heatwaves, storms, and rising sea levels describe the second way.

2 Literature Review

Chan (2011) & Shen (2017) pointed there is a growing concern about the accumulation of greenhouse gases (GHG) on the atmosphere, and the associated climate change has been a focus to the academic world. Buildings, as part of the infrastructure, should withstand changing climatic conditions for an extended period (50-100 years). Current and future building stocks should perform satisfactorily under changing climatic conditions (Guan, 2009). It's reasonable to state that many of the factors that affect building energy demand, functionality, durability, occupancy comfort, and safety are those related to the external environment. Studying all potential adverse effects of changing climate conditions should be a requirement. Climate and earth scientists, as well as other affiliated professionals, review climate change. Their activities are mainly concerned with keeping climate records, explaining any changes to that record, and predicting future changes (De Wilde et al., 2012).

As shown in Figure 1, De Wilde et al. (2012) have graphically illustrated the ties between climate and building. The first box column shows the primary driving forces of climate change and the associated change on weather variables. The second column indicates the resulting environmental effects such as the intensity, frequency of gradual and extreme weather conditions, sea-level rise, the impact on environmental degradation and ecosystem loss. The third column shows climate change impact on the building sector, such as the effect on energy use, HVAC systems performance, water damages, and other environmental loads. The fourth column indicates the potential impact on occupant comfort, health, productivity, economic effects, and other vital processes taking place in buildings. Consequently, the climate process which occurs far from buildings location has a direct link on the fundamental role & operation of buildings.

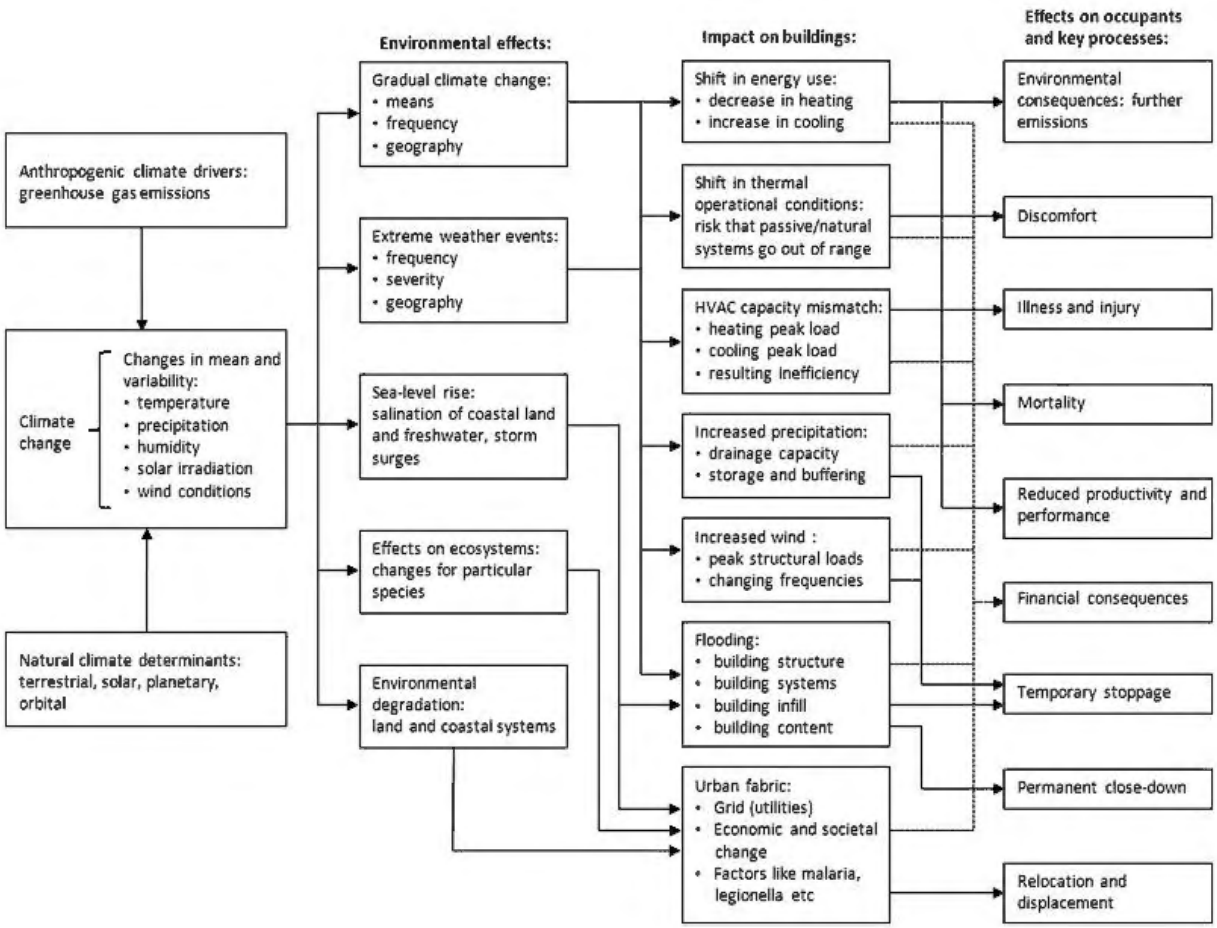

Figure 1: Schematic overview of main mechanisms in which climate change impacts buildings, occupants, and key processes taking place in buildings. (De Wilde et al., 2012)

2.1 Climate Change Impact on Built Environment

Gaur et al. (2019) pointed out in the future different annual and seasonal climatic conditions could impact buildings and infrastructures across Canada. Adding that failure to account for the non-stationarity of climate could lead to premature failure of Canada's buildings and infrastructures. Most of the current building standards, design guidelines, and practices used current or past weather data as a representative of the outdoor conditions. However, buildings and other infrastructures can have a long lifespan. Thus buildings are going to encounter future climate conditions. As a result, it is essential to design buildings not only using climate data at the time of construction but also considering the future.

Liso et al. (2017) discussed in Norway insurance-related cost due to water intrusion into buildings in a single year have accounted for more than $200 million. Besides, due to climate change, annual maintenance cost is expected to reach $1 billion by the year 2100, indicating a fivefold increase. De Wilde et al. (2012) pointed buildings constructed today need to perform successfully in both current and future climate.

Cox et al. (2015) mentioned adaptation measures are necessary to address climate change impacts even in a dramatic reduction of anthropogenic emissions of greenhouse gasses. Adding that optimizing building for energy use can significantly reduce CO2 emission. However, building construction should always consider the changing climate, including the intensity of extreme events.

On Building Energy Use

Several climate models have been used in various studies to assess the potential impact of climate change in the energy consumption of different buildings (Zhai et al., 2019). Wang et al. (2017), based on Hadley Centre Coupled Model (HadCM3) and Community Earth System Model (CESM1), studied climate change impact on energy usage for a medium-sized office building. Cellura et al. (2018) found that for ambient temperature increase by 9°C in Southern Europe, the cooling energy demand of an office building in 2090 could rise by 120 %. Moreover, another study by Pérez-Andreu et al. (2018) conducted in a Mediterranean climate for a residential building using two Global Circulation Models (GCM) for the year 2050 and 2100. They have found a significant decrease in heating energy and an increase in cooling energy, pointing that thermal insulation and infiltration as having the most significant effect on total energy demand. Spandagos et al. (2017) studied climate change impacts on building cooling and heating energy in large Asian cities. They concluded switching to more efficient air-conditioning devices can offset much of the energy increase. Hwang et al. (2018)

pointed out thermal insulation is gaining more concern in warmer regions as climate change continues.

Invidiata et al. (2016) for different locations studied the effect of climate change on thermal comfort and energy demand. The study indicates increased annual energy demand ranging from 19% to 65%, 56% to 112%, and 112% to 185% in 2020, 2050, and 2080 years respectively. However, for a cold location due to an increase in temperature and global solar radiation, annual heating demand could decrease by around 94 % in 2080. Also, referring to various studies, they pointed cooling energy can increase due to warming conditions, but heating energy can reduce in cold regions. Flores-Larsen et al. (2019) studied the impact of climate change on the energy performance of residential buildings. The study shows reduced annual heating demand by 8 to 25% in 2080 as compared to a baseline period of 1961-1990, while cooling energy could rose by 350-790%. Table 1 summarises some previous research on building energy usage by climate change.

Table 1: Summary of previous climate change impact studies on buildings. (Invidata et al., 2016)

Author	Country	Type of building	Period	Conclusion
Guan [5,6]	Australia	Commercial	2070	Increase cooling demand from 28% to 59%
Wang et al. [7]	Australia	Residential	2100	Total energy variation −48% to 350%
Wan et al. [8]	China	Commercial	2100	11–20% increase in cooling energy and 13–55% decrease in heating energy
Frank [9]	Swiss	Commercial and residential	2100	36–58% decrease in heating demand and 223–1050% increase in cooling demand
Berger et al. [10]	Austria	Commercial	2050	11–56% decrease in heating demand and 28–91% increase in cooling demand
Dodoo et al. [11]	Sweden	Residential	2050–2100	13–22% decrease in heating demand and 33–49% increase in cooling demand
Pilli-Sihvola et al. [12]	Finland, Holland, Germany, France and Spain	Commercial and residential	Not mentioned	Increase cooling demand and decrease heating demand
Yilha et al. [21]	Finland	Residential	2030–2050–2100	20–40% decrease in heating demand and 40–80% increase in cooling demand
Asimakopouloset al. [15]	Greece	Commercial and residential	2100	44–75% decrease in heating demand and 28–59% increase in cooling demand
Amato et al. [16]	United States	Commercial and residential	Not mentioned	1.2–2.1% increase in electricity, 7–14% decrease in gas
Wang and Chan [17]	United States	Commercial, residential and public	2040–2080	Increase cooling demand and decrease heating demand
Dirks et al. [22]	United States	Commercial, residential	2052–2089	−31.4%/+15.4% total energy demand variation
Radhi [13]	United Arab Emirates	Residential	2050–2100	23.5% increase in cooling demand
Huang and Hwang [19]	Taiwan	Residential	2020–2050–2080	31–82% increase in cooling demand
Casagrande and Alvarez [14]	Brazil	Commercial	2020–2050–2080	10.7–25.6% increase in cooling demand

On Building Enclosure

Studies have been carried out on the thermal performance of energy-efficient buildings under future climates, while studies on the durability of building envelopes over future climates are limited (Sehizadeh et al., 2016). Nik et al. (2012) assessed the impact of future climates on the mold growth effect in ventilated attics through hygrothermal simulations from 1961 to 2100 using Regional Climate Model. The study concluded that the potential effect of mold growth would increase over future climates. Nijland et al. (2009) found increased temperature and precipitation under future climate could decrease the number of freeze-thaw cycles on porous materials. However, such conditions would likely speed up the biodegradation for timber, stony materials, and coatings (Sehizadeh et al., 2016). The current large number of wooden buildings and a high number of building defects indicates that new and refurbished

buildings must be far more robust to meet a changing climate with an enhanced maintenance (Liso et al., 2017).

2.2 Climate System

To understand the complex dynamics of the global climate system as well as to forecast future climate conditions, it is essential to look at the significant constituents of the climate system. North et al. (2017) explained the global climate system consists of a large number of interacting parts; first, the atmosphere and its constituents such as free molecules, radicals of different chemical species, aerosol particles, and clouds. Second, the ocean water and its members such as floating ice, dissolved species including electrolytes and gases as well as undissolved matter (i.e., biological origin and dust). Third, land component, like topographical features and vegetation. Also, the study of climate system combines every subfield of geoscience like physics, chemistry, and biology. The processes involve the quantum mechanics of photons scattered, absorbed, and emitted by or from atmospheric molecules in radiative transfer processes to the study of tree-ring widths and isotopic evidence based on fossilized species deposited and buried in sediments deep below the ocean's floor (North et al., 2017). Figure 2 shows the components and sub-members of the climate system.

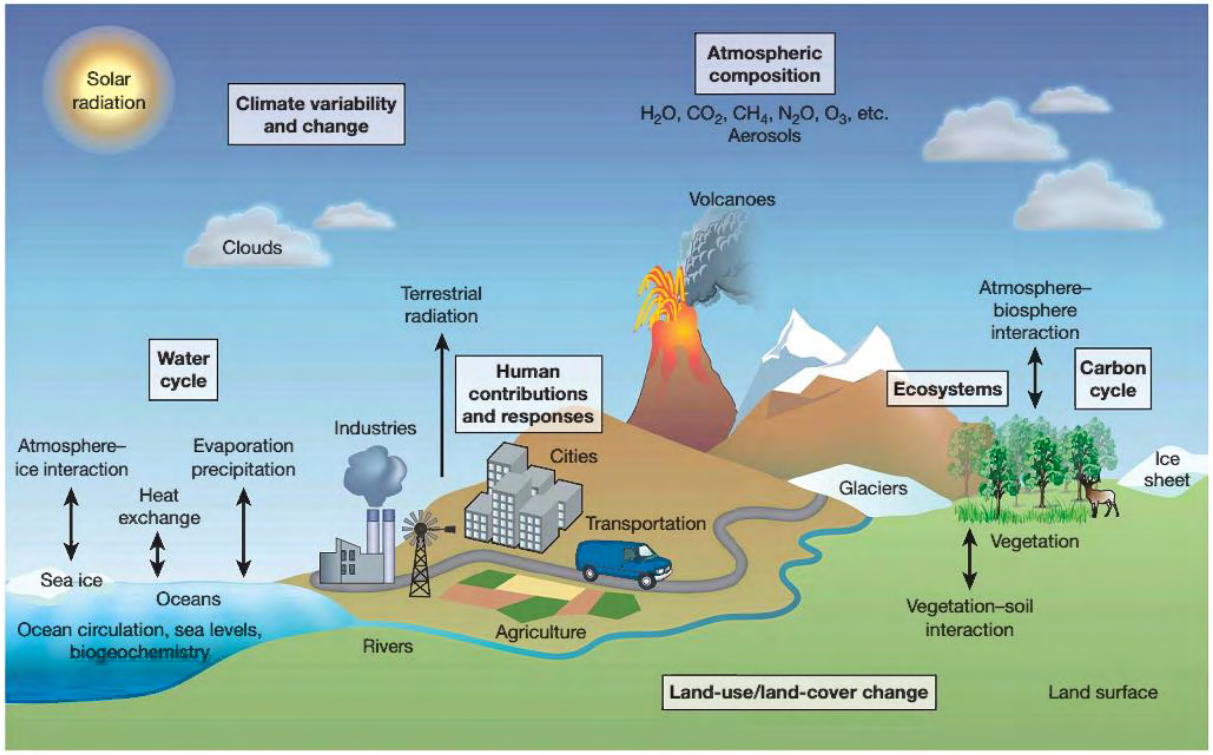

Figure 2: Major natural and anthropogenic processes and influences on the climate system. (Moss et al., 2010)

2.3 Climate Model

Climate models are complex mathematical representations of the vast process of the earth climate and associated components. As shown by the grid box in Figure 3, these components include the atmosphere, land surface, ecosystems, oceans, sea ice, human activities, and natural conditions. The most sophisticated climate models couple the circulation of the atmosphere with that of the ocean, biosphere, and cryosphere. Such models are vital to understanding the climate system, to forecast weather conditions, and also to simulate past weather. Physical laws of fluid mechanics that are known for centuries, such as conservation of mass, momentum, and energy, together with ideal gas law, are used to represent the atmospheric motion. The solution approach to such sets of equations employs numerical methods. As a result, weather prediction using climate model also called numerical weather prediction.

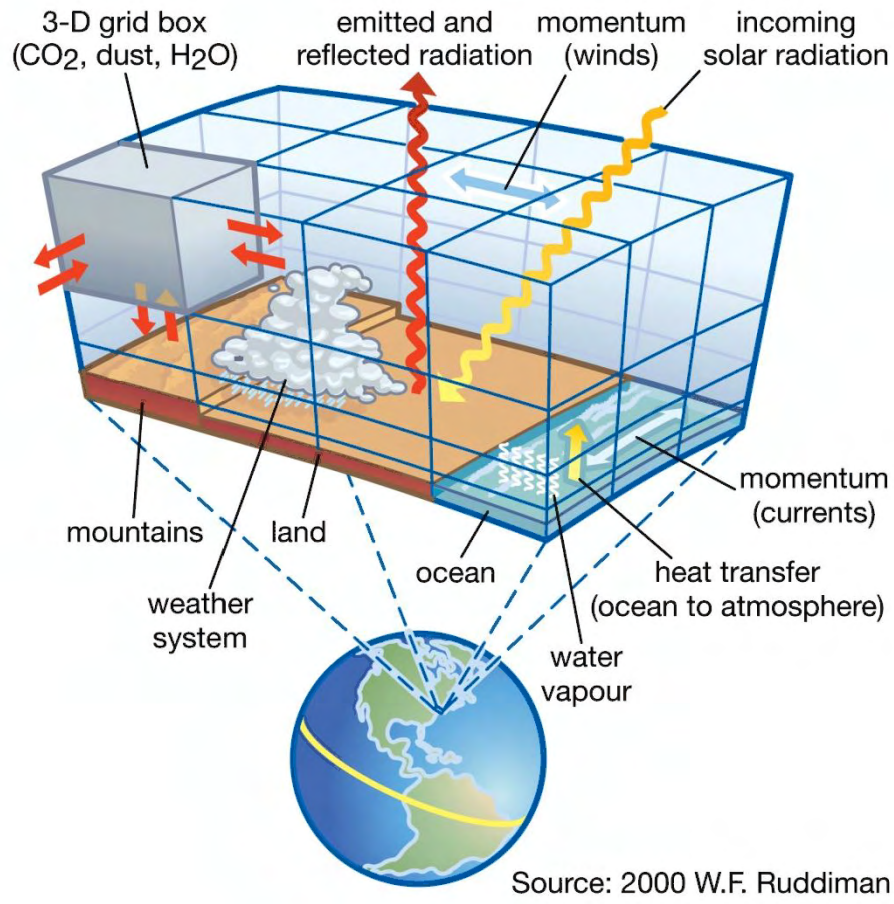

Figure 3: Schematic illustration of a three-dimensional grid of climate model.

Source: https://www.britannica.com/science/scientific-modeling

The capability of climate models in representing the climate system depends on the extent and complexity of the model used to describe the sophisticated process (Abiodun et al., 2016). Adding that both the complexity and number of equations considered in a model determines the computational demand. The choice of a climate model depends on the intended applications and purposes of a model output. For instance, a complex model may be required for some studies, while a simpler model may be adequate for others. The different types of climate model includes; Energy Balance Model (EBM), Radiative Convective Model (RM), Regional Climate Model (RCM), and Global Circulation Model (GCM).

GCM is the most advanced numerical tools which represent the actual physical process and interaction between the atmosphere, ocean, cryosphere, and land surface. Even though

simpler models can be used to simulate the climate at the global or regional scale, only GCM's have the potential to provide geographically and physically consistent estimates of climate change, suitable for impact study (Guarino et al., 2019). GCM has been used to project future climate conditions, which generates time series of future climate conditions under scenarios where the concentrations of greenhouse gases and aerosols in the air are assumed (Kikumoto et al., 2014). The model represents the atmosphere using a three-dimensional grid with a horizontal resolution of 250 to 600 km, 10 to 20 vertical grid boxes in the atmosphere, and sometimes as many as 30 in the oceans (Guarino et al., 2019). The Second Generation Canadian Earth System Model (CanESM2), Community Climate System Model (CCSM4), Hadley Centre Coupled Model (HadCM3), and Model for Interdisciplinary Research on Climate (MIROC5) are some of GCMs. Even though different GCMs are available, the performance of the models against measurement can be different where some models have better climate projection capability than others, as shown in Figure 4.

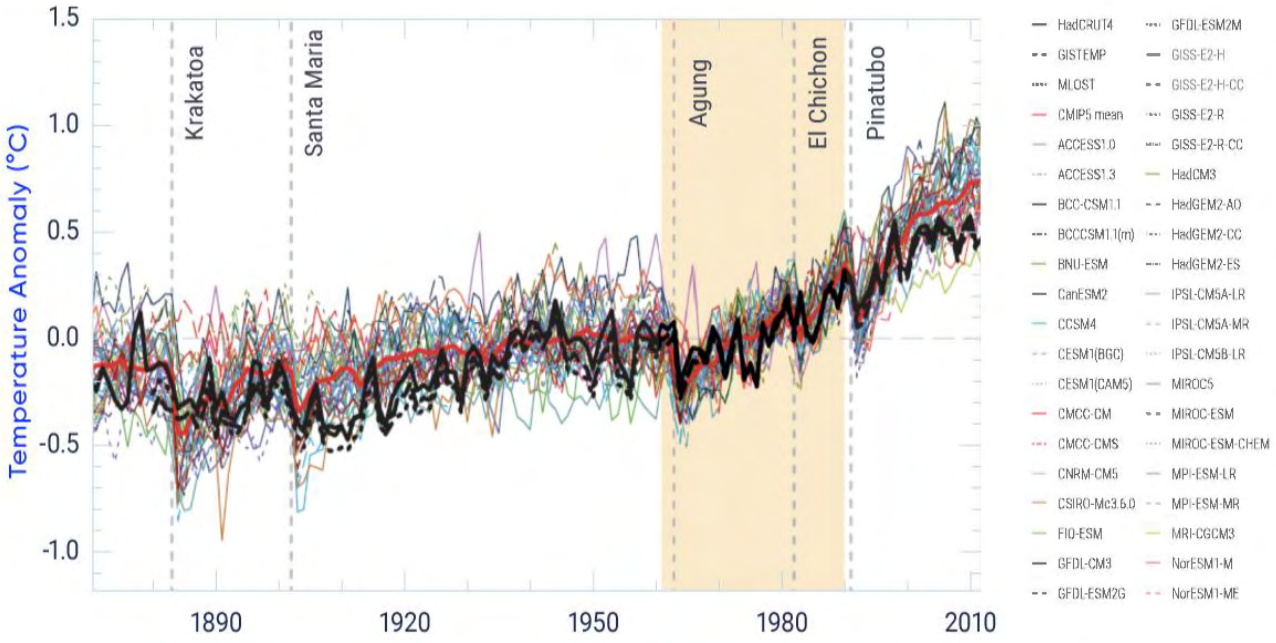

Figure 4: Global annual mean surface air temperature anomalies from 1850 to 2012. (Flat et al., 2013)

2.4 IPCC Scenarios

Climate models require data on the time-evolving emissions or concentrations of active radiative constituents, and some have additional requirements for information about the time-evolving paths for land use and land cover (Moss et al., 2010). The fifth assessment report (AR5) by the Intergovernmental Panel on Climate Change (IPCC, 2014) outlined that anthropogenic greenhouse gases emission, mainly driven by economic and population growth has been increasing since the pre-industrial era. Atmospheric concentrations of carbon dioxide, methane and nitrous oxide, together with other anthropogenic drivers, are extremely likely to have been the dominant cause of the observed warming since the mid-20th century. To understand the complex interactions of the climate system, ecosystems, and human activities, the research community develops and uses scenarios (Moss et al., 2010). Adding that these scenarios describe how the future will change in various key areas such as socioeconomic, technological and environmental conditions, emissions of greenhouse gases, and aerosols.

The Third Assessment Report (IPCC, 2001) assessed the first climate model using these scenarios as inputs, and in 2007 IPCC published its Fourth Assessment Report, which consists of a complete set of emission scenarios. This Special Report on Emission Scenarios (SRES) developed by the International Panel on Climate Change defines a family of possible emission scenarios for the next 100 years, based on economic, social, technological, and environmental assumptions (Cox et al., 2015).

SRES provides scenarios of future greenhouse gases emissions accompanied by storylines of social, economic, and technological development (IPCC, 2007). As shown in Table 2, SRES consists of four storylines, namely, A1, A2, B1, and B2. The groups depend on social, economic, and political factors. Scenario A1 assumes a market-oriented world with fast

growth and population peaks in 2050. This scenario further divided into three technology groups A1FI, A1T, & A1B. A1F1 driven by intensive fossil fuel, A1B a balanced economy, and A1T predominantly non-fossil fuel growth. Scenario A2 assumes a slow growth regional economy with a continuously increasing population. B1 is a more integrated and ecologically friendly world with clean technologies and expects the same population growth rate as A2. However, scenario B2 assumes moderate growth, continuously increasing population, localized solution to environmental issues with rapid technological advancement than A2, but reduced and more diverse than A1 and B1. B1 and A1FI scenarios represent the lowest and highest overall emissions, respectively.

Table 2: Summary of SRES storylines (IPCC, 2007).

<table>
<tr><td></td><td colspan="2">→ Economic emphasis</td><td></td></tr>
<tr><td rowspan="2">↑

Global integration</td><td>A1 storyline
World: market-oriented
Economy: fastest per capita growth
Population: 2050 peak, then decline
Governance: strong regional interactions; income convergence
Technology: three scenario groups:
A1FI: fossil intensive
A1T: non-fossil energy sources
A1B: balanced across all sources</td><td>A2 storyline
World: differentiated
Economy: regionally oriented; lowest per capita growth
Population: continuously increasing
Governance: self-reliance with preservation of local identities
Technology: slowest and most fragmented development</td><td rowspan="2">↓

Regional emphasis</td></tr>
<tr><td>B1 storyline
World: convergent
Economy: service & information-based; lower growth than A1
Population: same as A1
Governance: global solutions to economic,</td><td>B2 storyline
World: local solutions
Economy: intermediate growth
Population: continuously increasing at a lower rate than A2
Governance: local and</td></tr>
</table>

	social and environmental sustainability Technology: clean and resource-efficient	regional solutions to environmental protection and social equity Technology: more rapid than A2 less rapid and more diverse A1/B1	
	← **Environmental emphasis**		

Continued GHG emissions at or above current rates would cause further warming and induce many changes in the global climate system during the 21st century, which would very likely be more extensive than those observed during the 20th century. The Special Report on Emissions Scenarios projects an increase of global GHG emissions by 25 to 90% (CO2-eq) between the years 2000 and 2030 (Figure 5), with fossil fuels maintaining their dominant position in the global energy mix to 2030 and beyond (IPCC, 2007).

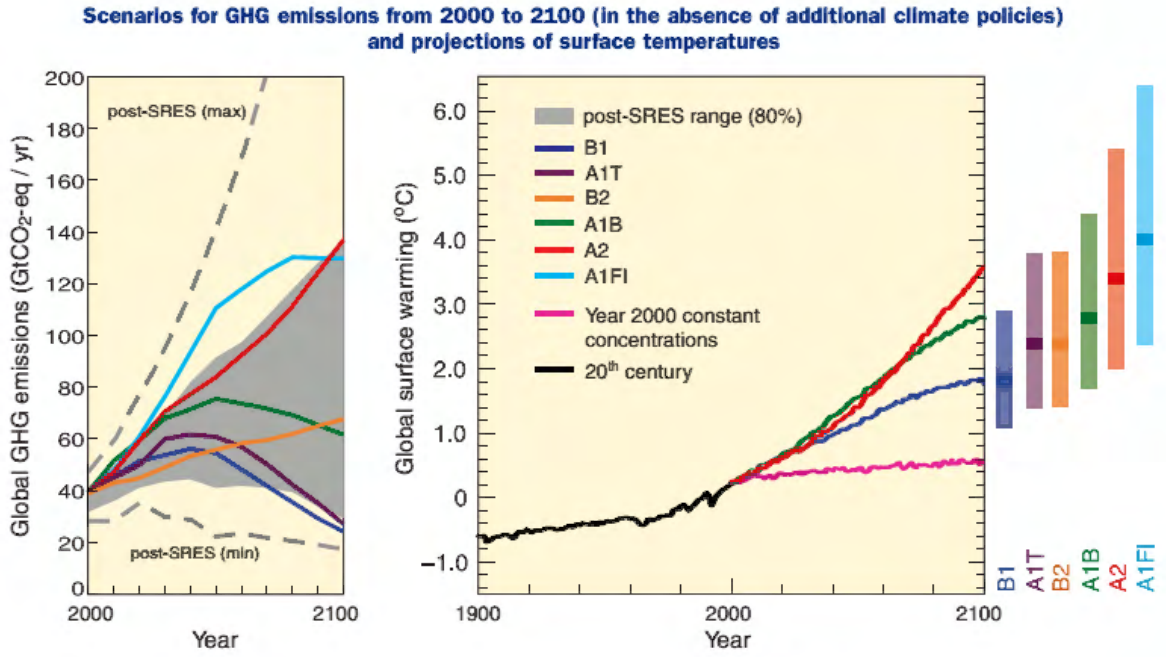

Figure 5: Projected global GHG emissions and Global surface warming of the 80th percentile under various SRES (IPCC, 2007).

Increases in temperature projections depend on specific emission scenarios (IPCC, 2007). As shown in Table 3, the predicted temperature changes between 2090 and 2099 compared to

1980 and 1999 is highest by scenario A1FI with best estimate of 4°C and likely range of 2.4°C to 6.4°C. The lowest projection is by scenario B1 with an increase of 1.8°C and possibly ranges between 1.1°C and 2.9°C, similarly for the other scenarios are shown in the table.

Table 3: Projected global average surface temperature and sea-level rise at the end of the 21st century. (IPCC, 2007)

Case	Temperature change (°C at 2090-2099 relative to 1980-1999)		Sea level rise (m at 2090-2099 relative to 1980-1999)
	Best estimate	Likely range	Model-based range excluding future rapid dynamical changes in ice flow
Constant year 2000 Concentrations	0.6	0.3-0.9	N.A
B1 scenario	1.8	1.1 – 2.9	0.18 – 0.38
A1T scenario	2.4	1.4 – 3.8	0.20 – 0.45
B2 scenario	2.4	1.4 – 3.8	0.20 – 0.43
A1B scenario	2.8	1.7 – 4.4	0.21 – 0.48
A2 scenario	3.4	2.0 – 5.4	0.23 – 0.51
A1FI scenario	4.0	2.4 – 6.4	0.26 – 0.59

In the fourth assessment report (IPCC, 2007), some of the listed points are:

a) The hierarchy of models of varying complexity, as well as observational constraints, are used to assess best estimates and uncertainty ranges.

b) The year 2000 composition is derived from Atmosphere-Ocean General Circulation Models (AOGCMs) only.

c) Temperature changes expressed as the difference between 1980 and 1999. Adding a temperature of 0.5°C can represent the relative change from the period of 1850 to 1899.

Climate models project climate changes based on a standard set of greenhouse gases scenarios called Representative Concentration Pathways (RCPs) (Zhai et al., 2019). Table 4 shows the radiative force and CO_2 concentration of RCPs released in AR5. RCP2.6 assumes stringent mitigation, whereas scenarios RCP4.5, and RCP6.0 are intermediate. The fourth scenario or RCP8.5 assumes high GHG emissions (IPCC, 2014). For each category of emissions, RCP contains a set of starting values and the estimated emissions up to 2100, based on assumptions about economic activity, energy sources, population growth, and other socio-economic factors (IPCC, 2014). The four RCPs, RCP2.6, RCP4.5, RCP6, and RCP8.5, are named after a possible range of radiative forcing values in the year 2100 relative to pre-industrial values +2.6, +4.5, +6.0, and +8.5 W/m2, respectively (Zhai et al., 2019).

Table 4: Overview of RCP (Based on Guarino et al., 2019, and IPCC, 2014).

Scenario	Radiative Force by 2100	Co_2 concentration by 2100	Pathway	Increase in global-mean Temperature by 2100 relative to 1986-2005 period
RCP 8.5	>8.5 W/m2	>1370 ppm	Rising	2.6-4.8 C
RCP 6	~6 W/m2	~850 ppm	Stabilization without overshoot	1.4-3.1 C
RCP 4.5	~4.5 W/m2	~650 ppm	Stabilization without overshoot	1.1-2.6 C
RCP 2.6	Peak at ~3W/m2 in 2050 & then decline to 2.6 W/m2 by 2100	Peak at ~490 ppm before 2100 & then declines	Peak & Decline	0.3-1.7 C

Figure 6 shows a time series of projection and a measure of uncertainty (shading) for all RCP's. The temperature might rise by 3.7 °C, with a likely range between 2.6 °C and 4.8 °C by RCP8.5. RCP2.6 or the best scenario assumes effective strategies to reduce GHG could result in a radiative force of 2.6 W/m² by 2100. RCP8.5, or worst scenario, projects radiative force to reach 8.5 W/m² by 2100.

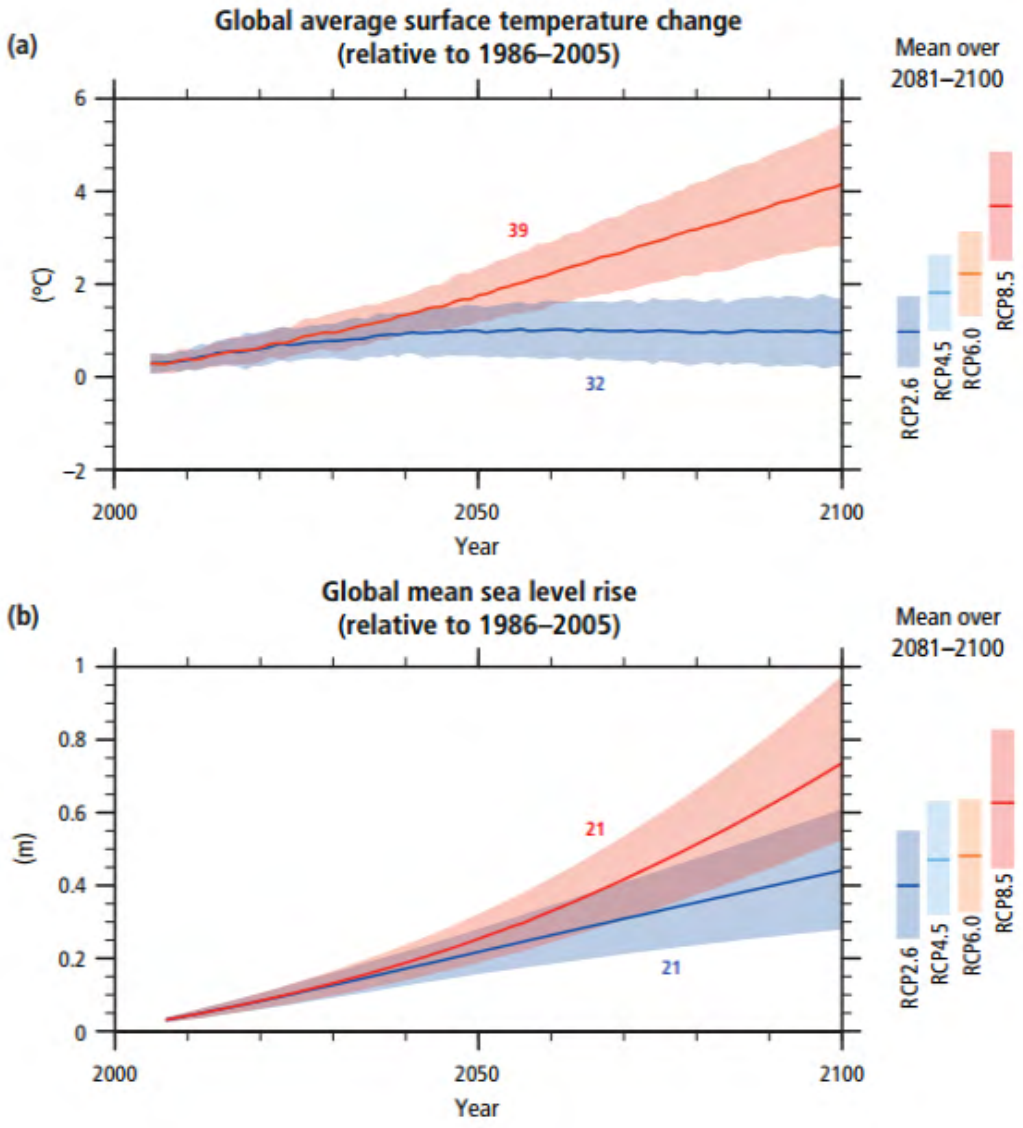

Figure 6: Global average surface temperature change (a) and global mean sea level rise (b) from 2006 to 2100 as determined by multi-model simulations (IPCC, 2014).

AR5 covers a broader range of scenarios than the Special Report on Emissions Scenarios (Zhai et al., 2019). Adding that when comparing AR5 scenarios to the previous SRES

scenarios, 3 of the 4 have a similar situation. But, the stringent mitigation scenario has no equivalent, so there can be a difference in magnitude between SRES and AR5 climate projections due to an extensive range of emissions (IPCC, 2014).

Kolio et al. (2014) pointed facades could receive more driving rain as in the future, temperature, precipitation, and windiness could be most likely to increase. Stanzel et al. (2018) have reviewed a projected temperature and precipitation anomalies for a specific study location using two RCPs. As shown in Figure 7, the projection shows an increasing trend until the year 2090 in both scenarios. Based on the Intergovernmental Panel on Climate change (IPCC) report, Guan et al. (2009) listed major changes on meteorological parameters by the year 2100 as compared to 1990;

i. The average surface temperature of the Earth is likely to increase by 1.4–5.8
ii. Global mean sea level could rise by 9–88 cm.
iii. Precipitation (rainfall and snowfall) is likely to increase over the northern mid to high latitudes and Antarctica in winter.
iv. The occurrence of extreme events (drought, tropical cyclone intensity) expected to increase over some regions.
v. There will be significant changes to snow cover and ice extent.
vi. Reduced circulation in the ocean.

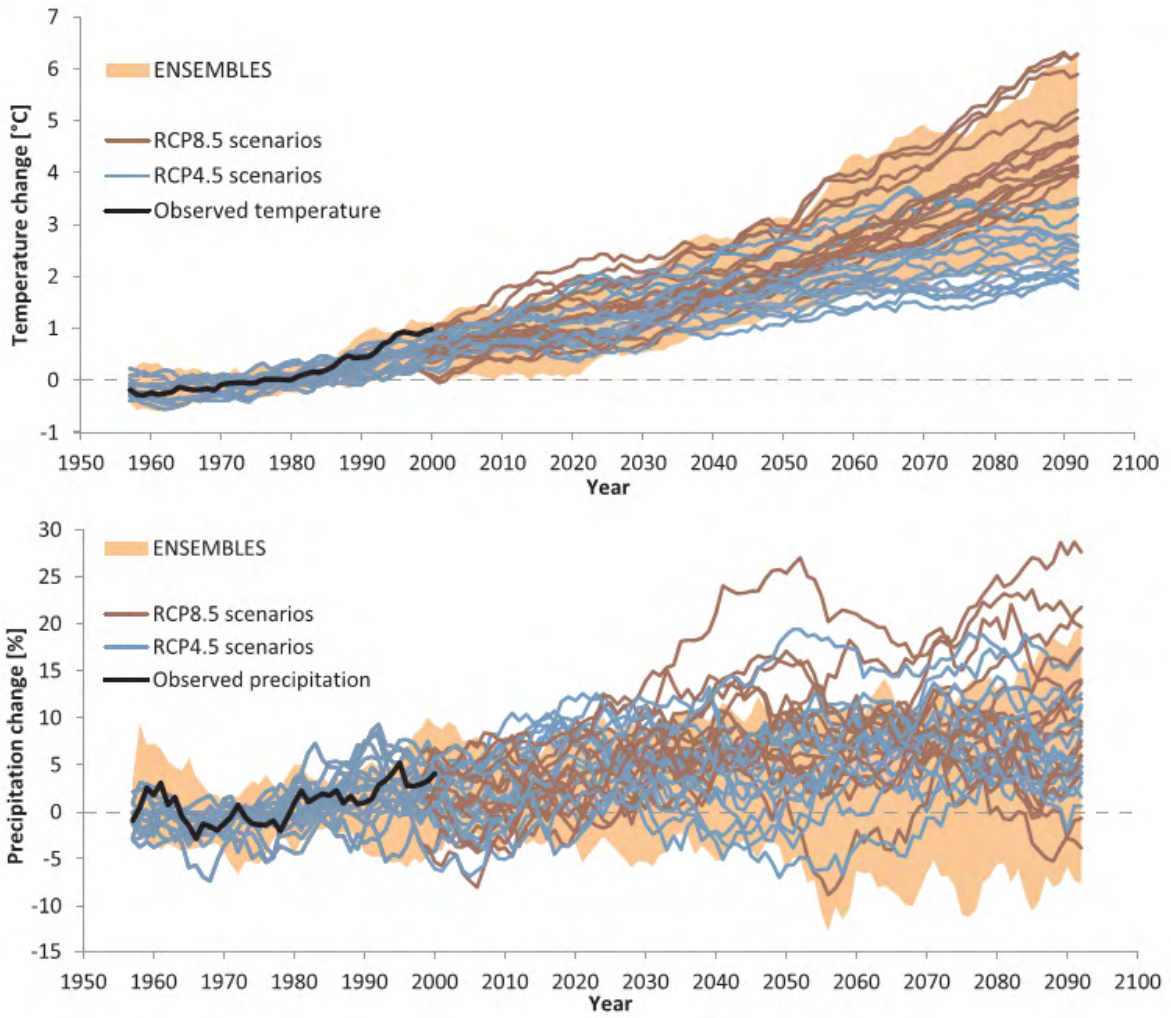

Figure 7: Temperature and Precipitation anomalies. (Stanzel et al., 2018)

2.5 Vancouver Future Climate Prediction

Gaur et al. (2019) developed three groups of 31 year long time-series weather data for eleven Canadian locations using 15 realizations from CanESM2 and CanRCM4 LE. The data includes future projection as well as simulated past weather data for 12 weather variables. One of the data sets corresponds to past weather (1986-2016), and the other two data groups are future time-periods coincident with global average future warmings of 2°C (2034-2064) and 3.5°C (2062-2092). As shown in Table 5, some of the predicted weather variables changes in Vancouver are an increase in temperature (TEMP), relative humidity (RHUM), and precipitation (RAIN), a decrease in wind speed (WSP) and uncertain changes in global horizontal irradiance (GHI).

Table 5: Projected weather variables change in Vancouver compared to the baseline period for a global warming of 2°C and 3.5°C.

Statistic	GHI (%)		Total Cloud Cover (%)		RAIN (%)		Wind Direction (C)		WSP (%)		RHUM (%)		TEMP (°C)	
	2°C	3.5°C	2°C	3.5°C	2°C	3.5°C	2°C	3.5°C	2°C	3.5°C	2°C	3.5°C	2°C	3.5°C
Mean	1.3	2.5	0	-0.4	3.9	4.4	-1.0	-2	-3.0	-5.8	0.5	0.5	2.6	4.3
Max	2.9	3.9	1.5	0.6	12	9.7	1.3	-0.6	-0.5	-4.1	1.0	1.1	2.9	4.8
Min	-0.5	0.7	-1.6	-1.8	-2.4	-2.8	-4.3	-4.5	-4.9	-7.7	0	0.2	2.2	4

One way of increasing confidence in the use of climate models is through an ensemble method. Varying the initial conditions of a climate model can generate different outputs. Initial conditions are core inputs to simulate a climate model. The use of future weather data from multiple realizations can provide better confidence in climate change-related decision making. The next discussion uses weather data developed by Gaur et al. (2019) for Vancouver. However, here the review takes only one realization from each weather variable, refer Appendix C for the rest of the predictions. Figure 8 shows the data content of 15 future realizations for dry bulb temperature in the coming 30 years. The statistical content of median, quartiles, and whiskers shows similarity in all realizations, except for one of the predictions (Prediction7 or P7), which indicates a lower projection with extreme lower outliers.

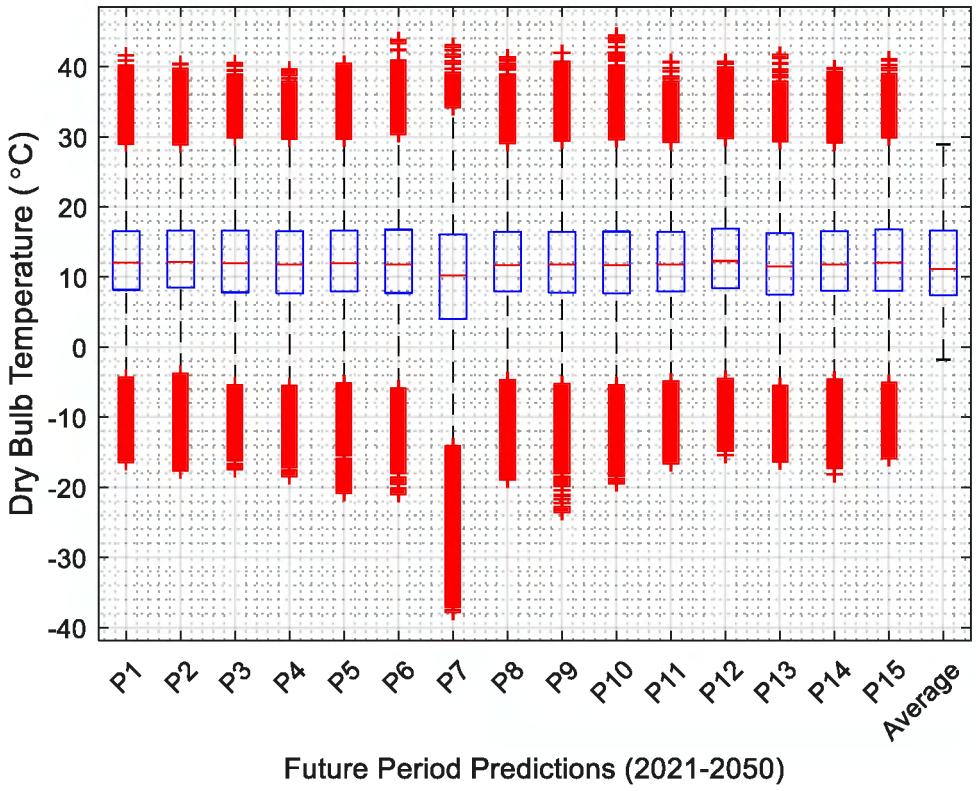

Figure 8: Box plot of dry bulb temperature from 2021 to 2050 for 15 realizations.

Figure 9 shows a box plot of dry bulb temperature for every five years. Consistent increases in median, quartile as well as whisker shows the increasing temperature. The distribution of temperature data follows symmetric distribution, which fits better with normal probability density function (PDF). The overall comparison between past and future 30 year time periods is depicted in Figure 10 using the first realization from past and future periods. The probability density function indicates a shift from past to future periods showing a temperature increase.

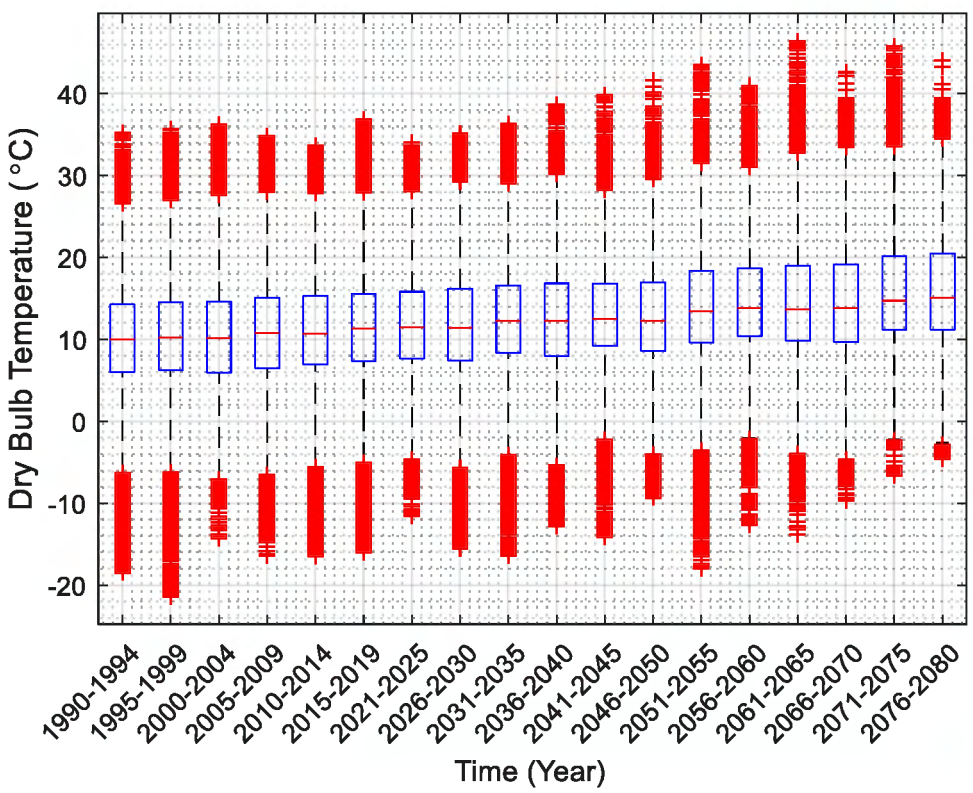

Figure 9: Boxplot of dry-bulb temperature for every five years from 1990 to 2080.

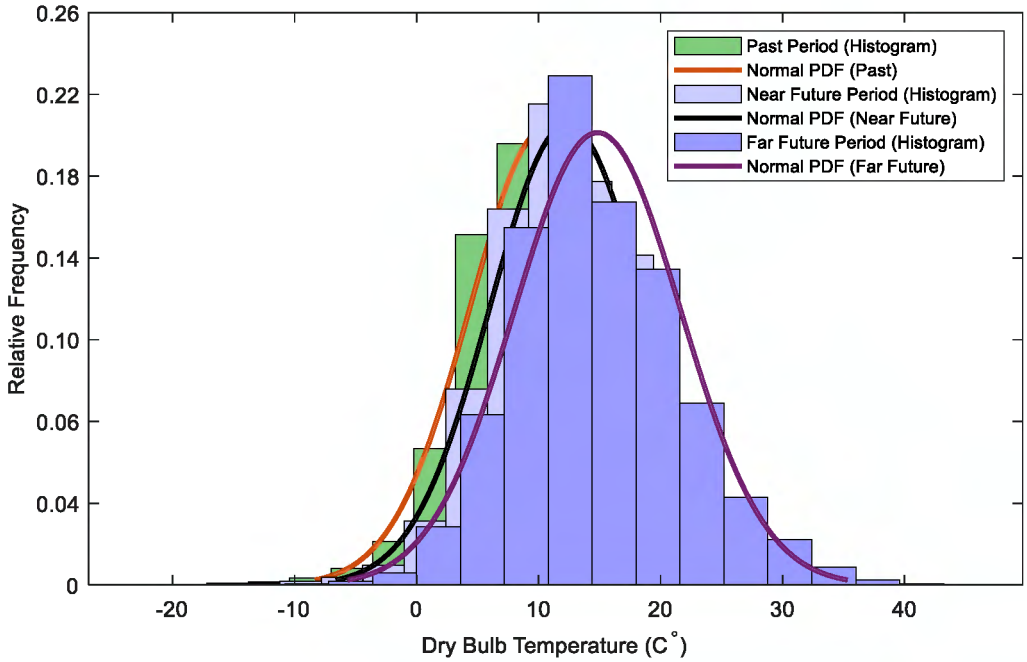

Figure 10: Histogram and normal distribution comparison of dry bulb temperature between past (1990-2019), near future (2021-2050), and far future (2051-2080) periods.

An increase in annual and seasonal mean temperature is projected everywhere, with much more significant changes in northern Canada in winter. Warming projection by a low emission scenario is about 2°C higher than the 1986-2005 reference period, remaining relatively steady after 2050. Whereas, in a high emission scenario, temperature increases will continue to reach more than 6°C by late the 21st century (Canada's Changing Climate Report, 2019). Climate change impact varies based on geographical locations. For instance, as shown in Figure 11, the temperature increase in the northern region is higher as compared to the pacific coast or other areas.

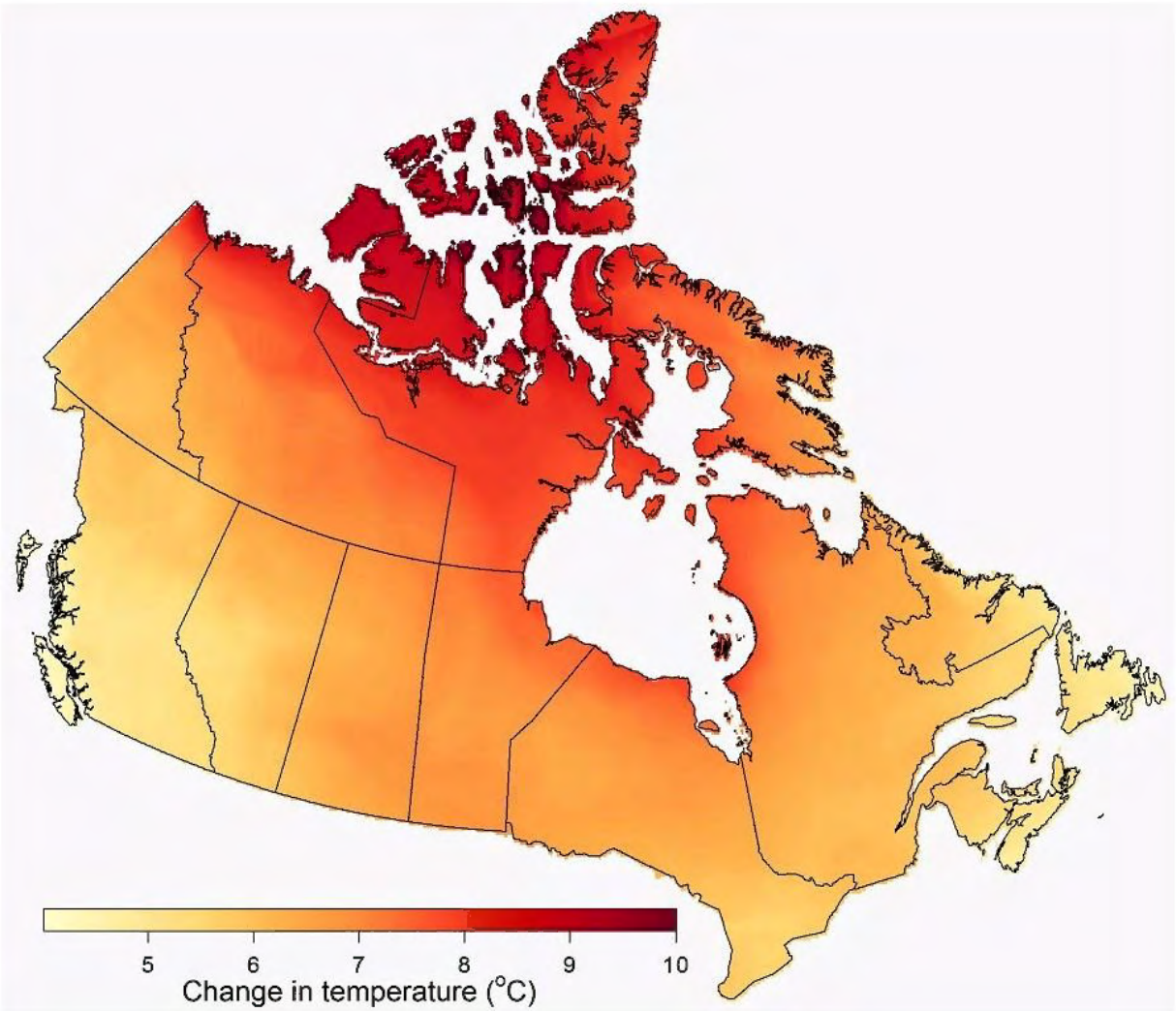

Figure 11: Projected changes in annual temperature by the end of the century from 1986 to 2005 reference period assuming the high emission scenario.

Source:https://www.canada.ca/en/environmentclimatechange/services/climatechange/canadian-center-climate-services/basics/trends projections/changes-temperature

The other weather variable predicted to change is relative humidity. In the first realization, as shown in Figures 12 and 13, slight but uncertain change can be seen between periods. The future periods indicate a higher frequency and a shift in kernel PDF. The distribution of relative humidity deviated from normal PDF and skewed negatively. Relative humidity fits better with other PDF (i.e., Kernel). Unlike the temperature, as shown in Figure 14, the relative humidity of all realization looks to be the same, where all have nearly close statistical data, including prediction 7 (P7).

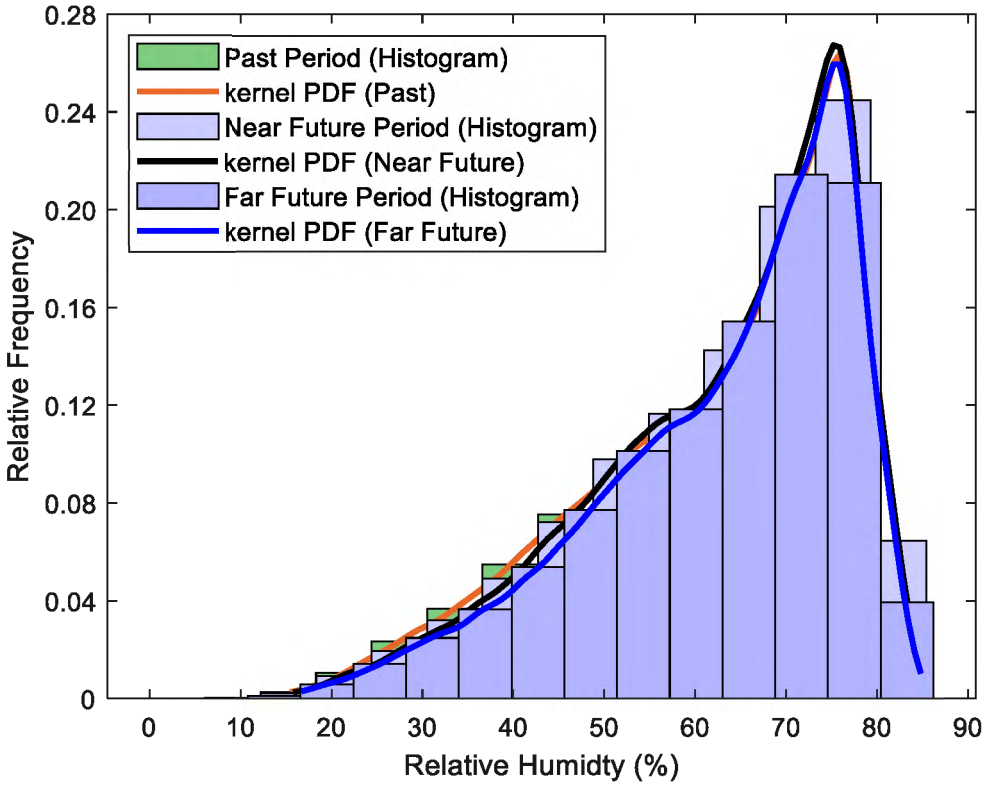

Figure 12: Histogram and kernel distribution comparison for relative humidity in the past (1990-2019), near future (2021-2050), and far future (2051-2080) periods.

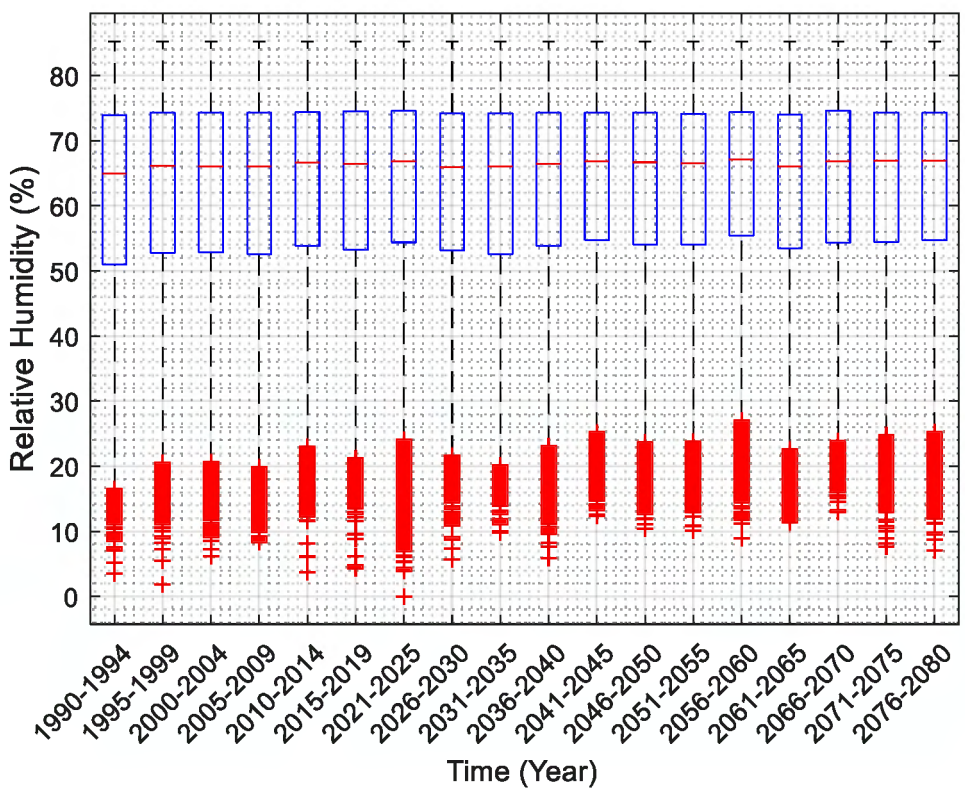

Figure 13: Boxplot of relative humidity for every five years from 1990 to 2080.

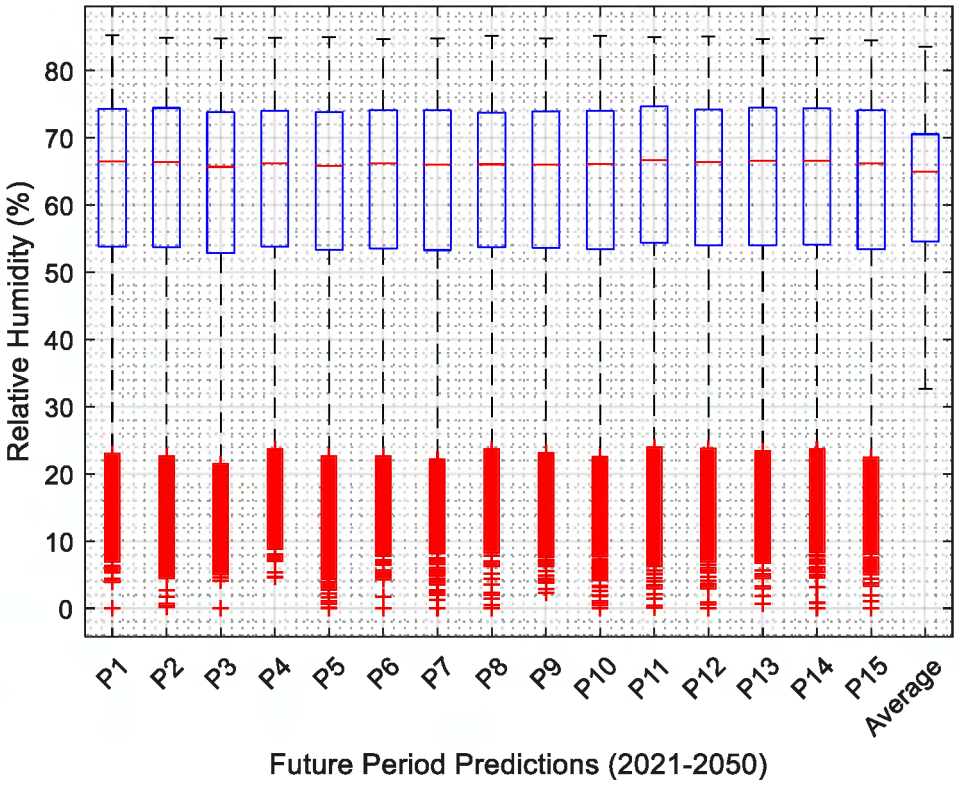

Figure 14: Box plot of relative humidity from 2021 to 2050 for 15 realizations.

The third weather variable projected to increase is rainfall. Figure 15 shows the averaged precipitation data of the realizations. The plot indicates an increasing trend from 1990 to 2080. The data means a 55 mm increase in annual rainfall from baseline to the end of the first study period. Similarly, about 83 mm to the end of the second period.

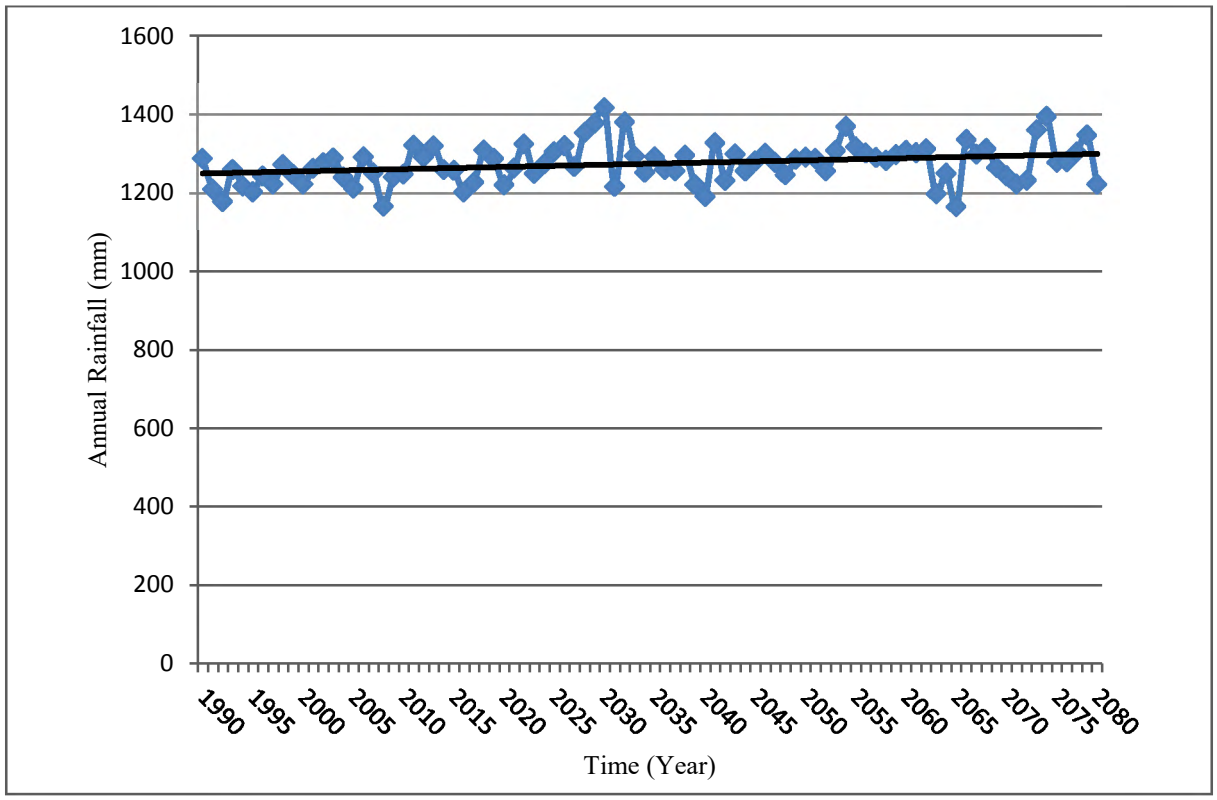

Figure 15: Annual average precipitation trend from 1990 to 2080.

Unlike temperature, which increases everywhere in every season, precipitation shows a different increase and decrease patterns (Figure 16). In the near term, the projection shows a small (generally less than 10%) increase in precipitation in all seasons, with slightly larger values in northeastern Canada. Under the high emission scenario between 2081 and 2100, the changes can be much more significant. The annual precipitation increase in northern Canada can change by more than 30 % (Canada's Changing Climate Report, 2019).

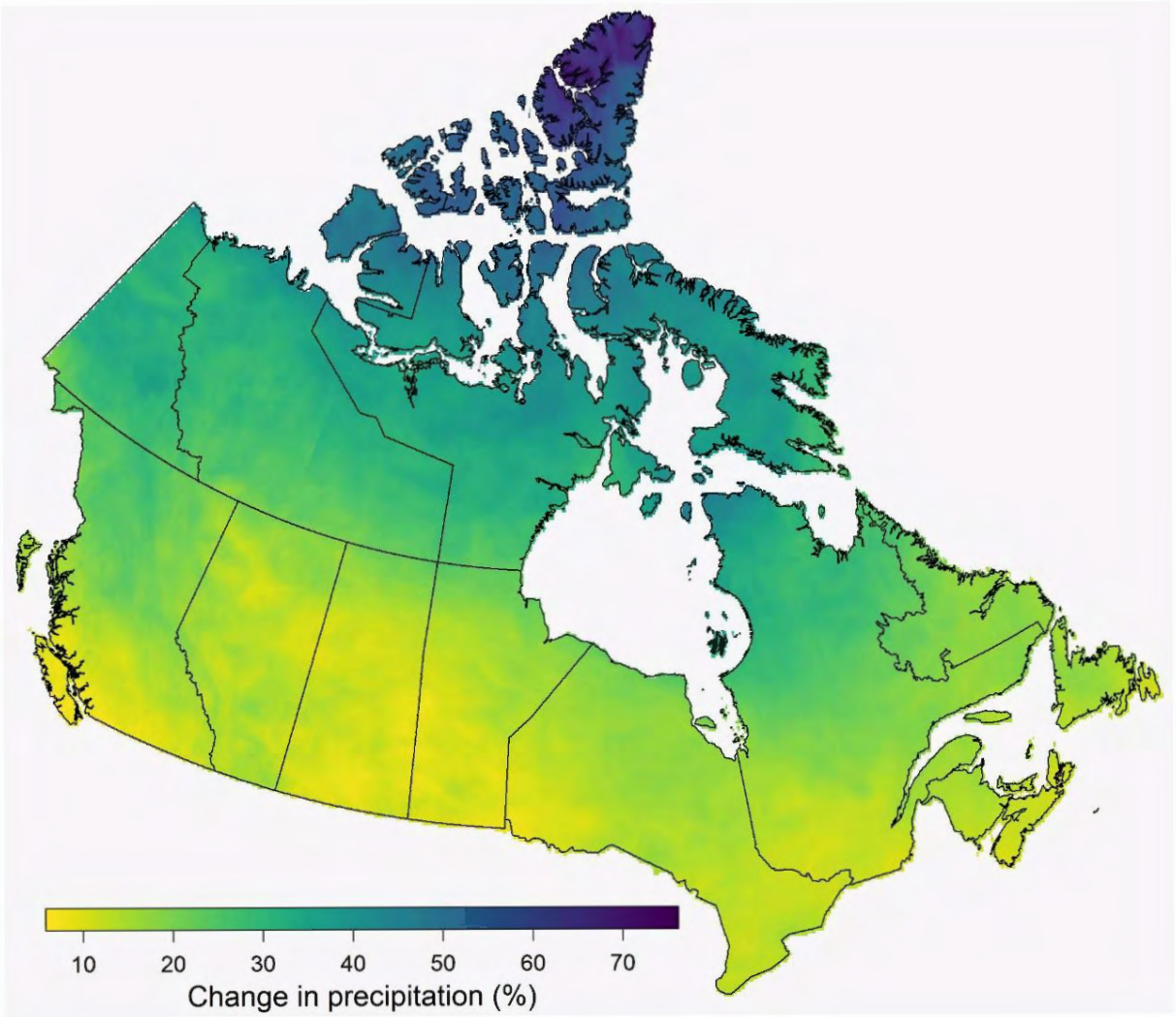

Figure 16: Projected percentage change in annual precipitation by the end of the century from 1986 to 2005 reference period assuming a high global emission scenario.

Source: https://www.canada.ca/en/environment-climate-change/services/climate change/canadian-centre-climate-services/basics/trends-projections/changes-precipitation

The fourth climate parameter, which has a significant impact on energy consumption and hygrothermal performance study, is the amount of solar energy. As discussed in Gaur et al. (2019), there will be an uncertain change in Global Horizontal Irradiance (GHI). Figure 17 shows inconsistent change where the number of years with annual average GHI of above 125 W/m^2 shows an increase and decrease between past and future periods. This data is for the average of realizations.

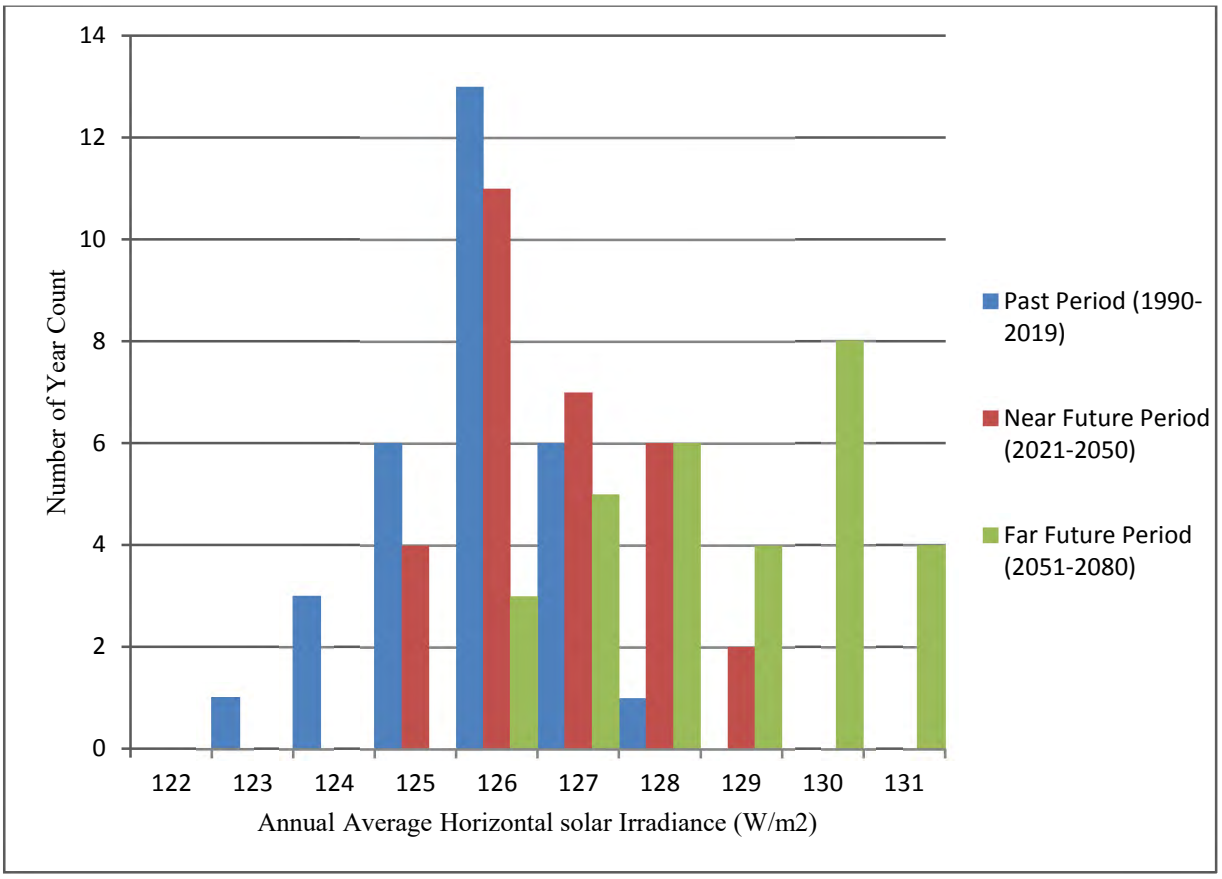

Figure 17: Histogram plot of annual Global Horizontal Irradiance variations between periods.

2.6 High-Resolution Future Weather Data

Despite a significant interest in using future weather data, there is a lack of availability. Mainly due to the difficulty in developing future weather projections within a sufficiently localized region and hourly temporal resolution as required by standard weather file formats (Cox et al., 2015). Generating data typically requires downscaling GCM to regional levels by using a local climate model. Absolute or relative methods can be used to create future weather data (Cox et al., 2015). In the former method, the projection of weather variables from a climate model directly applied. Whereas in the latter approach, projected changes added to an existing weather file.

2.6.1 Projection of climate data using a statistical model (Relative method)

As Kikumoto et al. (2014) pointed there has been an attempt to study the impact of climate change on building energy usage, and most of the efforts rely on modifying current weather data sets by using statistical methods. The most widely used approach is morphing, which works by adjusting present-day design weather data by GCM's climate changes. For instance, the morphing method used to downscale monthly weather forecast to hourly data to study climate change impact on building energy use (Wang et al., 2017). This method modifies existing weather data by using average and standard deviation changes between current and future climate projections from GCM (Kikumoto et al., 2014). Moreover, that one of the essential advantages of this method is to decrease GCM's bias, due to coarser resolution and inaccuracy in parameterization. Besides, since the process relies on statistics, it is not computationally intensive.

A methodology called morphing developed by Belcher et al. (2005) adjusts present-day design weather data by predicted climate changes. By applying the morphing method to the outcome of HadCM3, we developed future data (Shen, 2017). HadCM3 is one of the most widely used GCM. Many researches adopt HadCM3 to generate future weather data. The emission scenarios used in HadCM3 are Special Report on Emission Scenarios A1, A2, B1, and B2 (Robert et al., 2012). HadCM3 model is used for every group of IPCC SRES scenarios to project future weather data. For a specific location, the HadCM3 outputs are monthly mean changes compared to 1961-1990 baselines. World Meteorological Organization recommends using an average period of 30 years to study climate change impact and to use the period 1961-1990 as a baseline for climate reference (Shen, 2017). The application of Weather Morph uses the morphing method. It generates weather data using

IPCC's carbon emission scenarios of B1 (low), B2 (medium-low), A2 (medium-high), and A1FI (high) in 3 time-slices namely 2020s, 2050s and 2080s (Jiang et al., 2019).

2.6.2 Projection of climate data using dynamic climate model (Absolute method)

This approach employs the direct use of climate model outputs. However, to study the impact of climate change on the built environment, weather data generated using GCM cannot be directly applied due to the coarser spatial grid resolution of (100-300 km) and temporal resolution of a monthly forecast. GCM is far enough to evaluate precisely the impact of climate change on buildings since hourly building energy use data is required (Shen, 2017). Besides, GCM cannot represent the details of local phenomena as pointed by Nik et al. (2012), Kikumoto et al. (2014), and Cox et al. (2015). Downscaling using Regional Climate Model (RCM) provides climate projections at a grid resolution of typically 10-50 km and temporal resolution of days or hours. RCM's enables to generate a higher spatial resolution weather data suitable for direct use in building simulations (Nik et al., 2012; Nik et al., 2013). The method used to generate the data discussed in section 2.5 is one example of this method. However, GCM and RCM outputs may involve a systematic error when compared to observation data. As a result, before using climate models, data first bias correction needs to be applied.

2.7 Heat, Air and Moisture Transport in Building Envelope

Building enclosures are exposed to a random climatic loading on the exterior surface and relatively stable indoor conditions on the interior side which causes a transient process of Heat, Air and Moisture (HAM) transport across the structure (Tariku, 2008). Figure 18 shows the dominant climatic variables that affect heat, air, and moisture flow in building enclosure. These variables include temperature, humidity, rain intensity, wind speed, wind direction, solar radiation, and longwave radiation on the outer side. Similarly, temperature and relative humidity on the inner side.

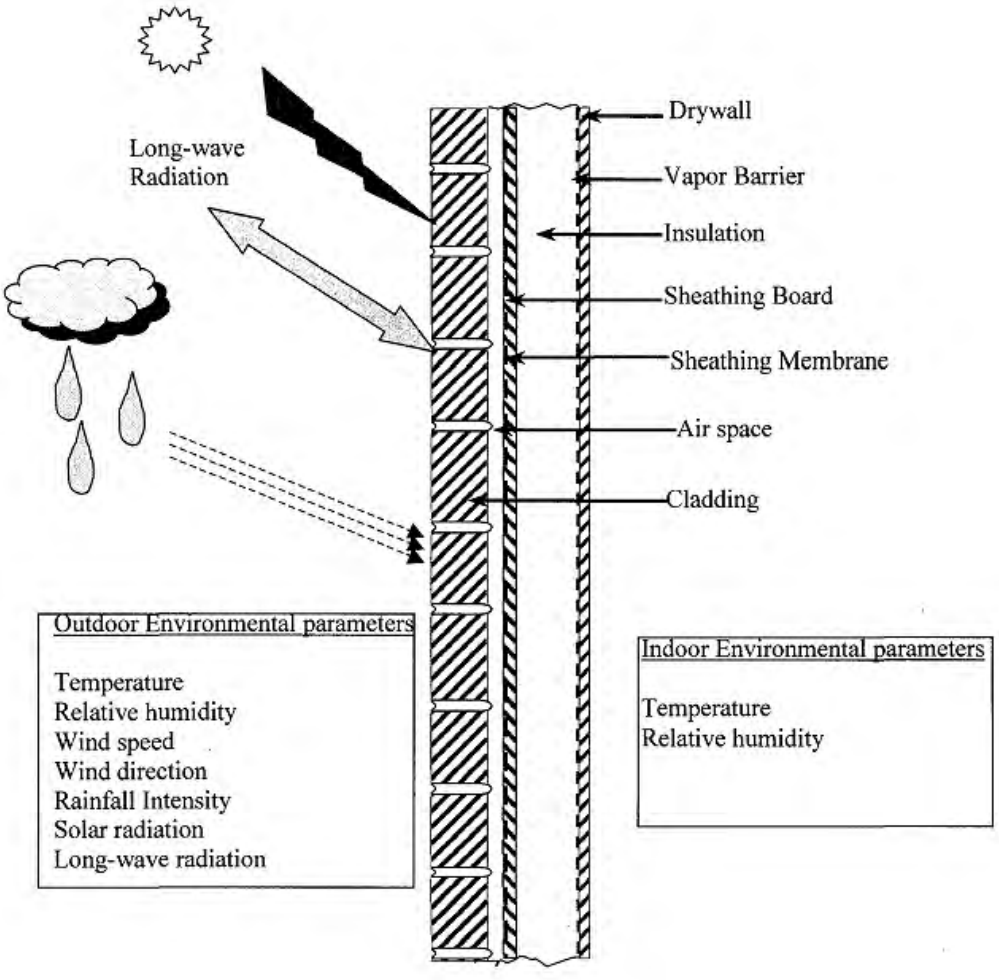

Figure 18: Hygrothermal Loads on Building Envelope. (Tariku, 2008)

Heat and moisture transports are a coupled process, as temperature obtained from a heat transfer equation determines the saturated vapor pressure, which on the other hand,

determines moisture storage and transport properties (Tariku, 2008). Adding that heat transfer depends on moisture conditions such as;

1) Heat release and sink due to phase change (condensation and evaporation),

2) Enthalpy transfer due to moisture transport and

3) The difference in thermal conductivity and heat capacity of the material due to the presence of moisture.

Uncontrolled moisture flow is the primary source of building premature enclosure failure by causing mold growth and deterioration in building materials. Moisture flow in building envelope may cause condensation inside the structure, creating favorable conditions for fungi growth. However, based on climatic conditions, condensation may occur at some time and evaporation in another time, which enables drying. Thus, wetting and drying in building envelopes are dynamical processes determined by the environment. When the moisture content of exterior air exceeds the interior side, the moisture flow occurs from outside to inside and vice versa. The sources of moisture in building envelopes are wind-driven rain, built-in moisture content, and humidity.

The exterior material plays a significant role by deflecting most of the rain that strike walls. However, some amounts of rain could pass through the material, usually controlled by a second protecting layer or using a water-resistive barrier. The vapor retarder layer applied on the internal or external sides depending on the climate condition used to controls moisture flow. Moisture can also be transported by convection, causing a large amount of moisture to flow across a structure. Airflow occurs when there is damage on the layers or if the structure is leaky due to poor sealing. Airflow leads to moisture accumulation, which creates favorable conditions for mold growth in the building envelope. Air movement and ventilation can

induce wetting as well as drying at various times with water entering the assembly can be dynamically stored and released. Also, water vapor retarder helps to (ASHRAE, 2013);

(1) Keep thermal insulation dry;

(2) Prevent structural damage from rot, corrosion, freeze/thaw, and other environmental actions; and

(3) Reduce paint problems on exterior walls.

Several measures help to avoid moisture-related problems in building envelopes. These include reducing air infiltration, preventing water leakage, pressurizing or depressurizing building to prevent moist air from entering into the building envelope and by installing a vapor retarder material either on the inside or outside of insulation for cold and warmer climates respectively.

2.7.1 Wind-Driven Rain

Global future climate projection shows an increase in frequency as well as extreme weather conditions, which can lead to moisture-induced deterioration and decay in construction materials. Even though every building can be affected by severe climate conditions, the effect could be significant for historical buildings. Among the climate conditions, the most significant factor, especially in old buildings, is wind-driven rain (WDR), as it facilitates moisture penetration and bio-deterioration. An increase in extreme weather conditions can intensify a hygrothermal cyclic loading of a traditional building made out of porous materials, which gradually increases the rate of decay (Ayala et al., 2016). Rain can lead to film runoff on building facades, which may cause leakage, or be absorbed by the facade, and transport moisture to internal layers of the facade causing moisture damage (Kubilay et al., 2017). Hansen et al., (2019) pointed out previous studies, and hygrothermal analysis indicates higher

WDR loads result in higher moisture content behind the interior insulation. WDR can cause frost damage on exterior wall surfaces, erosion of building materials, discoloration by efflorescence, moisture-induced salt migration, and mold growth (Kubilay et al., 2017).

The factors that govern the distribution and intensity of WDR on buildings include (Kubilay et al., 2017; Ge et al., 2017; Hansen et al., 2019);

1) Building Geometry
2) Location, and Position of the facade
3) Local Topography
4) Climate Conditions (air temperature, air relative humidity, wind speed, wind direction, rainfall intensity & duration, and solar radiation)

WDR is the type of rain, which is carried by wind and thus characterized by a horizontal velocity vector (Derome et al., 2017). Wind flow affects the droplet trajectories. Three general methods used to assess the intensity of WDR;

1) Measurement
2) Semi-empirical models
3) Numerical methods

Measurement used to verify semi-empirical and numerical models (Orr et al., 2018). Field measurement of WDR is challenging to measure, likely lead to error, and time-consuming (Derome et al., 2017).

Semi-empirical models are based on climatic data from meteorological monitoring stations and can incorporate the anthropogenic and natural context by applying factors, which are being continually improved (Ge et al., 2018). A semi-empirical method is the fastest and easiest method, but it doesn't account for detailed factors (Derome et al., 2017). A semi-

empirical model of WDR considers regional characteristics. Such model represents the amount of WDR exposure over a specific time based on values of wind speed and direction and precipitation (Orr et al., 2018). Some of the main semi-empirical models are;

ISO Standard, (ISO, 2009)

Where the expression to calculate wind drive rain is given by;

$$R_{WDR} = \frac{2}{9} \cdot C_{R\cdot} \cdot C_T \cdot O \cdot W \cdot U_{10} \cdot {R_h}^{0.88} \cdot \cos\theta \quad (1)$$

Where, R_{WDR} is the WDR intensity over vertical surface, C_R roughness coefficient, C_T topography coefficient, O obstruction factor, W wall factor, U_{10} is the reference wind speed at 10m, R_h horizontal rainfall intensity, and θ wind incidence angle

ASHRAE Standard (ASHRAE, 2016)

ASHRAE Standard 160 "Criteria for Moisture-Control Design Analysis" is used to calculate WDR. The amount of rain received by a vertical wall is given by:

$$r_{bv} = F_E \cdot F_D \cdot F_L \cdot U \cdot Cos\theta \cdot r_h \quad (2)$$

Where, F_E rain exposure factor, F_D rain deposition factor, F_L empirical constant, U hourly average wind speed at 10 m height (m/s), θ angle between wind direction and normal to the wall, r_h rainfall intensity on a horizontal surface (mm/h), r_{bv} is rain deposition on a vertical wall kg/(m2.h).

These coefficients have constant value and read from a tabulated table based on different conditions. The exposure factor is a topographic and height factor, which is determined based on three exposure categories (severe, medium, & sheltered). The exposure factor doesn't include in the equation for medium exposure and buildings with less than 10-meter height and covered buildings between 10 and 20-meter height. The deposition factor has three

values; 0.35 for wall below a steep-slope roof, 0.5 for wall below low slope roof, and a value of 1 when the wall subjected to rain runoff.

Straube and Burnett, 2000

Straube and Burnett semi-empirical model relates wind-driven rain by the following equation;

$$R_{WDR} = DRF \cdot RDF \cdot U(z) \cdot R_h \cdot Cos\theta \cdot EHF \cdot TOF \quad (3)$$

Where, U (z) is a power-law function that accounts for moderate wind speed profile, DRF driving rain factor, RDF rain deposition factor, EHF exposure and height factor, TOF topography factor.

The third method relies on a numerical approach or computational fluid dynamics. This method used to obtain accurate and detailed spatial and temporal information on WDR. However, it is computationally expensive and resource-intensive (Orr et al., 2018; & Derome et al., 2017).

2.7.2 Cavity Ventilation

Recently, rain screen wall systems have become a common practice. However, there is a lack of study which indicates the moisture performance of such wall systems compared to walls without a cavity. The study by Tariku et al. (2019) based on experiment, empirical model, and hygrothermal performance assessment found out that wall without ventilation cavity accumulated high moisture content compared to vented and ventilated wall systems. Also the study shows that the sheathing material temperature in vented and ventilated walls was warmer by 85.5 % and 73 % for the period of simulation compared to a non-cavity wall. However, the moisture performance difference between vented and ventilated wall systems has appeared to be insignificant.

A combination of thermal and moisture buoyancy with wind pressures determines ventilation flow. Finch & Straube (2007) assessed ventilated cladding based on field measurements from several residential buildings with ventilated claddings in Vancouver. For a typical four-story building with stucco cladding and a 19mm ventilation cavity, their analysis shows annual ventilation air change per hour of 529 ACH maximum, 140 ACH average, with 106 ACH standard deviation. Ge et al. (2007) pointed air cavity behind cladding can serve as a capillary break by draining out water that penetrates a cavity and enhance drying if vents provided at the bottom and top. Also, using steady-state condition, the drying potential of cavity ventilation was studied, which indicates cavity depth and vent size has a direct effect on airflow in a cavity. For instance, an air cavity depth of 19 mm provides higher airflow and drying rates compared to a 10 mm cavity. But, above 19 mm drying rates weren't significantly affected which the sheathing membrane has a direct effect on the amount of moisture removed by ventilation. Besides, based on simulation results, it's mentioned that an optimum ventilation rate exists, and increasing ventilation above optimum level can result in wetting.

2.8 Moisture Transport Mechanisms

The transport mechanism of heat, air, and moisture is directional across the structure, depending on driving potential direction due to convection (flow), conduction (diffusion), or both (Tariku, 2008). Typical moisture transport process and associated driving potential includes; Vapour Diffusion caused by vapor pressure difference, Capillary Flow caused by suction pressure difference, Convection flow driven by air pressure difference, and Gravitational flow caused by height difference. Likewise, for heat transfer conduction and convection are the dominant transport mechanisms.

2.8.1 Vapour Diffusion

The diffusion caused by differences in the mass fraction is often called Fick's diffusion (Kuenzel, 1995). The driving potentials for water vapor diffusion are vapor pressure difference and temperature difference, which can also act as a driving potential for vapor transport (Tariku, 2008). The latter phenomena is negligible as compared to vapor diffusion and other mechanisms, thus ignoring temperature gradient as driving force, the vapor diffusion equation governed by concentration difference is given by Equation 4;

$$j_v = -\delta_v \frac{\partial(P_V)}{\partial X} \tag{4}$$

Where, j_v represent vapor flux, δ_v is water vapor permeability of the material, and P_v is vapor pressure.

2.8.2 Liquid Transport

Moisture in building materials can present in solid, liquid, or vapor states, and it is difficult to determine the different physical states by measuring separately. Because the fraction of individual state continuously changes due to natural conditions. As a result, it is crucial to examine the combined effect (Kuenzel, 1995). Liquid flow is transported differently within two regions of interest in building materials. The first region characterized by a state of equilibrium called capillary water region, here water transport occurs due to suction pressure or force in the capillary regime. The second region is called supersaturated capillary. In this region, liquid flows through diffusion by a temperature or external pressure under suction. The process of capillary conduction occurs at water contents above the critical moisture content. The suction pressure is usually described by employing a cylinder capillary model, as shown in Figure 19, and is given by Equation 5.

$$P_k = \frac{2\sigma Cos\theta_c}{r} \tag{5}$$

Where, P_k Capillary pressure [pa], σ Water surface tension (N/m), θ_c contact angle, r capillary radius (m)

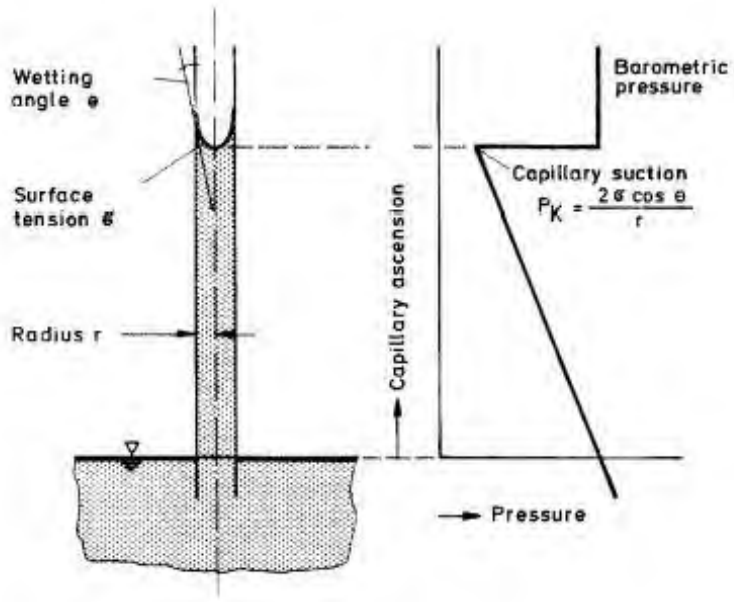

Figure 19: Suction pressure in a cylinder capillary. (Kuenzel, 1995)

The magnitude of suction pressure is equivalent to pore pressure, assuming negligible atmospheric pressure as compared with pore pressure. The relation between vapor pressure over meniscus and pore pressure defined using kelvins equation (Tariku, 2008),

$$P_l = \frac{RT\rho_w}{M_W} \ln\emptyset \tag{6}$$

Where, P_l is pore pressure (Pa), R is the universal gas constant (8.314 J/kmol), Mw is the molar mass of water (0.018 kg/mol), ρ_w is water density (kg/m3), ∅ is relative humidity.

Although capillary suction is a flow the diffusion equation used by many authors, with the capillary transport coefficient strongly dependent on the water content, can lead to a good approximation of the suction process under certain conditions. Capillary conduction occurs at

water contents above the critical moisture content, and liquid transport occurs in microcapillaries (Kuenzel, 1995).

In porous building materials, liquid water transport due to suction pressure gradient and gravity force is given by (Tariku, 2008),

$$j_l = D_l \left(\frac{\partial P_s}{\partial X} + \rho_w g \right) \quad (7)$$

Where, D_l is liquid permeability (s), Ps is suction pressure (Pa), ρ_w density of water (Kg/m^3), and g gravity (m/s^2)

When a capillary active building material comes in contact with liquid water, it absorbs water until it reaches free water saturation. There is also a moisture exchange until equilibrium achieved. In this case, the smaller capillaries have higher suction forces and therefore draw off water from the larger capillaries until all pores filled with water. (Kuenzel, 1995)

2.8.3 Moisture Storage

As mentioned above, a building material can theoretically absorb moisture until all pores filled with water. However, this fact provides no information about its real moisture storage capacity under natural conditions, which indicates the importance of understanding the relations between the water content of a building material and the ambient conditions. As shown in Figure 20, moisture storage grouped into three regimes. The first region ranges from the dry state up to critical water content (around 95 % relative humidity) and is called a hygroscopic (indicated by A, B, & C). The second regime represented by D is called the capillary water region, which ranges from sorption equilibrium up to capillary (free water) saturation. The third region E is the supersaturated region, and it starts from capillary saturation until all pores become filled with no more states of equilibrium. However, in

reality, this region occurs through diffusion by a temperature gradient, and in a laboratory, it occurs through suction under pressure (Kuenzel, 1995).

When hygroscopic building material is in contact with moist air, they become subjected to equilibrium moisture determined by the ambient relative humidity. The hysteresis between absorption and desorption isotherms is not very distinct in most building materials. Generally, the absorption isotherm is enough to characterize the moisture storage of building material. (Kuenzel, 1995)

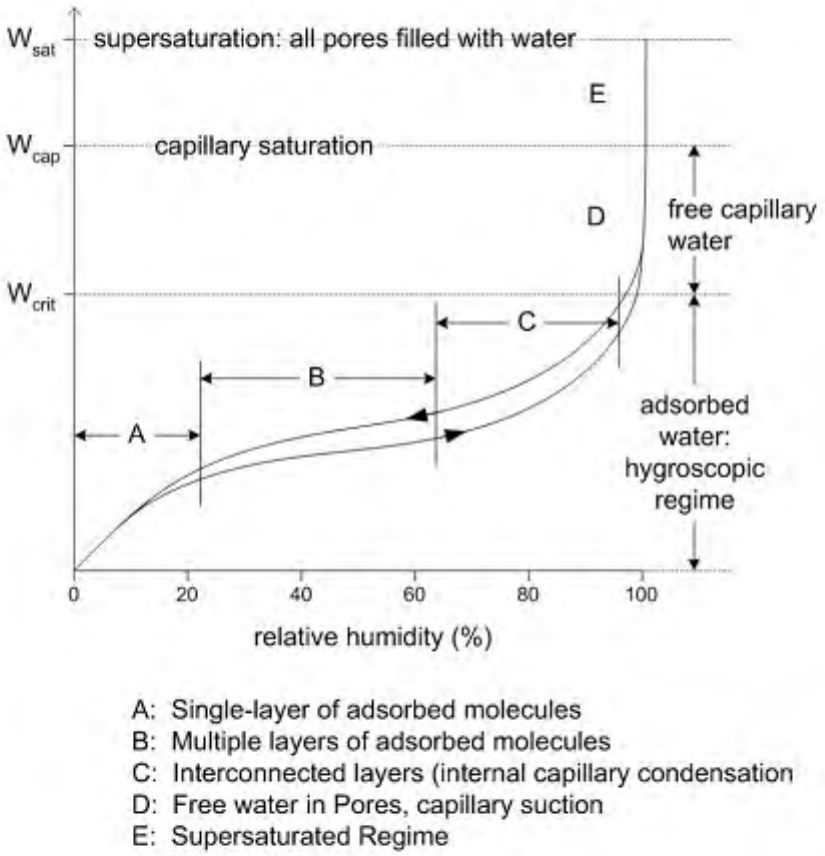

Figure 20: Moisture Storage in Hygroscopic Materials. (Straube, 2006)

2.8.4 Hygrothermal Model and Building Material Properties

Hygrothermal model are crucial tools to understand the heat, air, and moisture flow through building materials which make up a wall structure. Many authors develop various models, and one varies from others based on dimensions, and the scope of physics represents actual

phenomena. Equation 8 to 10 describe the complete transport process of heat, air, and moisture in porous building material (Tariku, 2008);

$$\Theta\frac{\partial \emptyset}{\partial t} = \frac{\partial}{\partial x_i}\left(\left(\delta_v\widehat{P} + D_l\frac{\rho_w R}{M}\frac{T}{\emptyset}\right)\frac{\partial \emptyset}{\partial x_i} + \left(\delta_v\emptyset\frac{\widehat{\partial P}}{\partial T} - D_l\frac{\rho_w R}{M}\ln(\emptyset)\right)\frac{\partial T}{\partial x_i}\right) \quad (8)$$

$$-\frac{\partial}{\partial x_i}\left(D_l\rho_w\vec{g} + \rho V_i\left(C_c\widehat{P}\emptyset\right)\right)$$

Where, $\Theta$is sorption capacity, δ_v vapor permeability $\widehat{P}$ saturation pressure, D_l Liquid conductivity, ρ_w density of water R Universal gas constant, T temperature, M Molecular weight of water,$\emptyset$ relative humidity ρ density of air V_i airflow speed, C_c is a constant term

$$\rho_m Cp_{eff}\frac{\partial T}{\partial t} + \rho_a(Cp_a + \omega Cp_v)\mathrm{div}(VT) + \mathrm{div}\left(-\lambda_{eff}\mathrm{grad}(T)\right) + \{(Cp_a j_a + Cp_v j_v + Cp_l j_l)\mathrm{div}(T)\} = \dot{m}_c h_{fg} + \dot{m}_c T(Cp_v - Cp_l) + \dot{Q}_s \quad (9)$$

Where, ρ_m matrix density, Cp_{eff} effective specific heat capacity, ρ_a air density, Cp_v water vapor specific heat, Cp_a specific heat of air, T temperature, λ_{eff} is thermal conductivity, $\dot{m}_c$ rate of mass change due to phase change, h_{fg} latent heat of evaporation or condensation, $\dot{Q}_s$ heat source, j_a, j_v , j_l represent diffusion flux of air, water vapor, and liquid water, respectively.

The governing equation which represents airflow through a porous medium as defined by Darcy equation,

$$V = -\frac{K_a}{\mu}\mathrm{div}\,(P) \quad (10)$$

Where, K_a and μ represent airflow coefficient and dynamic viscosity, respectively.

Assuming constant air density and by combining with mass and momentum equations the above equation converted to;

$$-\mathrm{div}\left(\rho_a \frac{K_a}{\mu}(P)\right) = -\mathrm{div}\left(\delta_a \mathrm{div}(P)\right) = 0 \quad (11)$$

Where, $\delta_a = \rho_a \frac{K_a}{\mu}$ represent air permeability

Computer-aided numerical simulation tools are widely used to analyze the transport of heat-air moisture (HAM) on building envelopes. However, these practical and user-friendly design tools require reliable inputs to generate useful and meaningful information for the building envelope designers. One of these inputs is the detailed heat, air, and moisture transport properties of construction materials. (Mukhopadhyaya et al., 2007)

The material properties required in hygrothermal modeling includes;

1. Thermal conductivity
2. Specific Heat Capacity
3. Dry Density
4. Equilibrium Moisture Content (Sorption Isotherm), mostly defined as a function of Relative Humidity
5. Water Vapour Permeability as a function of RH, or moisture content
6. Water Absorption coefficient
7. Liquid Diffusivity as a function of RH, or moisture content
8. Porosity
9. Air Permeability
10. Surface absorptivity
11. Surface emissivity
12. Surface reflectivity

Table 6 summarizes commonly used standards to measure material properties. The properties present variation with moisture content and temperature, while constant values approximately represent in some properties.

Table 6: Summary of standards to measure hygrothermal properties (based on Ramos et al., 2009)

Property	Standard
Bulk Density	EN ISO 10545-3 (1995) for ceramic tiles, EN 12390-7 (2000) for concrete, EN 772-13 (2000) for masonry units
Porosity	EN ISO 10545-3 (1995) for ceramic tiles and ASTM C 20 (2000) for fired white ware products
Specific Heat Capacity	ASTM C 351-92b (1999)
Thermal Conductivity	ISO 8302 (1991), EN 12664 (2001), EN 12667 (2001) and EN 12939 (2001)
Moisture Storage Function	EN ISO 12571 (2000)
Water Vapour Permeability	EN ISO 12572 (2001)
Water Absorption coefficient	EN ISO 15148 (2002)

3 Problem Statement

As briefly discussed in the previous sections, buildings and climate are directly related. Since the fundamental reason for the existence of buildings is to provide shelter from undesirable climate conditions. Nowadays, the impact of climate change on human life is becoming more apparent than ever before. Most importantly, it can have a significant impact on the building sector from various aspects. The effects imposed by climate change include an increased energy load due to warming temperature and an increased hygrothermal load from heavy wind-driven rain. Besides, strong structural load due to severe wind, poor outdoor air quality due to frequent wildfires and biodiversity losses, and increased Freeze-Thaw cycles by temperature fluctuations are some of the challenges.

Various studies have been done primarily on how climate change affects building heating and cooling energy demand. However, the impact of climate change on building envelope durability, particularly for wooden frame walls, are not well studied. Moreover, since buildings have a long life span, enclosures are most likely to experience different annual and seasonal climate rather than familiarized weather conditions. Also existing building codes and standards doesn't primarily account for climate change. Which implies during design stages besides practicing codes and standards building enclosure should be designed to perform satisfactorily using past, current as well as future climate conditions. Therefore, the associated adverse effects of climate change can be avoided in the early stages.

4 Research Approach

4.1 Research Objectives

The overall objective of the research is to assess how climate change could impact wood frame walls for residential houses situated in Vancouver in terms of moisture performance. Besides, considering current and future climate conditions, it is aimed to conduct a performance comparison between different wooden frame wall assemblies and various modeling factors.

The specific objective of the research includes;

- To assess how different future climate projections based on SRES (AR4) affects the durability of wall assemblies.
- To estimate long term hygrothermal performance and moisture-related problems by considering climate conditions that the wall systems are most likely to encounter over their life span.
- To evaluate the combined effect of weather variables on orientations in terms of moisture performance and to analyze the directional impact on geographical location.
- To asses how indoor moisture condition affects wall assembly performance.

4.2 Scope

The research is conducted for typical residential buildings, considering the most widely used wooden frame wall assemblies, building materials, and construction practices. The climate change impacts are studied only regionally by exclusively considering the marine climate of Vancouver. Also, the research focused on component level study rather than the whole building.

4.3 Methodology

First, using a combination of absolute and relative approaches, current and future weather data are developed. The data generation used changes in climate variables from HadCM3 with four emission scenarios released by IPCC. The higher temporal and spatial resolution data projected from the GCM are then statistically downscaled using the morphing method to a resolution suitable for the intended study. For precipitation, a weighted average of fifteen projections developed based on CanESM2 by dynamical downscaling CanRCM4 LE as discussed in section 2.5, are used. Then a typical year, which represents the median of all year, is chosen from the series year data. The internal conditions are determined using a class model developed by Sandberg based on a large scale field survey. The indoor humidity conditions have five classes, namely, very low, low, medium, high, and very high. For modeling heat and moisture flow through wall assemblies HAMFit model is combined with COMSOL5.5 Multiphysics Software Heat and Moisture Transport modules by adding a cavity ventilation model. Then hygrothermal performance analyses are performed for typical wood frame wall assemblies using different building materials, various configurations, orientations, and modeling factors. Finally, the wood frame walls durability and the climate change impact are assessed based on moisture content, and its implications on mold growth and biodegradation potential.

5 Hygrothermal Simulation Setup

5.1 Hygrothermal Model

The presented model considered vapor diffusion and capillary suction as moisture transport. Similarly, conduction and latent energy as heat transport mechanisms. In practice diffusion phenomenon is the dominant form of transport mechanism than convection flow, thus for nonporous building materials and unidirectional process without bulk flow the equations that govern moisture and heat flow can be described as;

$$\Theta \frac{\partial ø}{\partial t} - \frac{\partial}{\partial x}\left(\Theta D_w \frac{\partial ø}{\partial x} + \delta_p \frac{\partial}{\partial x}(øP_{sat})\right) = Q_m \tag{12}$$

$$\left(\rho C_p\right)_{eff} \frac{\partial T}{\partial t} - \frac{\partial}{\partial x}\left(k_{eff} \frac{\partial T}{\partial x} + L_v \delta_p \frac{\partial}{\partial x}(øP_{sat})\right) = Q_s \tag{13}$$

Where, Θ is moisture storage capacity (kg/m^3), ø relative humidity, D_w moisture diffusivity (m^2/s), P_{sat} saturation pressure of water (pa), Q_m moisture source (kg/m^3), ρ (kg/m^3) density, C_p (J/kg.K) is heat capacity, T temperature (K), k_{eff} (W/m.K) is effective thermal conductivity, Lv (J/kg) is latent heat of evaporation, and Q_s heat source (W/m^3).

The moisture transport equation assumes;

1) Moisture diffusion due to vapor pressure difference
2) Capillary flow by suction pressure

The heat transfer equation assumes;

1) Heat diffusion or conduction by temperature difference
2) Latent heat transport of moisture

The hygrothermal models are developed in the most recent COMSOL Multiphysics software package version 5.5, where a transient model of heat, air, and moisture transport in building

materials is available. Then heat transfer and moisture transfer in building materials modules were linked through dependent variables and material properties. HAMFit Model represents the transfer of heat and moisture on the enclosure boundaries. A time-dependent study with an hourly time step is selected. The solver setting is manually controlled and assigned absolute tolerance to 10^{-5} and relative tolerance to 10^{-4} while optimizing meshing based on the tolerances.

5.2 Hygrothermal Loads on Boundaries

Boundary conditions are very critical for the accuracy of hygrothermal model outcomes. Thus, the representation of the actual external conditions has a great significance to obtain good results. For the heat transfer between the building envelope and the environment, there exist various mechanisms for energy exchange such as short wave radiation, longwave radiation, heat transfer due to temperature gradient between ambient and surface temperature, and latent heat from wind-driven rain and water vapor diffusion. The variables that make up the hygrothermal load on the external boundary include;

1) Temperature
2) Humidity
3) Solar radiation
4) Sky long-wave radiation
5) Wind speed and
6) Wind direction
7) Horizontal rainfall

Wind-Driven Rain

As discussed earlier, a different modeling approach exists to model wind-driven rain. This study used a semi-empirical model by ASHRAE Standard 160. The model correlates wind speed, direction, and rainfall. The coefficients are determined to assume buildings with less than 10 meters height, building with medium exposure factor, and considering walls exposed to rain runoff. Figure 21 shows the total amount of directional rain received in 2019 in Vancouver. The east wall subjected to most of the driving rain, and Figure 22 shows the hourly amount of wind-driven rain received on this orientation.

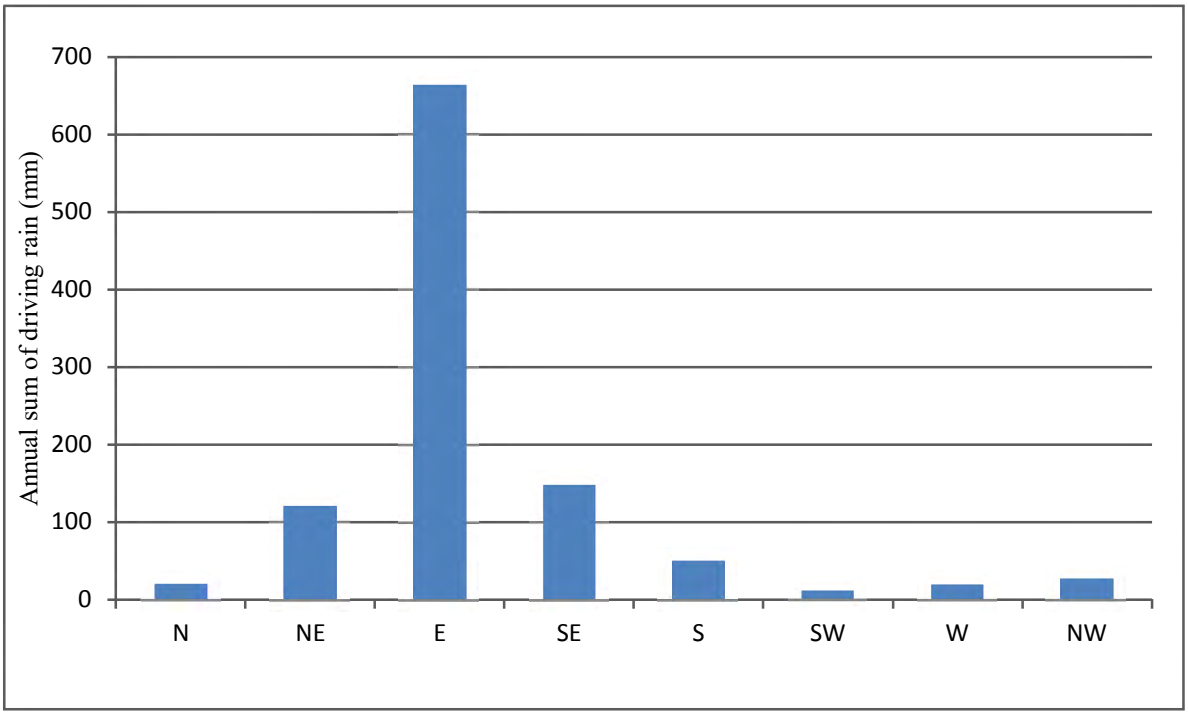

Figure 21: Histogram of the annual sum of directional rain.

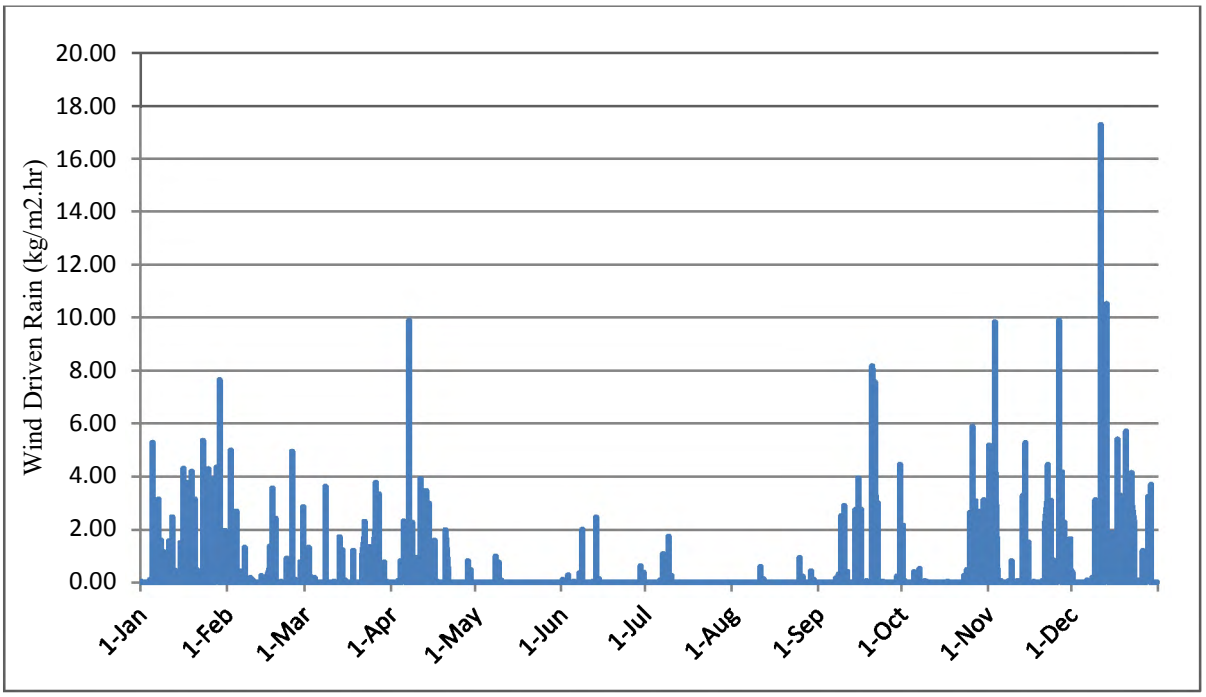

Figure 22: Hourly wind-driven rain on the east wall.

The initial conditions of all materials set to 20°C temperature and 75 % relative humidity. The internal temperature setpoint assumed as 21°C. As shown in Table 7, the indoor vapor pressure determined by summing the outdoor vapor pressure and vapor pressure difference using the Sandberg class model. The model has five group levels which resemble different types of buildings. Very low, low, medium, high, and very high represent storage, office, family house, kitchen, and swimming pool, respectively.

Table 7: Water vapor pressure of class models.

Class-Level	Maximum Pressure Difference (Pa), for monthly average outdoor temperature below 0°C	Minimum Pressure Difference (Pa), for monthly average outdoor temperature above20°C	Equation of a line for monthly mean outdoor temperature between 0 °C and 20 °C
Low	1080	0	$1080 - 13.5xT_{mean,month}$
Medium	810	0	$810 - 27xT_{mean,month}$
High	540	0	$540 - 40.5xT_{mean,month}$
Very High	270	0	$270 - 54xT_{mean,month}$

Figure 23 shows a typical vapor pressure difference calculated using current weather data for outdoor temperature and relative humidity. It includes four class levels, as defined in Table 7. The vapor pressure difference changes monthly in stepwise, where the minimum difference occurs in the summer month and maximum in winter month. Later the two middle classes or medium and high, are considered for indoor moisture condition study.

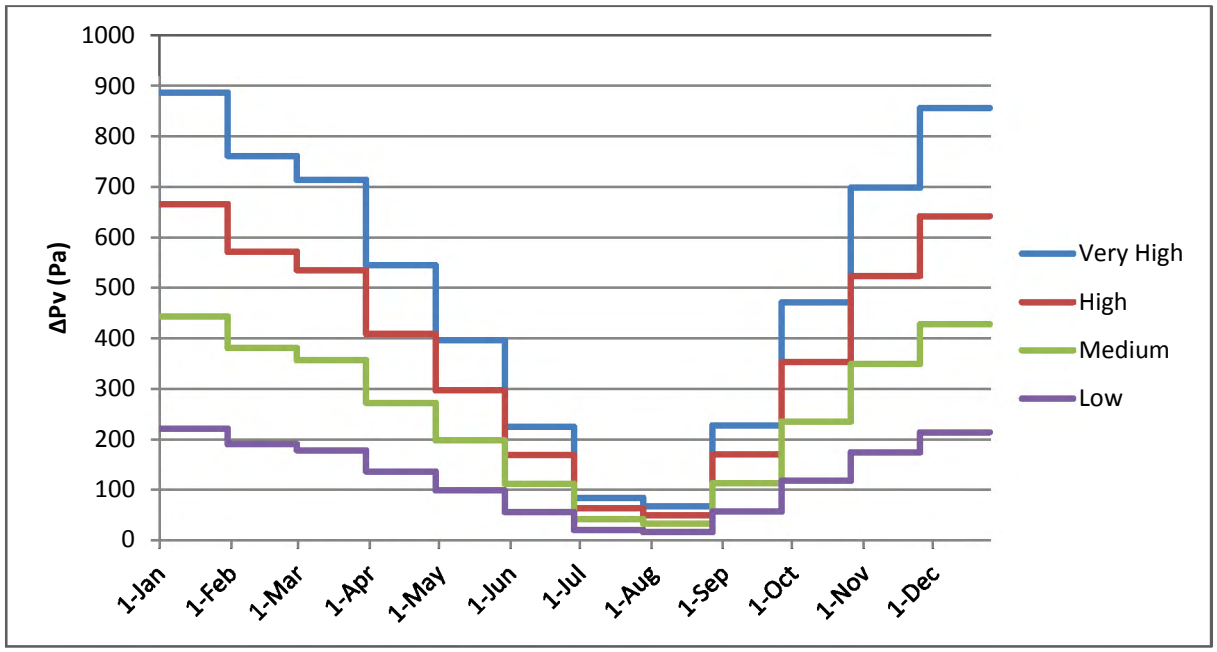

Figure 23: Vapour pressure difference between indoor and outdoor conditions for different class levels.

Moisture Boundary Conditions on Interior surface

Equations 14 and 15 are for air flowing into and out of a structure, respectively. These equations assume water vapor transported by convection (For more about boundary conditions in hygrothermal modeling refer to Append D).

$$q_{m,i} = \beta_i\left(P_{v,i} - P_{vsurf,i}\right) + V_a \cdot \hat{n} \cdot v_i \tag{14}$$

$$q_{m,i} = \beta_i\left(P_{v,i} - P_{vsurf,i}\right) + V_a \cdot \hat{n} \cdot v_{surf} \tag{15}$$

Where,

$q_{m,i}$: Total moisture flux to the interior surface (kg/m^{2}s)

$P_{vsurf,i}$: Partial water vapor pressure at the indoor surface (Pa)

$P_{v,i}$: Partial water vapor pressure of indoor air (Pa)

β_i: Indoor moisture film coefficient (5.4x10^{-10} s/m)

ρ_v: Density of water vapor (kg/m^3)

$\hat{n}$: Indicates direction normal to the material

v_i: Humidity by volume of indoor air (kg/m^3)

v_{surf}: Humidity by volume on the interior surface (kg/m^3)

V_a: Air flow rate (m/s)

Moisture Boundary Conditions on Exterior surface

Similarly, Equations 16 and 17 represent air flowing into and out of a structure respectively,

$$q_{m,e} = \beta_e\left(P_{v,o} - P_{vsurf,o}\right) + V_a \cdot \hat{n} \cdot v_o + \min(WDR, MaxAbs) \quad (16)$$

$$q_{m,e} = \beta_e\left(P_{v,o} - P_{vsurf,o}\right) + V_a \cdot \hat{n} \cdot v_{surf} + \min(WDR, MaxAbs) \quad (17)$$

Where:

$q_{m,e}$: Moisture flux normal to the exterior surface (kg/m^{2}s)

β_e: Outdoor surface film coefficient (25x10^{-10} s/m)

$P_{v,o}$: Vapour pressure of outdoor air (Pa)

$P_{vsurf,o}$: Vapour pressure at the exterior surface (Pa)

v_o: Humidity by volume of outdoor air (kg/m^3)

WDR: Wind-driven rain (mm/h or kg/m^2.s)

$MaxAbs$: Maximum moisture absorption capacity of the exterior material

The term $\min(WDR, MaxAbs)$ chooses the minimum value from wind-driven rain and maximum absorption capacity. So that, the excess water flows over the exterior wall surface is excluded from the simulation.

Heat Boundary Conditions on Outdoor Surface

Assuming both air and liquid water flow into a structure, and only liquid water flow out of the structure, the consecutive equation is given by Equation 18 and Equation 19,

$$q_{h,e} = h_0(T_o - T_{s,e}) + \varepsilon\sigma({T_{sky}}^4 - {T_{s,e}}^4) + V_a \cdot \hat{n} \cdot \rho_a \cdot c_{p,a+v} \cdot T_o + q_{l,e} c_{p,l} \cdot T_o + q_{v,e} \cdot L_v \quad (18)$$

$$q_{h,e} = h_0(T_o - T_{s,e}) + \varepsilon\sigma({T_{sky}}^4 - {T_{s,e}}^4) + V_a \cdot \hat{n} \cdot \rho_a \cdot c_{p,a+v} \cdot T_{s,e} + q_{v,e} \cdot L_v \quad (19)$$

Where

ε: Emissivity of the material

σ: Stefan Boltzmann constant

$q_{h,e}$: Total heat flux on the exterior surface (W/m^2)

h_o: Film coefficient for heat transfer (25 W/m^{2}K), which is the sum of convective and radiative heat transfer

T_o: Outdoor temperature (K)

$T_{s,e}$: Exterior wall surface temperature (K)

T_{sky}: Sky temperature (K)

$c_{p,a+v}$: Specific heat capacity of air and water vapor (J/kg K)

$c_{p,l}$: Specific heat capacity of liquid water (J/kg K)

ρ_a: Density of air (kg/m^3)

$q_{l,e}$: Liquid water flow (kg/m^{2}s)

$q_{v,e}$: Water vapour flow (kg/m^{2}s)

L_v: Latent heat of evaporation (J/kg)

Heat boundary condition on the interior surface

At the indoor wall surface, heat flow includes convection, radiation, advection and latent heat the equation represent airflow into and out of a structure is given by Equation 20 & 21 respectively;

$$q_{h,in} = h_i\left(T_{e,in} - T_{s,in}\right) + V_a \cdot \hat{n} \cdot \rho_a \cdot c_{p,a+v} \cdot T_{e,in} + q_{l,e} c_{p,l} \cdot T_{s,in} + q_{v,e} \cdot L_v \quad (20)$$

$$q_{h,in} = h_i\left(T_{e,in} - T_{s,in}\right) + V_a \cdot \hat{n} \cdot \rho_a \cdot c_{p,a+v} \cdot T_{s,in} + q_{v,e} \cdot L_v \quad (21)$$

Where:

$q_{h,in}$: Total heat flow across the exterior surface (W/m^2)

h_i: Sum of convective and radiative heat transfer at the interior surface (8.3 W/m^2.k)

$T_{e,in}$: Equivalent indoor temperature or sol-air temperature (°C)

$T_{s,in}$: Indoor wall surface temperature (°C or K)

5.3 Cavity Ventilation Model

The one-dimensional simulation of the hygrothermal model of building envelope deals with heat and moisture transport processes through the system. Since cavity ventilation acts perpendicular, it can only be defined as a source or sink in the transport equations. The source terms for heat S_h and moisture S_m is given by Equation 22 and 23 (Kuenzel et al., 2008):

$$S_h = \rho_a \cdot c_{p,a} \cdot ACH_{vent} \cdot d_{vent} \frac{T_e - T_{vent}}{\Delta x} \tag{22}$$

$$S_m = ACH_{vent} d_{vent} \left(\frac{p_{v,e}}{R_v T_e} - \frac{p_{v,vent}}{R_v T_{vent}} \right) / \Delta x \tag{23}$$

Where, $c_{p,a}$ (J/kg.K) Specific heat of air

d_{vent} (m) Cavity width

ACH_{vent} (s^{-1}) Cavity air change rate

p_v (Pa) Vapor Pressure

R_v (J/kg.K) Water vapor gas constant

T (K) absolute temperature

Δx (m) width of ventilation zone

ρ_a (kg/m3) outdoor air density

Index outdoor air conditions (e) and cavity ventilation (vent)

5.4 Material Properties

As previously discussed, hygrothermal modeling requires different heat, air, and moisture properties of the building materials, which involves transport, storage as well as combined properties. These properties are measured according to standards using various testing

equipment's and procedures, for this study the thermal and moisture properties of the building materials were taken from ASHRAE's Research Project 1018-RP by Kumaran et al. (2002), which includes;

1) Bulk density
2) Thermal conductivity
3) Specific heat
4) Sorption isotherm
5) Water vapor permeability
6) Moisture diffusivity

The first three properties are considered not to be affected by moisture or temperature since the variations are minimal. The equilibrium moisture content and vapor permeability expressed as a function of relative humidity. The moisture diffusivity defined as a function of moisture content. Figure 24 shows the sorption isotherm plot of three building materials to log scale for simple visualization, when relative humidity approaches 100 %, the sorption isotherm of some building material increases sharply than others. Similarly, Figure 25 shows the vapor permeability properties.

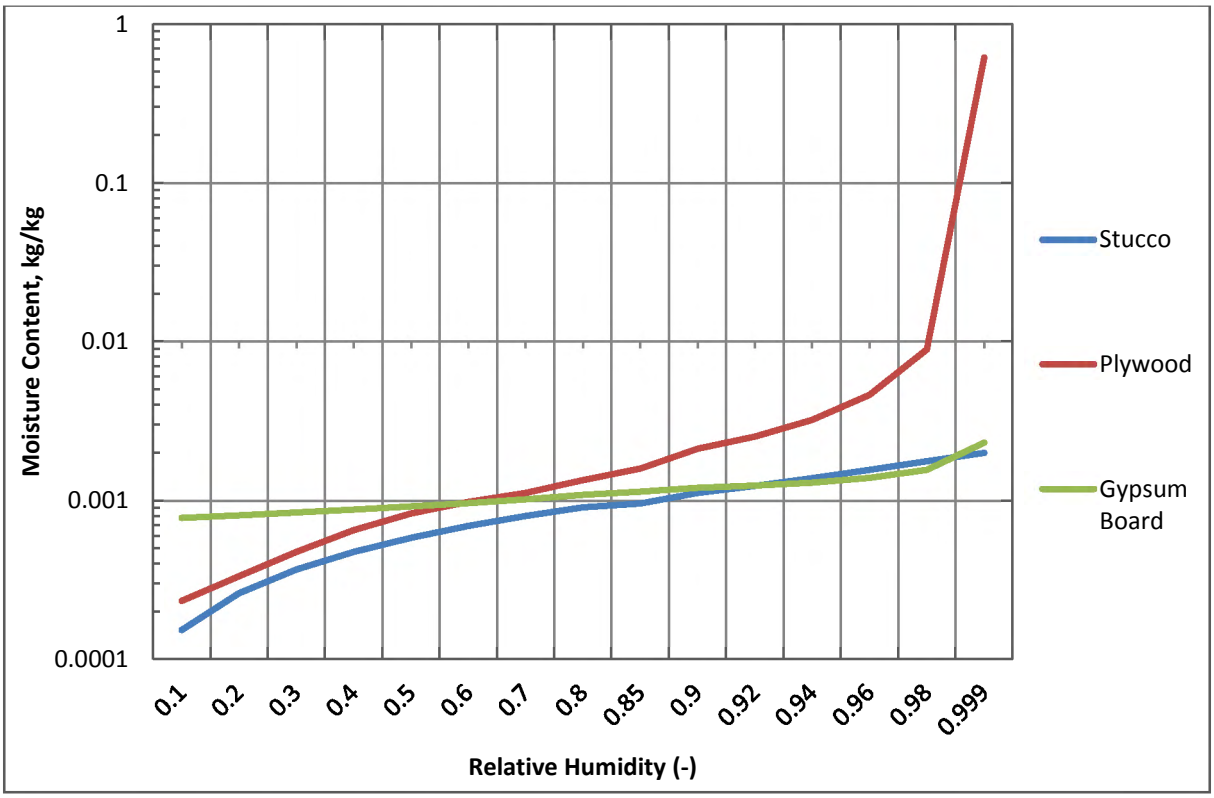

Figure 24: Moisture storage property of the building materials, y-axis plotted to log scale.

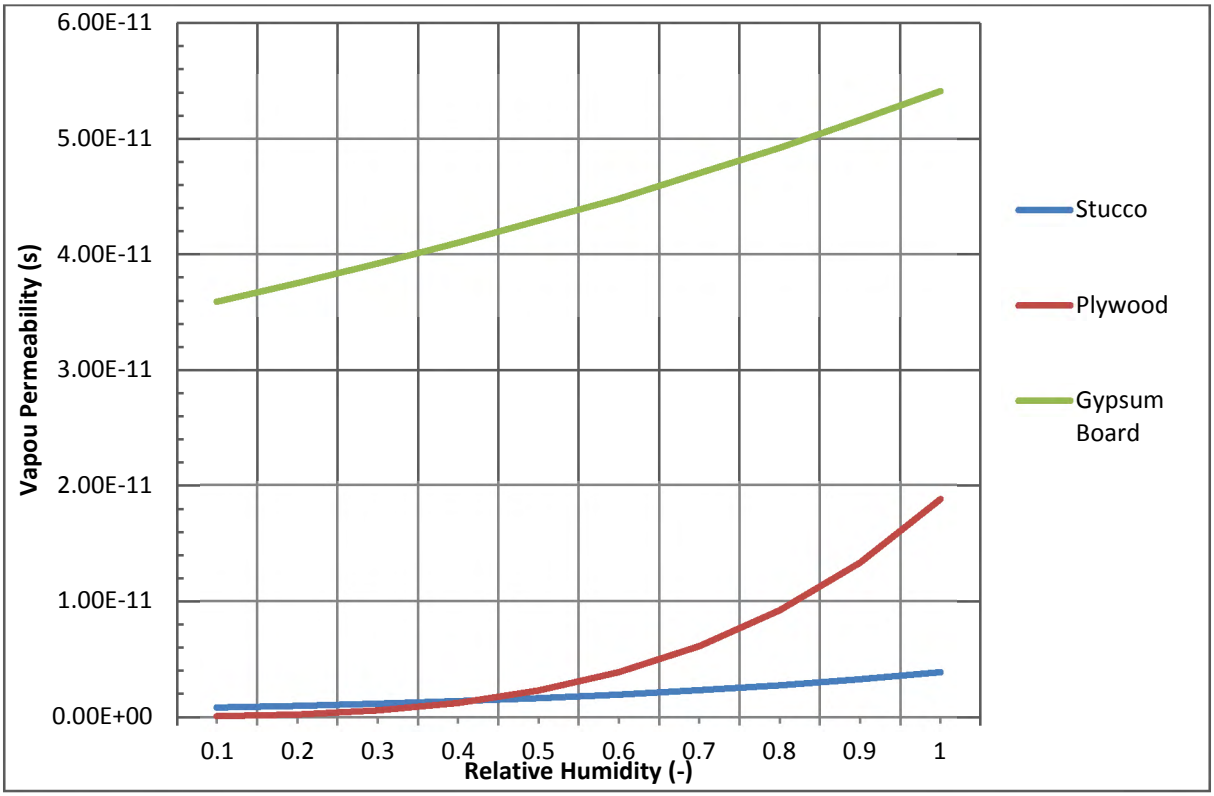

Figure 25: Vapour permeability property of the building materials.

5.5 Hourly Weather Data Development

As mentioned earlier, to generate future weather data, this study used the time series adjustment method or morphing technique for all climatic variables except precipitation. The procedure of morphing present-day weather data involves a set of steps. Depending on the change that the climatic variables defined, three types of adjusting methods are to be applied. Namely, Shifting, Stretching, and Combination of Shifting and Stretching. Which are given by (Equation 24-26),

$$x = x_0 + \Delta x_m \tag{24}$$

$$x = \alpha_m x_0 \tag{25}$$

$$x = x_0 + \Delta x_m + \alpha_m (x_0 - \langle x_o \rangle_m) \tag{26}$$

Where; x is the morphed climatic variable, x_0 is baseline climatic variable, Δx_m is the absolute change in monthly mean for month m, α_m is stretching factor, and $\langle x_o \rangle_m$) monthly mean of baseline.

The shifting method applies when the change of the climatic variables given as absolute change. For instance, HadCM3 predicts Total Cloud Cover as an absolute change in monthly mean. As a result, the shifting method is appropriate to adjust the current day weather data. However, for other climatic variables such as relative humidity and wind speed, the monthly changes are given as fractional change relative to baseline. The stretching method is applicable for fractional change. A combination of both applies when changes described by both an absolute increment and fractional, which is the case for dry blub temperature. Table 8 summarizes the type of method used to the climatic variables.

Table 8: The type of morphing method applied to climatic variables to adjust present-day weather data.

Climatic Variable	Adjustment Method		
	Shift	Stretch	Shift and Stretch
Dry-bulb Temperature			✓
Relative Humidity		✓	
Wind Speed		✓	
Global Horizontal Radiation		✓	
Atmospheric Pressure	✓		
Total Cloud Cover	✓		

As an example, let see how the transformation method applied for dry bulb temperature. As shown in the above table, this variable is adjusted using a combination of shift and stretch methods given by Equation 27,

$$T = T_0 + \Delta T_m + \alpha_m(T_0 - \langle T_0 \rangle_m) \tag{27}$$

Where T & T_0 represent future and current dry bulb temperature respectively, ΔT_m & $\langle T_0 \rangle_m$ are the mean monthly dry bulb temperature of future and current dry bulb temperature respectively, and α_m is stretching factor defined by Equation 28,

$$\alpha_m = \frac{\Delta T_{max,m} - \Delta T_{min,m}}{\langle T_{0,max} \rangle_m - \langle T_{0,min} \rangle_m} \tag{28}$$

Where, $\Delta T_{max,m}$& $\Delta T_{min,m}$ are maximum and minimum monthly change of dry bulb temperature, respectively. $\langle T_{0,max} \rangle_m$ & $\langle T_{0,min} \rangle_m$ represent current daily maximum and

minimum dry bulb temperatures, respectively. Figure 26 shows morphed present-day data for the first five days of June by applying the morphing equations.

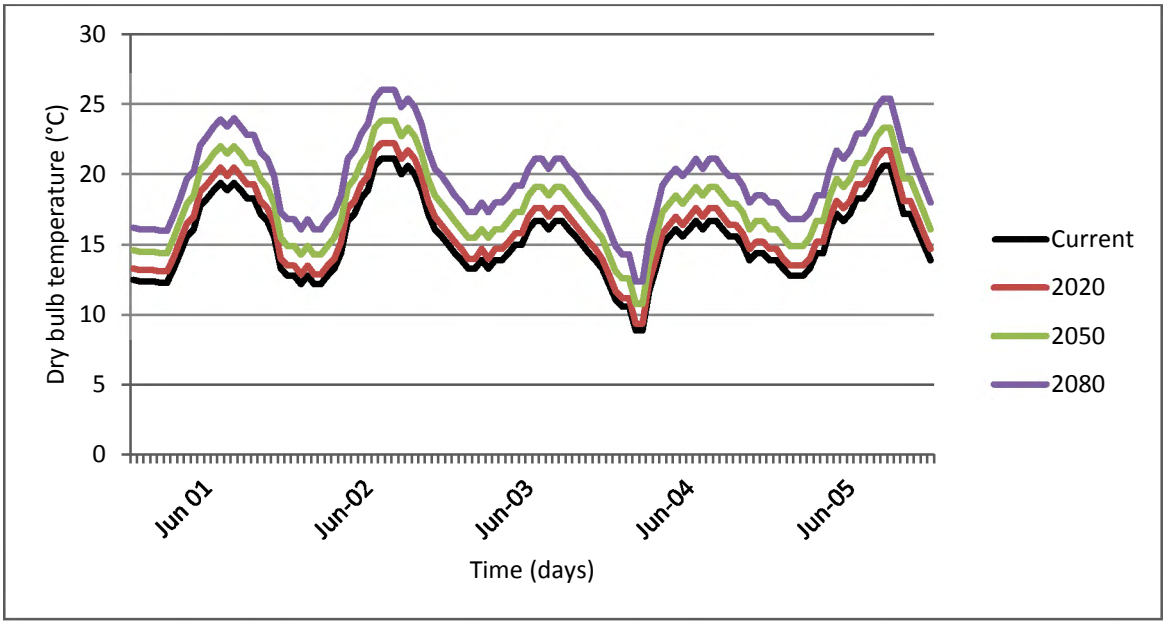

Figure 26: Morphed dry-bulb temperature (Scenario A2).

Likewise, other weather variables can be morphed depending on the type of adjustment method. For instance, relative humidity and global horizontal irradiance transformed using stretching method defined by Equation 29 and Equation 30 respectively;

$$RH = RH_o(1 + \alpha_{RHm}) \tag{29}$$

$$GHI = GHI_o(1 + \alpha_{GHIm}) \tag{30}$$

Where, RH & RH_0 are hourly future and current relative humidity respectively, similarly GHI & GHI_0 for global horizontal irradiance, α_{RHm}& α_{GHIm} are fractional mean monthly change for relative humidity and global horizontal irradiance, respectively. By following the above procedure, as shown in Figures 27 and 28, the weather variables are morphed.

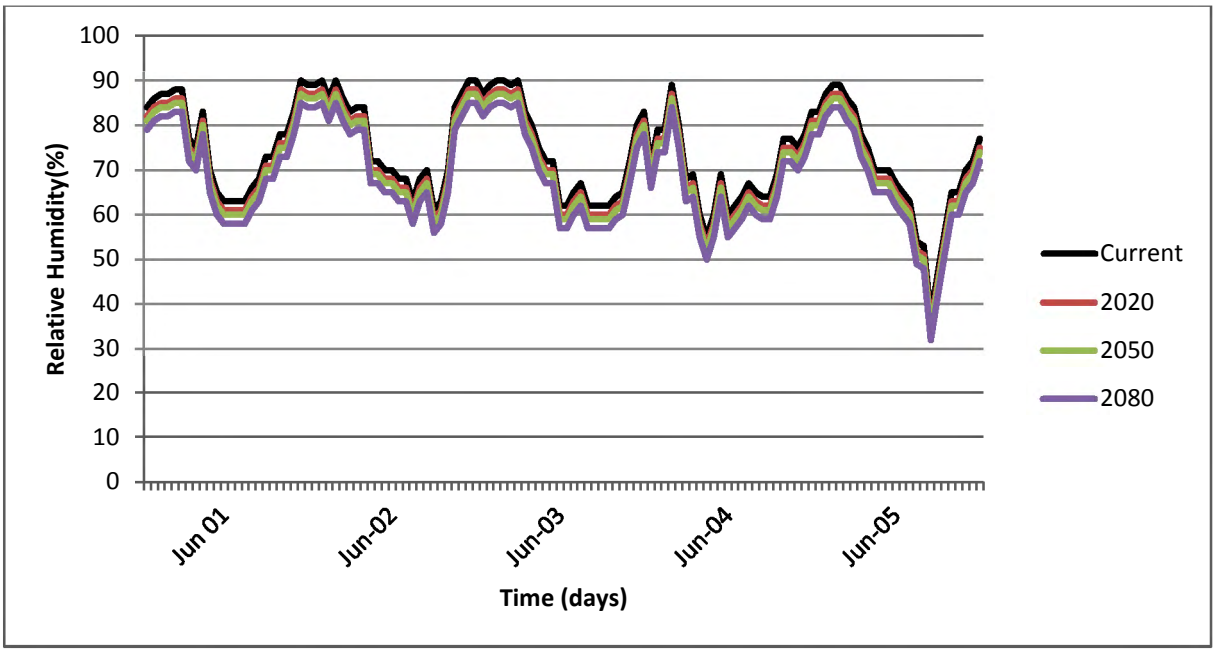

Figure 27: Morphed relative humidity (Scenario A2).

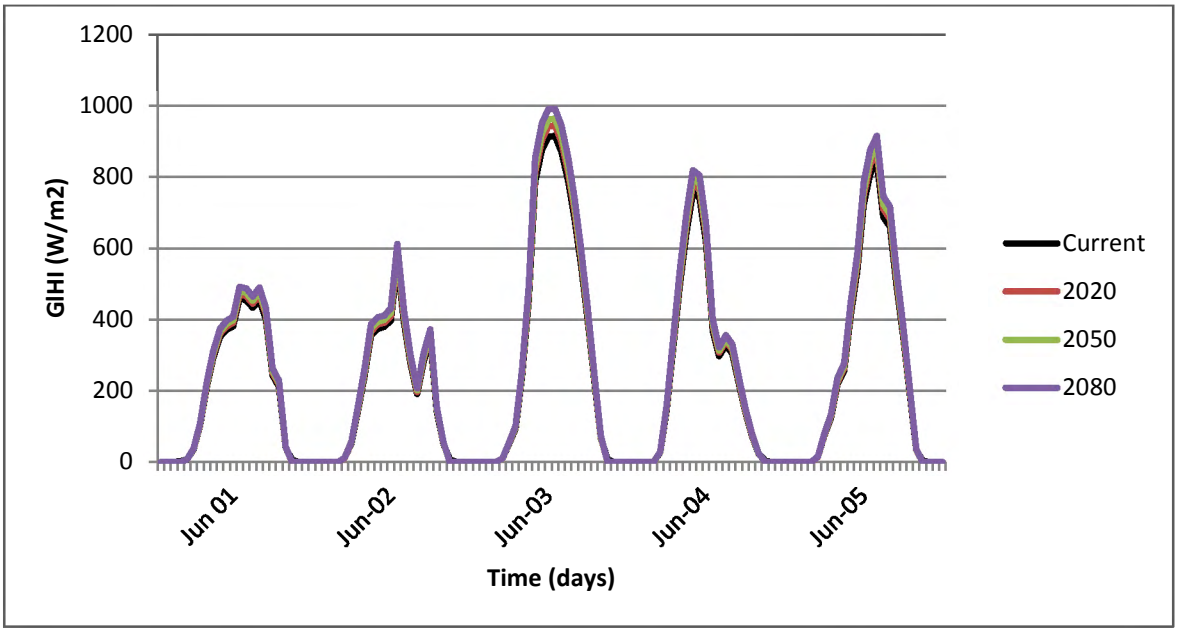

Figure 28: Morphed global horizontal irradiance for scenario A2.

As discussed earlier, the weather data generation involves absolute and relative methods. All-weather variables except precipitation developed using the latter approach. The morphing processes are applied using the Weather Morph application. For precipitation, three groups of 31 years long hourly weather data developed by Gaur et al., (2019) using CanESM2 and

CanRCM4 are used by averaging predictions. For times slices such as the 2020s, 2050s, & 2080s, a representative years are constructed by choosing the months with the smallest daily absolute deviation from the overall monthly mean, which aims to select a year which could represent average effect.

5.6 Mold Growth

Mold growth in building materials caused by the combined effect of environmental factors and material properties. Some building materials have better mold resistance capability than others. Both the availability of water and optimum temperature favors the growth of fungi and other organisms. The surface of the material is where the growth of fungi starts. Therefore, the surface conditions have greater importance in the study of mold growth. This study used ASHRAE (2016) mold growth model. The mold index ranges from zero to six, where a low value indicates less effect, and a higher value above three shows a higher chance for mold-related problems (Table 9). First, the building material assigned in one of four sensitivity classes, namely, high, high to medium, medium, and low sensitivities. Wood related products assigned to an insensitive class. For sensitive & very sensitive groups the critical relative humidity value is calculated by;

$$RH_{crit} = \begin{Bmatrix} -0.00267T_s^3 + 0.16T_S^2 - 3.13T_s + 100, when\ T_s \leq 20\ °C \\ 80\ when\ \ T_s > 20\ °C \end{Bmatrix} \quad (31)$$

Where T_s is surface temperature in °C

When the surface relative humidity is higher than the critical values mold index is calculated using the following equation;

$$\frac{dM}{dt} = \frac{k_1 k_2}{168 \cdot \exp\ (-0.68lnT_s - 13.9inRH_s + 0.14W + 66.02)} \quad (32)$$

Where k_1 represent mold growth intensity factor, chosen from a table according to sensitivity class and current mold index value, W is a constant value of 1 for all sensitivity classes except for very high sensitivity level and k2 is mold index attenuation factor calculated by,

$$k_2 = \max\{1 - \exp[2.3(M - M_{max})], 0\} \quad (33)$$

Where M_{max} is the maximum mold index corresponding to surface temperature and relative humidity,

$$M_{max} = A + B\left(\frac{RH_{crit} - RH_s}{RH_{crit} - 100}\right) + C\left(\frac{RH_{crit} - RH_s}{RH_{crit} - 100}\right)^2 \quad (34)$$

Where A, B, and C are coefficients to be chosen according to material sensitivity class.

Table 9: Mold Index Indication (Based on Vereecken et al., 2012)

Index	**Growth Rate**	**Description**	**Microscopic level**	**Visually detectable**
0	No mold growth	Spores not activated		
1	Small amounts of mold on a surface	Initial stages of growth	✓	
2	<10% coverage of mold on a surface		✓	
3	10-30% coverage of mold on a surface, or < 50% coverage of mold (microscope)	New spores produced	✓	✓
4	30-70% coverage of mold on a surface, or > 50% coverage of mold (microscope	Moderate growth	✓	✓
5	>70% coverage of mold on a surface	Plenty of growth		✓
6	Very heavy, dense mold growth covers nearly 100% of the surface	Coverage around 100%		✓

Relative Humidity and Temperature (RHT) Index

It is widely accepted that deterioration in building materials caused by the combined effect of temperature and moisture conditions. Favorable humidity and temperature for an extended period can facilitate degradation. RHT index developed to quantify and compare the localized hygrothermal response in a critical region. This index captures the moisture and thermal conditions coexisting above a pair of threshold levels (Beaulieu et al., 2002). The chosen critical values are 5°C for temperature and 80 % for relative humidity.

Where: n is the number of hours

$$RHT = \begin{cases} \sum_{i=0}^{n} (RH - RH_{critical}) x (T - T_{critical}) \text{ , } for\ RH \geq 80\%, T \geq 5°C \\ 0,\ otherwise \end{cases} \quad (35)$$

5.7 Benchmarking

Heat, Air, & Moisture Standards Development (HAMSTAD) is a European project primarily developed to validate hygrothermal modeling tools. HAMSTAD consists of five benchmarking exercises. The exercises involve two or more transfer mechanisms from heat, air, and moisture, which also considers non-linear problems (Tariku, 2008). One of the benchmark has an analytical solution. Thus, exact solutions are even available, making it ideal for validating HAM models solved by numerical methods. HAMFit model used to address the benchmarks. The solutions obtained from the model shown by Research-Model indicates a compatible result compared with various HAM models developed by different authors.

Benchmark-1

The first exercise is an internally insulated roof structure with three layers. From inside to outside; insulation material (50mm), load-bearing material (100mm), and sealing layer

(0.5mm). The transport mechanisms considered here are heat and moisture transfer. The initial conditions assumed on this exercise are; 10°C for temperature in both insulation & load-bearing materials, 145 kg/m^3 & 0.065kg/m^3 moisture content for load-bearing, and insulation material respectively. The surface film coefficients for heat transfer are 25 W/m^2.k and 7 W/m^2.k on outdoor and indoor sides, respectively. Similarly 0 and $2x10^{-8}$ s/m as moisture film coefficients on outdoor and indoor sides. The sealing layer only serve as a vapor retarder with 10^{-12} s/m vapor permeability. Table 10 shows the interdependence of the material properties.

Table 10: Material properties expressions of first benchmark exercise.

Properties	Materials	
	Load Bearing	Insulation
Water retention	Function of suction pressure	Function of suction pressure
Equilibrium moisture content (EMC)	Function of relative humidity	Function of relative humidity
Vapour diffusion	Function of EMC	Function of EMC
Liquid water permeability	Function of EMC	-
Thermal conductivity	Function of EMC	Function of EMC
Heat capacity	Constant	Constant

The boundary conditions consider thermal gradient by temperature difference and diffusion by vapor pressure difference. The indoor temperature was maintained at a constant value of 20 °C while the outdoor equivalent temperature varies, as shown in Figure 29. The vapor pressures vary on both indoor and outdoor sides with the highest difference lies on the start and end of the simulation period (Figure 30).

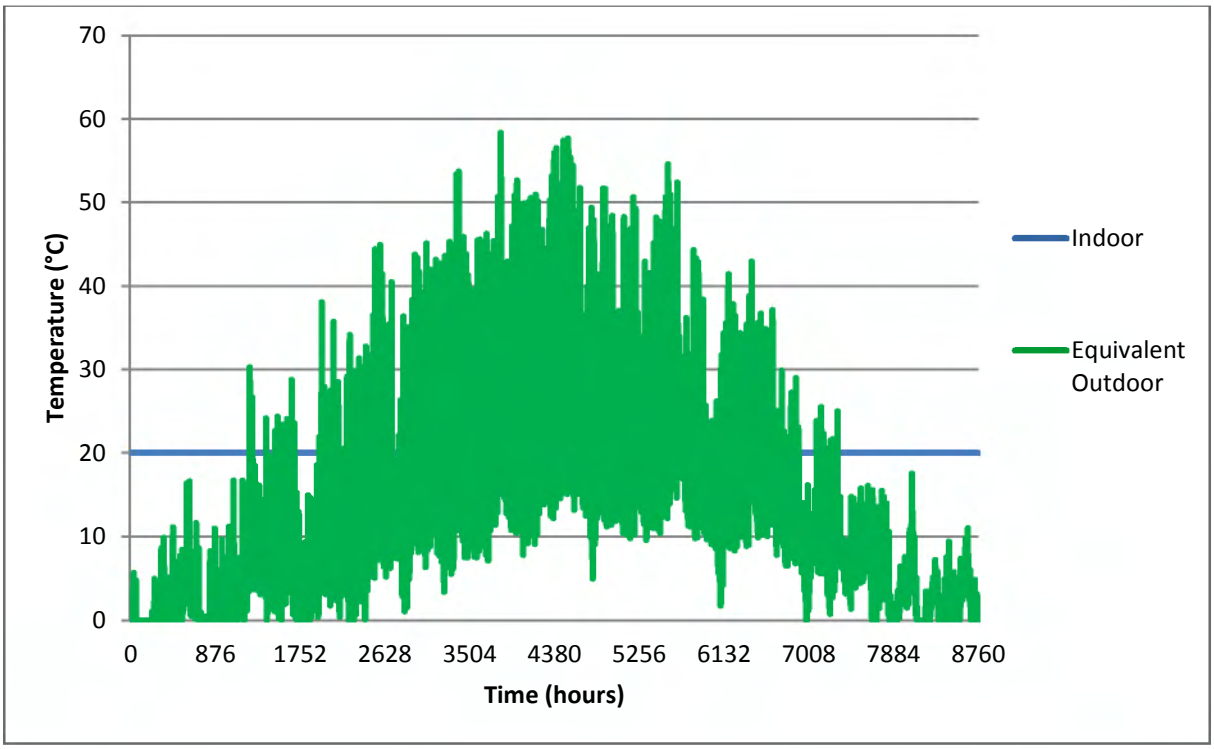

Figure 29: Temperature on the boundaries.

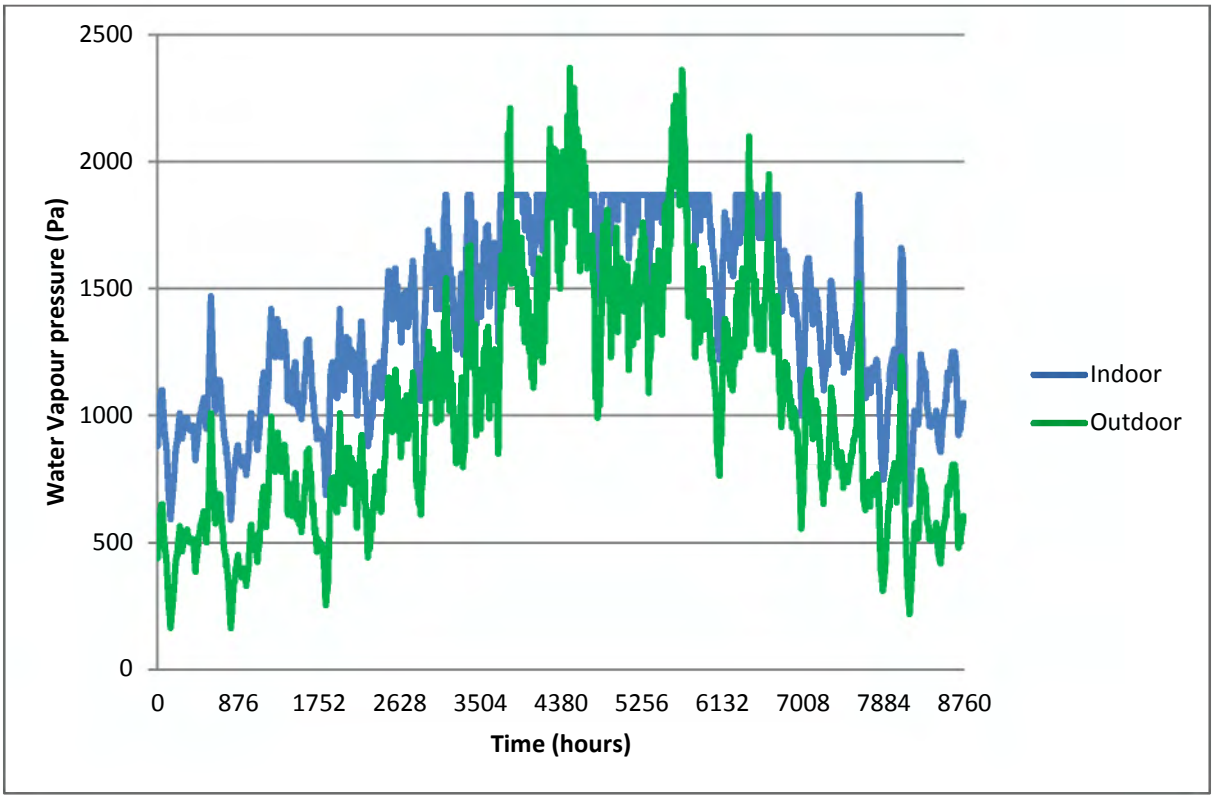

Figure 30: Vapour pressure on the boundaries.

The outputs from this exercise include moisture content on load-bearing and insulation materials, for different locations along the axis (1D), and as a function of time (hourly for a year). The other outputs are integrated moisture content for each material and heat flux on the interior boundary. As shown in Figure 31 to 33, the result obtained from this model indicates the best performance as compared to other models. The name Research model shows the model result used in this research.

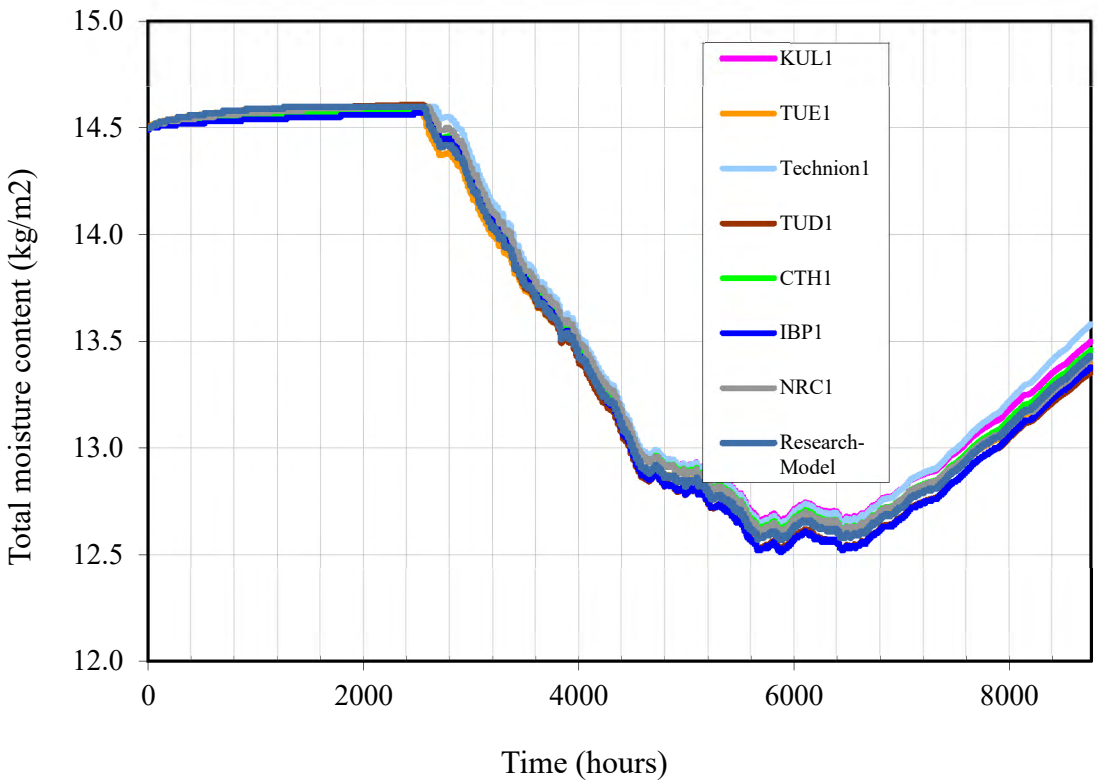

Figure 31: Total moisture content on load-bearing material in the first year.

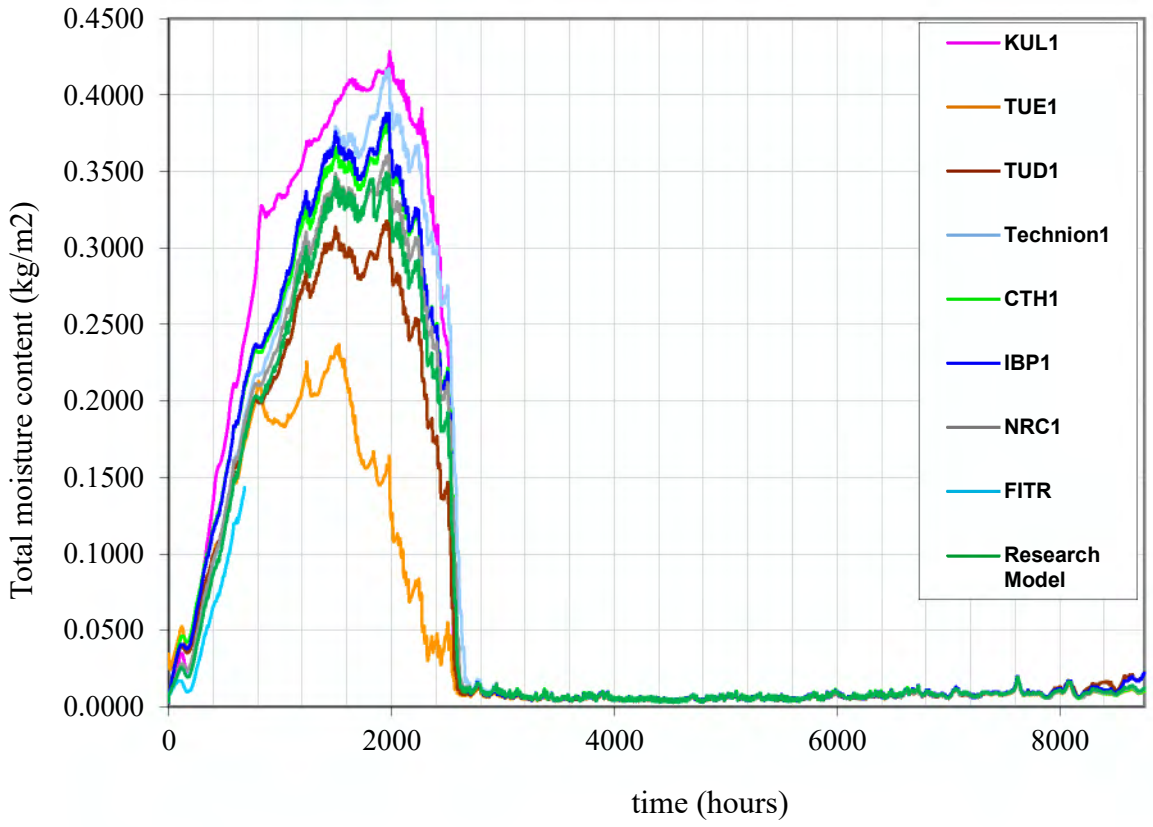

Figure 32: Total moisture content on insulation material in the first year.

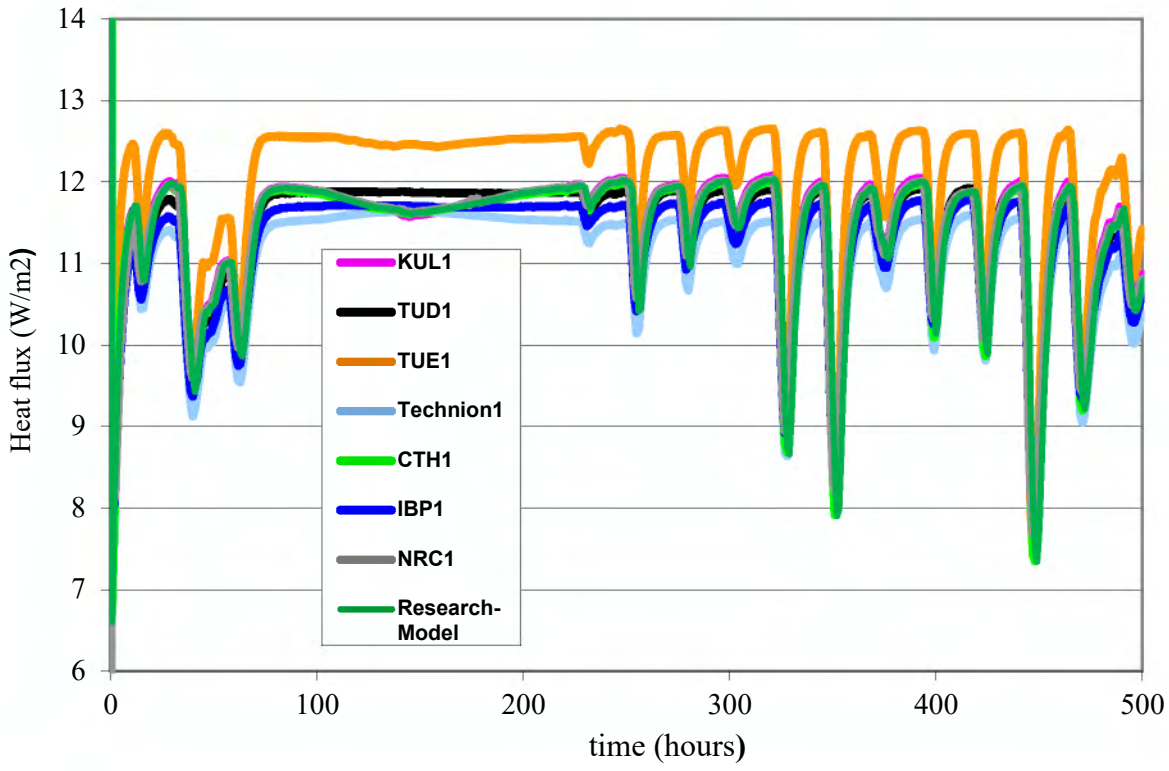

Figure 33: Heat flux on the interior boundary in the first year.

Benchmark 2

This exercise comes with an analytical solution for perfectly airtight homogeneous material. The structure has only one solid layer with 200 mm thickness. The problem analyzed under isothermal condition keeping both sides at 20°C equivalent temperature, which accounts for both convection and radiation exchange. The surface film coefficient for heat transfer is assumed to be the same on both sides, with 25 $W/m^2.k$, similarly 10^{-3} s/m as moisture transfer film coefficient. Table 11 shows the material properties of this exercise;

Table 11: Material properties in the second benchmark exercise.

Properties	Expression/Value
Equilibrium moisture content (kg/m^3)	$\frac{116}{(1-\frac{1}{0.118}\cdot\ln(RH))^{0.869}}$
Vapour diffusion (s)	10^{-15}
Moisture diffusivity (m^2/s)	$6x10^{-10}$
Thermal conductivity (W/m.K)	0.15
Specific heat capacity (J/kg.K)	800
Density (kg/m^3)	525

The initial conditions are 20°C temperature and 95% relative humidity. As shown in the following Figures, the moisture content of the material reduces over time from wet initial state. The outputs from this benchmarking exercise include moisture content on selected cross-sections at 0.01m interval for each hour and a time slices of moisture content throughout the material at 100, 300, and 100 hours. Some of the plots are cut-views to increase resolution. The results obtained from this research model perform best as compared to the analytical solution as well as other models.

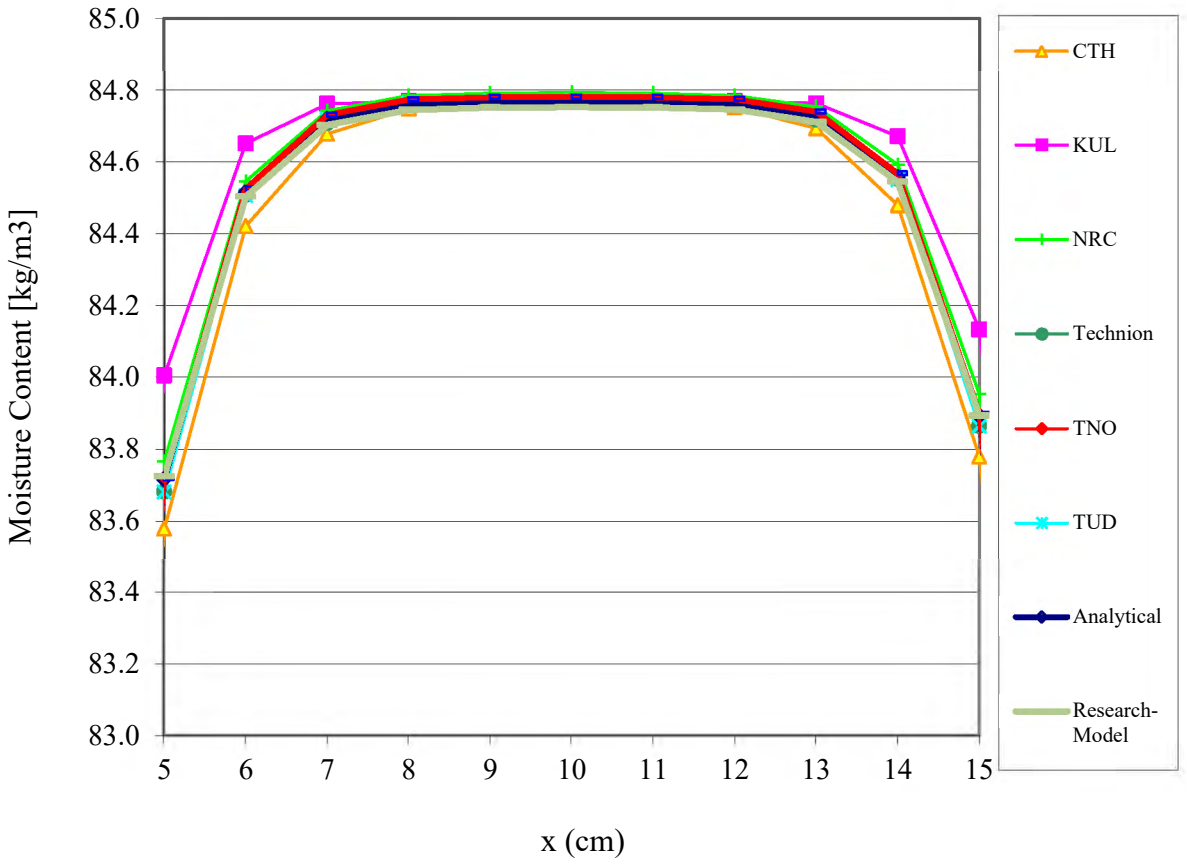

Figure 34: Moisture content along the x-axis at 100 hours.

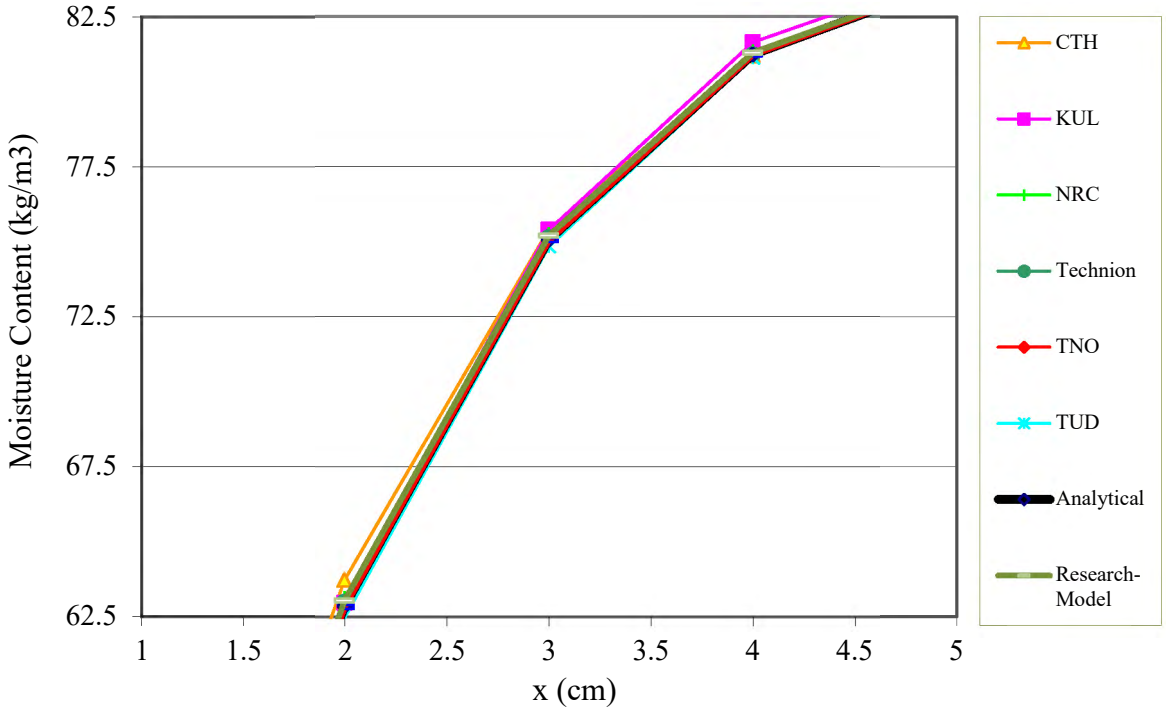

Figure 35: Cut view of moisture content along the x-axis at 100 hours.

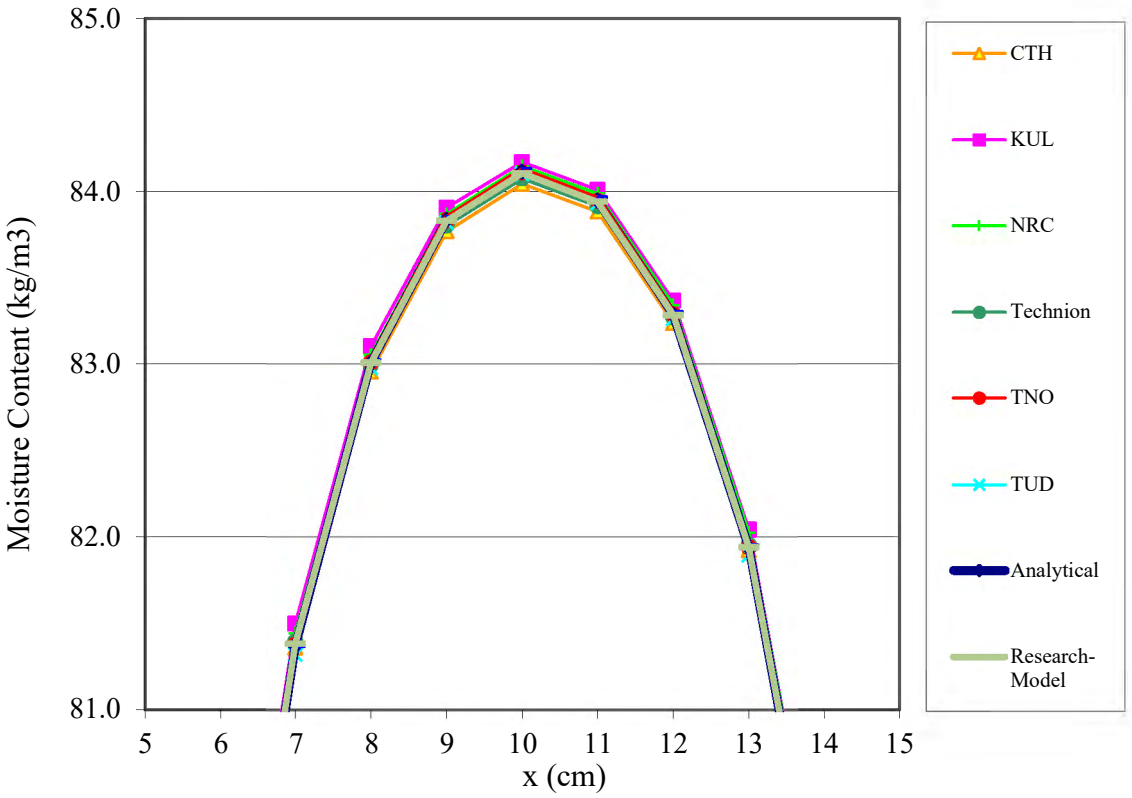

Figure 36: Moisture content along the x-axis at 300 hours.

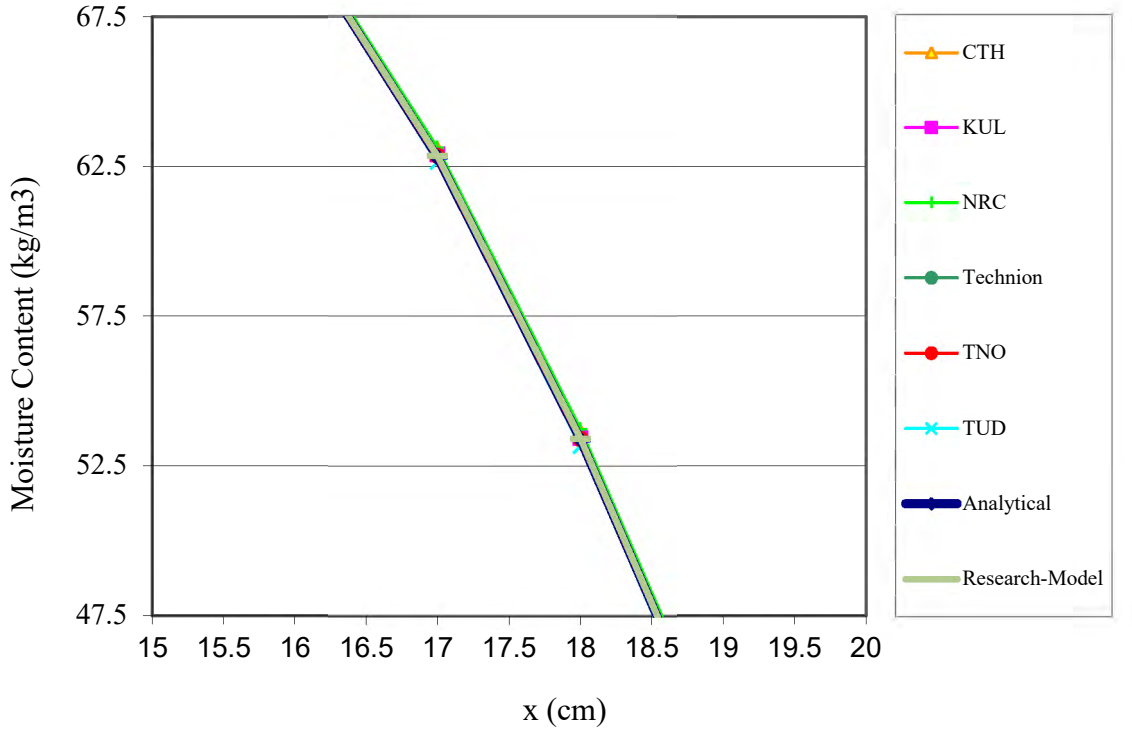

Figure 37: Cut view of moisture content along the x-axis at 300 hours.

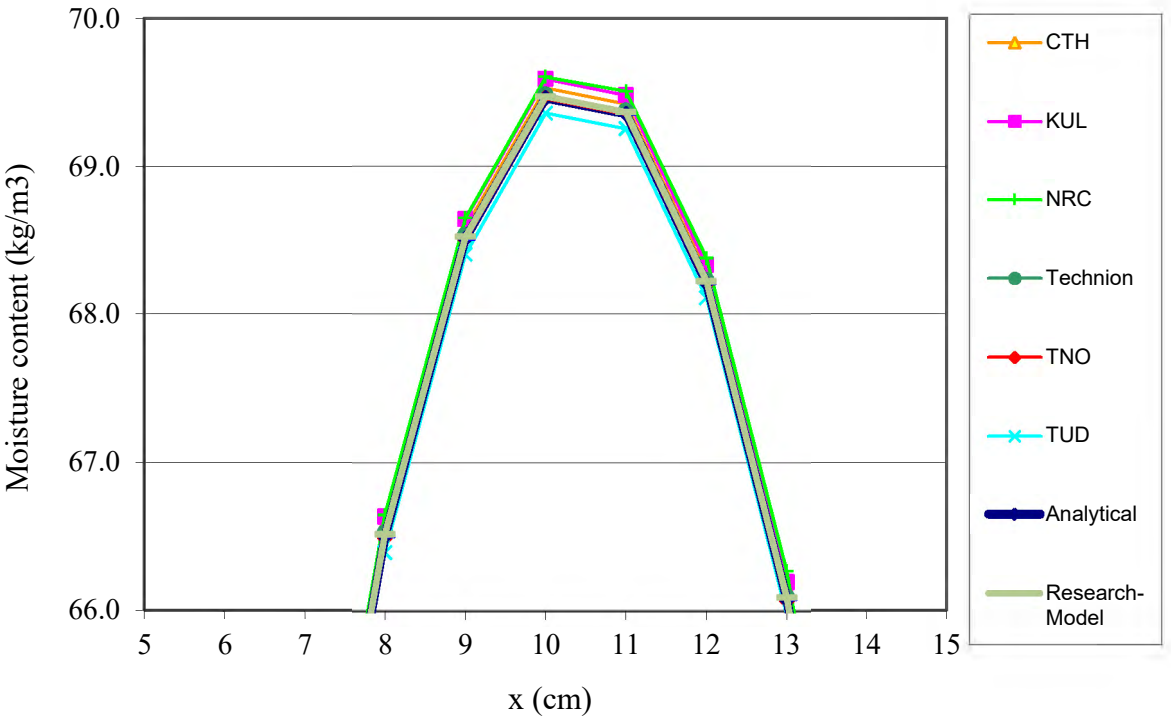

Figure 38: Moisture content along the x-axis at 1000 hours.

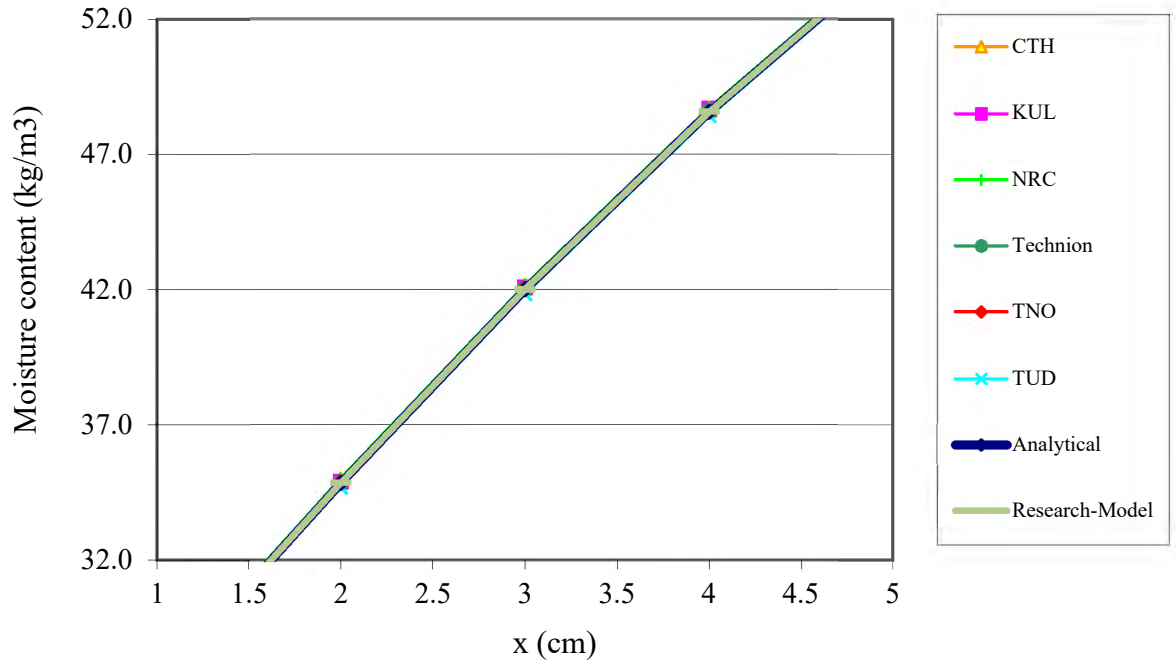

Figure 39: Cut view of moisture content along the x-axis at 1000 hours.

Benchmark-3

The third exercise assumes a light wall system with one layer. This problem involves airflow across the material, and it's ideal for modeling heat, air, and moisture transfer in nonporous building materials. The air flows from outside to inside for the first 20 days at the constant air pressure difference of 30 Pa. Between 20th and 21st days, the pressure difference reduces sharply and reverses the flow direction from inside to outside and maintains a constant pressure difference of 30 Pa. Darcy equation governs the airflow where the flow speed linearly increases with pressure difference. Indoor conditions maintained at constant values of 20 ℃ temperature and 70% relative humidity. Similarly, 2℃ and 80 % RH on the exterior side. The equilibrium moisture content (EMC) of the material given as a function of suction pressure. The expression of vapor diffusion, liquid water conductivity, and thermal conductivity are all given as a function of EMC. The outputs from this benchmark include temperature and moisture content on selected cross sections for all the simulation hours (2400 hrs). As shown in Figure 40 to Figure 45, the model result performs best with other models.

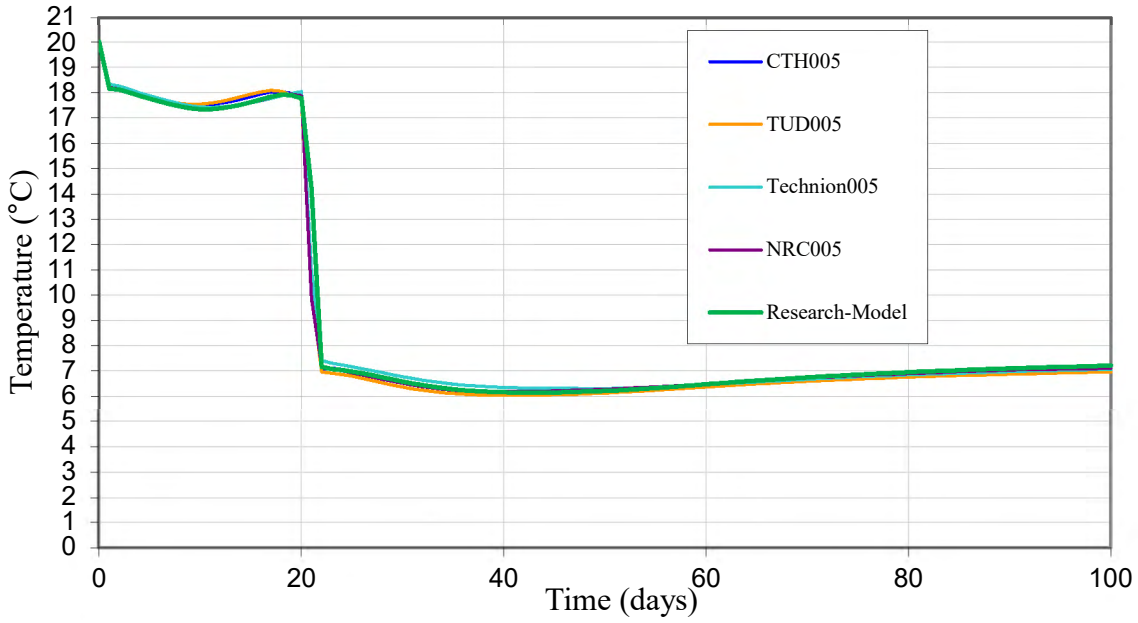

Figure 40: Temperature at 0.05m from the inside surface.

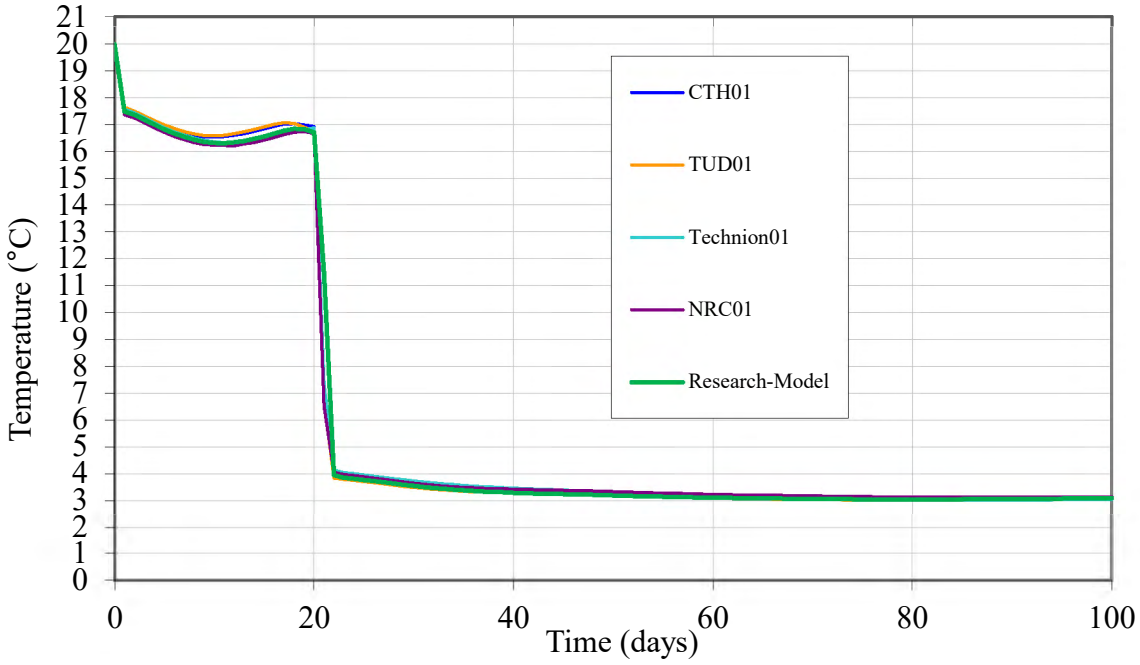

Figure 41: Temperature at 0.1m from the inside surface.

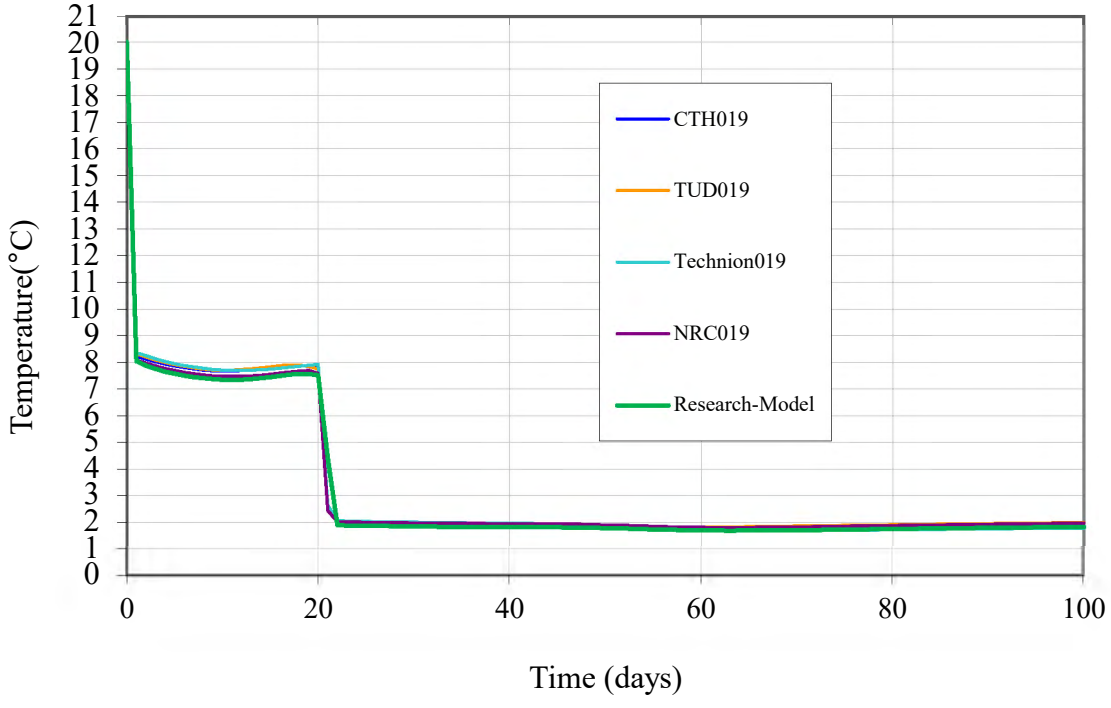

Figure 42: Temperature at 0.19m from the inside surface.

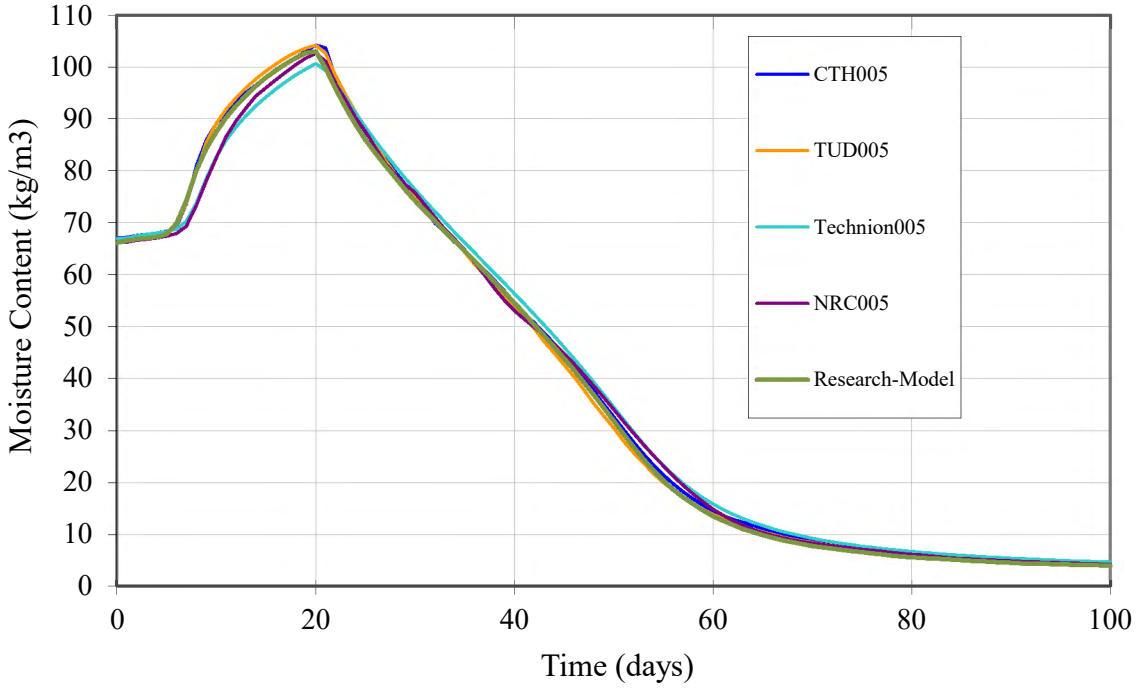

Figure 43: Moisture content at 0.05m from the inside surface.

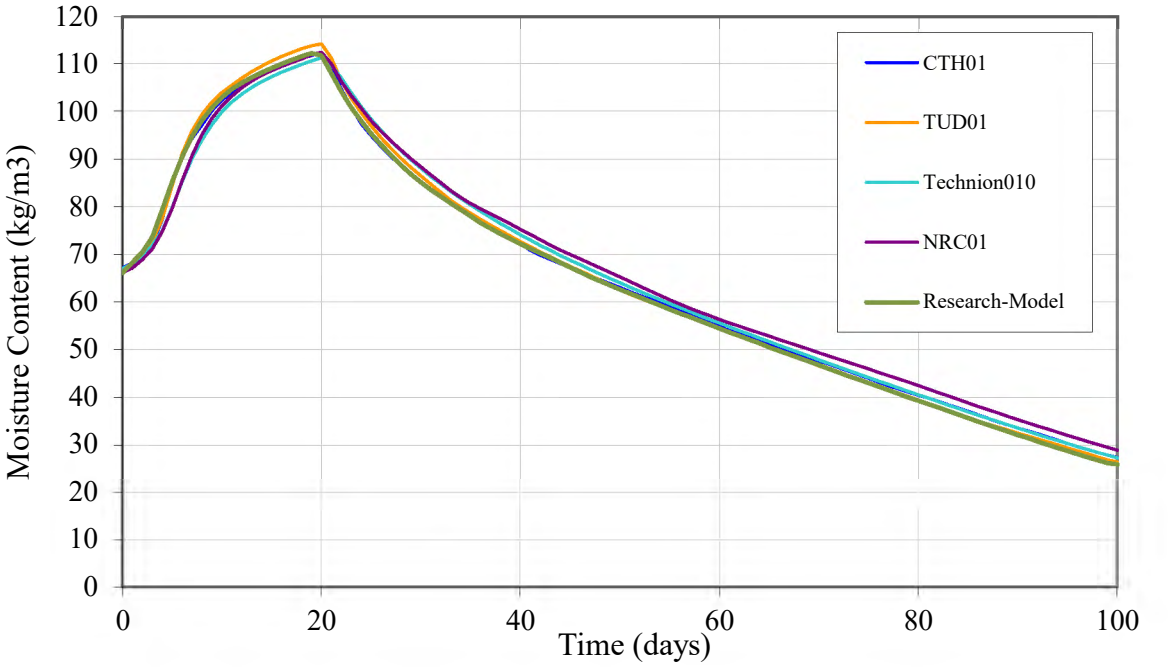

Figure 44: Moisture content at 0.1m from the inside surface.

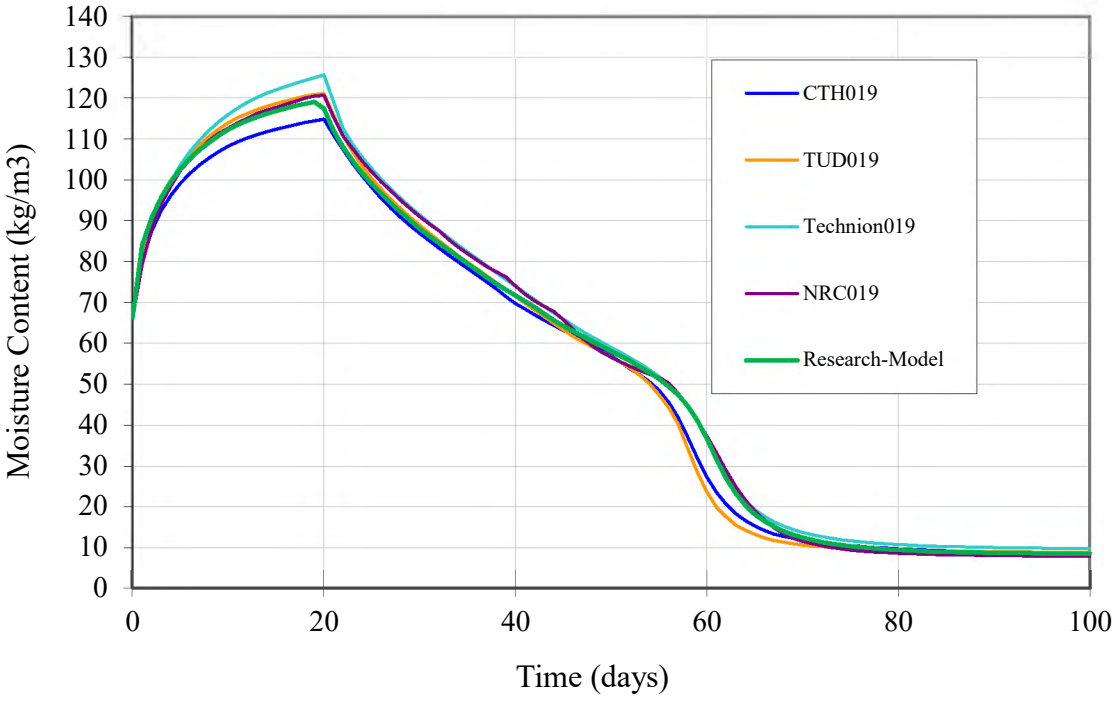

Figure 45: Moisture content at 0.19m from the inside surface.

Benchmark-4

The fourth benchmark exercise has two layers with hygroscopic finishing material on the interior side and assumed as an airtight enclosure. On the exterior side, a load-bearing layer with thickness 0.1m and a finishing material with 0.02m thickness made the structure. The moisture storage functions of both materials given as a function of suction pressure. Vapor diffusion and thermal conductivity defined as a function of moisture content. The film coefficients for heat transfer are 25W/m^2.K and 8 W/m2.K on the exterior and interior sides, respectively. Similarly, $2x10^{-7}$ s/m and $3x10^{-8}$ s/m film coefficient for moisture transfer on the outer and inner sides, respectively. Figures 46 and 47 show the moisture content and temperature.

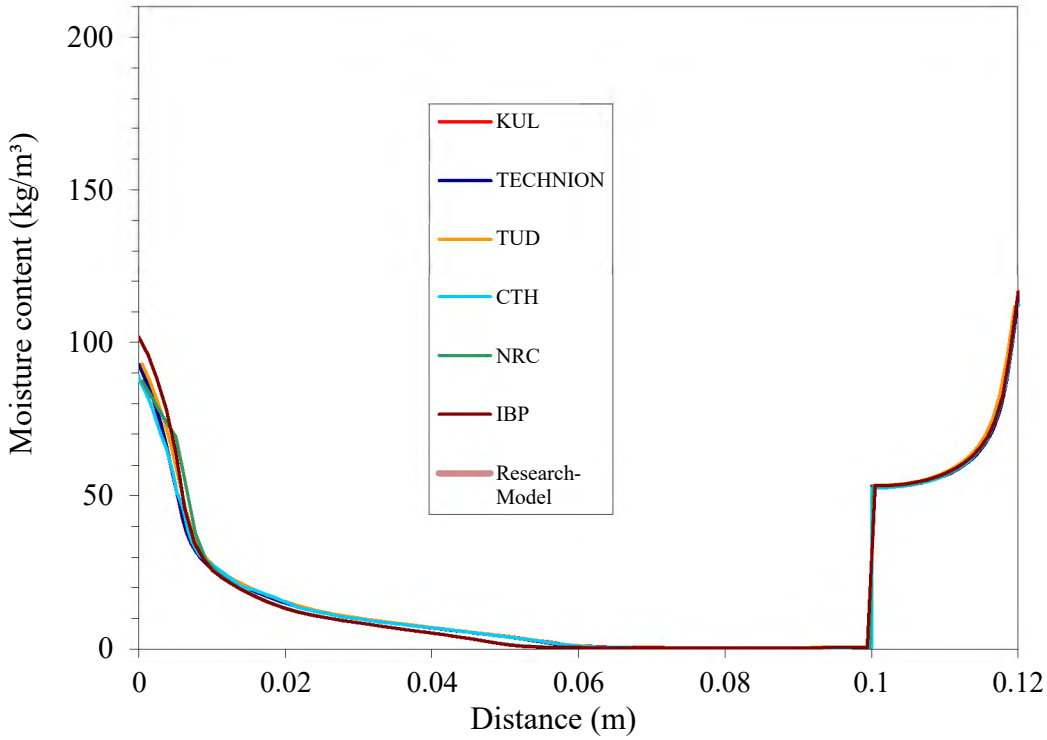

Figure 46: Moisture content at 12 hours.

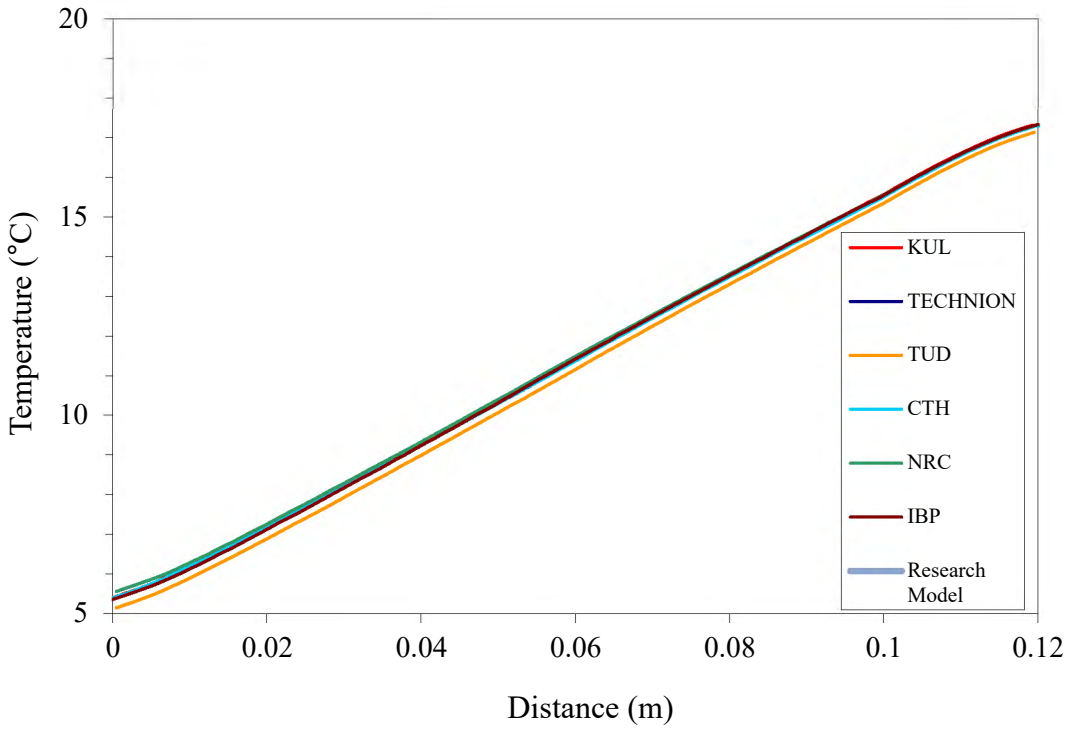

Figure 47: Temperature at 12 hours.

Benchmark-5

The fifth benchmark exercise is an internally insulated wall structure, with brick material on the outer side and mortar in the middle. The equilibrium moisture content of all materials given as a function of capillary suction. Vapour diffusion, liquid water conductivity, and thermal conductivity defined as a function of equilibrium moisture content. Initial conditions maintained at 25 °C temperature and 60 % relative humidity throughout the materials. Internal boundary conditions are 20 °C temperature & 60 % relative humidity, and similarly 0 °C & 60% on the external boundary. The output of this model includes relative humidity and moisture content at the end of simulation time or 60 days (Figures 48 and 49).

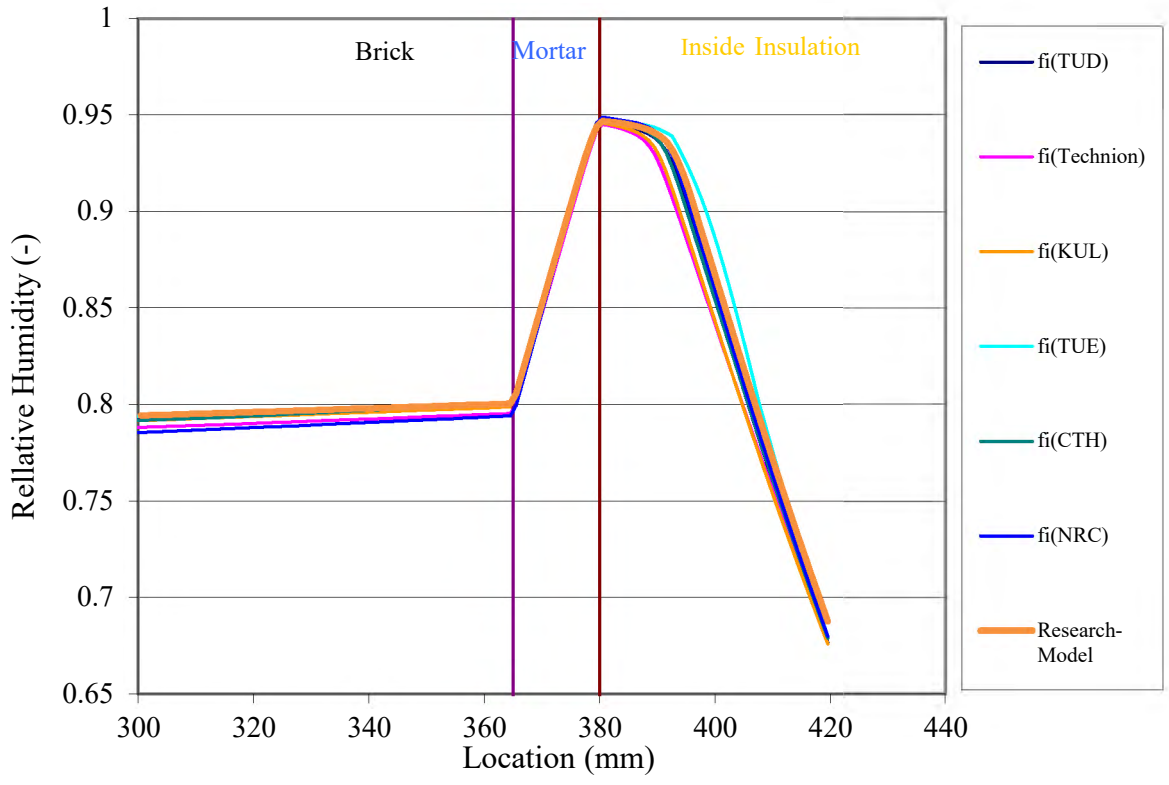

Figure 48: Relative humidity at the end of the simulation.

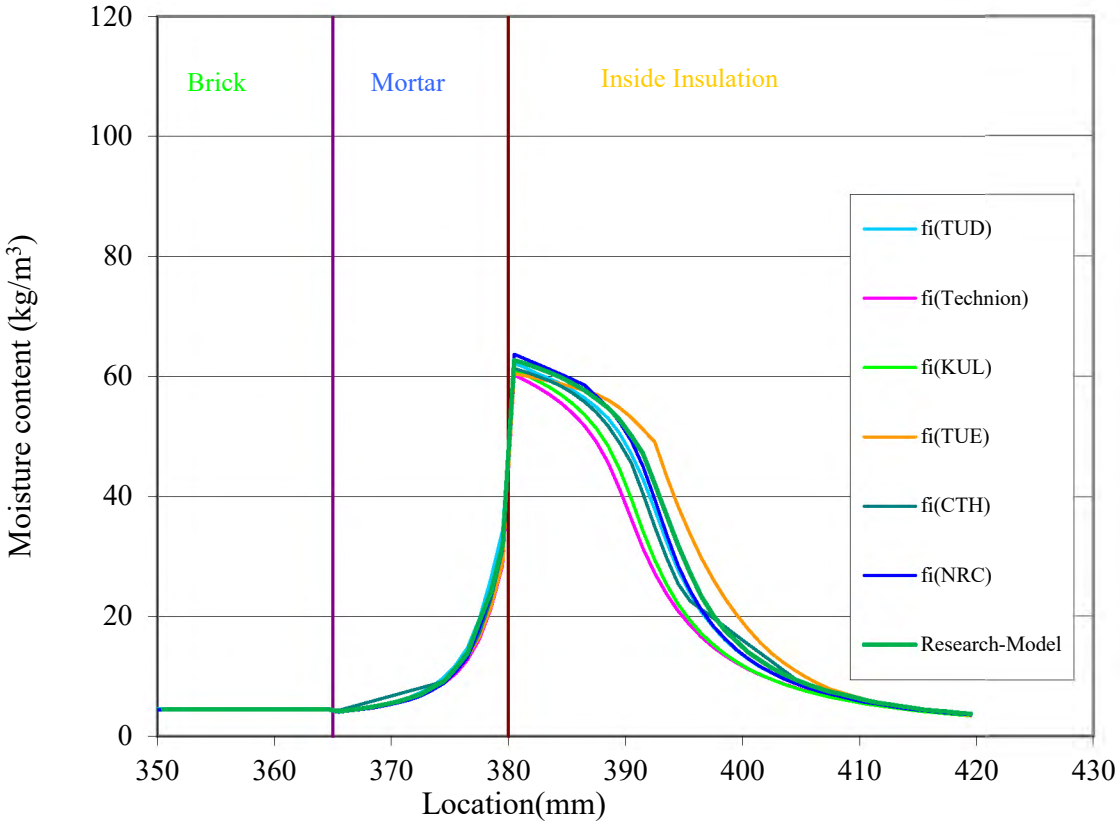

Figure 49: Moisture content at the end of the simulation.

6 Result and Discussion

The first two wall assemblies, as shown in Figure 50 (a) and (b), are internally insulated wall which have similar building materials and configuration, with the latter one including a 19 mm cavity ventilation behind the cladding. The building materials from outside to inside are cladding (stucco), vapor-permeable sheathing membrane, sheathing board (plywood), two by six wood framing filled with fiberglass batt insulation, and gypsum board with latex paint applied on the interior surface.

Figure 50 (c) shows the third wall assembly. This wall assembly includes four and six inches extruded polystyrene (XPS) insulation applied on the outer side of the sheathing board, and the wood framing (stud) is a two by four without fiberglass batt insulation. The sheathing membrane layer assumed as vapor-permeable, and there is no vapor retarder layer applied on the gypsum board surface.

The fourth wall assembly shown in (d) considered to represent a high insulation wall like the one used in passive houses. This wall added fiberglass batt insulation on the third wall assembly with a similar arrangement, so that it's both internally and externally insulated (split). Also, the wall assembly included a vapor retarder layer or the latex paint on the gypsum board. Some of the factors that varied during modeling include; wall orientation, indoor moisture conditions, material thickness, cavity ventilation, vapor retarder layer, and rain penetration factors.

Exterior

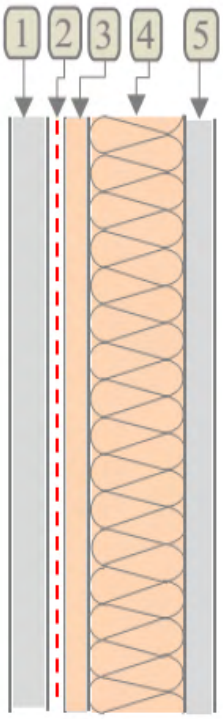

Interior

1. Cladding (stucco)
2. Sheathing membrane (vapor-permeable)
3. Sheathing board (plywood)
4. 2 x 6 wood framing with fiberglass batt insulation
5. Gypsum board with latex paint

a)

Exterior

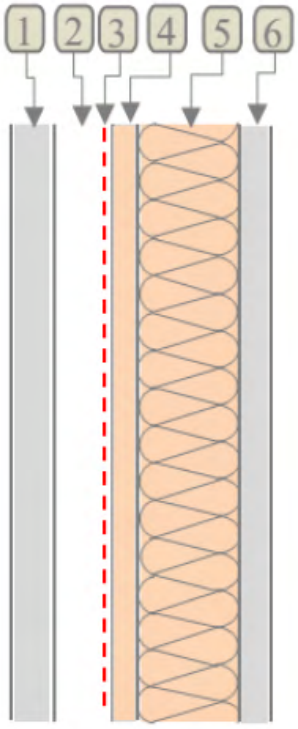

Interior

1. Cladding (stucco)
2. Ventilation cavity
3. Sheathing membrane (vapor-permeable)
4. Sheathing board (plywood)
5. 2x6 wood framing with fiberglass batt insulation
6. Gypsum board with latex paint

b)

Exterior

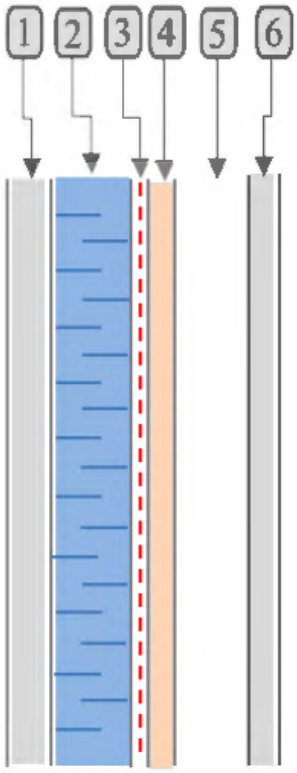

Interior

1. Cladding (stucco)
2. External insulation (4” & 6” XPS)
3. Sheathing membrane (vapor-permeable)
4. Sheathing board (plywood)
5. 2x4 wood framing (air cavity)
6. Gypsum board without latex paint

c)

Exterior

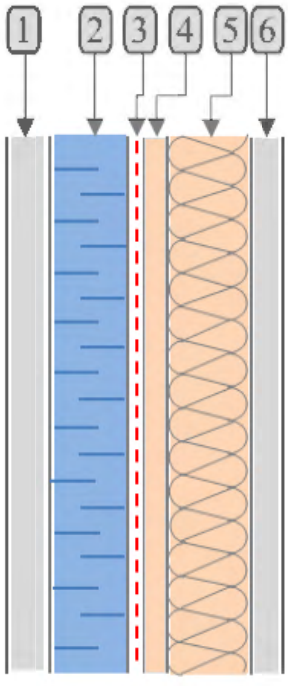

Interior

1. Cladding (stucco)
2. External insulation (4” & 6” XPS)
3. Sheathing membrane (vapor-permeable)
4. Sheathing board (plywood)
5. 2x4 wood framing with fiberglass batt insulation
6. Gypsum board with & without latex paint

d)

Figure 50: Building materials and configurations for the different wall assemblies, a) Interior insulation, b) Interior insulation with ventilation cavity, c) Exterior insulation, d) Split insulation.

From now on, plywood moisture content refers to the amount of moisture obtained near the plywood interior surface where condensation is most likely to occur. Referring to the first wall with east orientation, Figure 51, 52 & 53 shows plywood moisture content for the different scenarios and the three-time slices (2020s, 2050s, & 2080s). In 2020s and 2050s, all scenarios showed nearly similar moisture content. However, as shown in Figure 53 in 2080s the difference becomes significant where the moisture content increases in scenarios B's than A's. The highest and lowest moisture content observed by scenario B1 and A1FI, respectively. The reason for this is the highest projected temperature, and solar radiation by A1FI has enhanced moisture drying potential than the lowest projection by scenario B1.

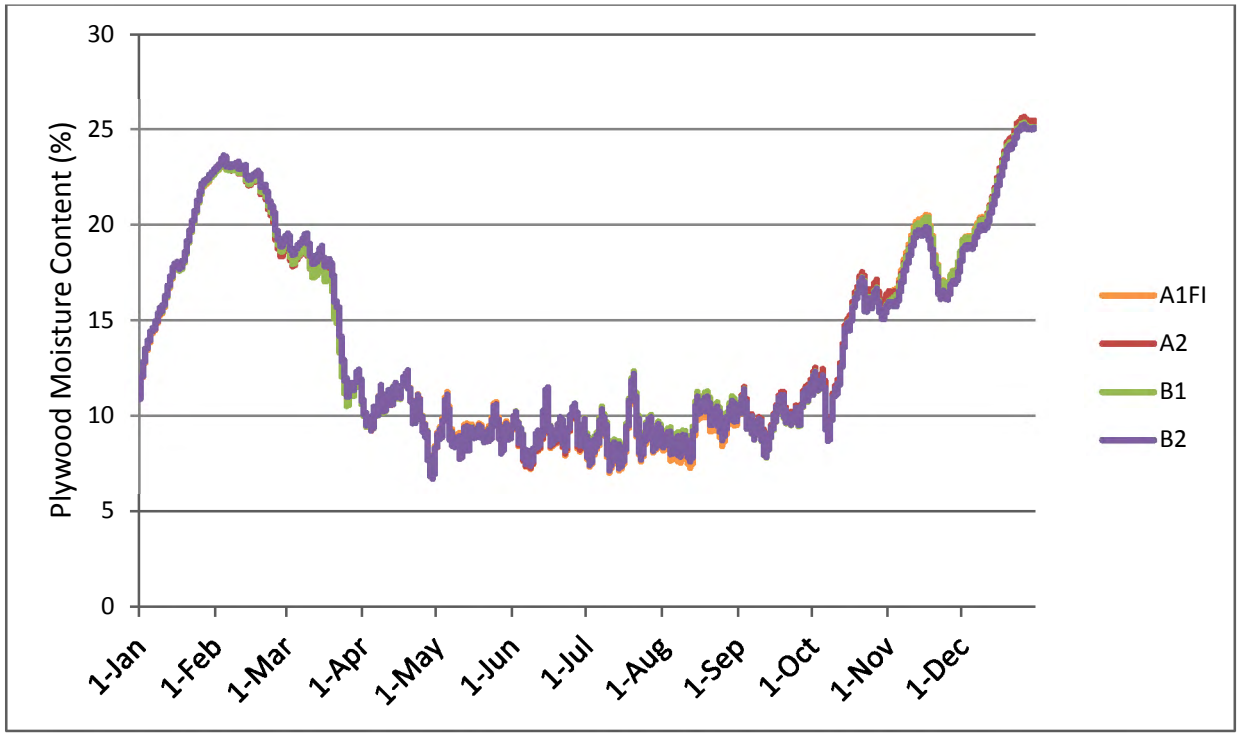

Figure 51: Plywood moisture content in 2020s on the east wall for the scenarios.

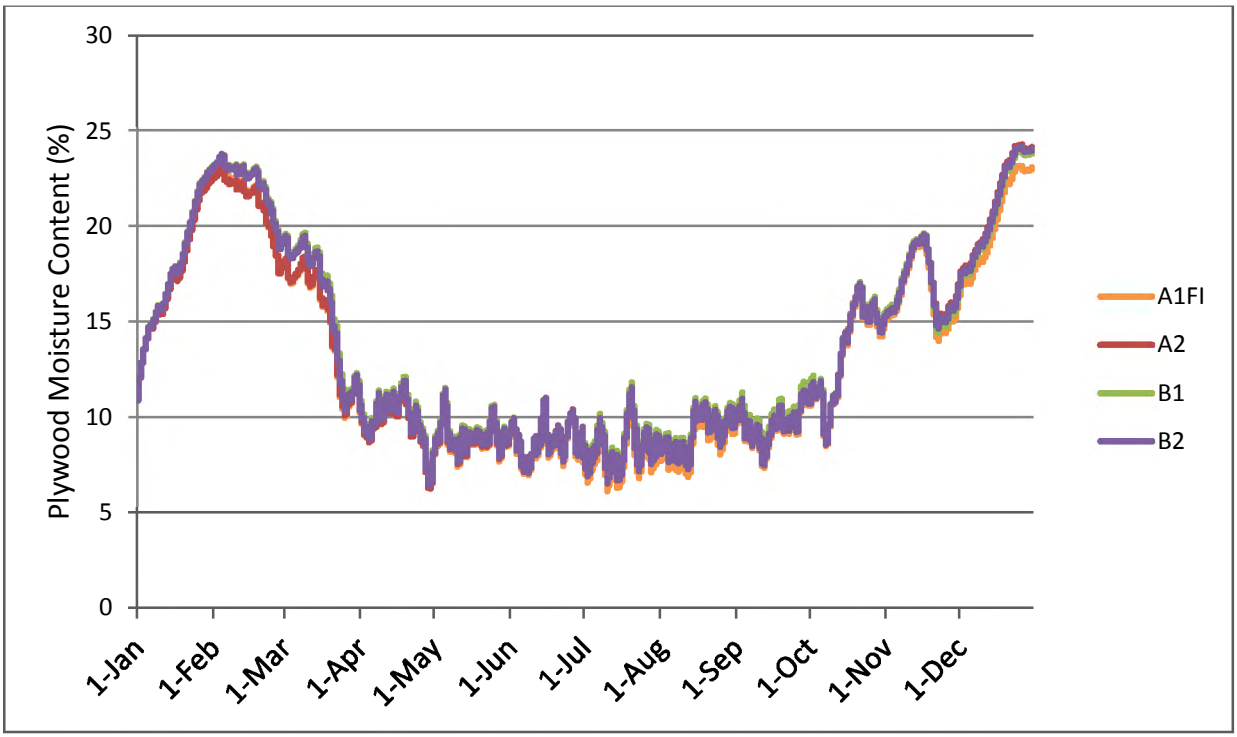

Figure 52: Plywood moisture content in 2050s on the east wall for the scenarios.

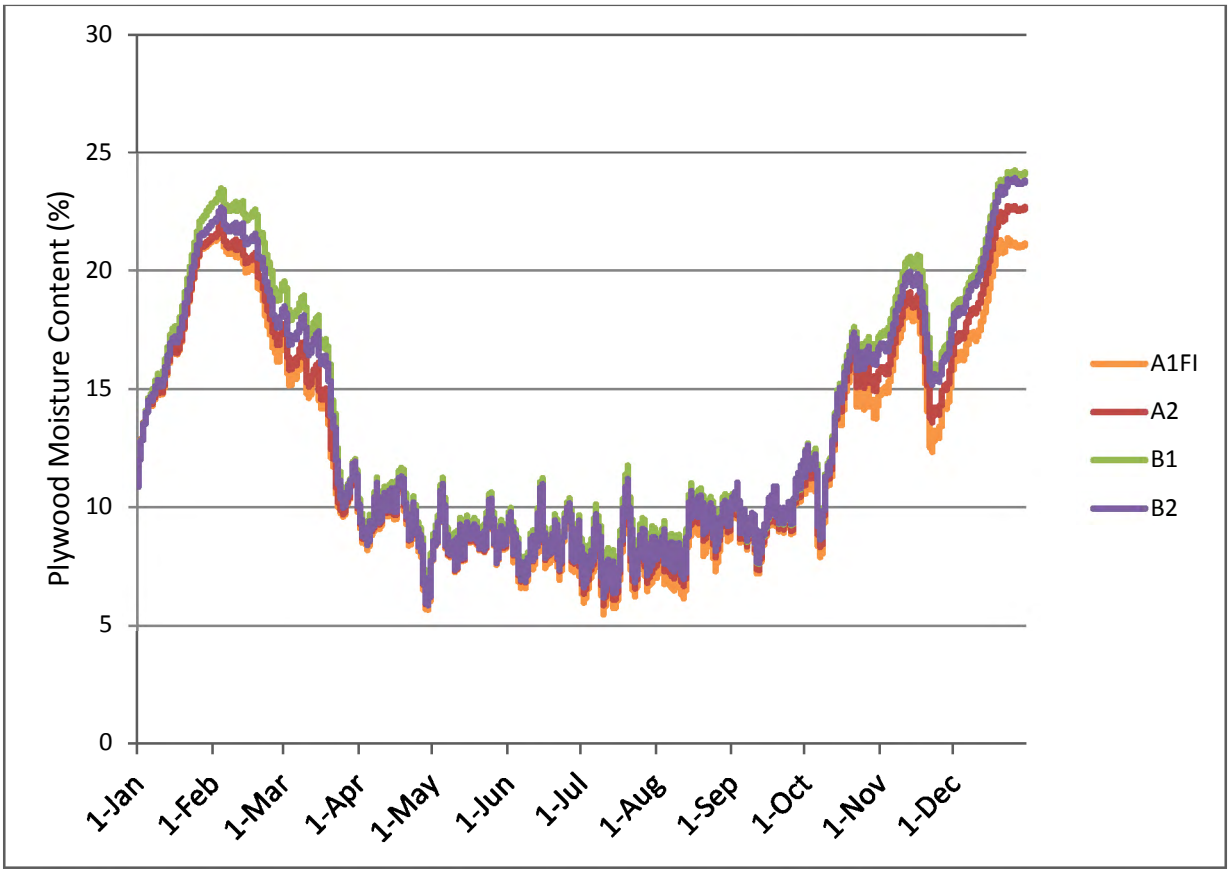

Figure 53: Plywood moisture content in 2080s on the east wall for the scenarios.

The differences between scenarios are more clearly apparent in the histogram plot (Figure 54), where the number of hours that plywood moisture content exceeds 20% is highest by scenario B1, followed by B2, A2, and A1FI in all years. However, the number of hours that RHT criteria (5°C temperature and 80% relative humidity) exceeded indicates a higher biodegradation effect by scenario A1FI and lower by scenario B2.

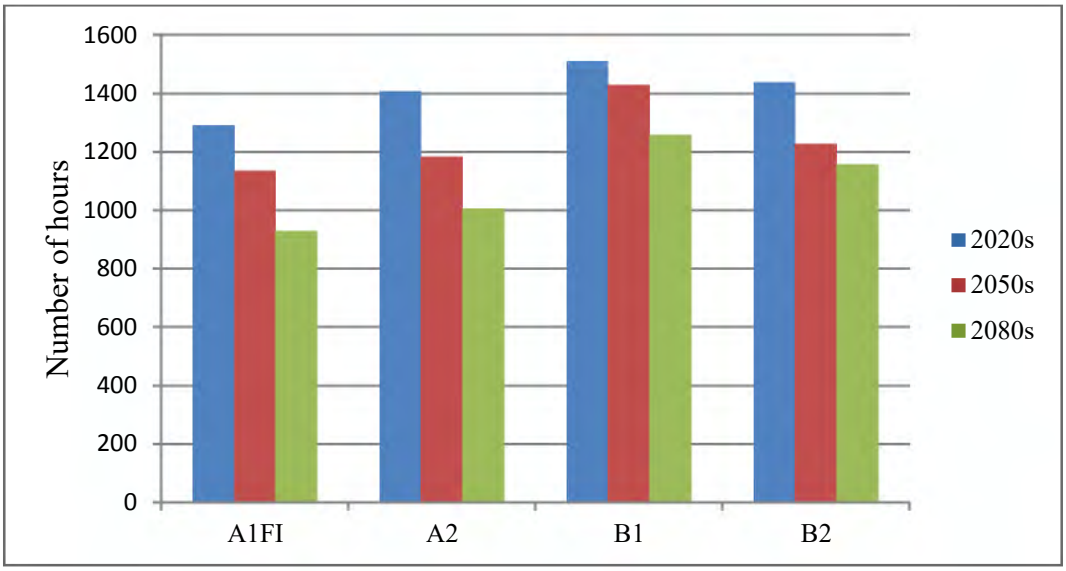

Figure 54: Histogram plot of the number of hours that plywood moisture content exceeds 20%.

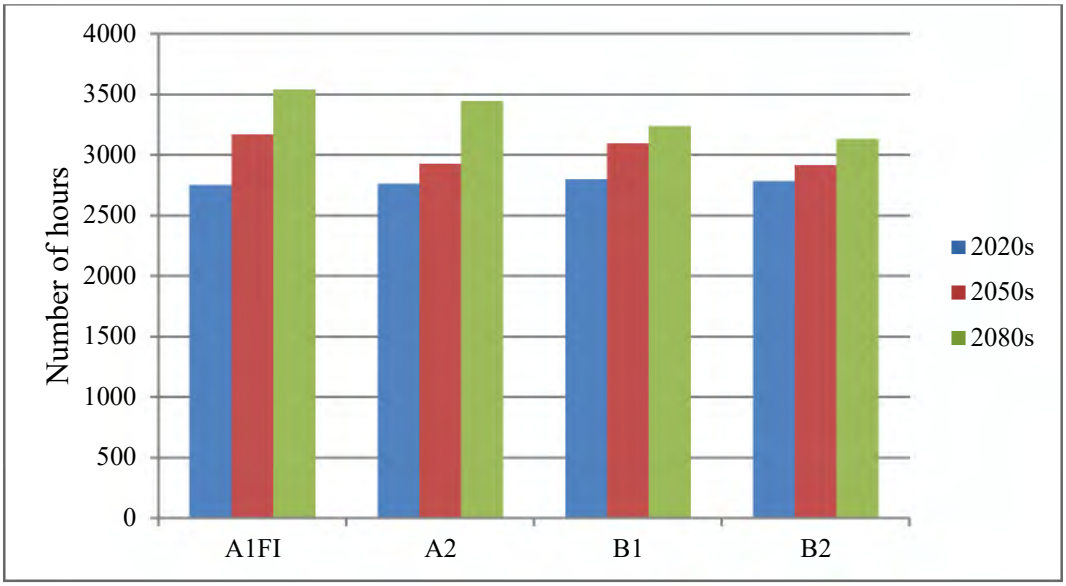

Figure 55: Histogram plot of the number of hours that RHT criteria exceeded.

The next discussion chooses the medium to high scenario A2. Using the first wall, Figure 56 to 58 shows moisture content comparison between north and east orientation. East wall receives the highest amount of wind-driven rain, and the north wall receives the least amount together with lower solar radiation. The moisture content in the east wall is higher than that of the north wall in all of the three years, the main reason for the difference is the amount of wind-driven rain received by east faced walls where the annual WDR exceeds by over fivefold than the north-oriented wall. Besides, even though year around the east wall receives more solar radiation than the north wall, the obtained result indicates the wetting caused by wind-driven rain outweighs the drying by solar radiation.

The mold growth on both walls shows an increasing trend during winter months and a decrease in summer (Figure 59). Since mold growth is a gradual process, the year-long weather data cannot accurately represent the real mold-related problems over extended years. Therefore, the result obtained using one year showed only the initial stage of growth. Again the result indicates the east wall to be more likely to be vulnerable to moisture-related problems where a mold index difference as high as 1/2 are obtained compared to the north wall. Therefore, in Vancouver, for assessing the hygrothermal performance of walls, the east orientation is crucial.

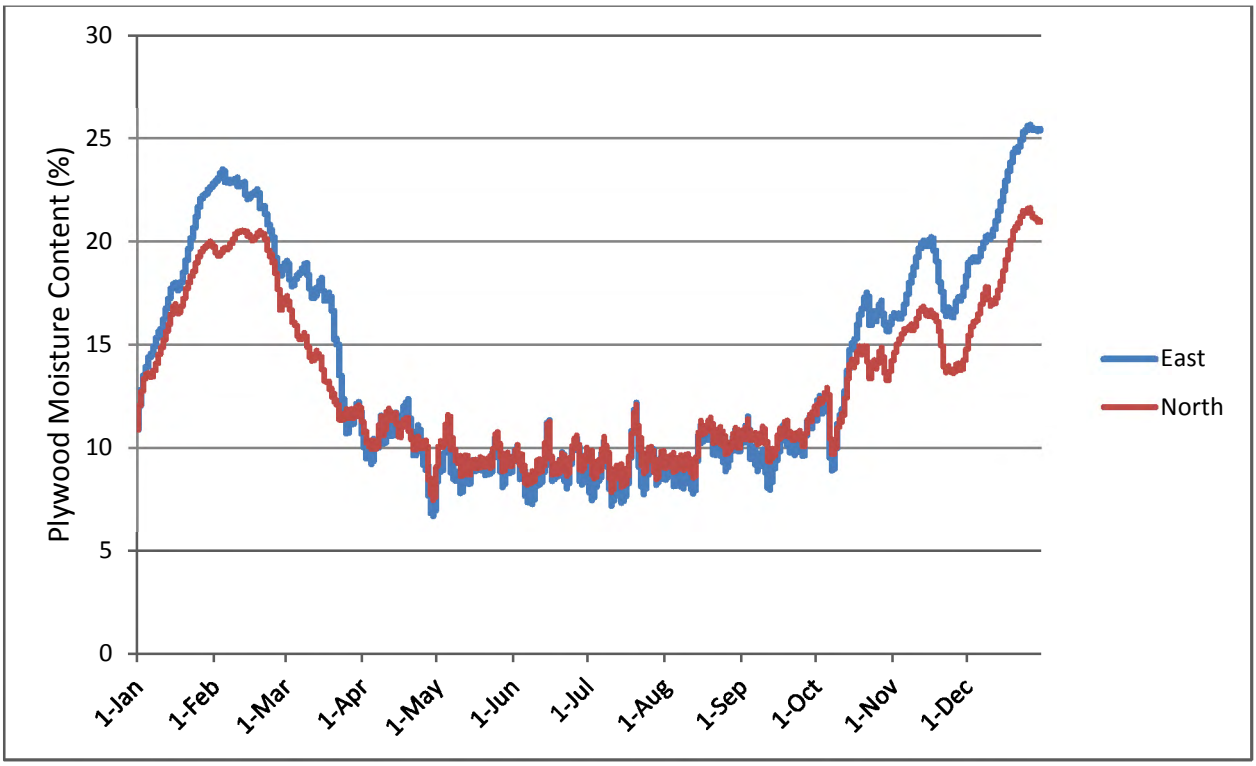

Figure 56: Plywood moisture content in 2020s on the east and north wall.

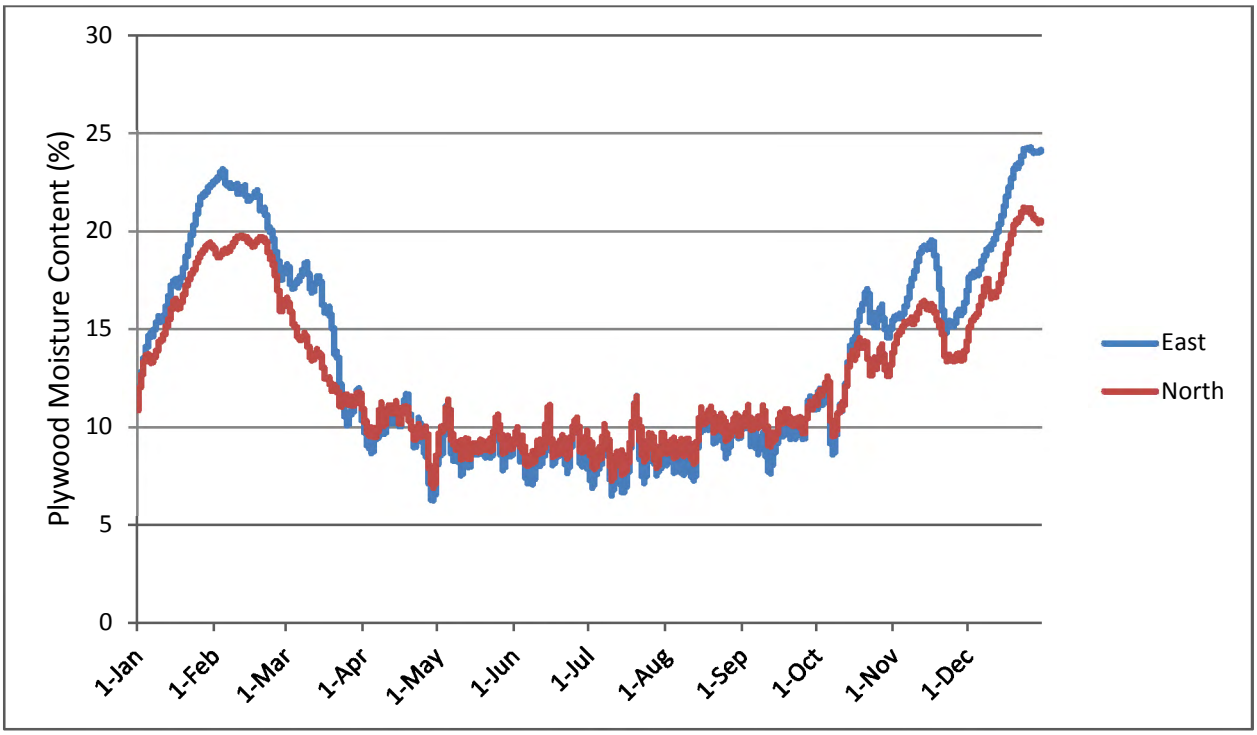

Figure 57: Plywood moisture content in 2050s on the east and north wall.

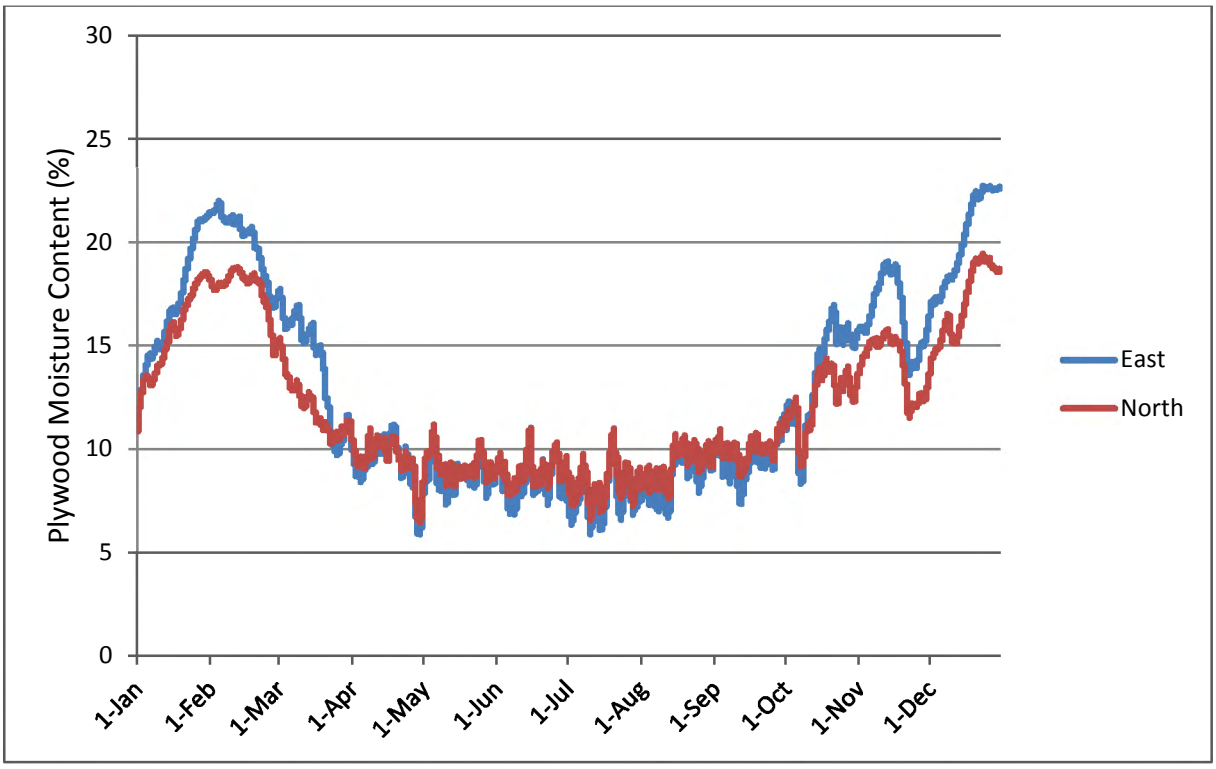

Figure 58: Plywood moisture content in 2080s on the east and north wall.

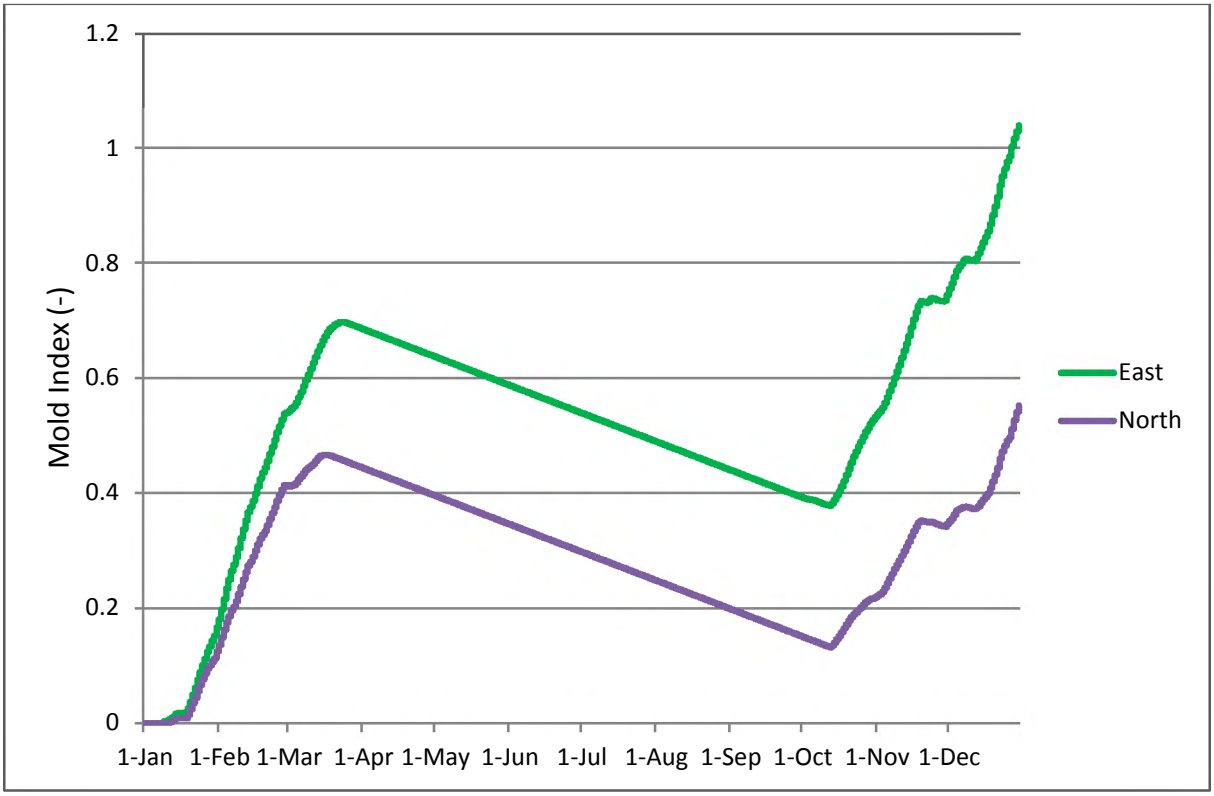

Figure 59: Plywood mold index in 2020s for the east and north walls.

The next discussion focused on the east wall as it is the critical orientation. Even though in future, the amount of precipitation projected to increase, the overall effect of climatic variables change on hygrothermal performance has appeared to bring benefit by improving drying potential rather than causing more wetting. As shown in Figure 60, the moisture content decreased in the future years than the current year. Also, as shown in Figure 61, the number of hours that plywood moisture content exceeds 20 % in east oriented wall reduced by 16% & 28% in the 2050s and 2080s from 2020s.

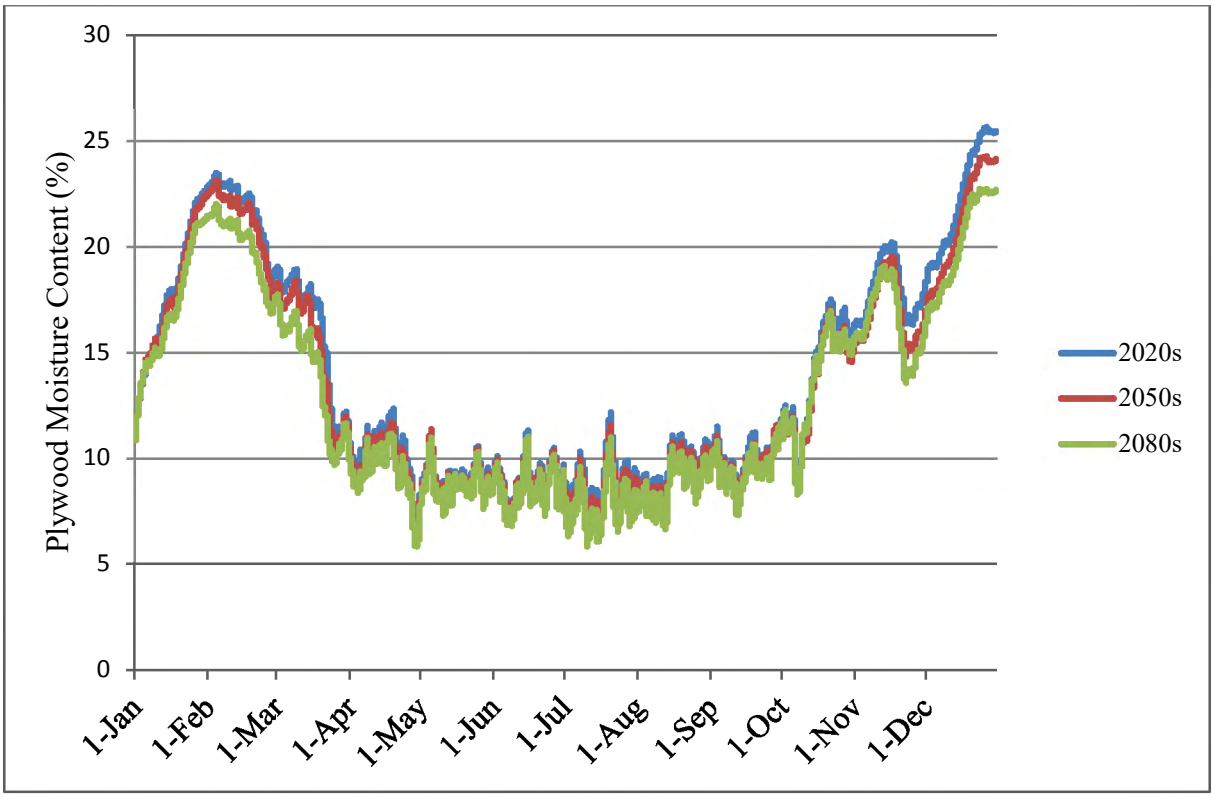

Figure 60: Plywood moisture content on the east wall.

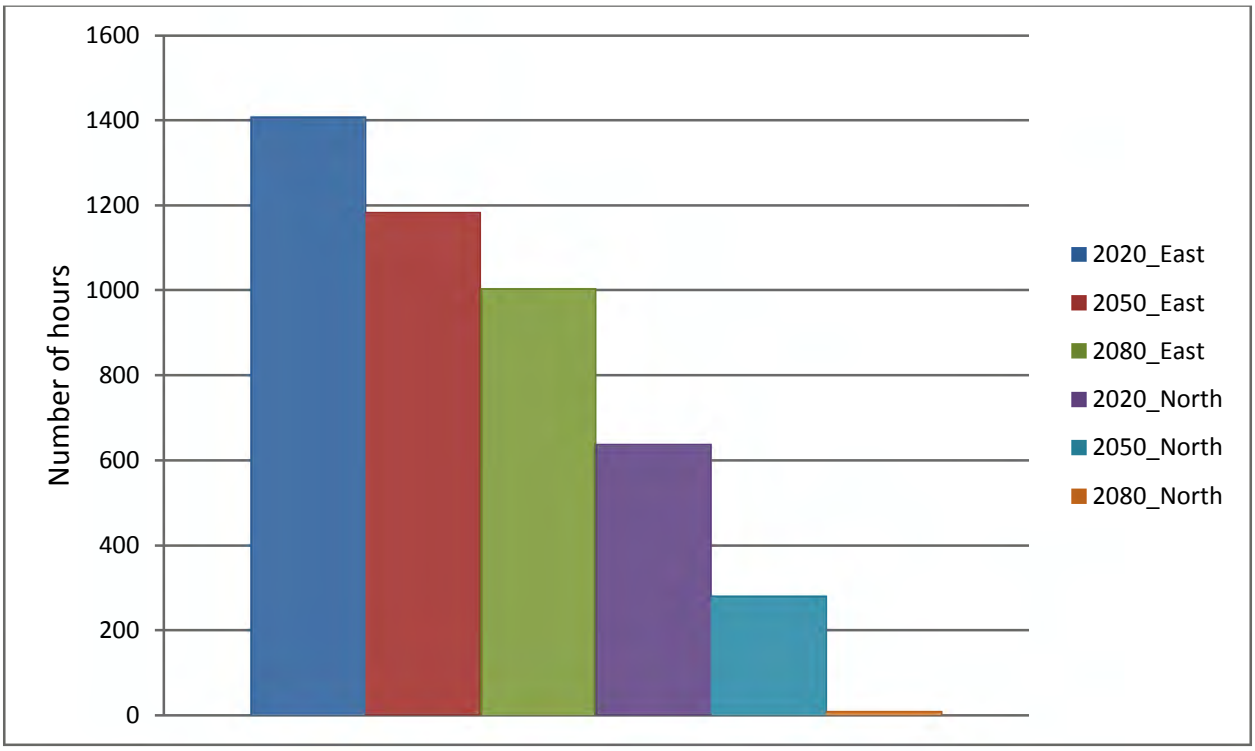

Figure 61: Histogram plot of the number of hours that plywood moisture content exceeds 20 % on east and north walls.

As shown in Figure 62, the mold growth shows a similar trend in all years, with the lowest index observed in the 2050s. The increasing trend at the end of the years indicates the mold would keep growing from the current end condition and could reach the other stages of mold growth.

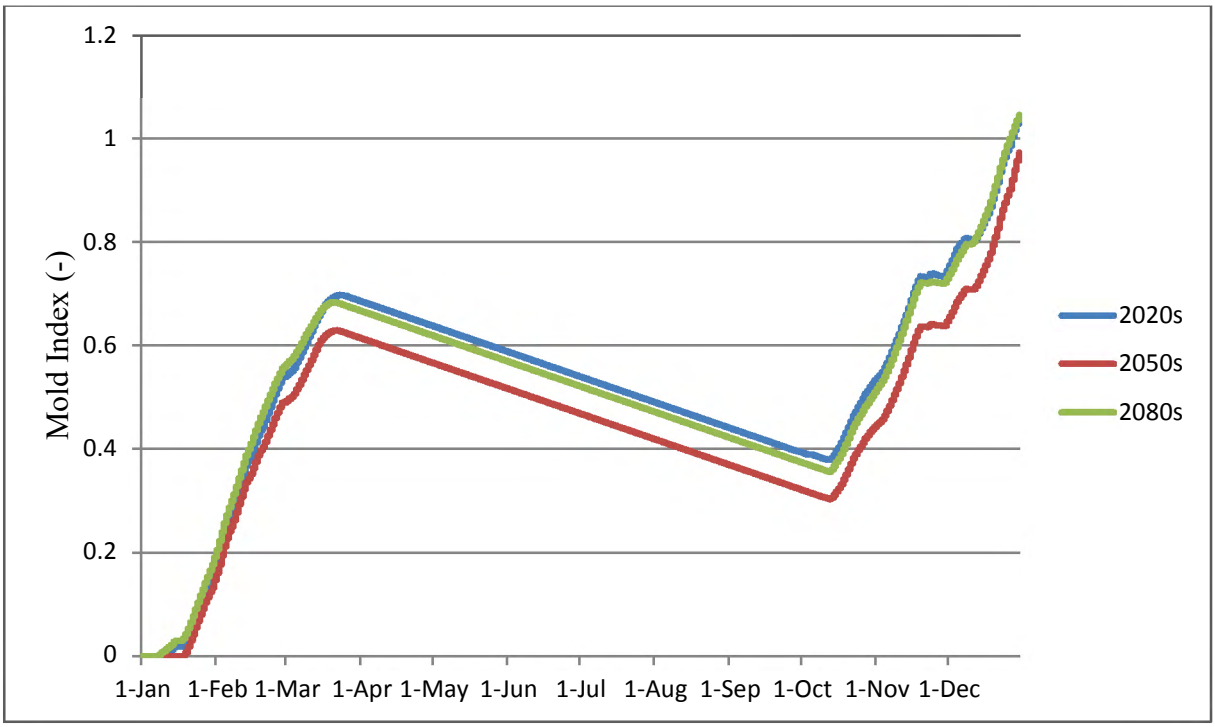

Figure 62: Mold Index of plywood on the east wall.

Referring 2020s of the first wall, Figure 63 shows the relation between indoor moisture conditions and the plywood, which indicates a direct link, as high indoor moisture shows higher plywood moisture content. This higher indoor moisture represents a house where an increased amount of moisture exists due to cooking or other activity compared to medium indoor moisture. Similarly, as shown in Figure 64, the mold index shows higher growth when the indoor moisture loads increases.

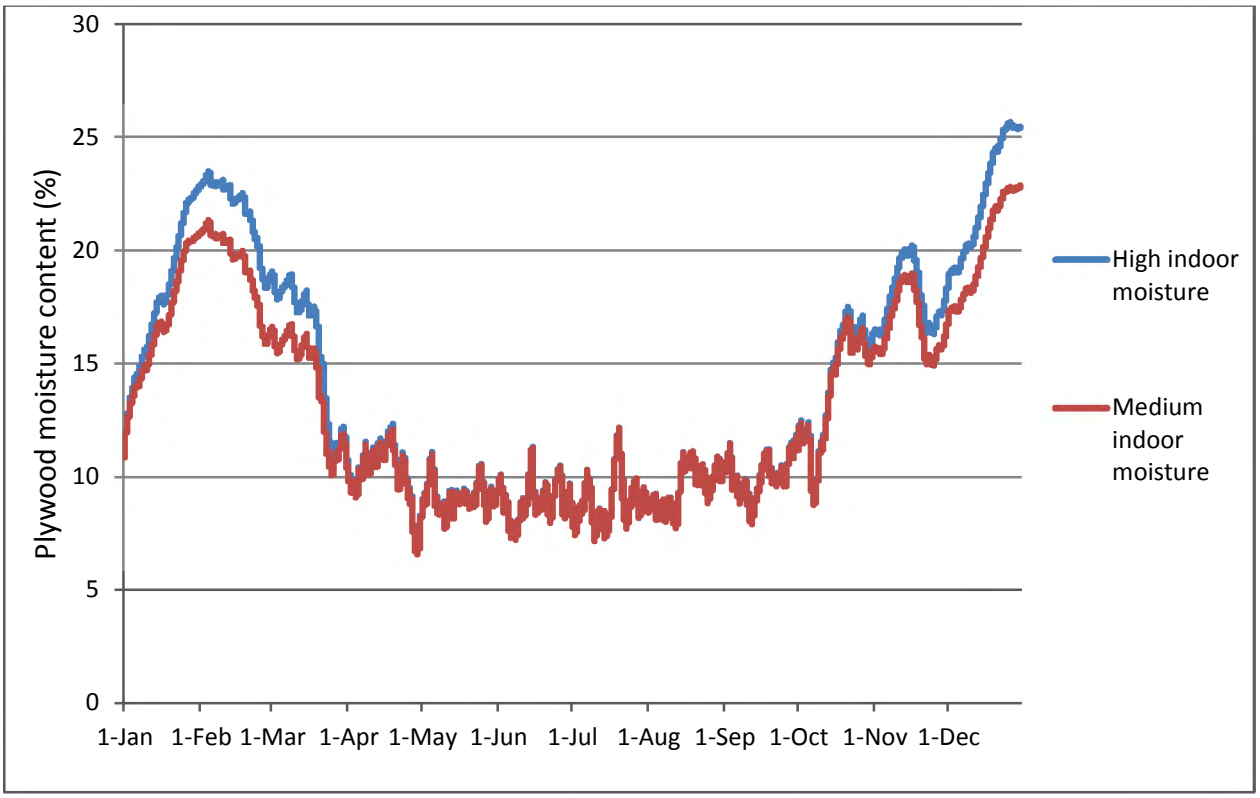

Figure 63: Plywood moisture content for medium and high indoor moisture conditions.

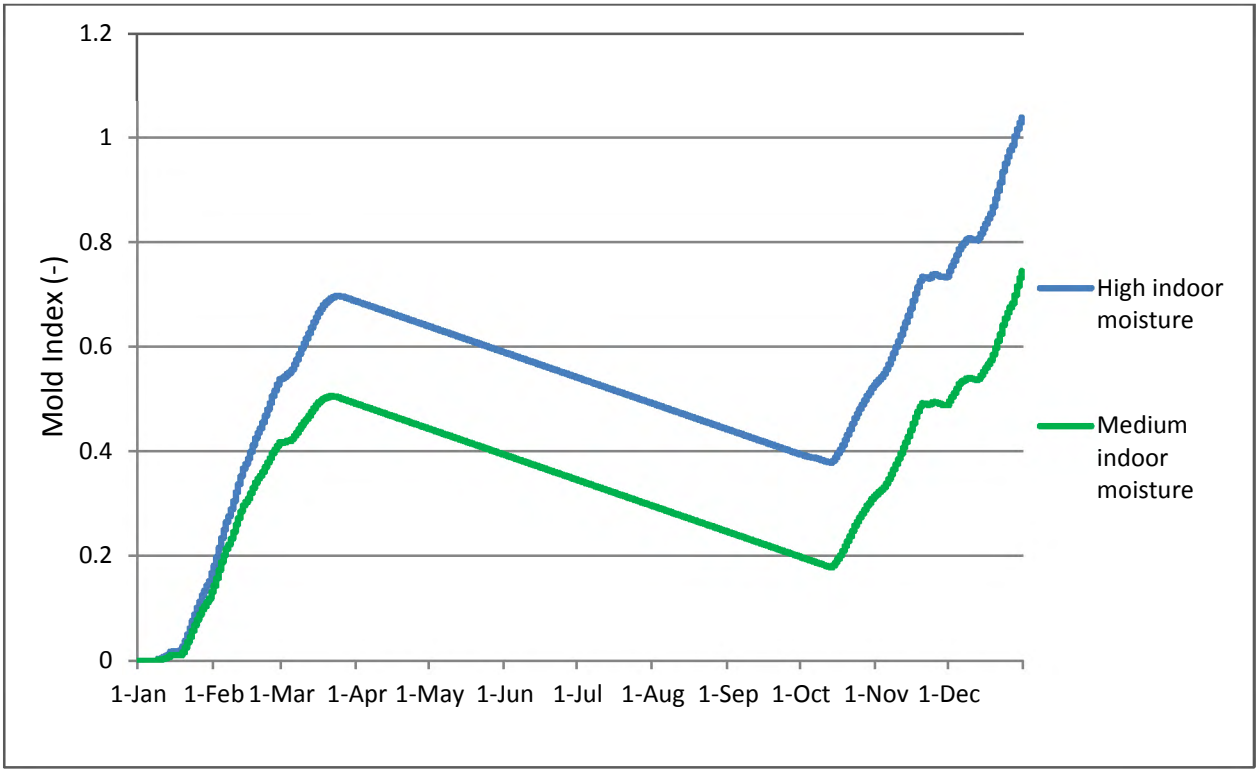

Figure 64: Mold Index of plywood for medium and high indoor moisture conditions.

The next discussion compares the internally insulated wall with and without a ventilation cavity using a typical ventilation rate of 100 ACH by considering rain penetration of 0.5% and without rain penetration. For all years, as shown from Figure 65 to 67, the wall assembly with cavity ventilation showed a reduced moisture content on the plywood by enhancing drying potential or by carrying moisture out from the cavity. The following figures show the drying potential, where a decreased moisture content obtained for the wall with a ventilation cavity than non-cavity walls in both rain leaks and non-rain leak cases.

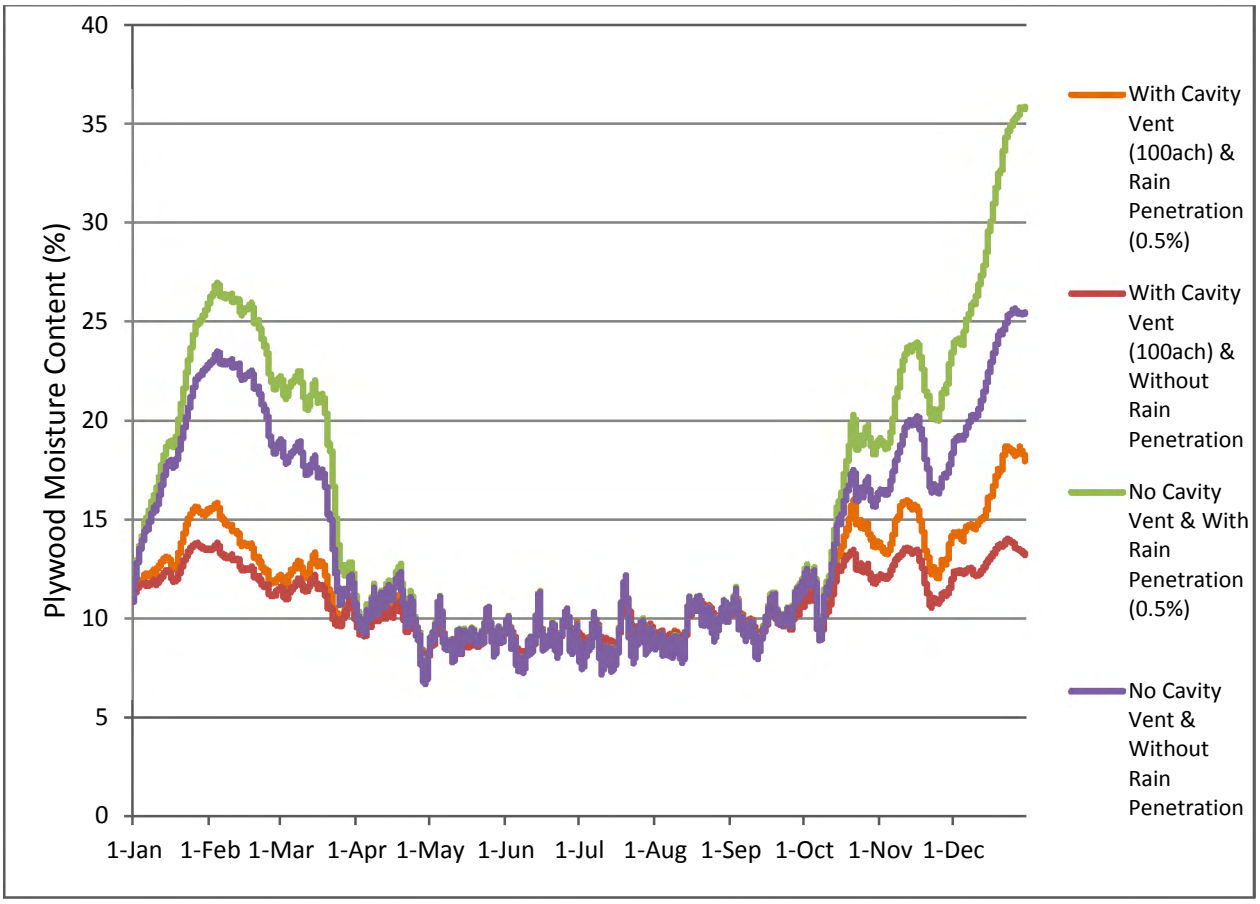

Figure 65: Plywood moisture content of internal insulation wall systems with and without cavity ventilation and rain leaks in 2020s.

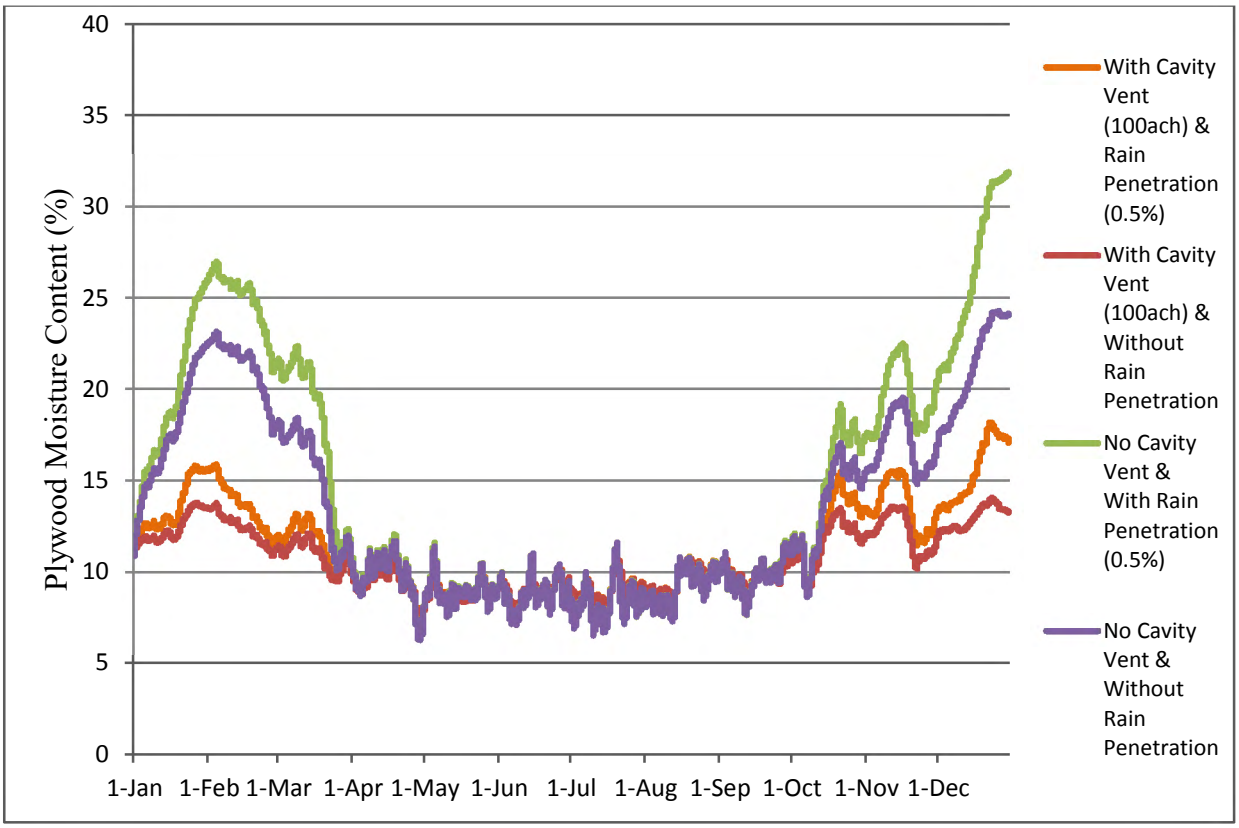

Figure 66: Plywood moisture content of internal insulation wall systems with and without cavity ventilation and rain leaks in 2050s.

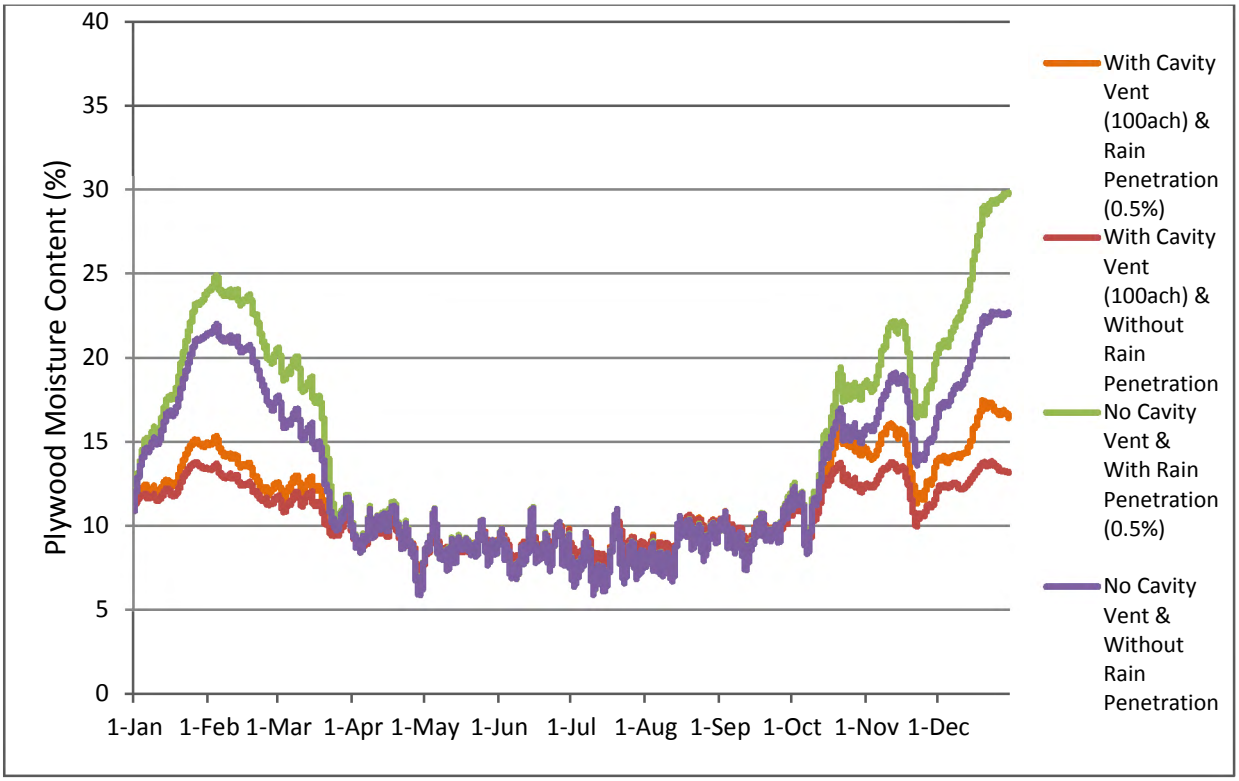

Figure 67: Plywood moisture content of internal insulation wall systems with and without cavity ventilation and rain leaks in 2080s.

Table 12 summarizes the moisture content (MC) and the biodegradation implication (RHT) for the above four cases. The number of hours of RHT appeared to be higher in the wall assembly with cavity ventilation and rain leak in 2020s and 2050s. In 2080s the wall with rain leaks and without cavity ventilation results in a higher effect. For the two walls with cavity ventilation in all three years, the MC lies under 20%. Also, when rain leaks considered on the non-cavity wall, the number of hours that MC exceeds 20% is higher by around three-fold than without rain leaks. Similarly, for MC above 25%, the difference increased by over tenfold. Besides, the biodegradation implication in 2080s, shows the number of hours exceeds by around 15% in the second case, with 2050s showing a relatively lower effect than 2020s.

Table 12: Summary of the number of hours that plywood interior surface temperature and relative humidity exceed 5°C and 80%, respectively, and the number of hours when MC exceeds 20% and 25%.

		T>5 °C & RH > 80%			Moisture Content > 20%			Moisture Content > 25%		
Cavity Ventilation (100 ACH)	Rain Penetration (0.5%)	2020s	2050s	2080s	2020s	2050s	2080s	2020s	2050s	2080s
×	×	2760	2926	3444	1408	1184	1005	189	0	0
×	✓	2988	2987	3501	2775	2336	1963	1125	936	373
✓	×	2090	2011	2223	0	0	0	0	0	0
✓	✓	3130	3042	3129	0	0	0	0	0	0

Figure 68 to 70 compares moisture content of the 4in & 6in externally insulated XPS wall (wall c) with the internally insulated one (wall a). Externally insulated wall assembly showed reduced moisture content than the internally insulated one due to increased plywood temperature when the insulation moved from inner to the outer side of the plywood. As a result, the condensation potential is reduced, which is typical in colder season when indoor

conditions maintained warmer. Thus, such assembly helps improves durability by minimizing condensation.

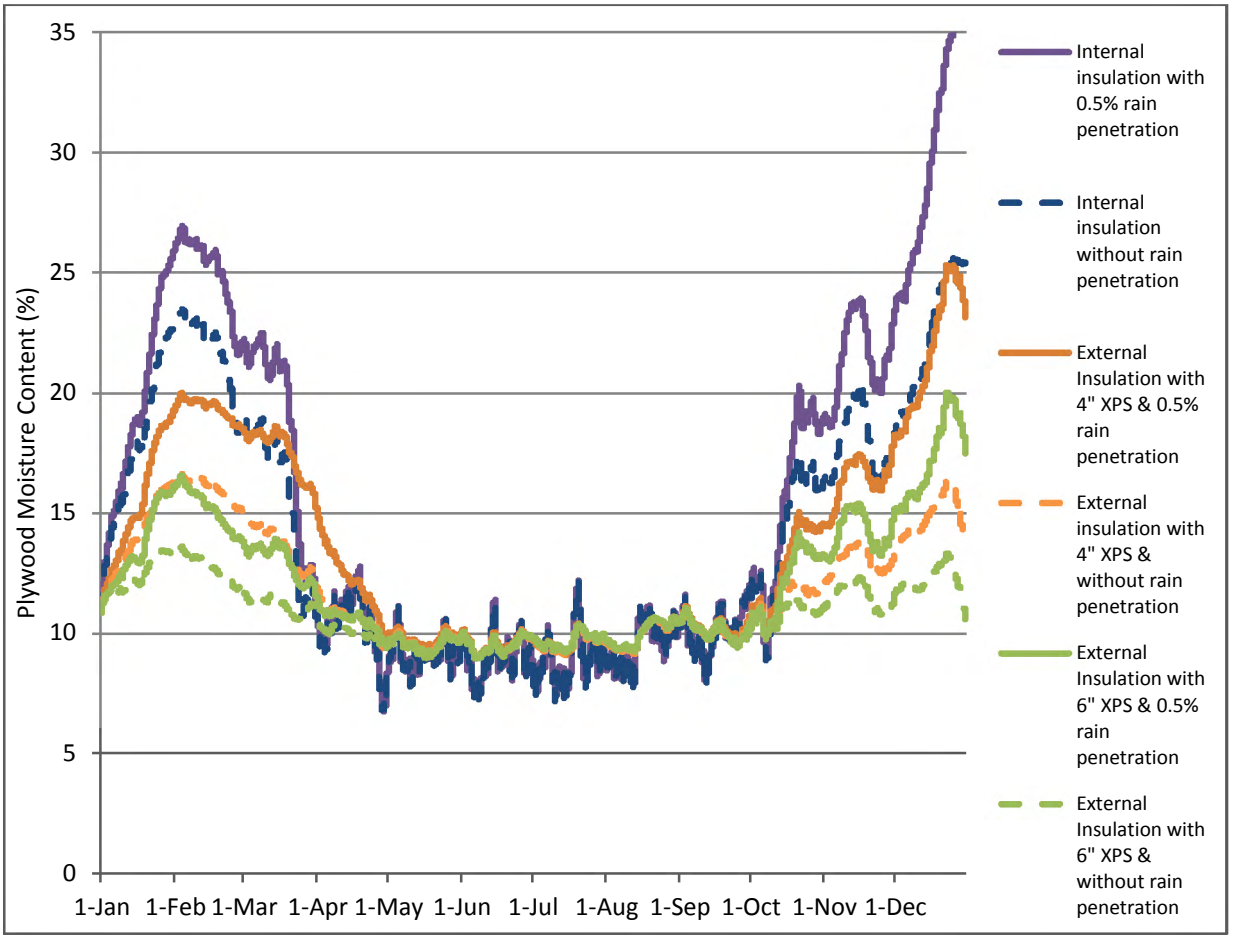

Figure 68: Plywood MC for internally insulated, and externally insulated wall assemblies with 4” and 6” XPS in 2020s.

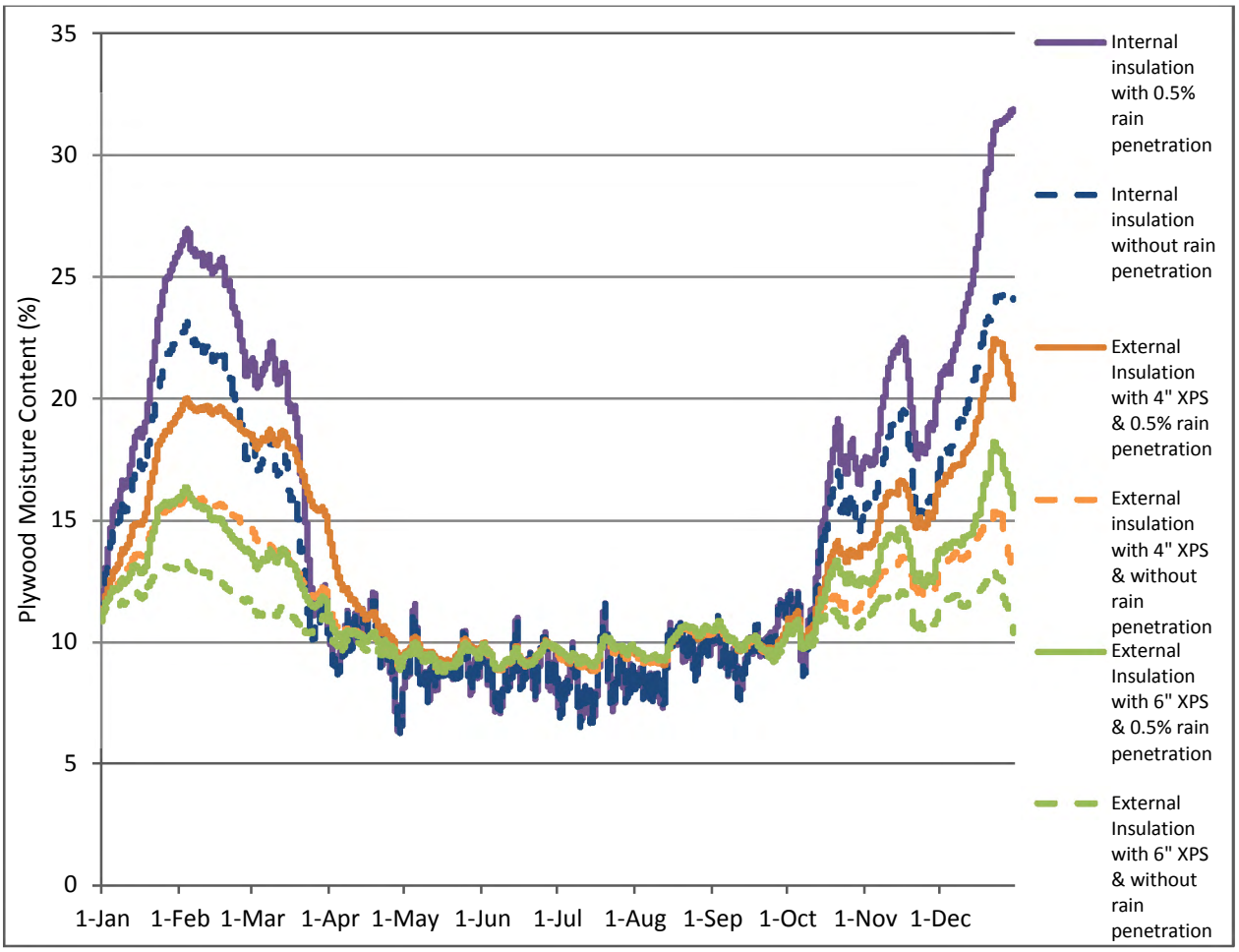

Figure 69: Plywood MC for internally insulated, and externally insulated wall assemblies with 4” and 6” XPS in 2050s.

External insulation also provides advantages such as; air, and vapor control layers can be easily applied continuously on the external side where few obstructions exist. Besides, external insulation helps to avoid temperature fluctuation in the internal structure of wall assemblies. Therefore, it reduces the cycling effect, which causes freeze-thaw or other affiliated thermal stress damages. As shown in the figures, the plywood moisture content has less fluctuation in the externally insulated walls than internally insulated ones. Moreover, such wall assembly reduces transport as well as storage properties variation in building materials.

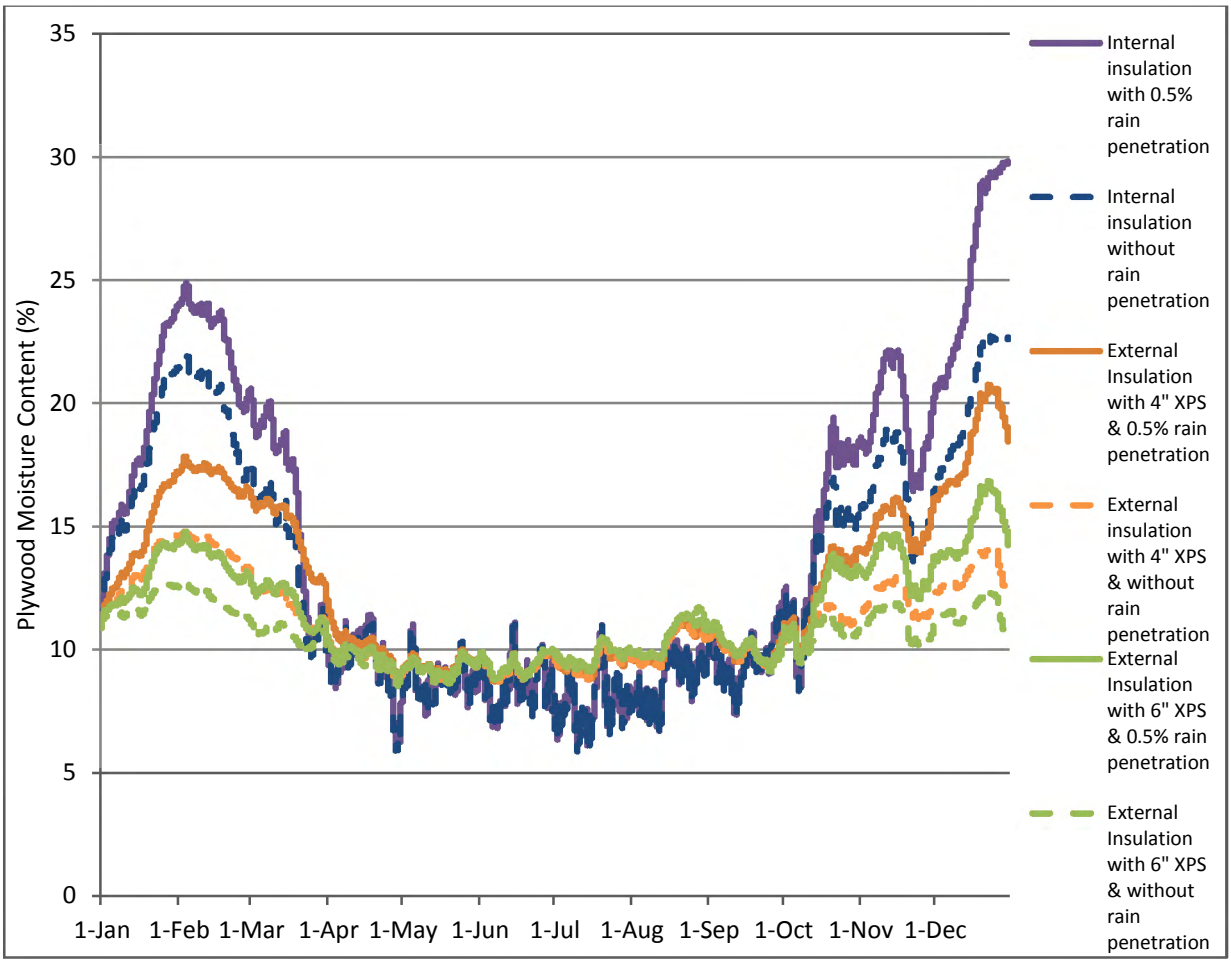

Figure 70: Plywood MC for internally insulated and externally insulated wall assemblies with 4" and 6" XPS in 2080s.

The vapor retarder layer has a significant role in reducing moisture diffusion from the warmer indoor air to the colder outdoor air, which lowers the plywood moisture content. However, this layer could have a negative effect when there is a moisture source inside the wall assembly, such as rain penetration or water leaks. When such moisture source exists, the vapor retarder can reduce drying potential to the interior side, which intern increases plywood MC. Figure 71 shows the plywood MC for the externally insulated wall with and without a vapor retarder layer, and no moisture source. Similarly, Figure 72 shows the same wall system but considering rain penetration or moisture source inside the wall. In both XPS thicknesses, the first figure indicates lower moisture content by the wall with a vapor retarder layer than the one without the layer. However, if there is a moisture source, as shown in the

second plot, the plywood MC is higher when there is a vapor retarder since having this layer has decreased the drying potential to the interior. Therefore, this layer has importance only when there is no internal moisture source in the wall system.

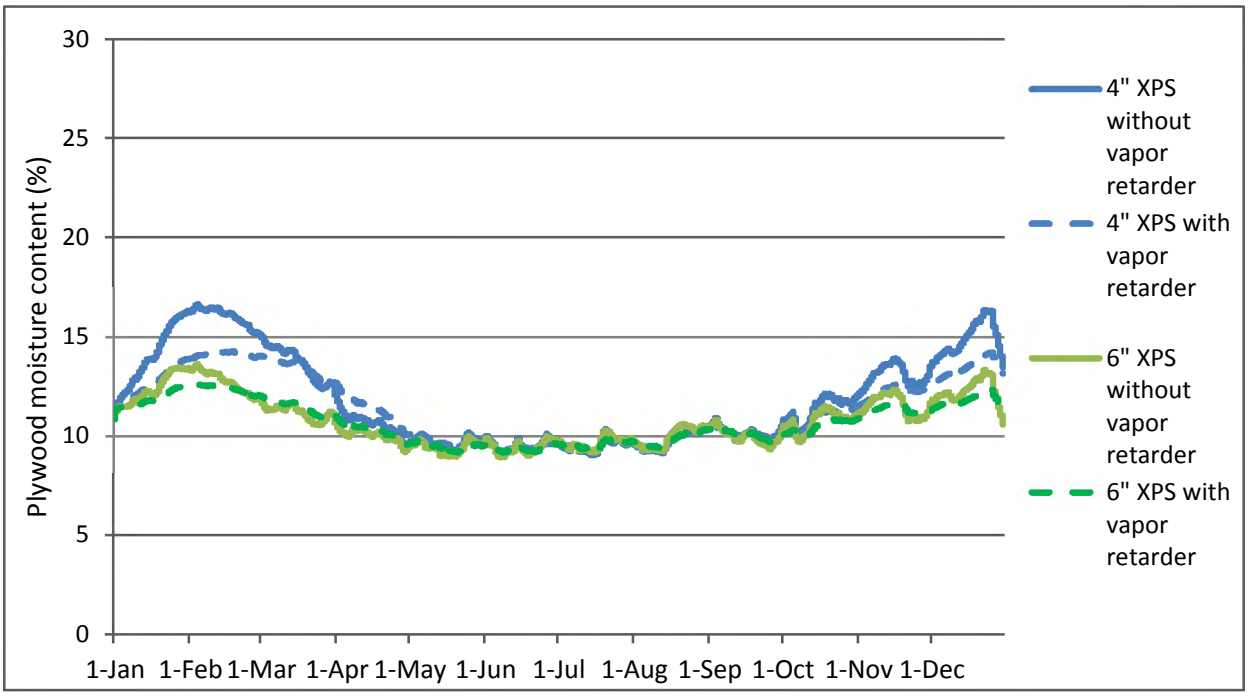

Figure 71: External insulation wall with and without vapor retarder when there is no rain penetration or moisture source.

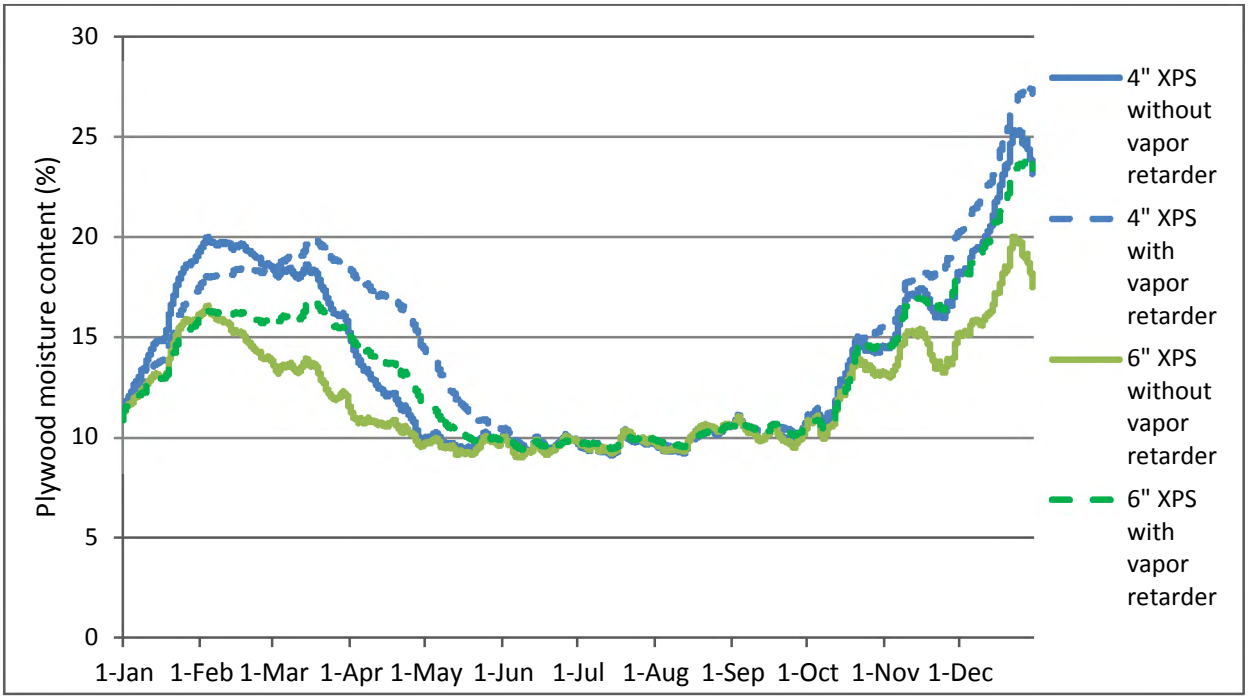

Figure 72: External insulation wall with and without vapor retarder when there is 0.5% rain penetration or moisture source.

Figure 73 and 74 show the plywood moisture content in the 2020s for the external and split insulation walls with and without vapor retarder, respectively. The moisture content by the externally insulated wall is higher in both XPS thicknesses than the split insulation. Since in a standard condition still air has a higher resistance to heat flow than fiberglass batt insulation, the plywood is warmer in the split insulation than external insulation. As a result, the plywood moisture content has reduced due to lower condensation potential by the split insulation. Besides, the two wall assembly show less moisture content fluctuation due to their improved protection from external cyclic loading. However, as shown in Figure 75 and 76, vapor retarder material in the split wall reduces moisture content only in the absence of internal moisture source, for the same reason discussed in the externally insulated wall.

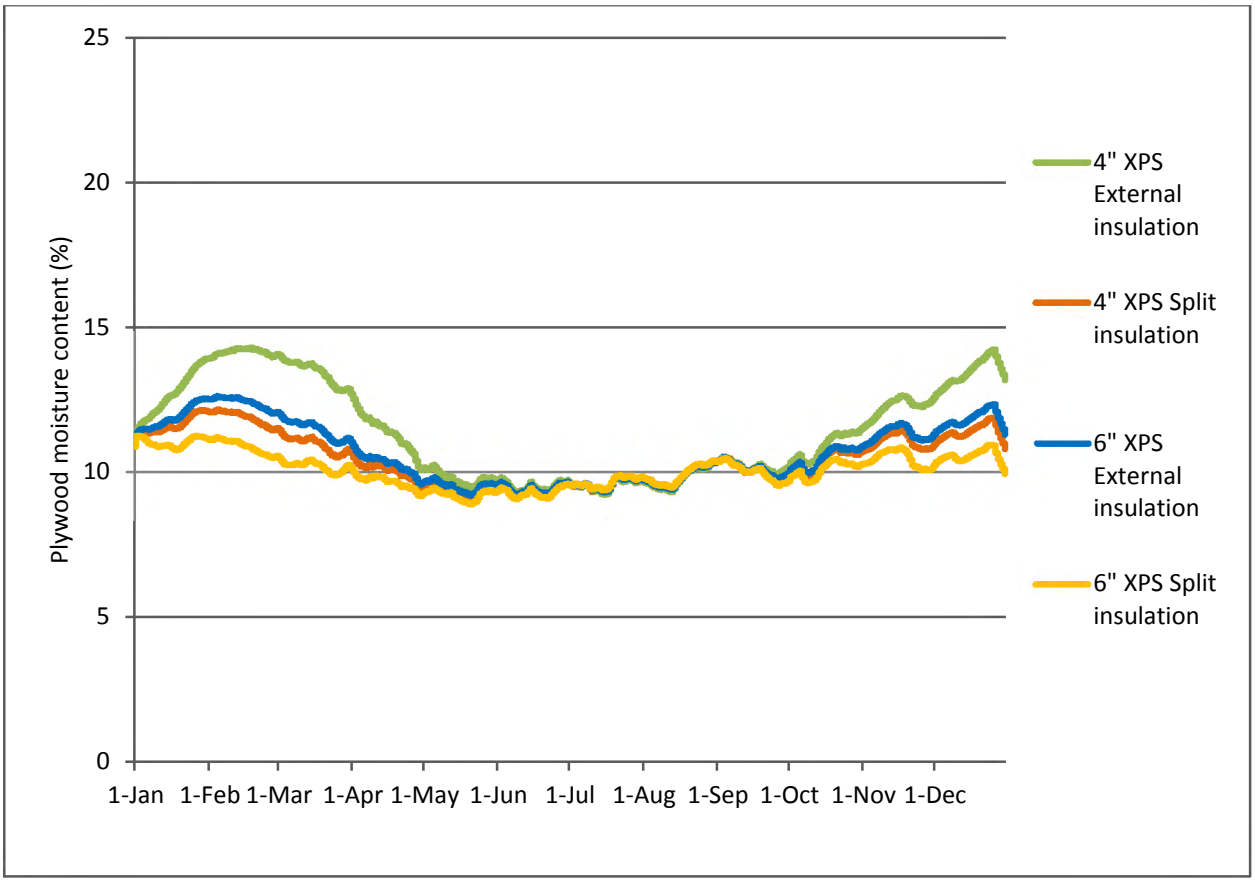

Figure 73: Plywood MC for external and split insulation wall systems with vapor retarder material.

Figure 74: Plywood MC for external and split insulation wall systems without vapor retarder material.

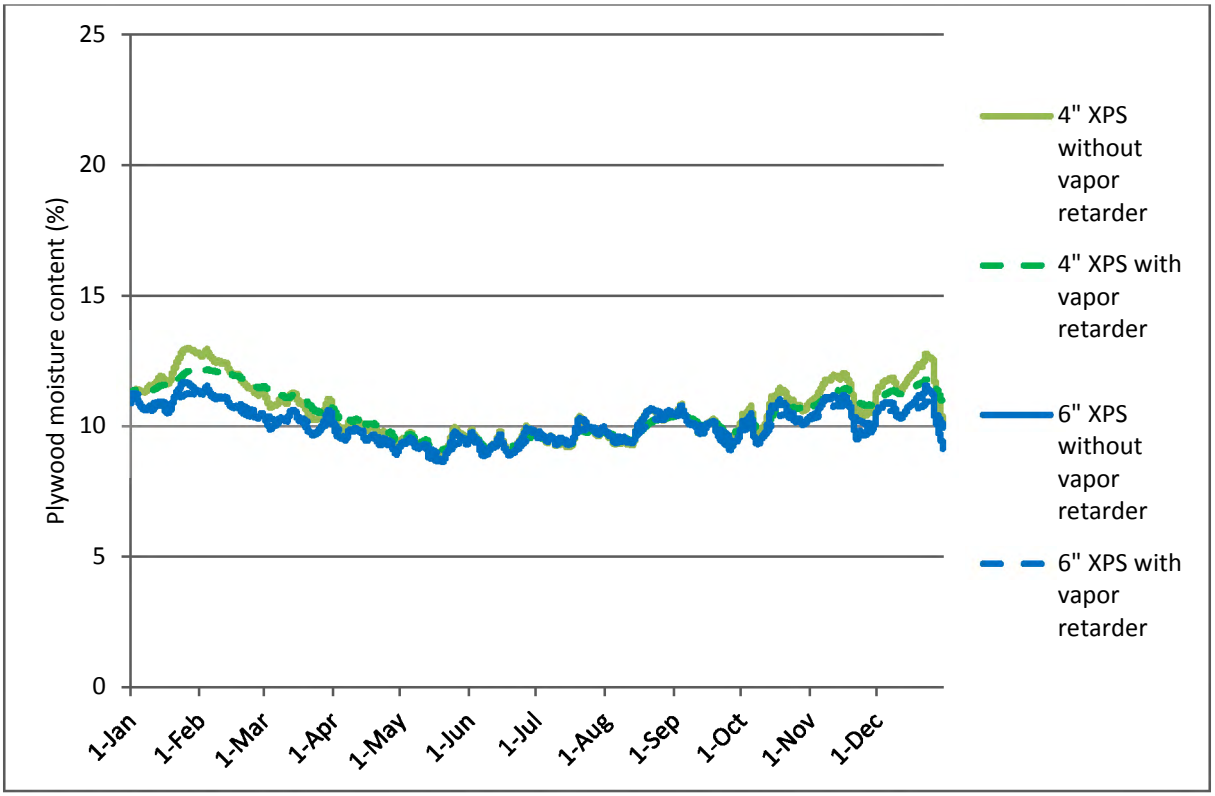

Figure 75: Split insulation wall with and without vapor retarder when there is no rain penetration or moisture source.

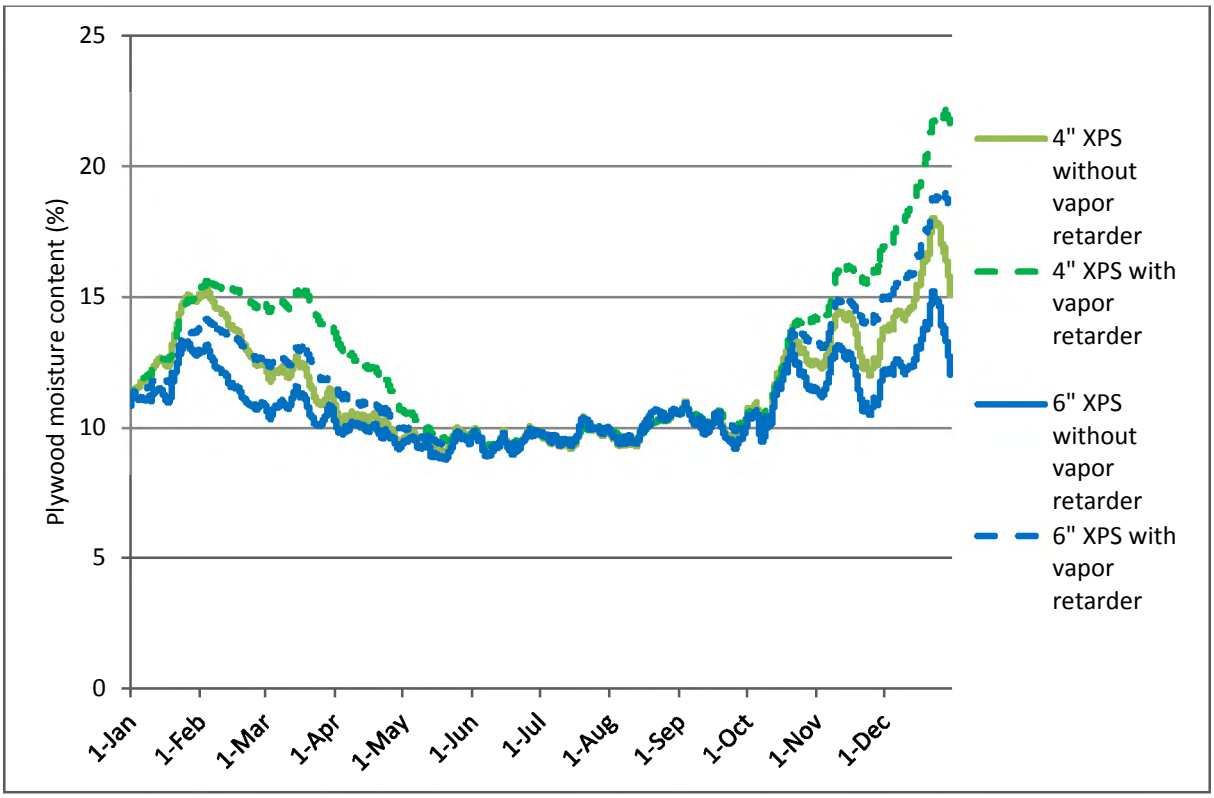

Figure 76: Split insulation wall with and without vapor retarder when there is 0.5% rain penetration or moisture source.

7 Conclusion

The presented research has assessed climate change impact on the durability of various wall systems considering both past and future weather conditions in the marine climate of Vancouver. As discussed in the previous section, the study has taken into account different IPCC emission scenarios determined by socioeconomic factors. Scenario A1FI with warmest temperature projection due to high GHG emission has resulted in the least moisture content on the sheathing material (plywood) than the lowest prediction by scenario B1. The moisture reduction resulted due to enhanced drying potential by a warmer climate. Also, when the biodegradation effect of the sheathing material is concerned, the damage potential shows highest by scenario A1FI, with scenario A2, B2, and B1 placed in second to fourth place, respectively.

When the performance of current climate conditions compared with the future, the sheathing material moisture content is reduced in the far-future year 2080s, followed by the near-future 2050s in comparison to 2020s. Due to increasing air temperature and solar radiation, drying potential appeared to enhance even though moisture load by precipitation projected to increase. However, the mold index based on the yearlong data showed the initial stage of growth. Cavity ventilation behind the cladding has proved a better drying potential using a constant ventilation rate. Besides, cavity ventilation may even further assist drying potential since, in the future, wind speed projected to increase. Therefore, cavity ventilation can serve as a passive adaptation strategy to overcome the adverse effects of climate change.

Externally insulated walls found to perform better than internally insulated ones resulting in lower moisture content since making the sheathing material to have a similar condition with the indoor environment could reduce equilibrium moisture content by keeping the plywood warmer. As a summary, this research has studied how different wall systems could perform

over their service life, considering climate change. Interestingly for the study location, the simulation result indicates future climate could bring benefit from a hygrothermal performance viewpoint. As well as from the heating energy demand aspect since, as discussed in the literature review section in colder regions, heating energy reduction has obtained by different studies. The study has focused on future-oriented building design where codes and standards didn't primarily developed in consideration with changing climate conditions. In the future, further works will be conducted by explicitly focusing approaches to study all potential impacts by climate change on moisture performance of building envelope.

8 Appendix A

Table A1 to A12 summarizes the monthly ensemble climate change predictions by HadCM3 for the different climatic variables, used for morphing by Weather Morph.

A1: Summary of combined HadCM3 projection by scenario A1FI (2020s).

	JAN	FEB	MAR	APR	MAY	JUN	JUL	AUG	SEP	OCT	NOV	DEC	ANN
Daily mean temperature TEMP(°C)	-0.8475	1.155	0.6125	1.415	1.035	1.13	1.5075	2.3675	1.9325	0.9425	1.565	1.5475	1.20
Maximum temperature TMAX(°C)	-0.4	0.7975	0.4075	1.4825	1.135	1.375	1.93	3.075	2.2325	1.0325	1.2425	1.1675	1.29
Minimum temperature TMIN(°C)	-1.1225	1.395	0.9625	1.9525	0.92	0.87	0.76	1.4425	1.5475	0.9125	1.895	1.9275	1.12
Horizontal solar irradiation DSWF W/m²	2.0075	-3.755	-1.3175	-13.73	-3.0625	15.435	20.2975	16.64	4.505	-2.285	-3.48	-2.42	2.40
Total cloud cover TCLW %points	-	-	-	-	-	-	-	-	-	-	-	-	-
Total precipitation rate PREC %	-6.2425	10.9487	-2.9812	9.7711	-0.384	-13.2408	-39.4722	-51.4987	-9.4028	7.0443	4.978	14.3387	-6.35
Relative humidity RHUM % points	-0.775	0.1575	-0.6925	-1.79	-1.1	-2.2375	-4.1275	-6.825	-4.7675	-1.38	-0.44	-0.305	-2.02
Mean sea level pressure MSLP hpa	-	-	-	-	-	-	-	-	-	-	-	-	-
Wind speed WIND %	-2.68	2.2545	-0.2259	1.1509	-1.5501	1.9359	-0.6942	6.4062	3.6066	2.8245	-1.9792	2.3547	1.12

A2: Summary of combined HadCM3 projection by scenario A2 (2020s).

	JAN	FEB	MAR	APR	MAY	JUN	JUL	AUG	SEP	OCT	NOV	DEC	ANN
Daily mean temperature TEMP(°C)	0.4733	0.9342	0.5092	1.24	0.8892	0.8225	1.6342	1.5292	1.2317	1.1308	0.9908	1.2392	1.05
Maximum temperature TMAX(°C)	0.505	0.7733	0.4508	1.5233	1.0208	0.9767	1.8608	1.7808	1.6217	1.1858	0.84	0.985	1.13
Minimum temperature TMIN(°C)	0.4792	0.97	0.7417	1.4317	0.7625	0.6292	1.1933	1.1442	0.7983	1.15	1.1992	1.4675	1.00
Horizontal solar irradiation DSWF W/m²	-0.1267	-1.1017	-2.1658	-6.1483	0.3833	8.0083	12.2033	6.0317	8.5375	-3.5633	-1.4917	-1.9775	1.55
Total cloud cover TCLW %points	0.625	1.625	1.0	0.125	-0.75	-2.625	-5.875	-5.125	-4.875	1.125	1.125	2.75	-0.91
Total precipitation rate PREC %	5.1124	2.0008	3.7692	6.3703	-1.2938	-14.4887	-21.1964	-22.3853	-17.2322	8.9203	-0.3179	12.5425	-3.18
Relative humidity RHUM % points	-0.2525	0.1008	-0.5067	-2.1983	-1.5875	-1.7308	-3.48	-4.1025	-3.5967	-1.0208	-0.5683	0.0192	-1.58
Mean sea level pressure MSLP hpa	-0.083	0.5838	-0.0306	-0.5216	-0.1678	0.1473	-1.1319	-0.7013	-0.4151	-0.312	1.1974	0.22	-0.10
Wind speed WIND %	0.7658	-2.3505	-0.3593	1.9868	-0.0451	-0.2253	0.8398	4.2421	1.5432	1.7856	-4.3593	1.1779	0.42

A3: Summary of combined HadCM3 projection by scenario B1 (2020s).

	JAN	FEB	MAR	APR	MAY	JUN	JUL	AUG	SEP	OCT	NOV	DEC	ANN
Daily mean temperature TEMP(°C)	0.625	0.9675	0.7075	1.625	1.0675	0.5775	1.3975	1.7475	1.4625	0.8075	1.4225	1.41	1.15
Maximum temperature TMAX(°C)	0.615	0.625	0.595	1.765	1.2075	0.565	1.5625	1.955	2.105	1.04	0.9425	1.09	1.17
Minimum temperature TMIN(°C)	0.59	1.1775	0.9475	2.1275	0.8575	0.52	1.125	1.345	0.7875	0.695	1.7575	1.7175	1.14
Horizontal solar irradiation DSWF W/m²	-1.1775	-2.42	1.2825	-11.49	4.535	4.4525	7.53	7.0825	12.5925	1.07	-3.655	-2.1275	1.47
Total cloud cover TCLW %points	-	-	-	-	-	-	-	-	-	-	-	-	-
Total precipitation rate PREC %	7.3616	-0.7513	-0.2408	7.7274	-0.343	-2.6761	-19.884	-36.1075	-25.8423	1.0231	8.8762	22.3118	-3.21
Relative humidity RHUM % points	-0.04	0.36	-0.745	-2.0325	-1.56	-1.42	-1.505	-2.95	-4.515	-1.5825	0.1525	-0.6525	-1.37
Mean sea level pressure MSLP hpa	-	-	-	-	-	-	-	-	-	-	-	-	-
Wind speed WIND %	-0.4701	-0.8298	-0.6174	1.0706	-0.3333	0.5878	-2.3702	0.0213	-0.6549	2.085	-1.2984	5.7242	0.24

A4: Summary of combined HadCM3 projection by scenario B2 (2020s).

	JAN	FEB	MAR	APR	MAY	JUN	JUL	AUG	SEP	OCT	NOV	DEC	ANN
Daily mean temperature TEMP(°C)	0.2838	0.8262	0.2675	1.3962	1.2688	0.9025	1.87	1.9612	1.5675	0.905	0.9937	1.7388	1.17
Maximum temperature TMAX(°C)	0.35	0.5725	0.325	1.65	1.4575	0.9737	2.2912	2.2713	2.0187	1.1587	0.9375	1.2662	1.27
Minimum temperature TMIN(°C)	0.2175	0.9888	0.305	1.7338	1.055	0.8563	1.2925	1.4025	1.0237	0.765	1.165	2.1	1.08
Horizontal solar irradiation DSWF W/m²	0.215	-3.3	1.7463	-7.3587	4.68	3.2738	16.1463	8.4213	8.2275	0.6325	-0.09	-3.0162	2.46
Total cloud cover TCLW %points	-	-	-	-	-	-	-	-	-	-	-	-	-
Total precipitation rate PREC %	5.1611	12.9978	-5.5762	7.5838	-4.6223	-9.7046	-29.3941	-34.8918	-22.0538	3.3483	-5.1494	17.2516	-5.42
Relative humidity RHUM % points	-0.2662	0.2437	-0.4875	-2.2275	-1.8237	-1.2763	-3.4063	-5.335	-4.9763	-2.1925	-0.6625	0.11	-1.86
Mean sea level pressure MSLP hpa	0.2673	-0.0965	0.4419	-1.1736	-0.2314	-0.442	-0.6743	-0.649	-0.7227	-0.259	0.7708	0.0107	-0.23
Wind speed WIND %	1.6076	1.5395	-3.1516	2.6175	0.0259	0.686	-1.1561	4.9975	1.493	1.8604	-3.9939	1.6036	0.68

A5: Summary of combined HadCM3 projection by scenario A1FI (2050s).

	JAN	FEB	MAR	APR	MAY	JUN	JUL	AUG	SEP	OCT	NOV	DEC	ANN
Daily mean temperature TEMP(°C)	1.2725	0.905	0.9725	3.265	2.1275	2.8775	4.55	4.4725	3.7425	2.07	3.0275	3.2625	2.71
Maximum temperature TMAX(°C)	1.2775	0.7875	1.2275	4.0125	2.575	3.2625	5.47	5.2625	4.69	2.2525	2.6025	2.63	3.00
Minimum temperature TMIN(°C)	1.3175	1.045	1.3575	3.5775	1.59	2.415	3.085	3.335	2.73	1.97	3.545	3.955	2.49
Horizontal solar irradiation DSWF W/m²	-0.33	-0.3725	1.1975	-12.288	11.9175	20.1475	39.005	19.9575	14.09	-3.4125	-5.3925	-4.385	6.68
Total cloud cover TCLW %points	-	-	-	-	-	-	-	-	-	-	-	-	-
Total precipitation rate PREC %	7.7771	-6.9757	-5.224	10.9637	-16.198	-28.4814	-53.4505	-64.7364	-32.3618	16.0259	7.3223	36.7905	-10.71
Relative humidity RHUM % points	-0.3875	-0.93	-2.4125	-5.0825	-4.23	-4.0675	-10.365	-9.5025	-8.3625	-2.865	-0.9025	-0.665	-4.15
Mean sea level pressure MSLP hpa	-	-	-	-	-	-	-	-	-	-	-	-	-
Wind speed WIND %	-3.8477	-4.4763	-0.2702	-1.4181	-0.6034	-1.3113	5.8275	9.56	1.5071	4.6094	-5.6147	4.3018	0.69

A6: Summary of combined HadCM3 projection by scenario A2 (2050s).

	JAN	FEB	MAR	APR	MAY	JUN	JUL	AUG	SEP	OCT	NOV	DEC	ANN
Daily mean temperature TEMP(°C)	0.8167	0.7	0.955	2.7492	2.0742	2.305	3.7358	3.5625	2.9892	2.31	1.8933	2.2175	2.19
Maximum temperature TMAX(°C)	0.8375	0.7137	1.12	3.5625	2.355	2.6037	4.3163	3.9287	3.415	2.3675	1.4087	1.5725	2.35
Minimum temperature TMIN(°C)	1.0675	0.695	1.3037	2.87	1.9725	2.0888	2.6725	2.8725	2.3475	2.2313	1.5975	2.2637	2.00
Horizontal solar irradiation DSWF W/m²	0.075	0.9025	-3.1767	-8.6708	1.54	13.2008	28.0192	10.9967	8.0175	-4.2825	-2.2858	-2.95	3.45
Total cloud cover TCLW %points	-1.0	-2.125	1.125	-0.875	-3.125	-5.0	-11.75	-7.0	-4.25	1.25	1.625	1.25	-2.49
Total precipitation rate PREC %	0.6713	-5.2169	7.5337	6.7792	0.2939	-16.5196	-45.7032	-43.0046	-19.1296	7.0931	1.0358	14.9244	-7.60
Relative humidity RHUM % points	-0.5742	-0.5283	-1.5267	-4.7342	-3.5983	-2.98	-7.3225	-7.4133	-5.8117	-1.6242	-1.0775	-0.2083	-3.12
Mean sea level pressure MSLP hpa	0.1163	-0.0314	1.0935	-0.7612	-0.2446	-0.5248	-1.9543	-1.6685	-1.3236	-0.697	0.1176	-0.1501	-0.50
Wind speed WIND %	-3.1324	-2.7772	0.9935	0.3312	0.8117	-1.0616	4.6559	8.6629	1.5978	-0.3971	-3.7284	-0.5176	0.45

A7: Summary of combined HadCM3 projection by scenario B1 (2050s).

	JAN	FEB	MAR	APR	MAY	JUN	JUL	AUG	SEP	OCT	NOV	DEC	ANN
Daily mean temperature TEMP(°C)	0.72	0.9025	0.6475	2.065	1.275	1.485	2.9125	2.8275	2.445	1.755	2.5825	2.6125	1.85
Maximum temperature TMAX(°C)	0.7425	0.6125	0.61	2.325	1.4325	1.69	3.405	3.155	2.7525	1.97	2.015	2.0575	1.90
Minimum temperature TMIN(°C)	0.72	1.0625	1.0775	2.6175	1.1625	1.11	2.12	2.245	1.9625	1.6125	3.145	3.0875	1.83
Horizontal solar irradiation DSWF W/m²	-1.29	-2.8675	-4.78	-14.558	-0.335	16.61	23.88	10.29	5.8425	-2.605	-5.2175	-4.2475	1.73
Total cloud cover TCLW %points	-	-	-	-	-	-	-	-	-	-	-	-	-
Total precipitation rate PREC %	8.8908	0.9586	5.5774	13.3433	5.205	-22.8468	-35.4275	-33.901	-20.3696	13.6627	9.3057	31.3452	-2.02
Relative humidity RHUM % points	-0.14	0.315	-0.93	-3.1375	-2.06	-3.1225	-5.0425	-5.4575	-4.4775	-1.705	-0.7125	0.13	-2.19
Mean sea level pressure MSLP hpa	-	-	-	-	-	-	-	-	-	-	-	-	-
Wind speed WIND %	-1.3709	-2.2221	2.046	1.2512	0.3573	0.0519	-0.01	5.1648	-0.8227	0.6809	-1.8459	2.0092	0.44

A8: Summary of combined HadCM3 projection by scenario B2 (2050s).

	JAN	FEB	MAR	APR	MAY	JUN	JUL	AUG	SEP	OCT	NOV	DEC	ANN
Daily mean temperature TEMP(°C)	0.5987	0.4912	0.7912	2.2325	1.7887	1.9962	3.3163	3.4987	3.2175	2.0012	2.105	2.1575	2.02
Maximum temperature TMAX(°C)	0.5625	0.5687	0.9487	2.8712	1.9875	2.2713	3.8775	3.9562	4.0625	2.3025	1.7988	1.7375	2.25
Minimum temperature TMIN(°C)	0.6438	0.42	0.9187	2.45	1.555	1.625	2.3325	2.7637	2.2637	1.8263	2.4725	2.535	1.82
Horizontal solar irradiation DSWF W/m²	-0.6513	1.4875	1.6438	-7.7675	5.9038	16.7288	25.2763	11.3213	13.0488	-1.395	-3.2313	-2.565	4.98
Total cloud cover TCLW %points	-	-	-	-	-	-	-	-	-	-	-	-	-
Total precipitation rate PREC %	4.2401	-1.4199	-1.958	8.5638	-3.1757	-20.0213	-42.8223	-41.9969	-28.282	6.6928	9.6312	12.9316	-8.13
Relative humidity RHUM % points	-0.3625	-0.285	-1.2475	-3.8887	-2.9663	-3.05	-7.1687	-7.0912	-7.3688	-2.285	-0.8925	0.0437	-3.05
Mean sea level pressure MSLP hpa	0.5988	1.409	0.5137	-0.7781	-0.2305	-0.5065	-1.5838	-1.5159	-1.7876	-0.9042	-0.5395	0.4352	-0.41
Wind speed WIND %	-1.1526	-3.0839	-3.4792	1.8477	2.3048	-0.2276	5.6198	8.3425	0.9748	1.2778	-1.2295	-0.4689	0.89

A9: Summary of combined HadCM3 projection by scenario A1FI (2080s).

	JAN	FEB	MAR	APR	MAY	JUN	JUL	AUG	SEP	OCT	NOV	DEC	ANN
Daily mean temperature TEMP(°C)	2.875	3.55	3.1825	5.2075	3.96	5.57	8.285	8.8425	6.67	4.615	5.1425	4.205	5.18
Maximum temperature TMAX(°C)	2.4625	2.6225	3.405	6.5525	4.2525	6.0025	9.43	9.9325	7.435	5.085	4.7475	3.485	5.45
Minimum temperature TMIN(°C)	3.305	4.45	4.1075	5.3275	3.615	4.835	6.525	7.2925	5.72	4.3125	5.7125	5.1475	5.03
Horizontal solar irradiation DSWF W/m²	-3.15	-9.3925	-8.83	-14.13	4.62	32.6275	49.905	29.3275	11.3125	-0.27	-7.07	-3.6	6.78
Total cloud cover TCLW %points	-	-	-	-	-	-	-	-	-	-	-	-	-
Total precipitation rate PREC %	21.777	10.4821	11.1951	20.4174	-7.1822	-30.726	-60.9042	-62.2658	-24.1009	21.0457	17.5167	28.6736	-4.51
Relative humidity RHUM % points	-1.265	-1.1475	-4.455	-9.02	-5.0875	-7.305	-15.0825	-14.5175	-9.37	-4.57	-2.3925	-3.01	-6.44
Mean sea level pressure MSLP hpa	-	-	-	-	-	-	-	-	-	-	-	-	-
Wind speed WIND %	-3.9229	-6.2135	-2.1449	1.5178	-2.1196	-2.7096	9.92	9.265	-2.8285	4.0612	-4.6577	1.8226	0.17

A10: Summary of combined HadCM3 projection by scenario A2 (2080s).

	JAN	FEB	MAR	APR	MAY	JUN	JUL	AUG	SEP	OCT	NOV	DEC	ANN
Daily mean temperature TEMP(°C)	2.3908	2.4608	2.8192	4.4483	3.2958	4.2133	6.5225	6.9142	5.465	3.7775	3.4183	3.45	4.10
Maximum temperature TMAX(°C)	2.0342	1.8725	2.865	5.585	3.5583	4.5558	7.4292	7.7625	6.1258	4.1433	3.1542	2.8408	4.33
Minimum temperature TMIN(°C)	2.7708	3.0192	3.795	4.7208	3.0567	3.7392	5.1142	5.7542	4.7208	3.6133	3.8942	4.155	4.03
Horizontal solar irradiation DSWF W/m²	-2.2533	-5.8267	-11.278	-15.876	2.1692	21.0392	38.1333	20.4033	10.085	-3.6667	-4.9008	-3.7675	3.69
Total cloud cover TCLW %points	0.0	2.5	1.0	-0.875	-4.0	-8.75	-15.625	-11.75	-5.375	-0.5	3.0	2.875	-3.12
Total precipitation rate PREC %	6.3436	10.6879	8.5509	15.9855	-2.8668	-21.0645	-54.1026	-56.5444	-20.8025	8.2542	6.6819	19.1393	-6.64
Relative humidity RHUM % points	-0.79	-0.9892	-3.5042	-7.5125	-4.8533	-4.8208	-11.6708	-11.2867	-7.7375	-2.695	-1.7033	-1.18	-4.90
Mean sea level pressure MSLP hpa	0.5154	0.2356	-0.6125	-1.2164	-0.2101	-1.0862	-2.7182	-2.5767	-1.9164	-1.7046	0.3501	-0.0526	-0.92
Wind speed WIND %	-4.6824	-2.8165	-3.9836	1.0837	0.0985	-0.9758	7.7582	8.3531	0.4455	-2.7212	-4.3831	-1.4265	-0.27

A11: Summary of combined HadCM3 projection by scenario B1 (2080s).

	JAN	FEB	MAR	APR	MAY	JUN	JUL	AUG	SEP	OCT	NOV	DEC	ANN
Daily mean temperature TEMP(°C)	0.78	0.9325	1.6925	3.1525	2.145	2.6275	3.79	4.265	4.0875	2.5825	3.07	2.8575	2.67
Maximum temperature TMAX(°C)	0.7575	0.8725	1.75	3.9325	2.3575	2.82	4.2	4.76	4.7275	2.59	2.435	2.125	2.78
Minimum temperature TMIN(°C)	0.8025	1.045	2.3425	3.48	1.96	2.2375	3.005	3.4625	3.2875	2.6075	3.6925	3.5375	2.62
Horizontal solar irradiation DSWF W/m²	-1.2975	0.75	-4.175	-11.978	1.22	19.38	24.715	16.445	12.0875	-6.4925	-7.0225	-4.2475	3.28
Total cloud cover TCLW %points	-	-	-	-	-	-	-	-	-	-	-	-	-
Total precipitation rate PREC %	14.4168	-7.8859	5.0389	9.951	4.6974	-14.229	-28.9749	-46.6137	-13.2755	23.0304	22.4119	26.5703	-0.41
Relative humidity RHUM % points	-0.1325	-0.3975	-2.27	-5.35	-2.385	-3.3225	-5.6375	-6.34	-6.07	-1.0425	-0.46	-0.4975	-2.83
Mean sea level pressure MSLP hpa	-	-	-	-	-	-	-	-	-	-	-	-	-
Wind speed WIND %	-2.2089	-6.248	-2.3611	-0.0286	0.4075	-1.1466	0.7044	4.4979	-0.7775	2.7283	0.2759	4.3208	0.01

A12: Summary of combined HadCM3 projection by scenario B2 (2080s).

	JAN	FEB	MAR	APR	MAY	JUN	JUL	AUG	SEP	OCT	NOV	DEC	ANN
Daily mean temperature TEMP(°C)	1.09	1.23	1.8113	3.5063	2.7225	2.7112	4.4988	4.835	4.0537	2.5112	2.6612	3.055	2.89
Maximum temperature TMAX(°C)	1.1062	1.0588	1.965	4.8563	3.1262	3.0637	5.2363	5.5038	4.545	2.6688	2.39	2.38	3.16
Minimum temperature TMIN(°C)	0.8825	1.275	2.5025	3.4425	2.4525	2.1725	3.395	3.7425	3.7575	2.4825	2.28	3.2225	2.63
Horizontal solar irradiation DSWF W/m²	0.45	-1.1887	-3.015	-1.6425	12.7125	22.495	31.4938	16.4525	6.835	-4.4588	-3.4025	-3.57	6.10
Total cloud cover TCLW %points	-	-	-	-	-	-	-	-	-	-	-	-	-
Total precipitation rate PREC %	3.5123	1.0567	-3.6408	-1.4526	-7.8198	-25.4141	-52.5648	-54.076	-18.0055	13.8142	8.9304	17.3177	-9.86
Relative humidity RHUM % points	-1.0088	-0.59	-2.425	-7.335	-4.2388	-4.5462	-9.7	-8.9725	-6.3175	-1.62	-1.1088	-0.4637	-4.03
Mean sea level pressure MSLP hpa	2.4435	1.165	-0.0158	-1.2247	-0.5887	-0.7004	-2.1499	-1.9798	-1.9771	-1.3155	1.0782	1.4886	-0.51
Wind speed WIND %	-2.9385	-2.1239	-5.642	1.5603	-0.466	-0.1792	6.7725	9.0547	-1.6091	2.3046	-3.3384	-2.8431	0.05

9 Appendix B

This section discussed the monthly dry bulb temperature difference between the years. As shown in plot B1 to B4 scenario A1FI, dry-bulb temperature prediction is the highest of all where the monthly average temperature exceeds by as much as 4.6 °C in 2080 than the corresponding projection by scenario B1. The temperature projection by scenario A2 is the second-highest after A1FI, which is followed by scenario B2. In 2020s the monthly average temperature of all scenarios is similar where the maximum difference lies in the range of 0.1 °C. In 2050s the mean annual temperature values are 12.5 °C for A1FI, 12 °C A2, 11.6 °C B1 and 11.8 °C for B2. Similarly, in 2080 15 °C, 13.9 °C, 12.5 °C, and 12.7 °C for A1FI, A2, B1, & B2 respectively which scenario A1FI shows the highest increment by 27 % and 17 % as compared to the corresponding 2020s and 2050s.

B1: Monthly average dry bulb temperature comparison of years (Scenario A1FI).

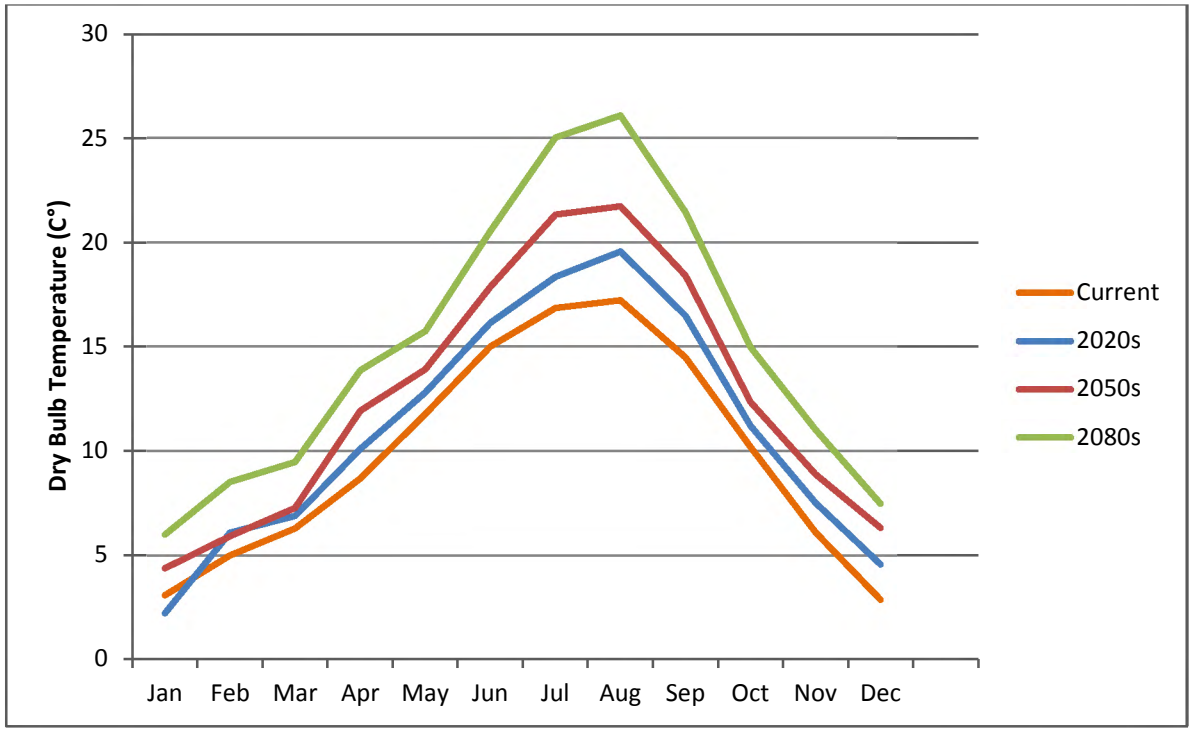

B2: Monthly average dry bulb temperature comparison of years (Scenario A2).

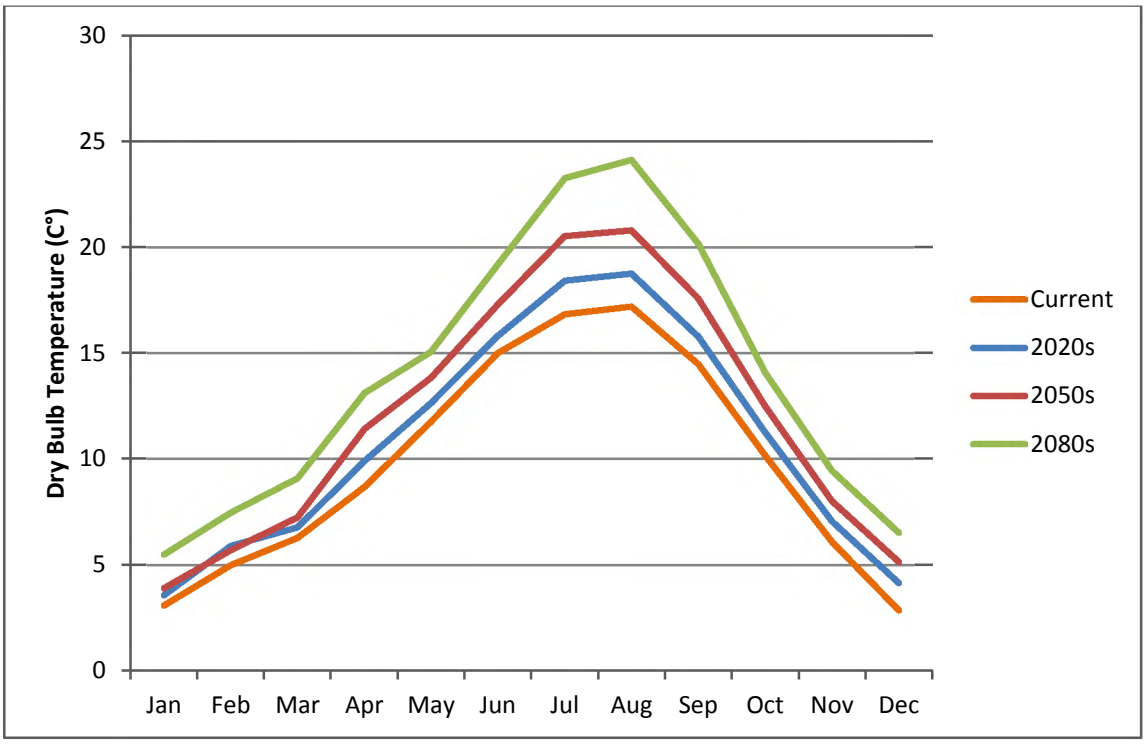

B3: Monthly average dry bulb temperature comparison of years (Scenario B1).

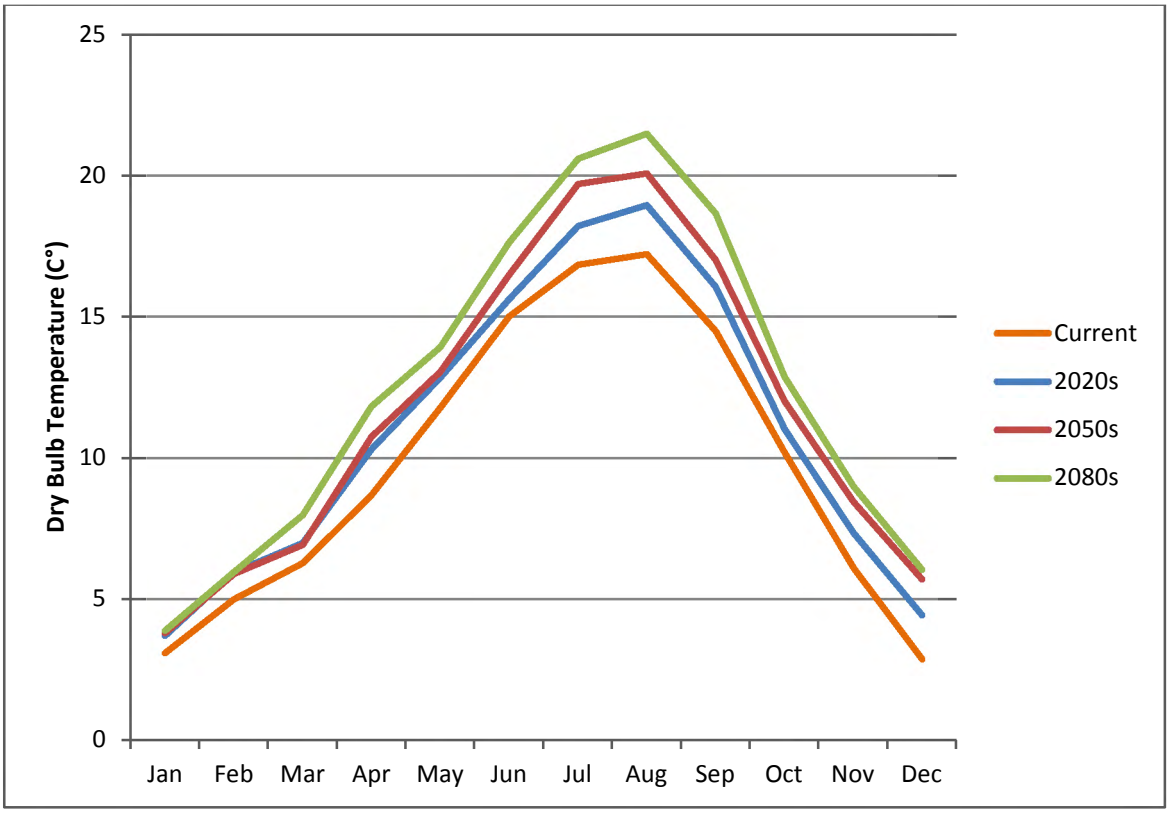

B4: Monthly average dry bulb temperature comparison of years (Scenario B2).

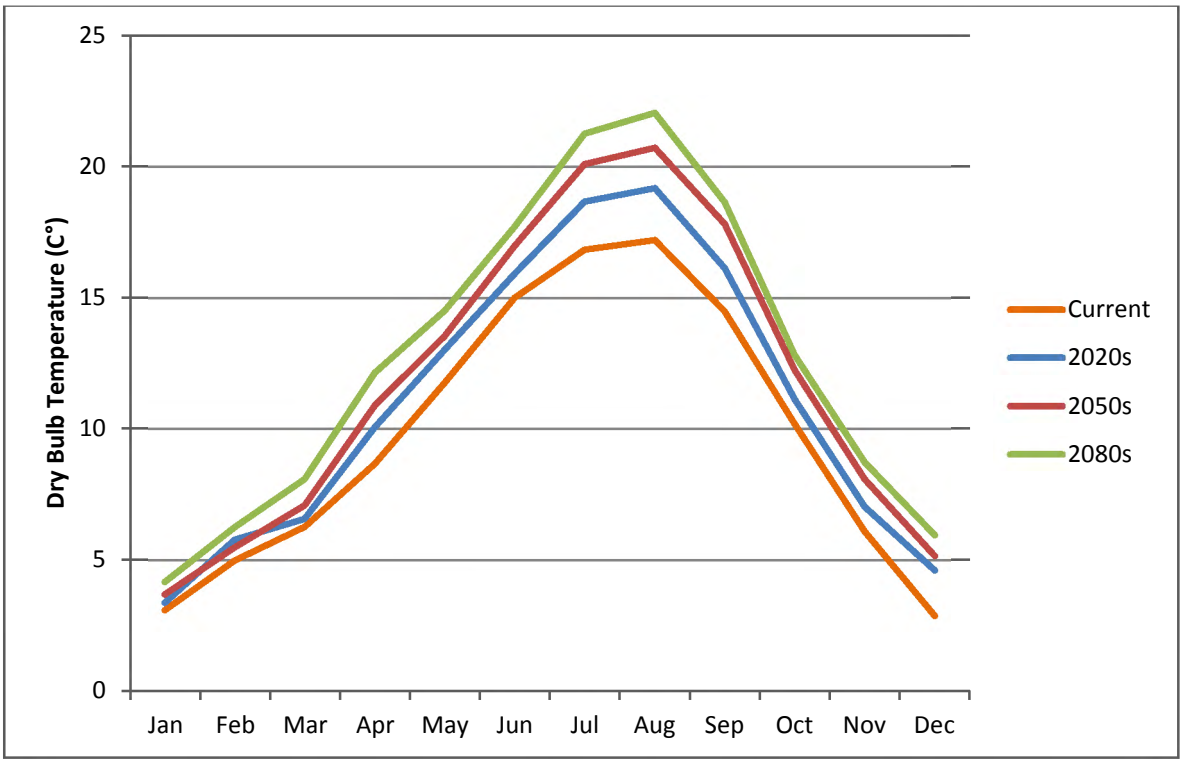

As shown in plot B5 to B8, the projected relative humidity by scenario A1FI is the lowest of all. Likewise, the projection by scenario B1 is the highest, which makes a point as the temperature increases the capacity of the air to hold moisture also increases (warm air can hold higher moisture than colder air), as a result, the relative humidity decreases. The relative humidity change depends on seasons. During winter months, the difference is small in all considered scenarios and years while the change grows further in winter months, where a seasonal mean relative humidity difference of around 12 % observed between 2020s and 2080s in A1FI.

B5: Monthly average relative humidity comparison of years (Scenario A1FI).

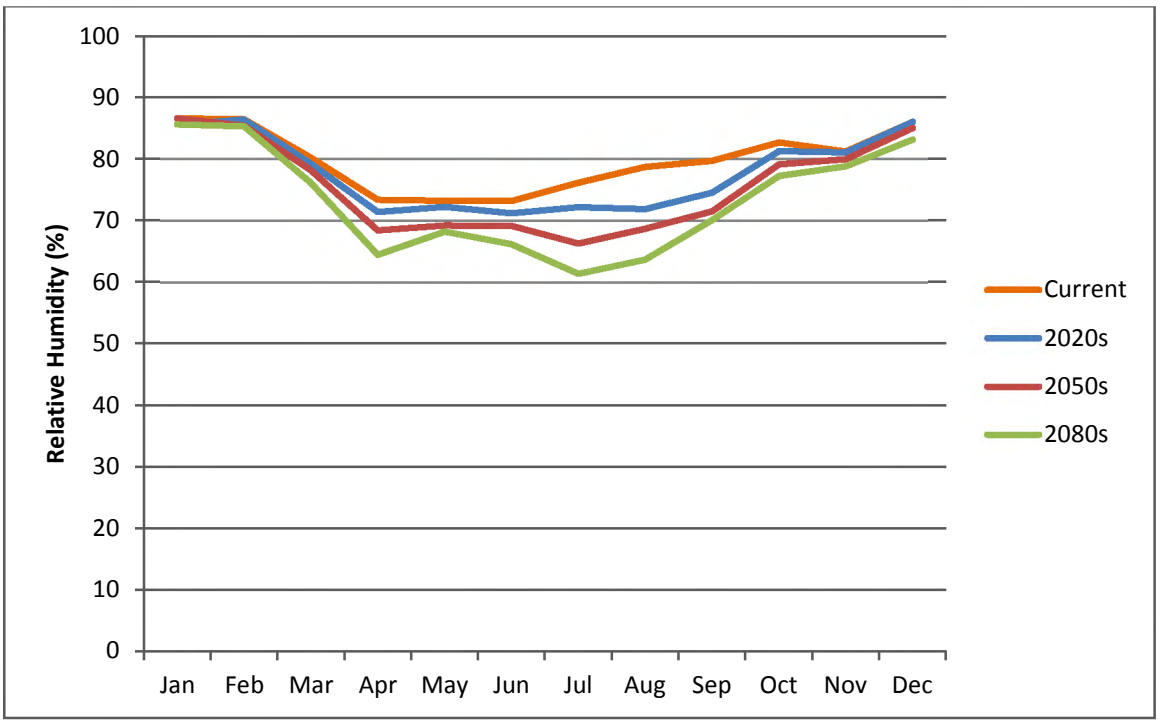

B6: Monthly average relative humidity comparison of years (Scenario A2).

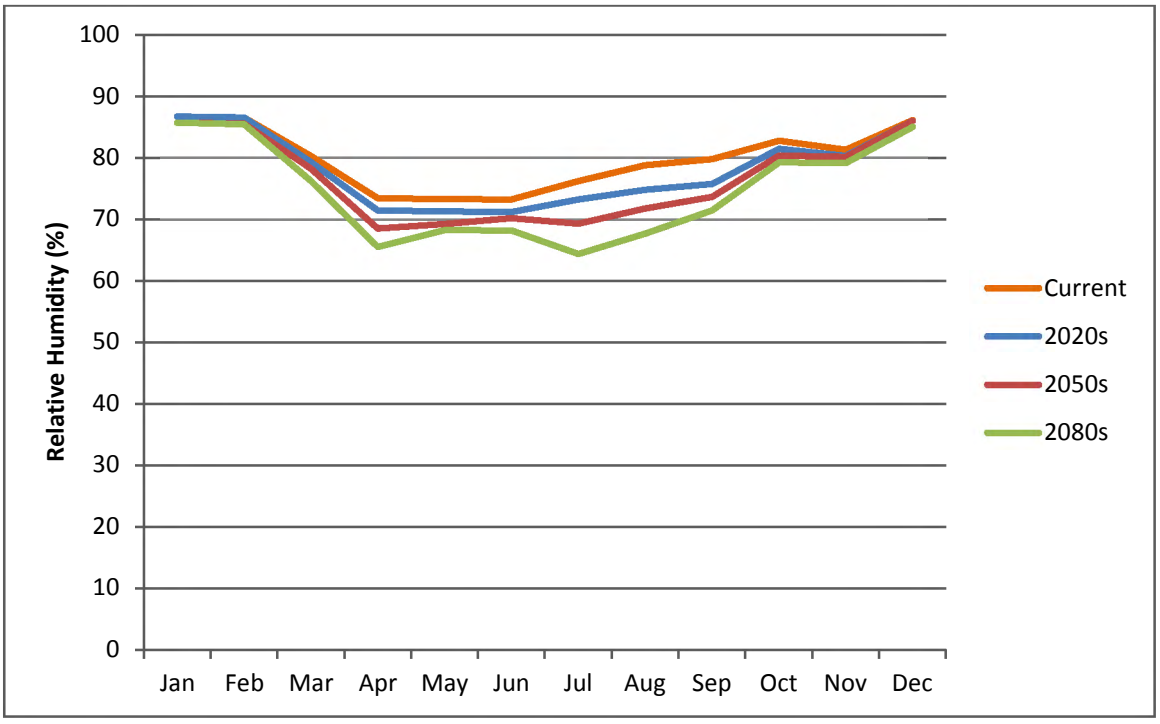

B7: Monthly average relative humidity comparison of years (Scenario B1).

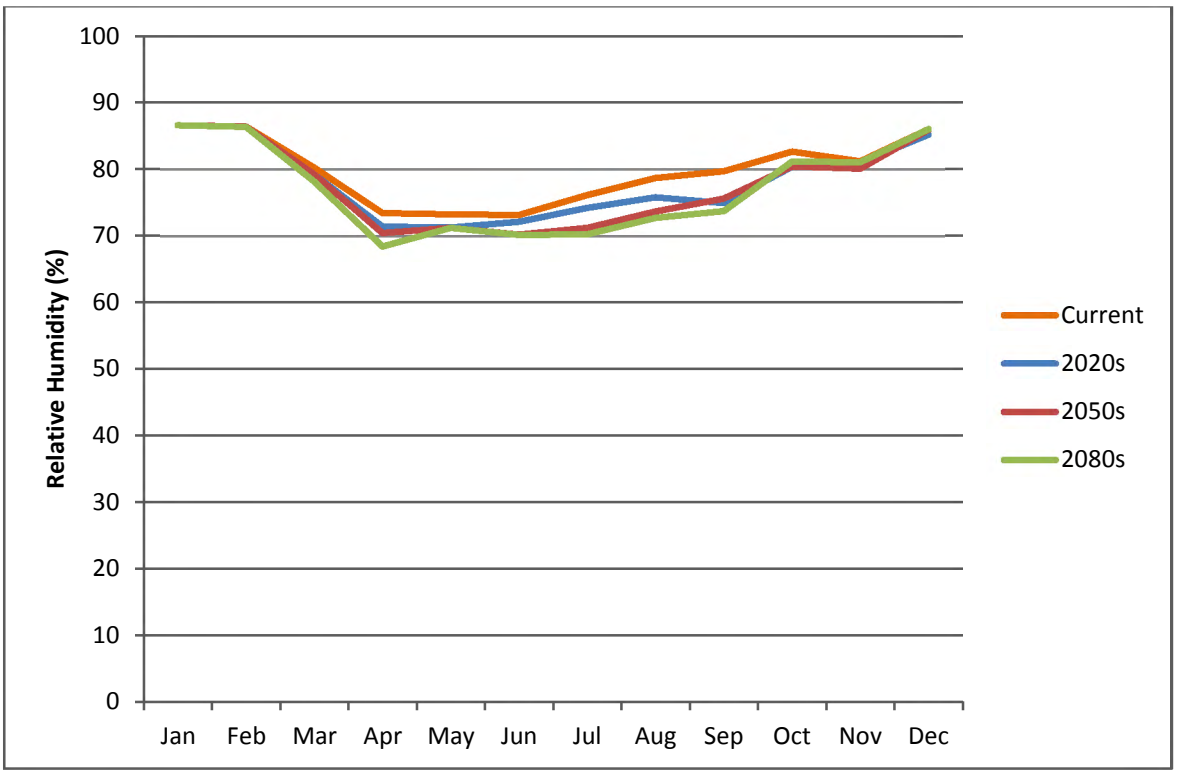

B8: Monthly average relative humidity comparison of years (Scenario B2).

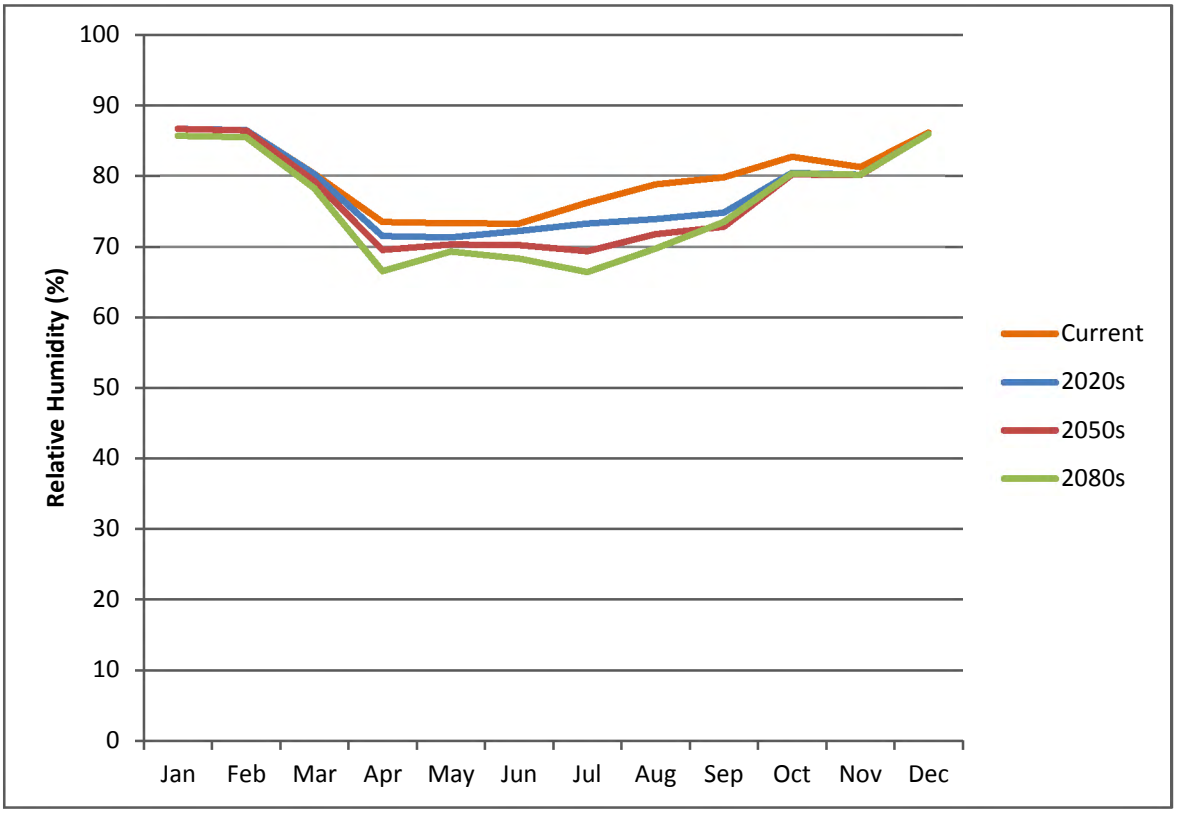

As shown from B10 to B13, the global horizontal radiation has a similar trend as temperature projection, where the highest prediction observed in scenario A1FI and lowest prediction in B1. Also, as relative humidity, the projected GHI changes show a seasonal effect with the highest difference between years observed in the summer season than the winter season. Plot B9 summarizes the mean annual global horizontal radiation for the three years and scenarios, where the lowest differences between scenarios observed in the year 2020, and the highest difference in the year 2080 between scenario A1FI and B1.

B9: Summary of annual average global horizontal radiation (W/m^2).

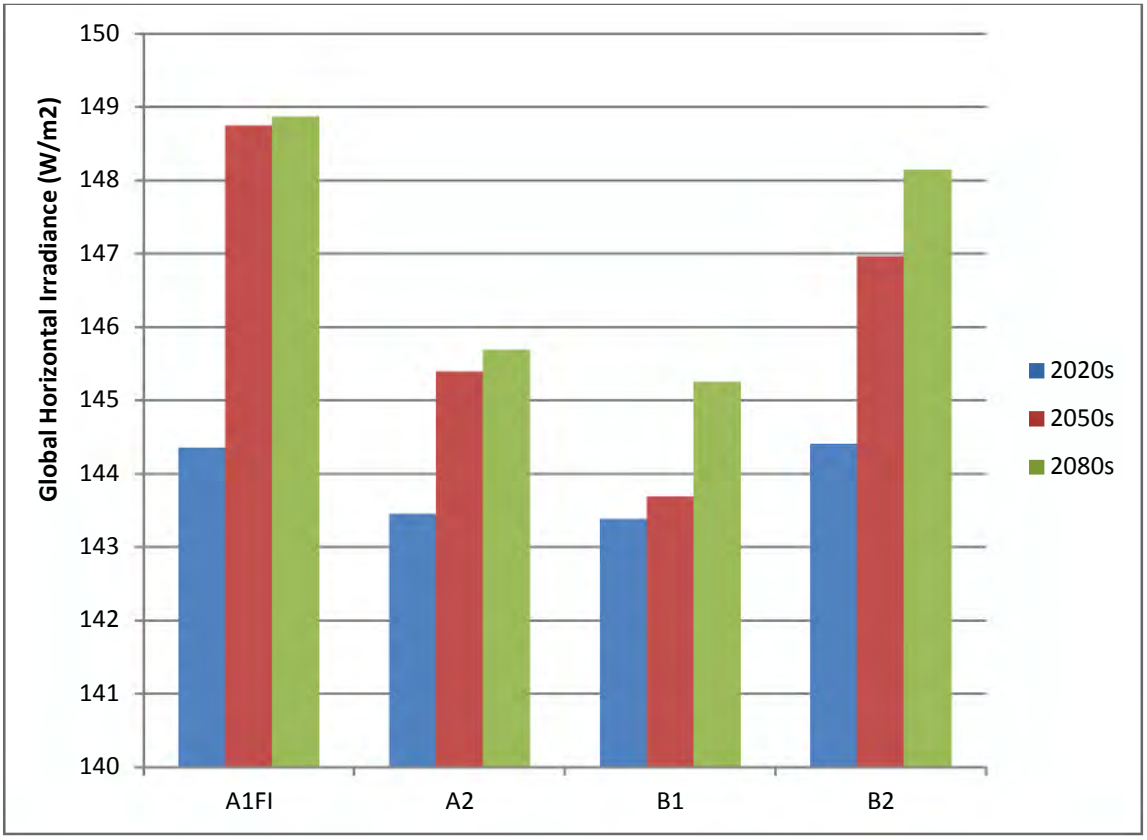

B10: Monthly average GHI comparison of years (Scenario A1FI).

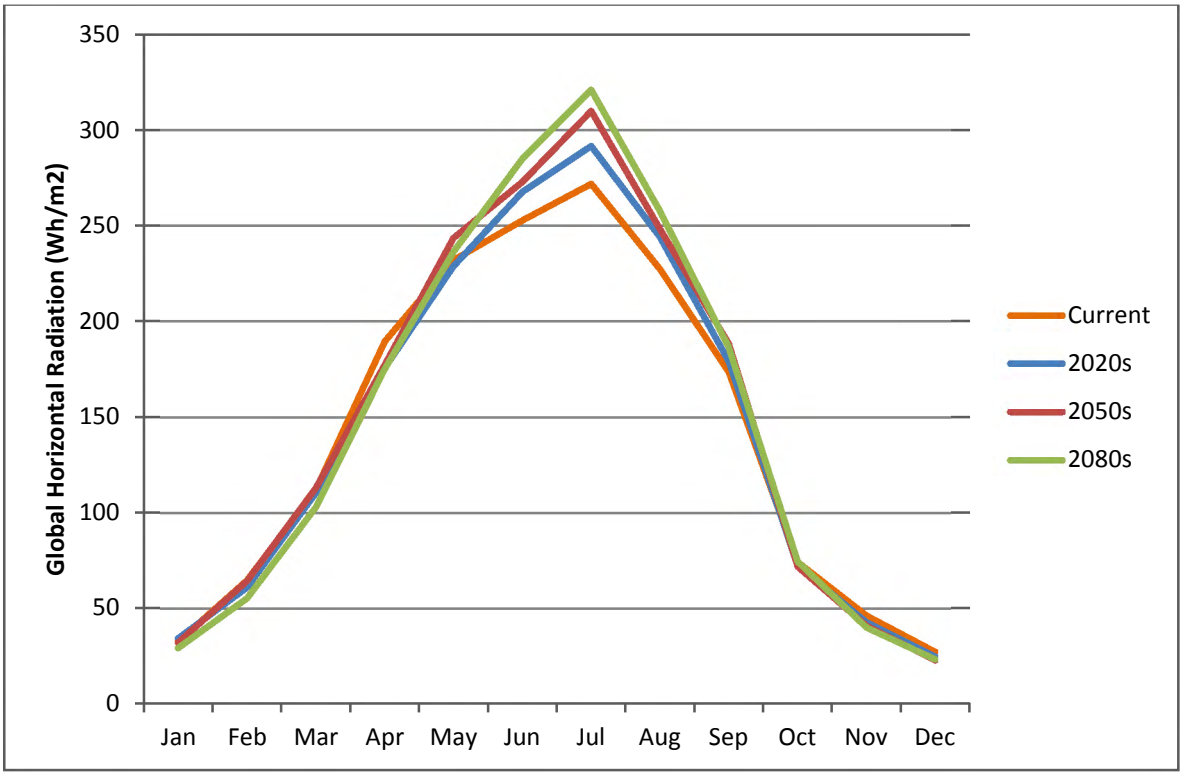

B11: Monthly average GHI comparison of years (Scenario A2).

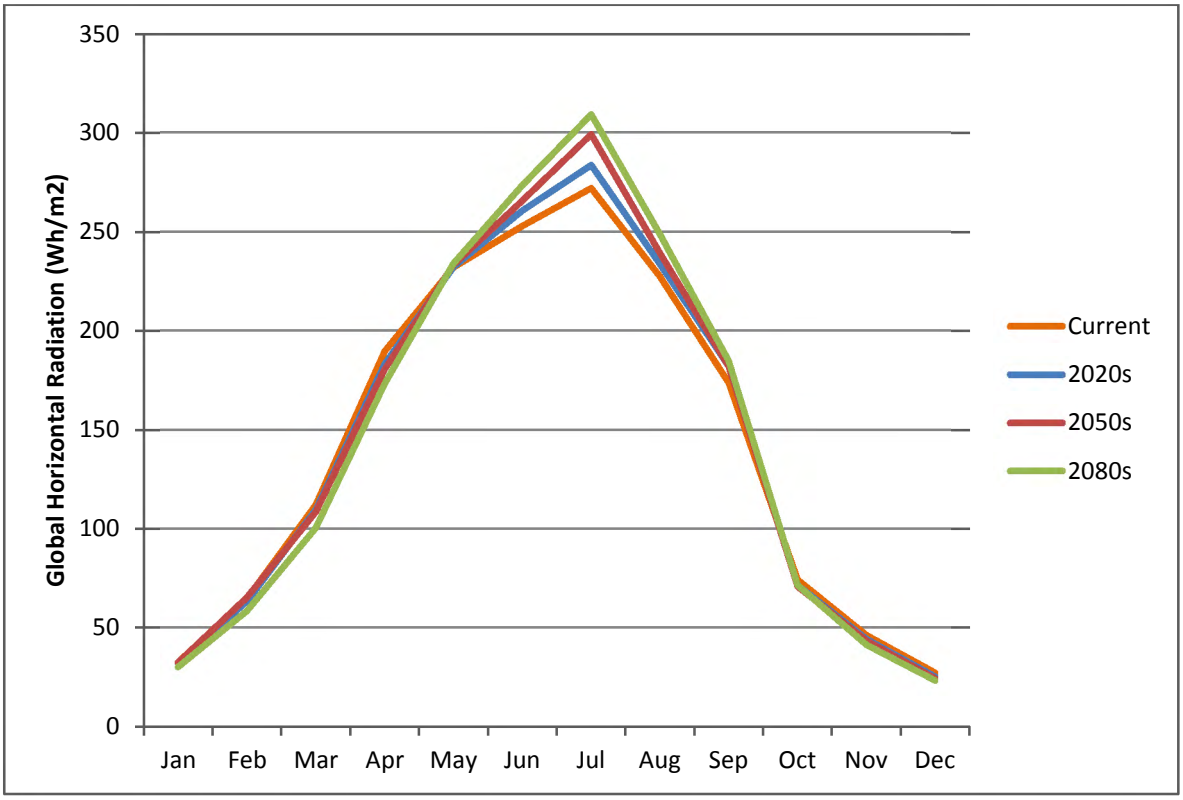

B12: Monthly average GHI comparison of years (Scenario B1).

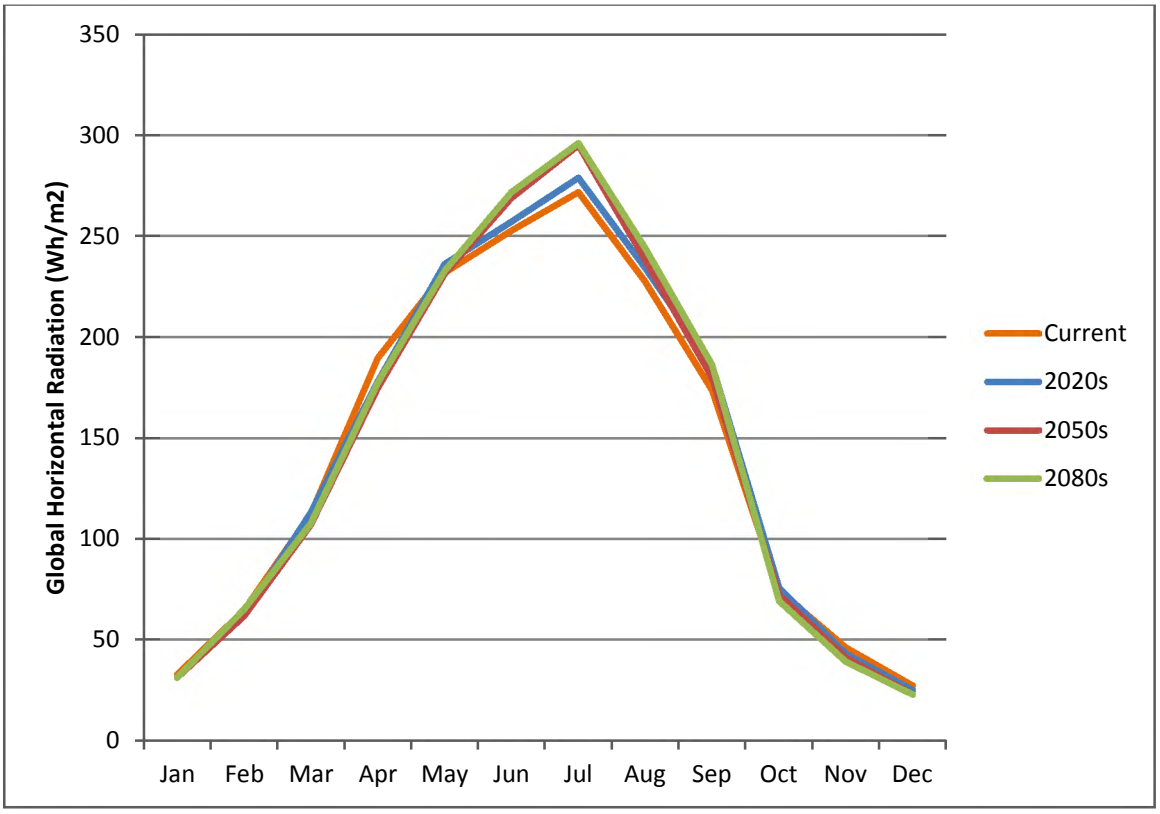

B13: Monthly average GHI comparison of years (Scenario b2).

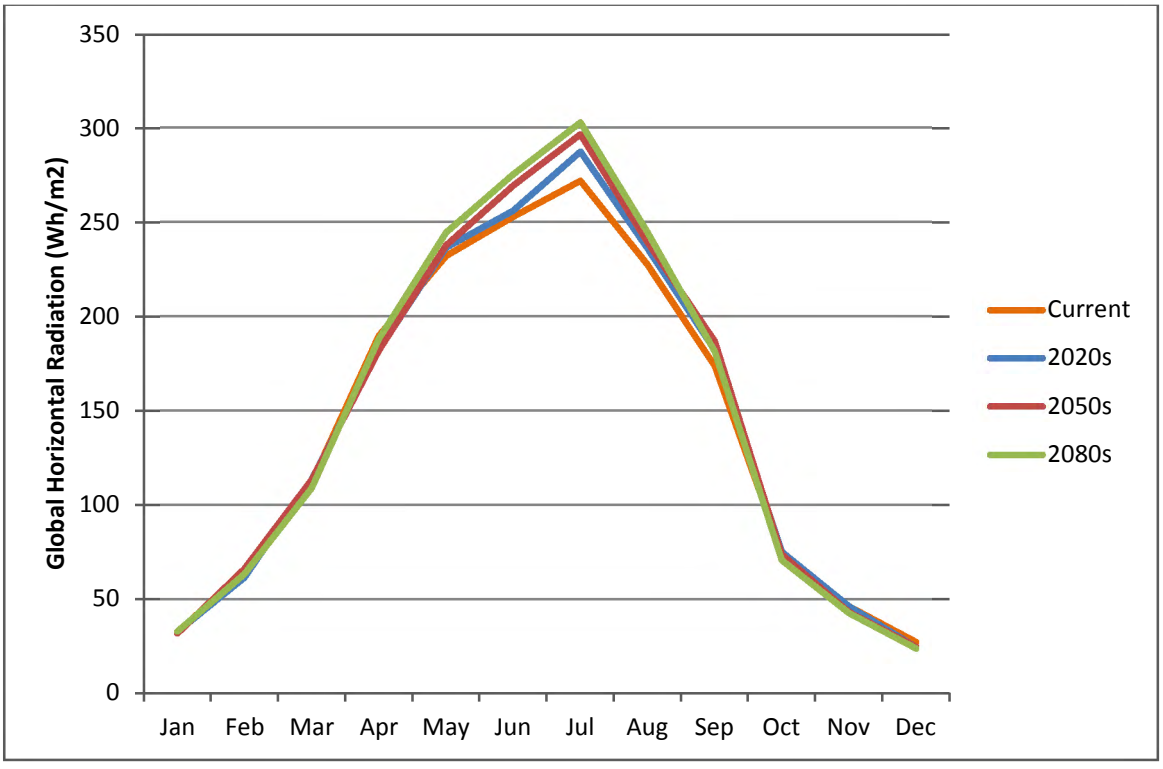

10 Appendix C

- Dynamically Downscaled Weather Data by Gaur et al., (2019)

C1: Past period Temperature box plot for 15 realizations.

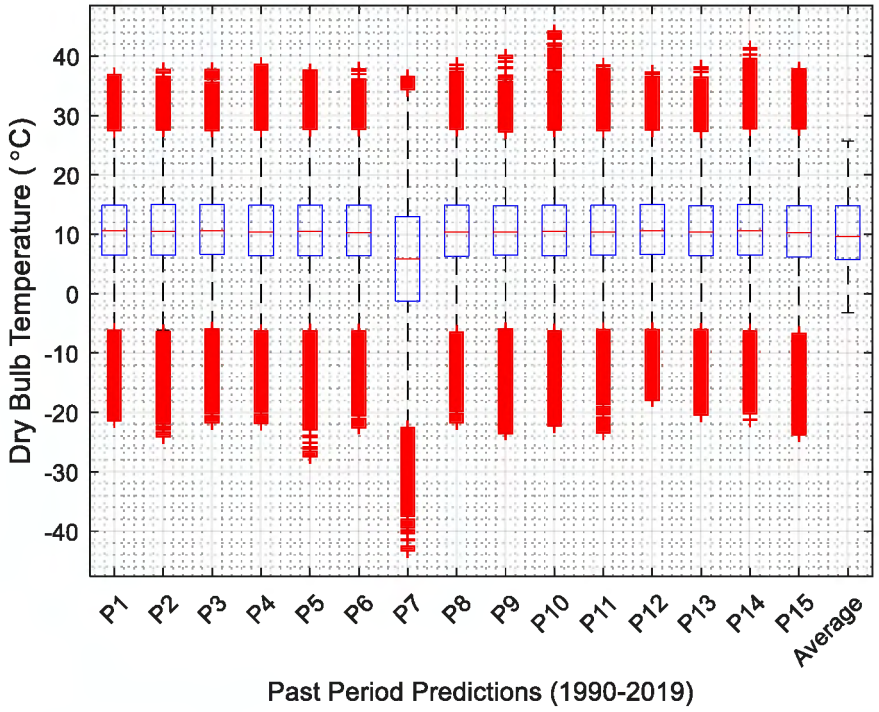

C2: Near future period Temperature box plot for 15 realizations.

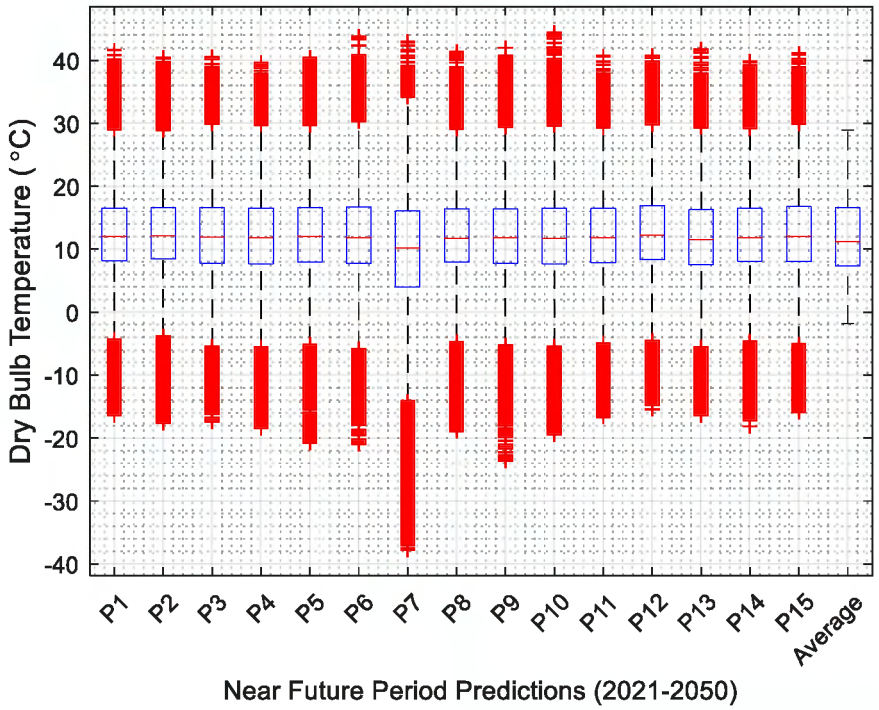

C3: Far future period Temperature box plot for 15 realizations.

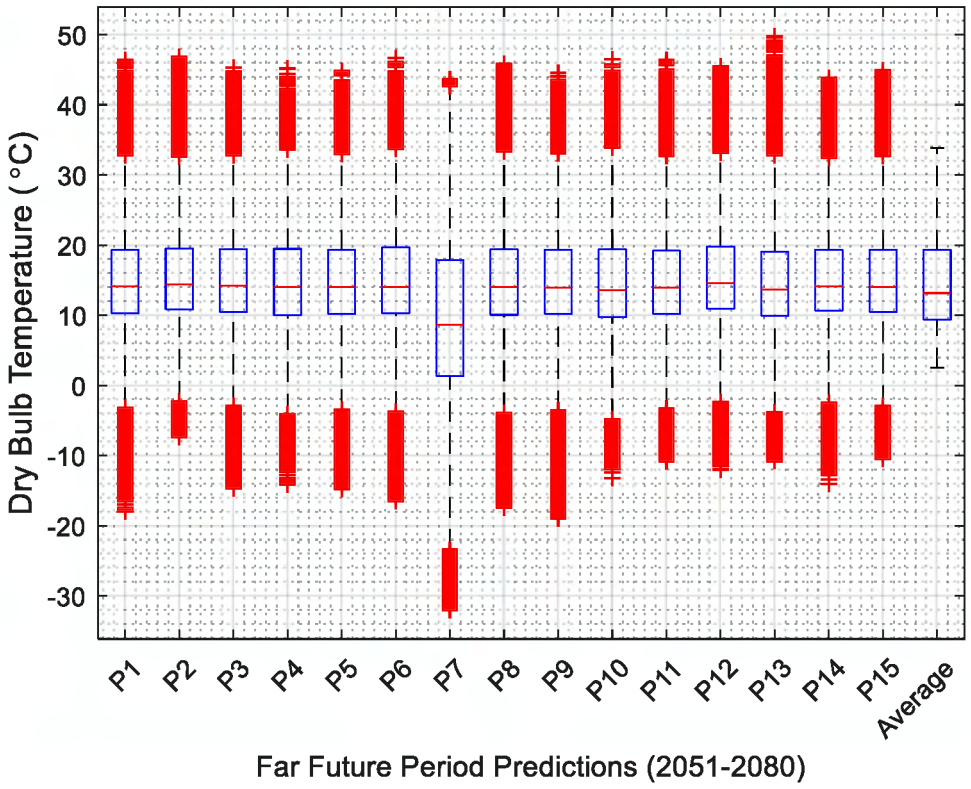

C4: Temperature Histogram with Normal PDF plot for Realization 1

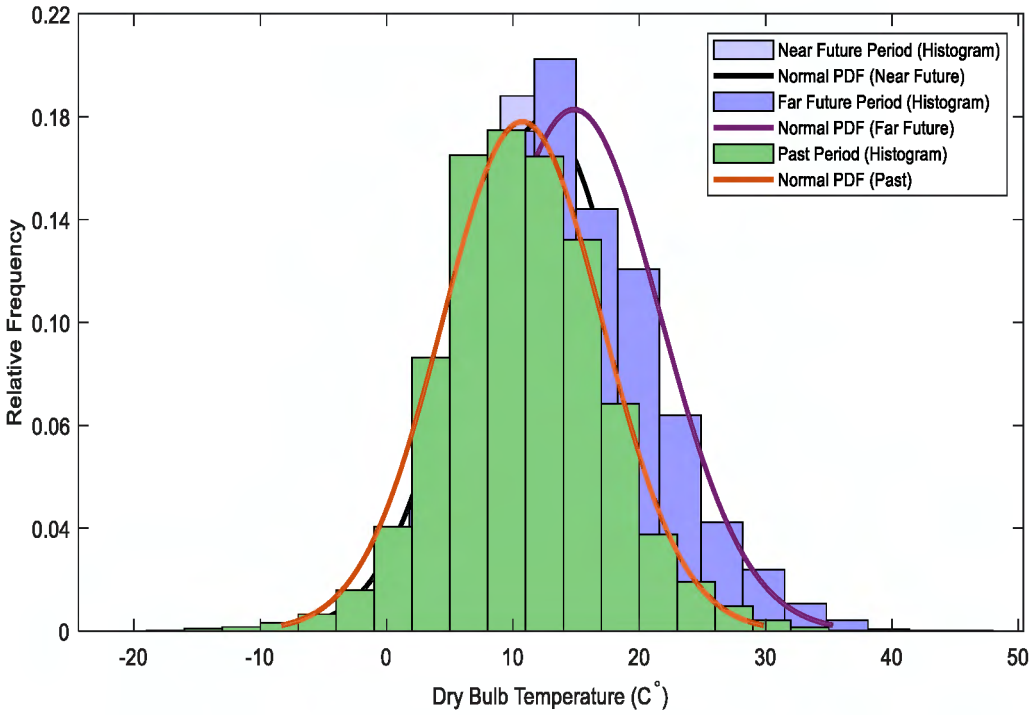

C5: Temperature box plot for every five years from 1990 to 2080 (Realization 1)

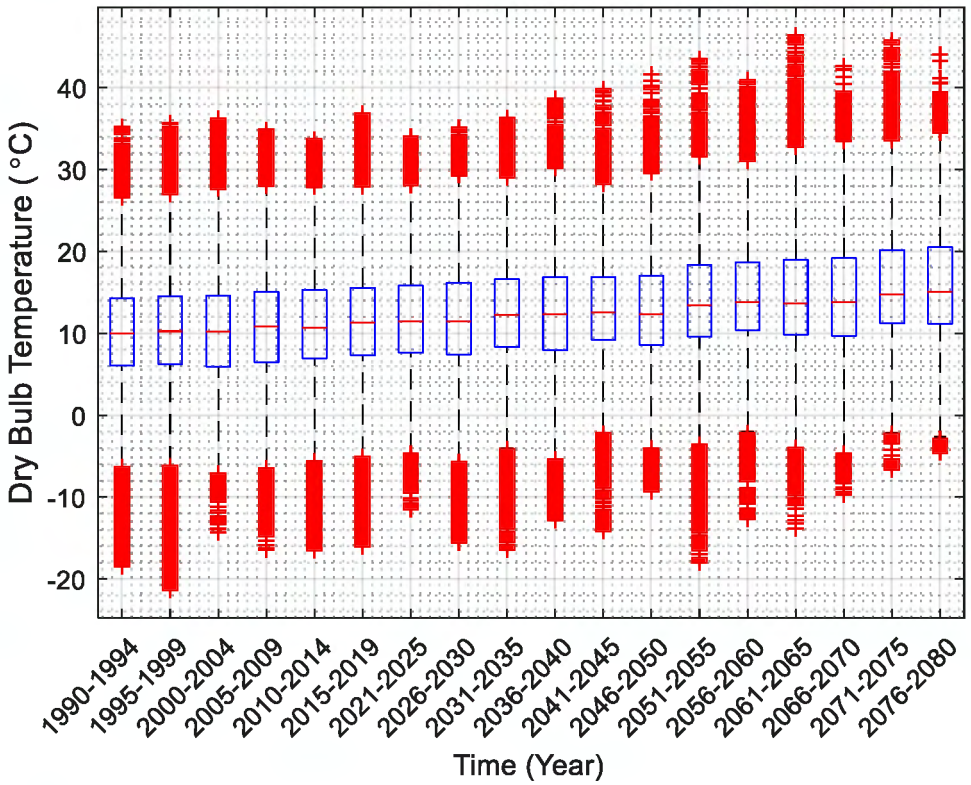

C6: Temperature Histogram with Normal PDF plot for Realization 2

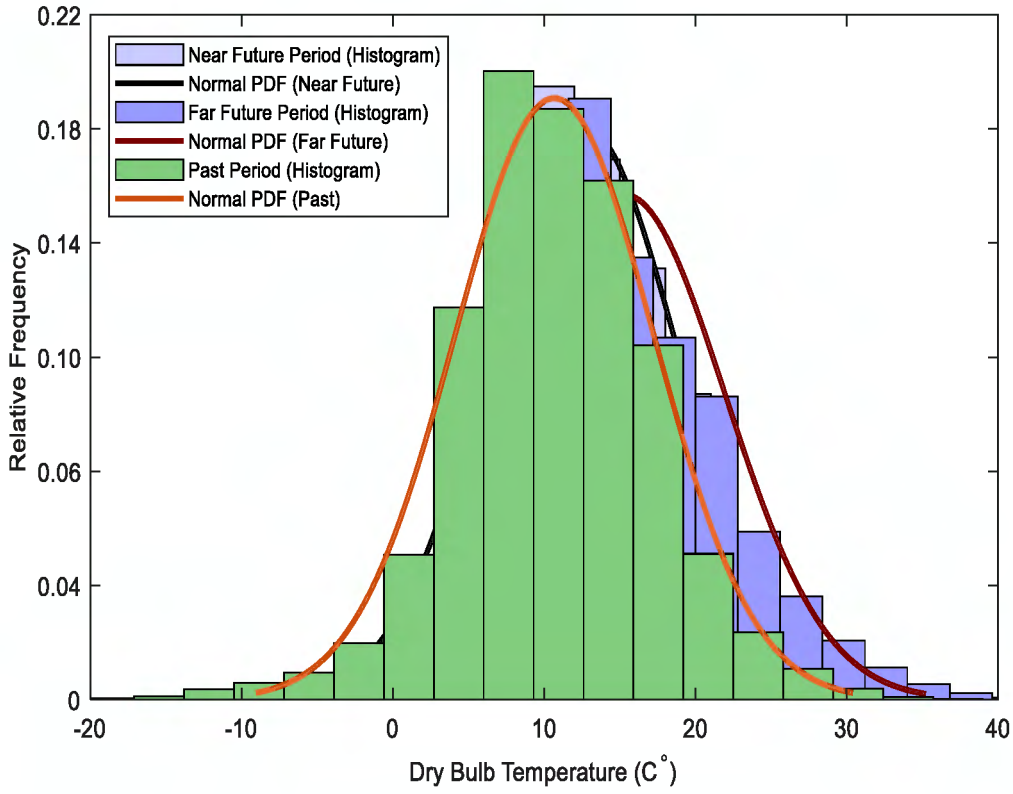

C7: Temperature box plot for every five years from 1990 to 2080 (Realization 2)

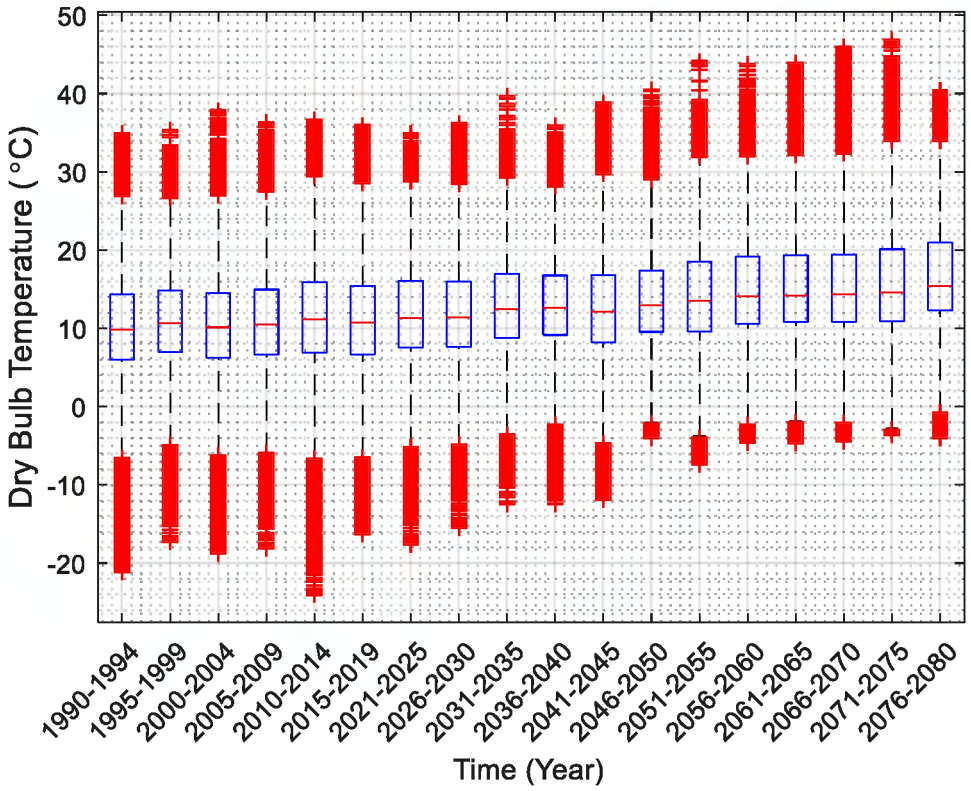

C8: Temperature Histogram with Normal PDF plot for Realization 3

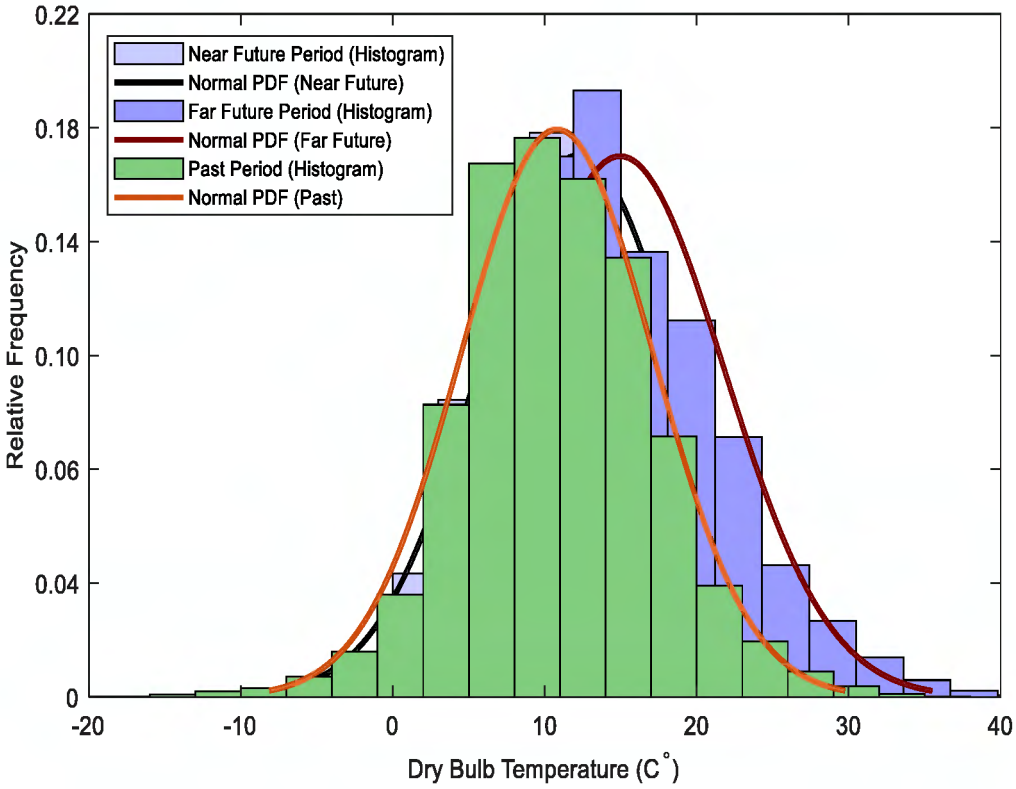

C9: Temperature box plot for every 5 years from 1990 to 2080 (Realization 3)

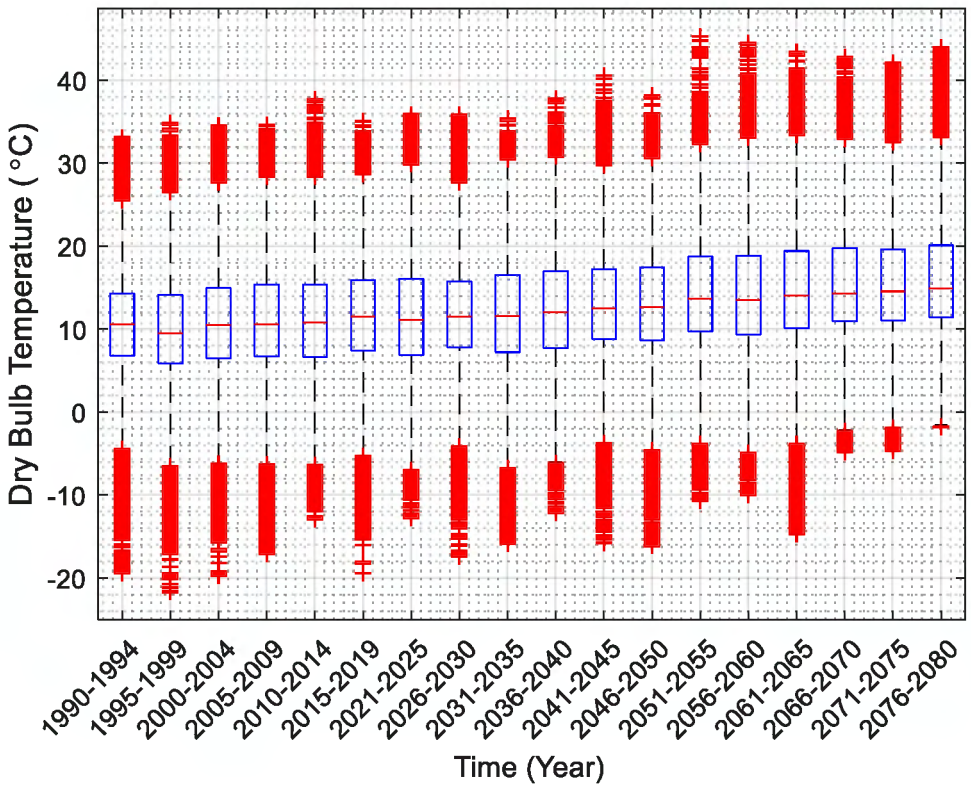

C10: Temperature Histogram with Normal PDF plot for Realization 4

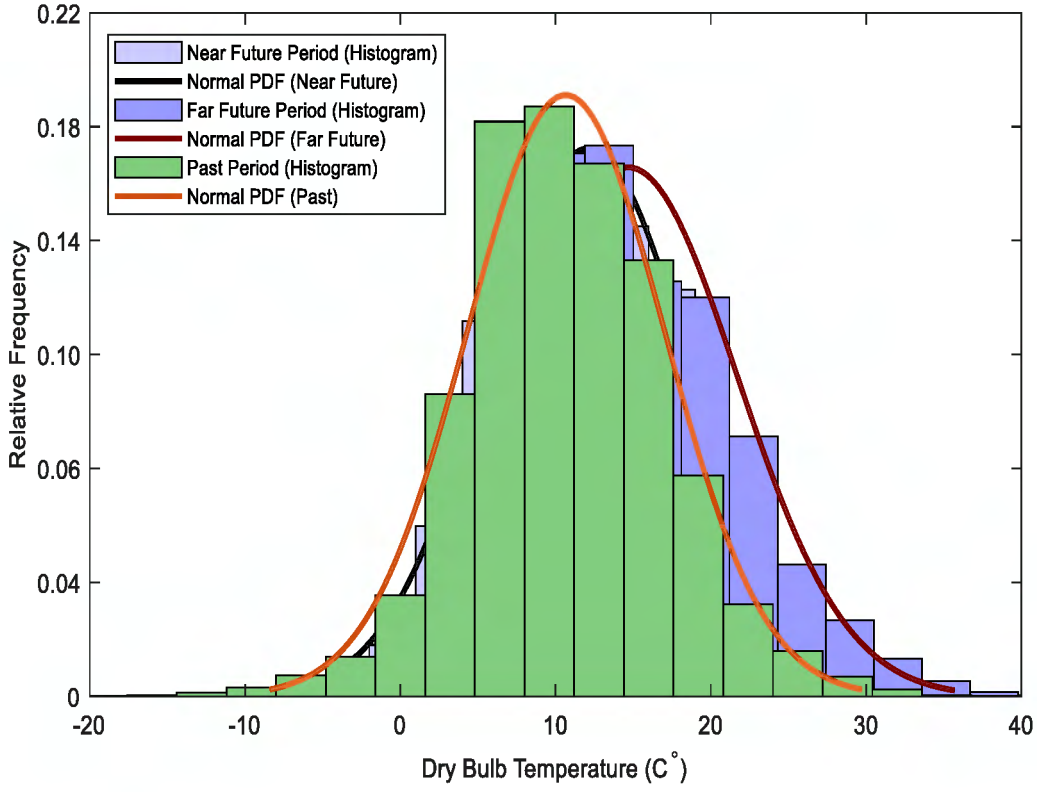

C11: Temperature box plot for every five years from 1990 to 2080 (Realization 4)

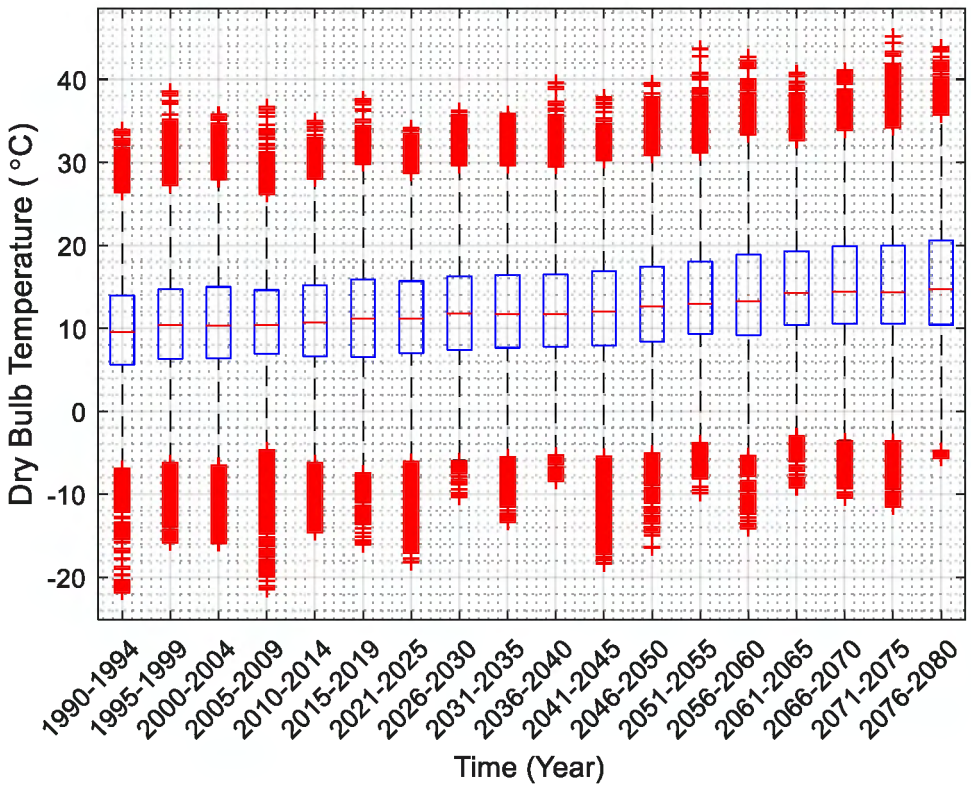

C12: Temperature Histogram with Normal PDF plot for Realization 5

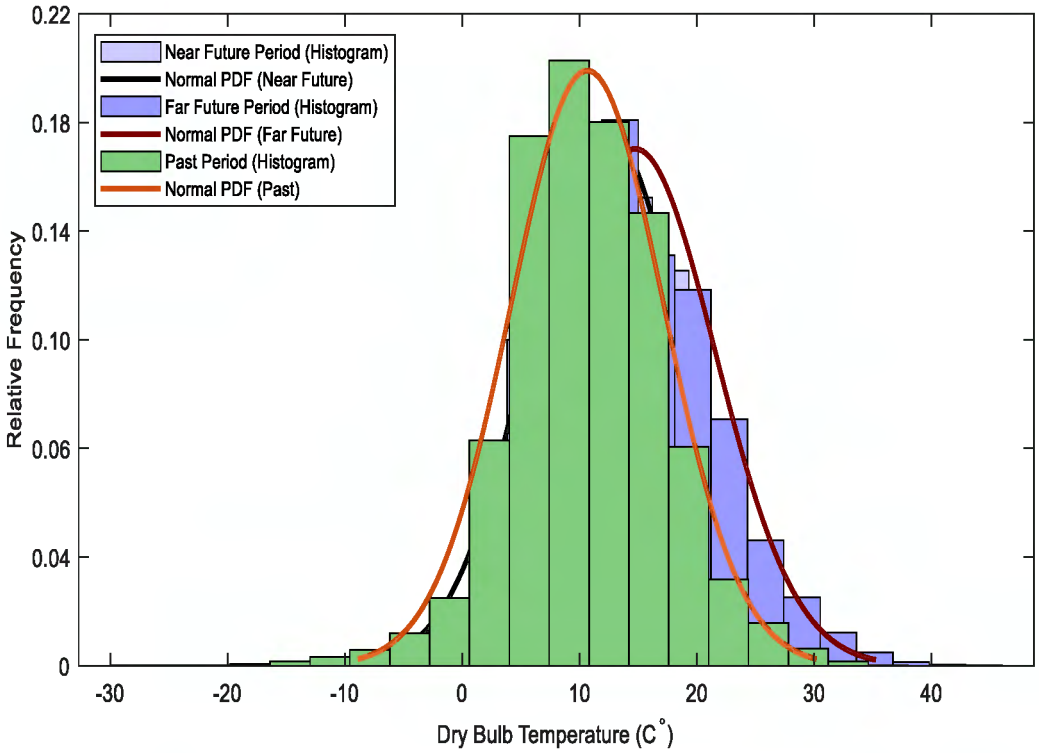

C13: Temperature box plot for every five years from 1990 to 2080 (Realization 5)

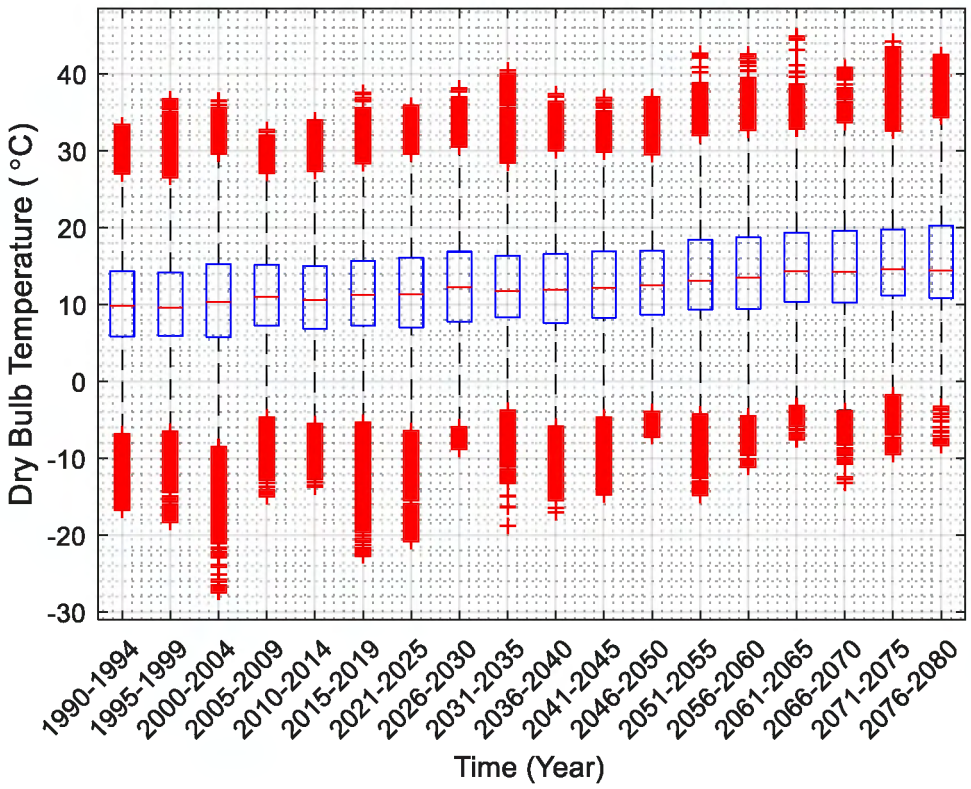

C14: Temperature Histogram with Normal PDF plot for Realization 6

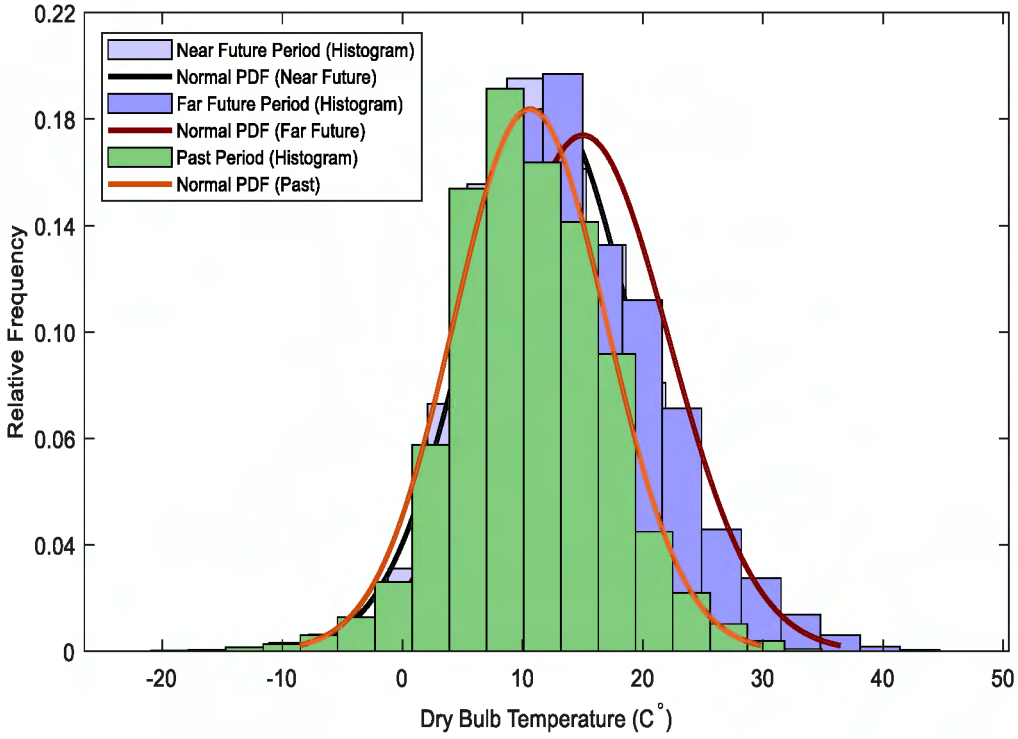

C15: Temperature box plot for every five years from 1990 to 2080 (Realization 6)

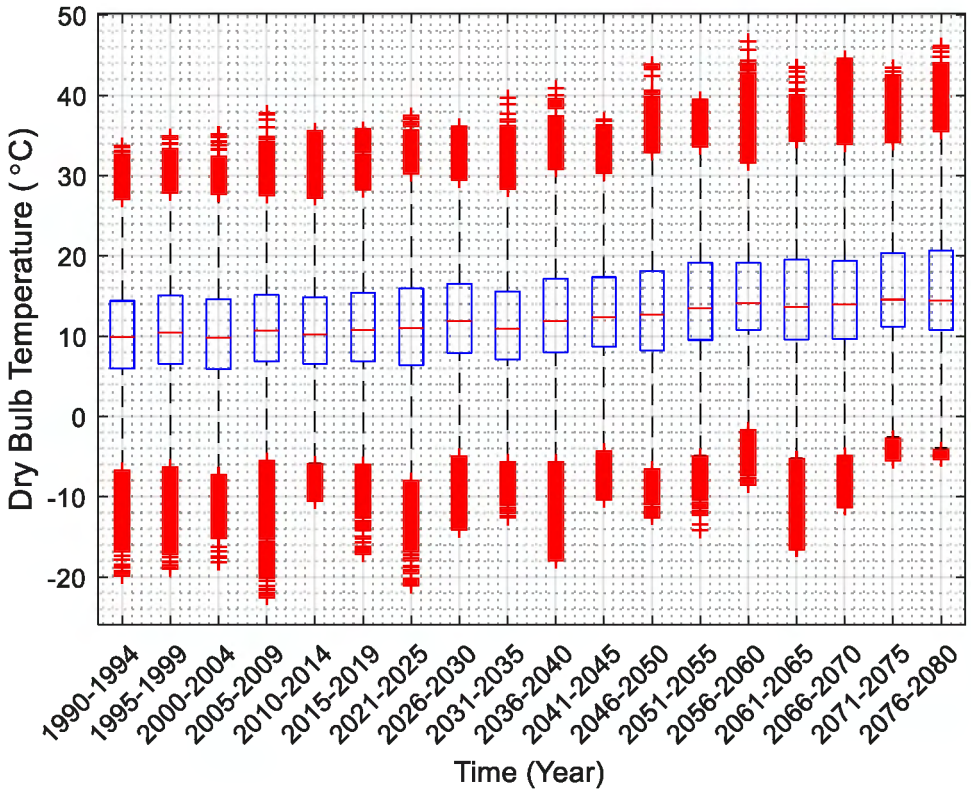

C16: Temperature Histogram with Normal PDF Temperature plot for Realization 7

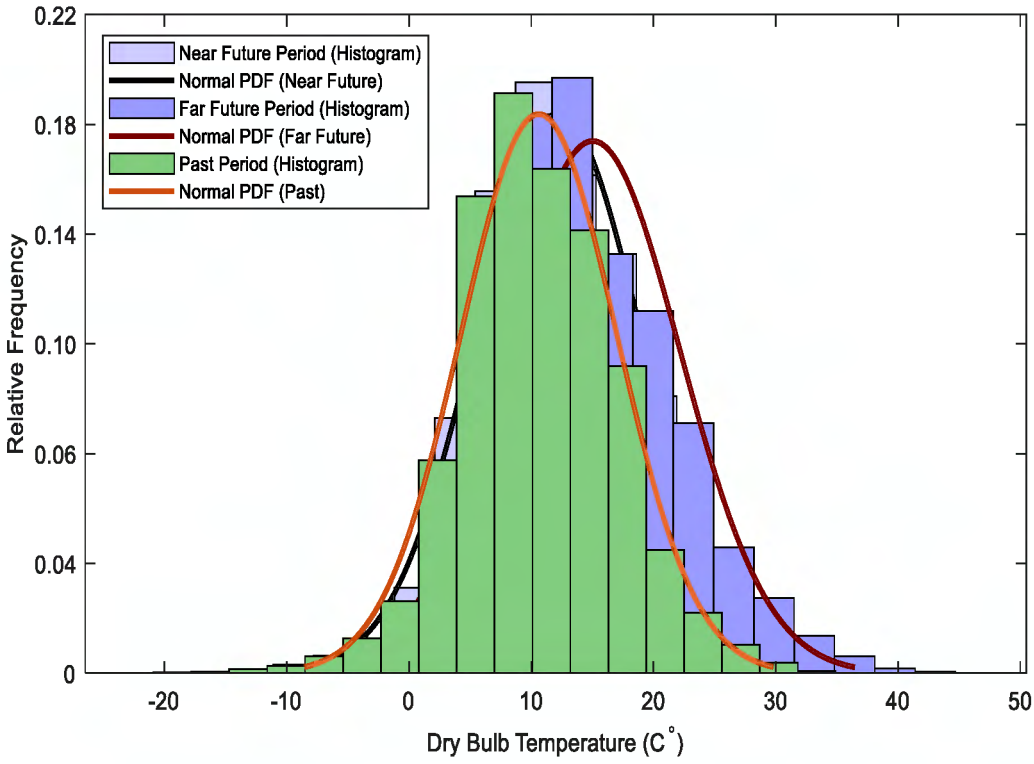

C17: Temperature box plot for every five years from 1990 to 2080 (Realization 7)

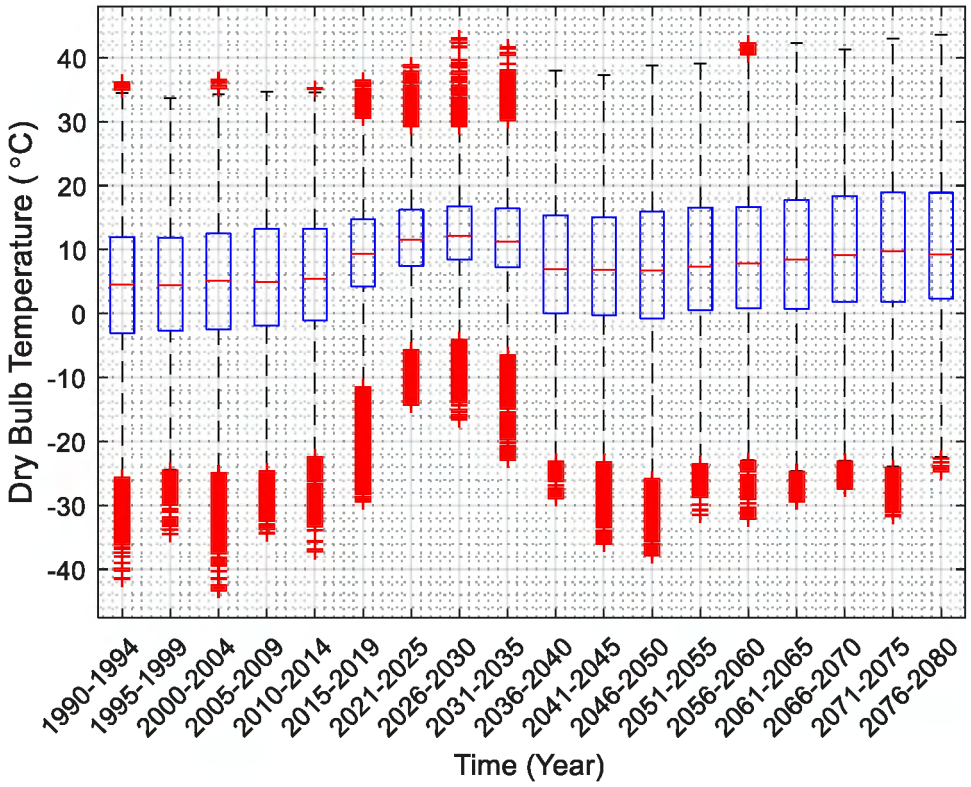

C18: Temperature Histogram with Normal PDF plot for Realization 8

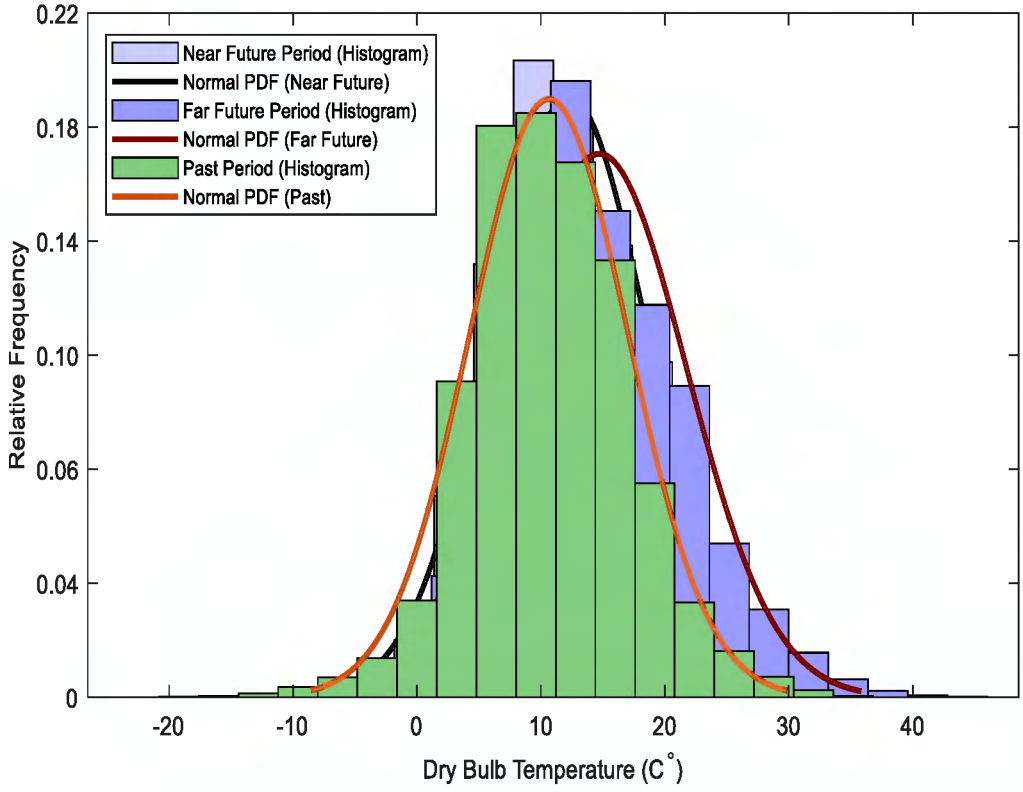

C19: Temperature box plot for every five years from 1990 to 2080 (Realization 8)

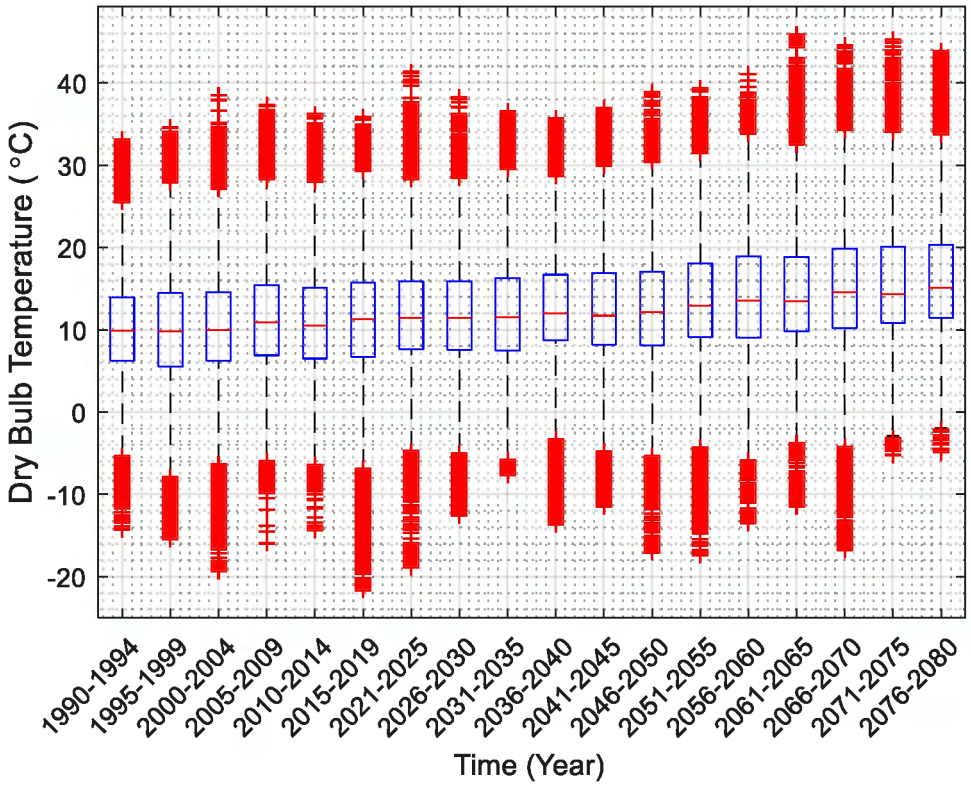

C20: Temperature Histogram with Normal PDF plot for Realization 9

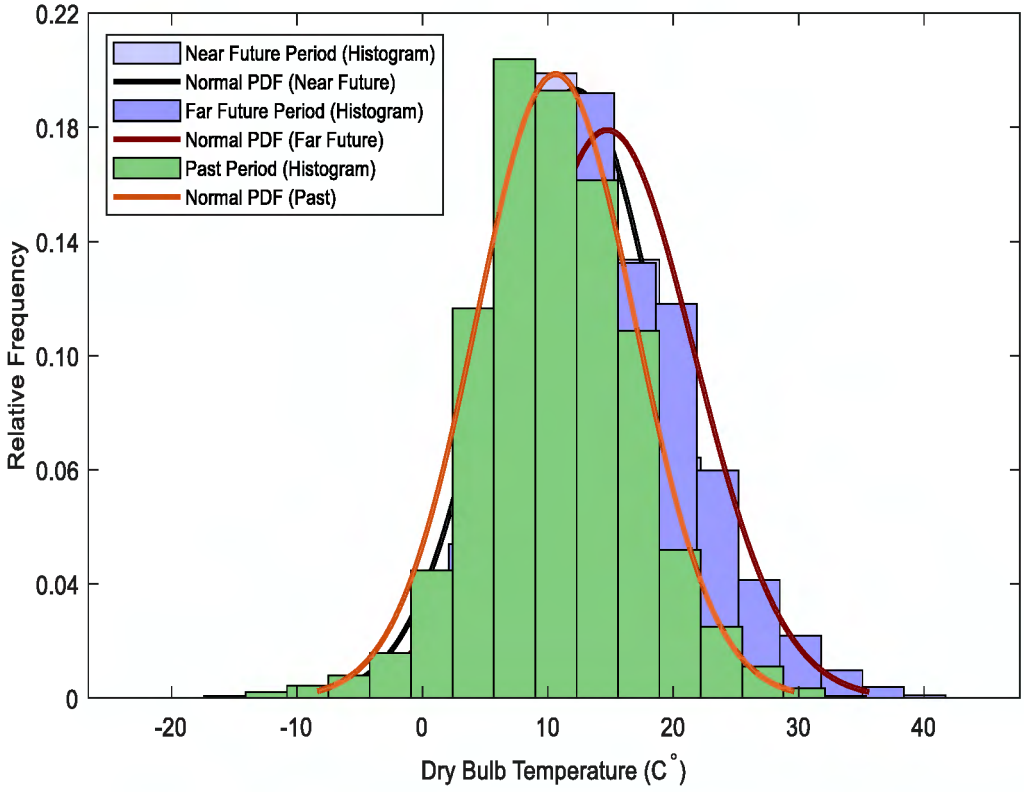

C21: Temperature box plot for every five years from 1990 to 2080 (Realization 9)

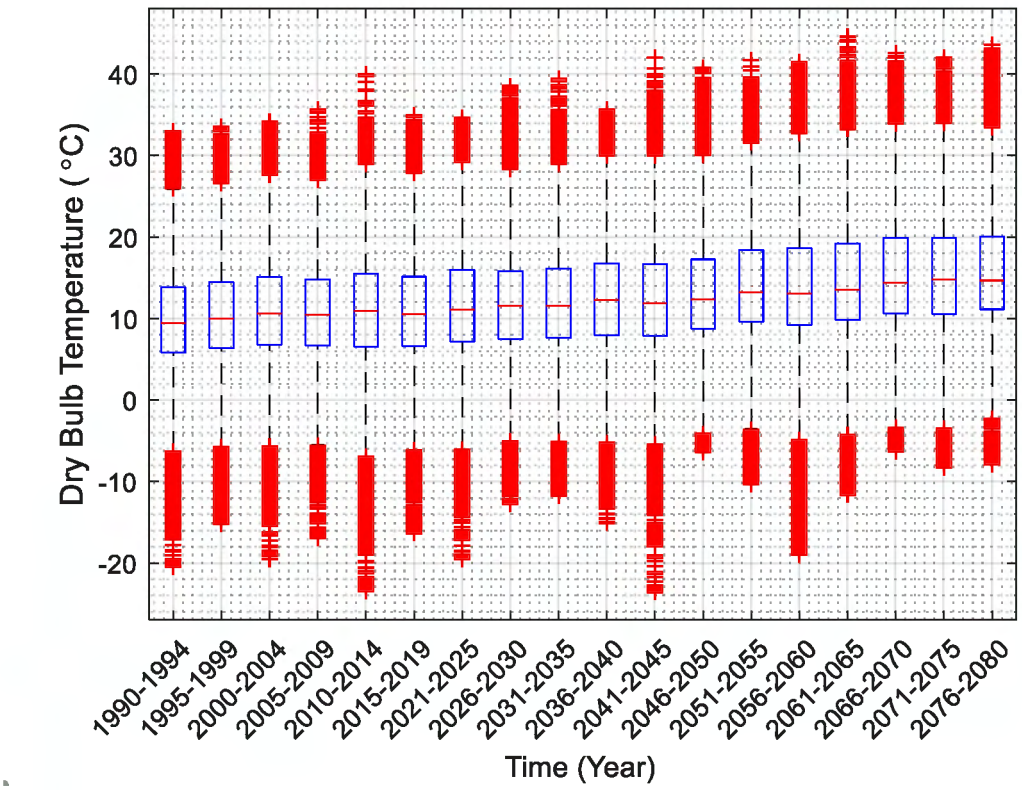

C22: Temperature Histogram with Normal PDF plot for Realization 10

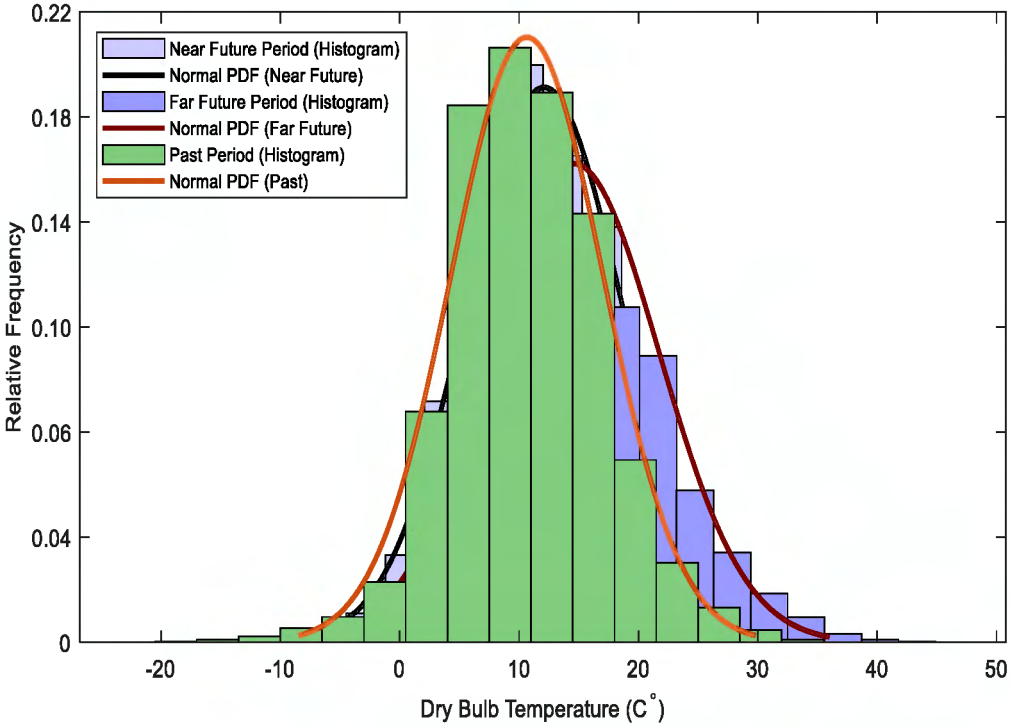

C23: Temperature box plot for every five years from 1990 to 2080 (Realization 10)

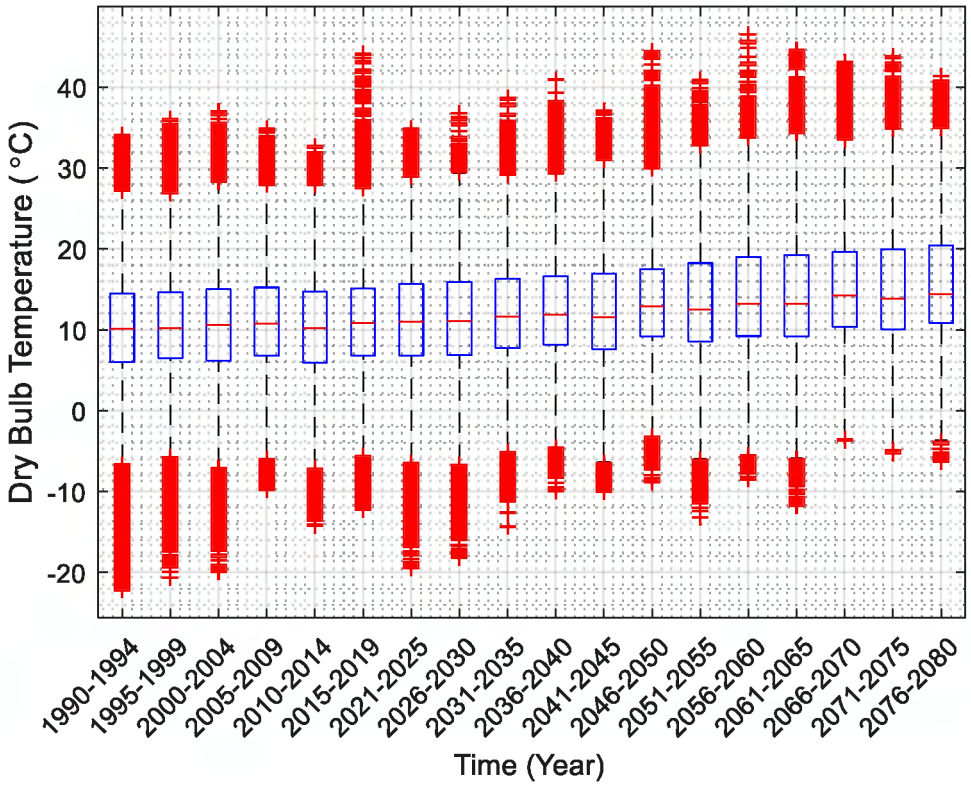

C24: Temperature Histogram with Normal PDF plot for Realization 11

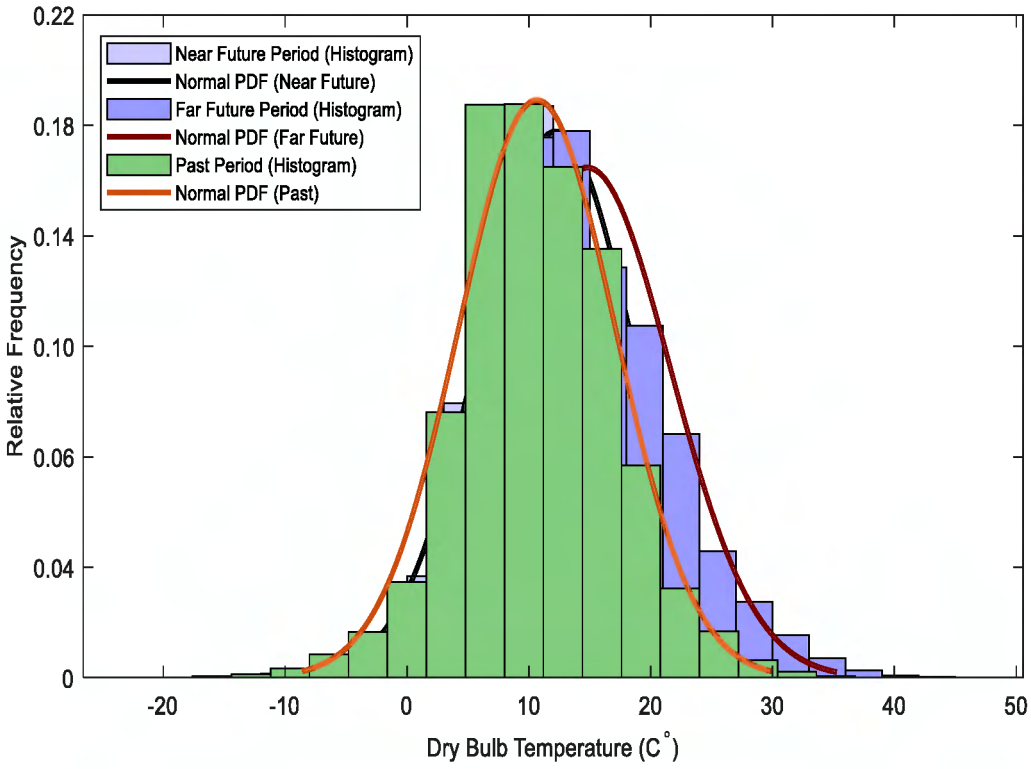

C25: Temperature box plot for every five years from 1990 to 2080 (Realization 11)

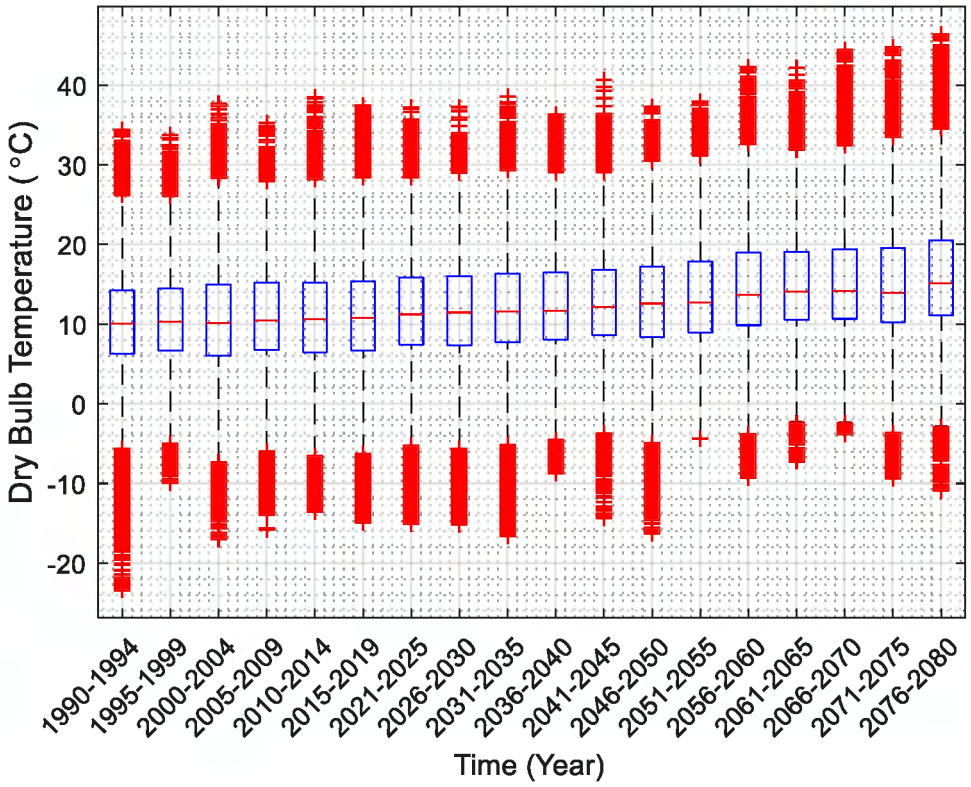

C26: Temperature Histogram with Normal PDF plot for Realization 12

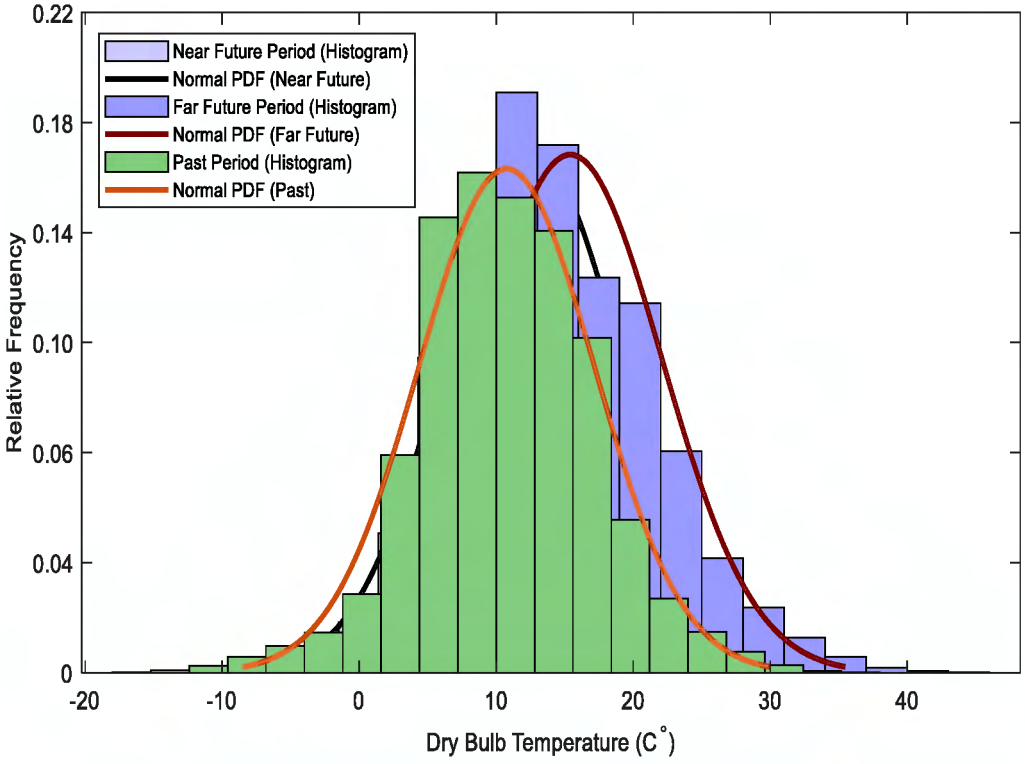

C27: Temperature box plot for every five years from 1990 to 2080 (Realization 12)

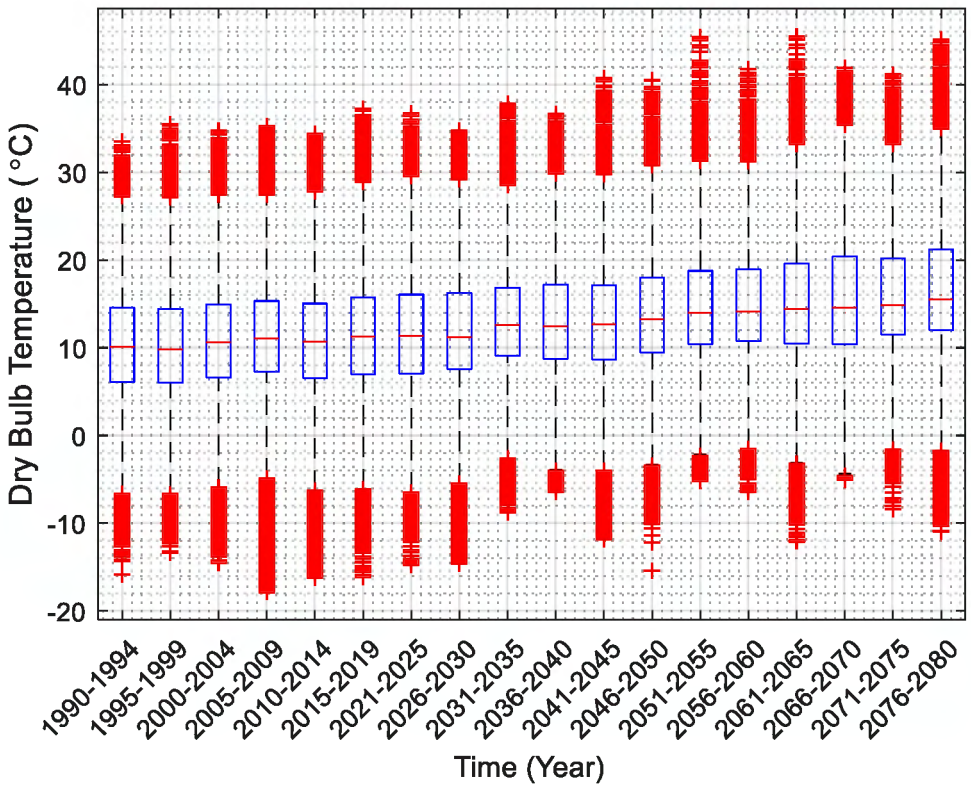

C28: Temperature Histogram with Normal PDF plot for Realization 13

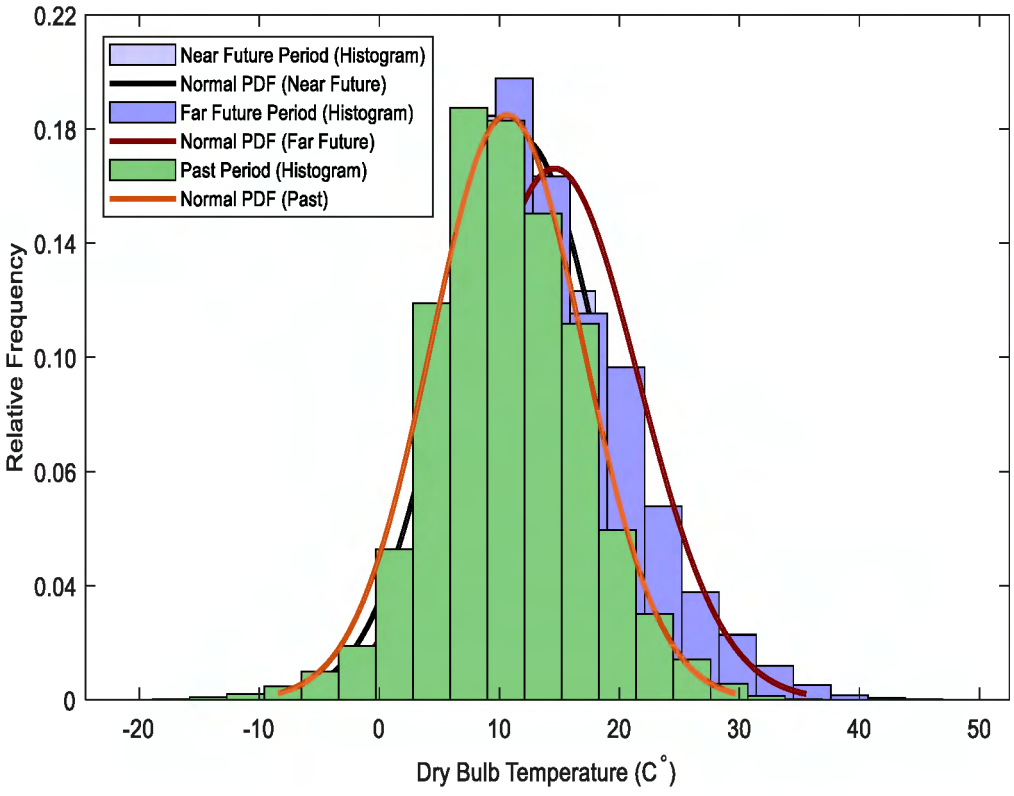

C29: Temperature box plot for every five years from 1990 to 2080 (Realization 13)

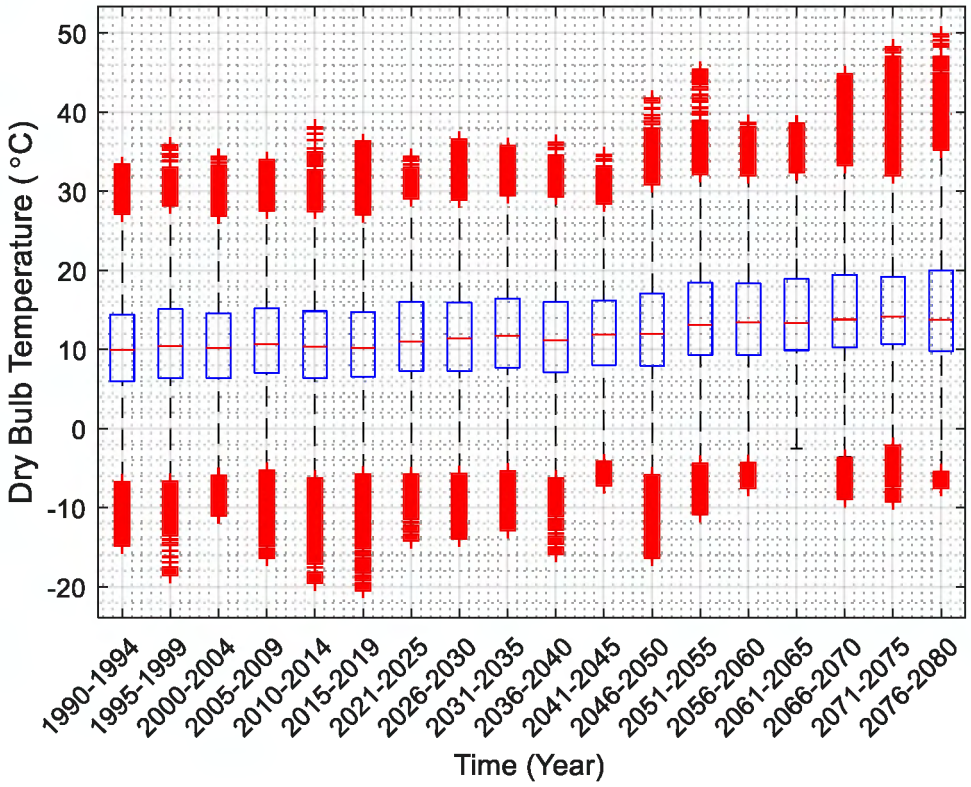

C30: Temperature Histogram with Normal PDF plot for Realization 14

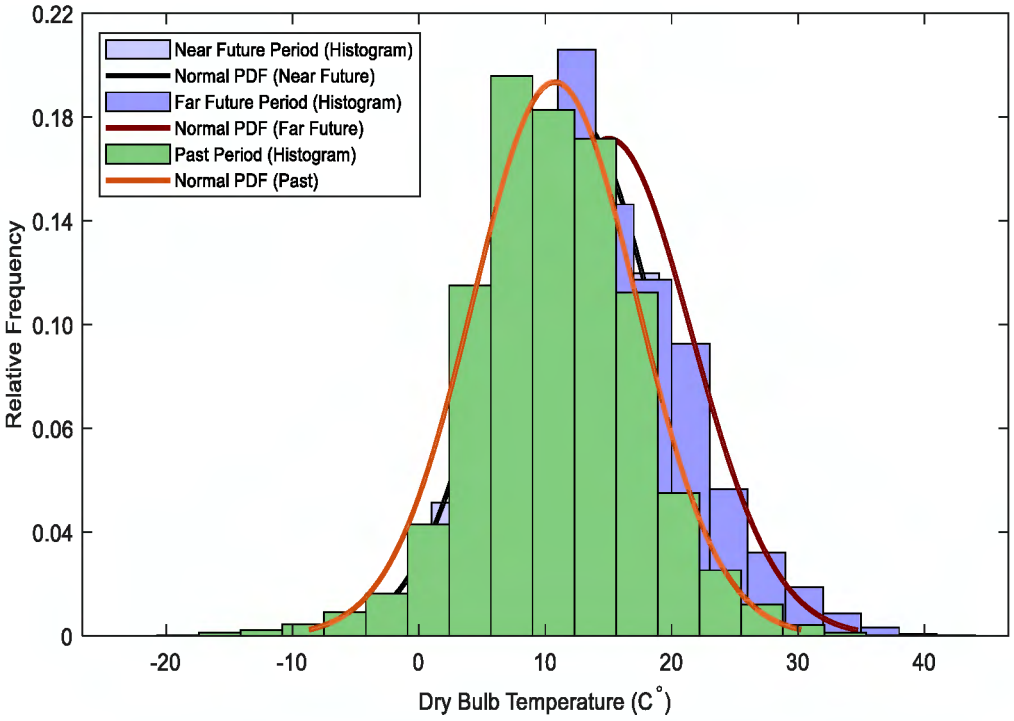

C31: Temperature box plot for every five years from 1990 to 2080 (Realization 14)

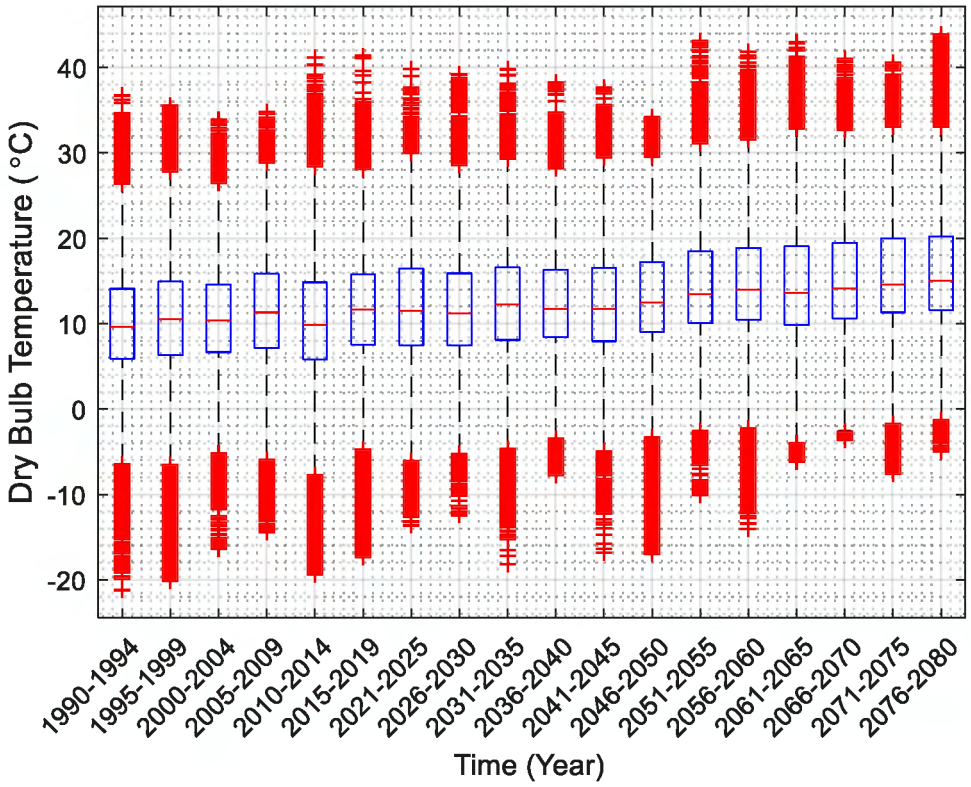

C32: Temperature Histogram with Normal PDF plot for Realization 15

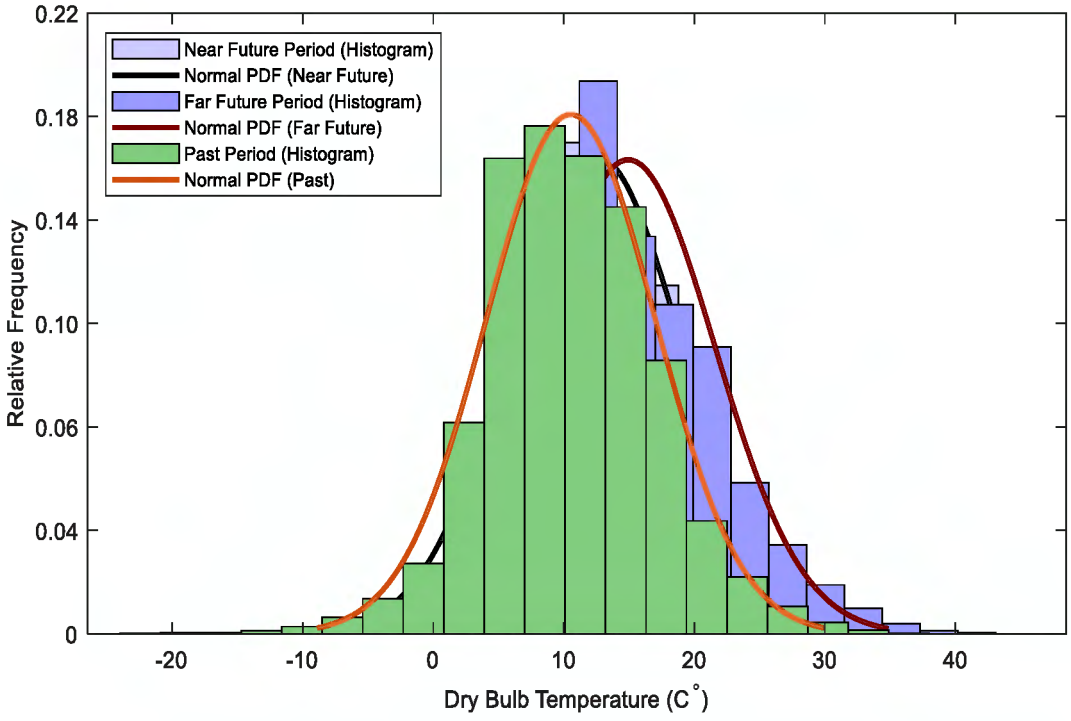

C33: Temperature box plot for every five years from 1990 to 2080 (Realization 15)

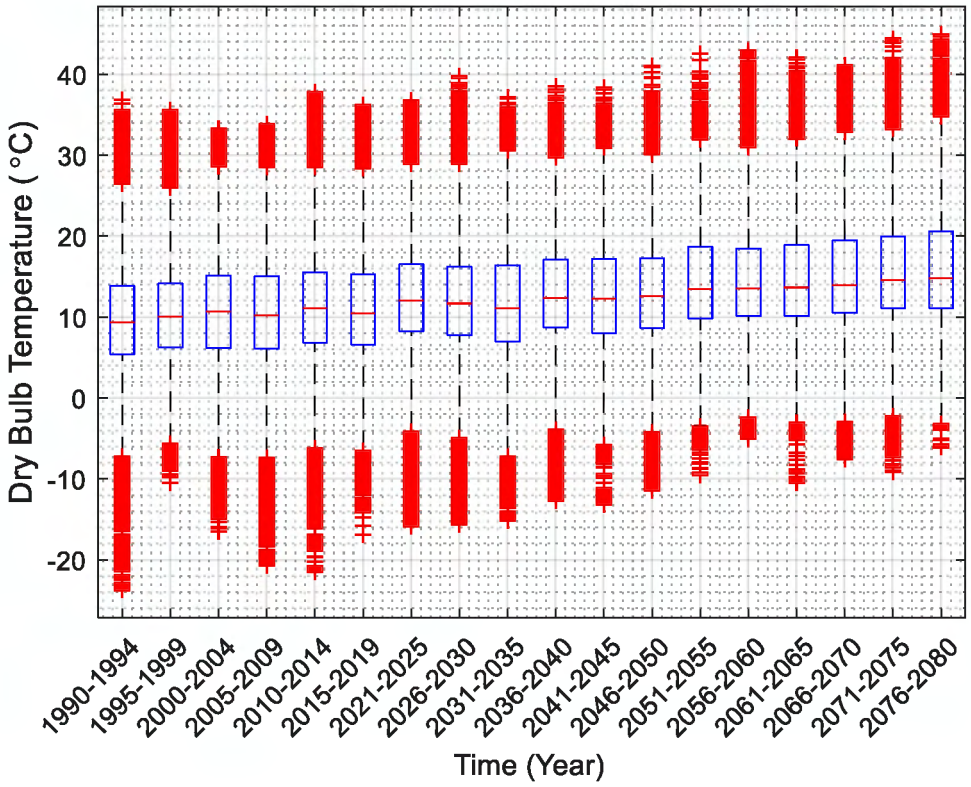

C34: Temperature Histogram with Normal PDF plot (Average)

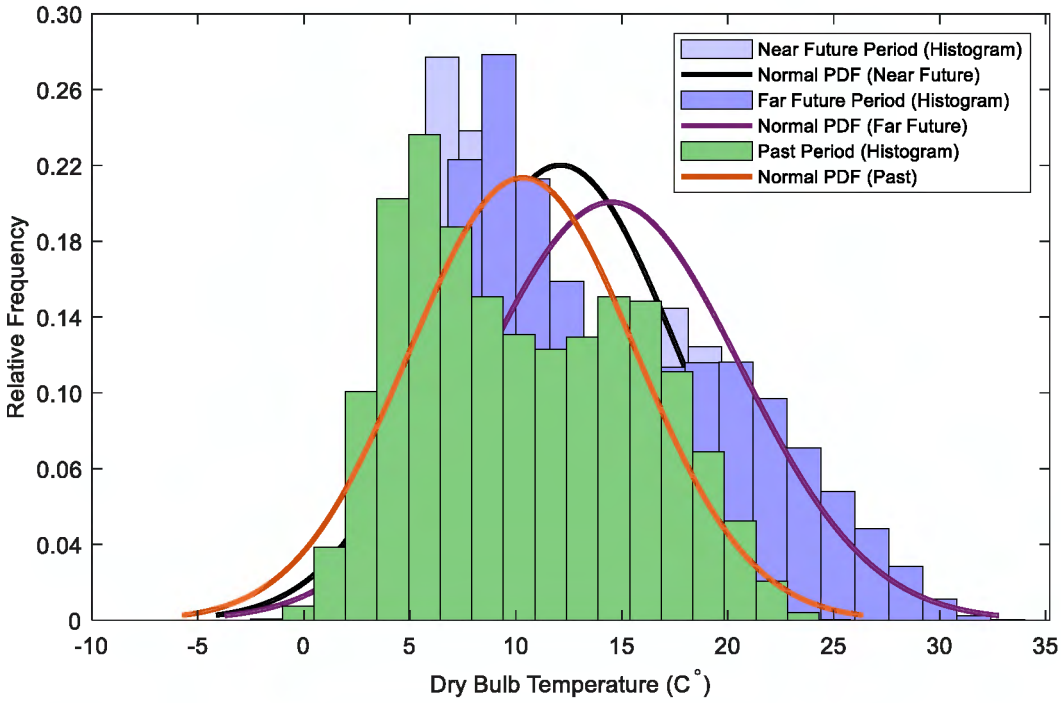

C35: Temperature box plot for every five years from 1990 to 2080 (Average)

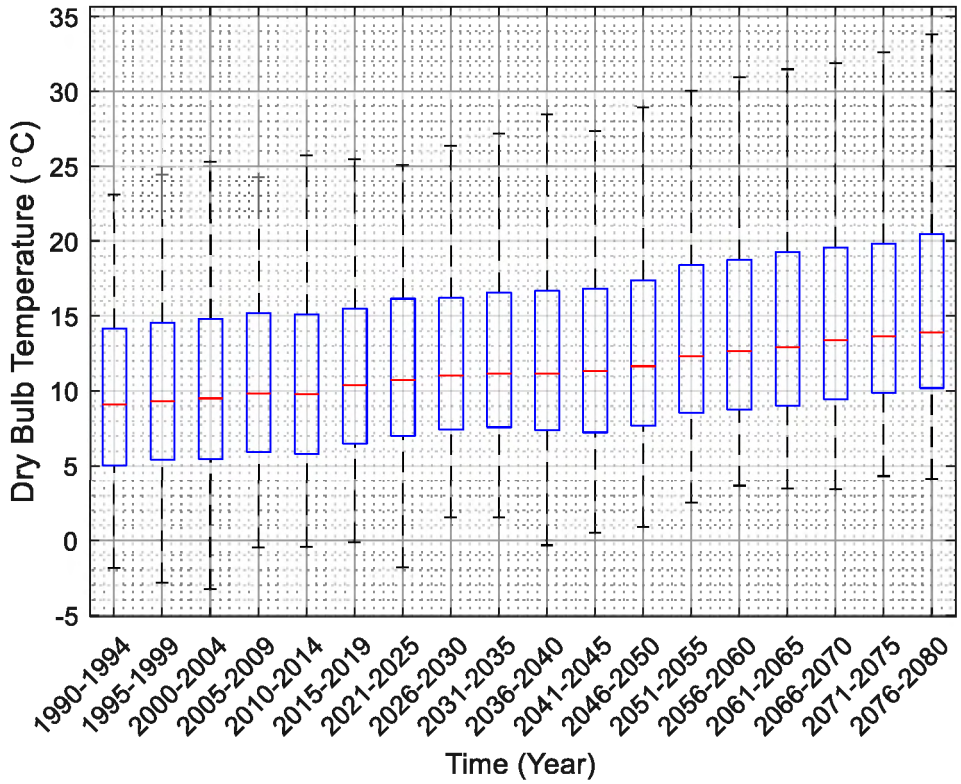

C36: Temperature box plot yearly 2021 to 2050 (Realization 1)

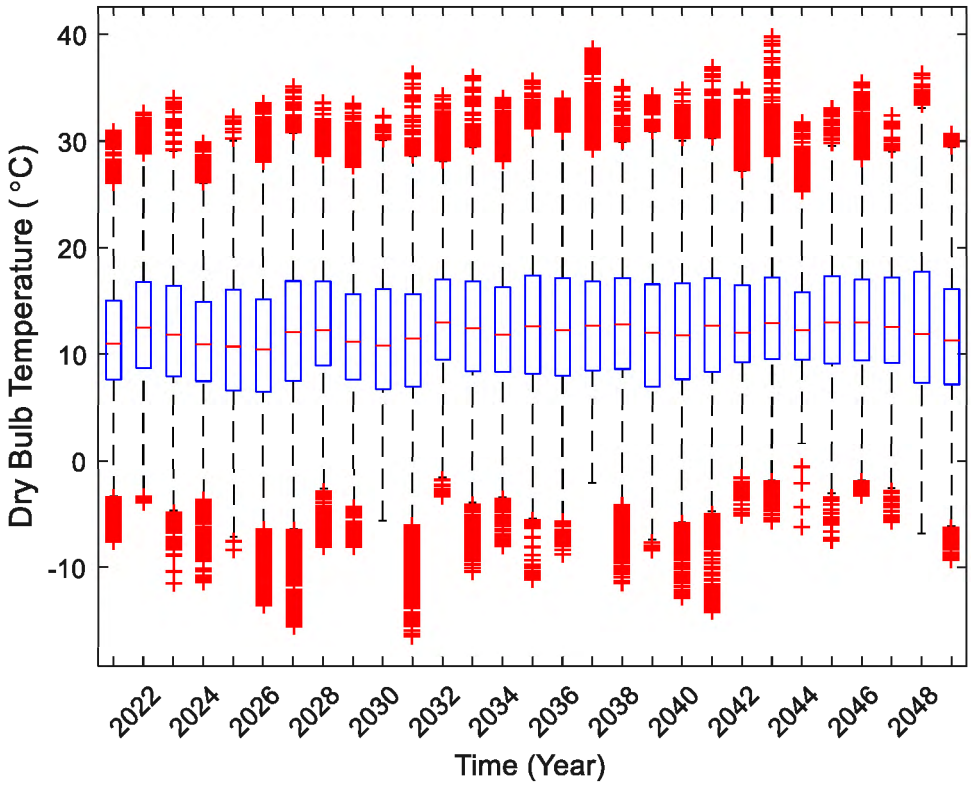

C37: Temperature box plot yearly 2021 to 2050 (Realization 2)

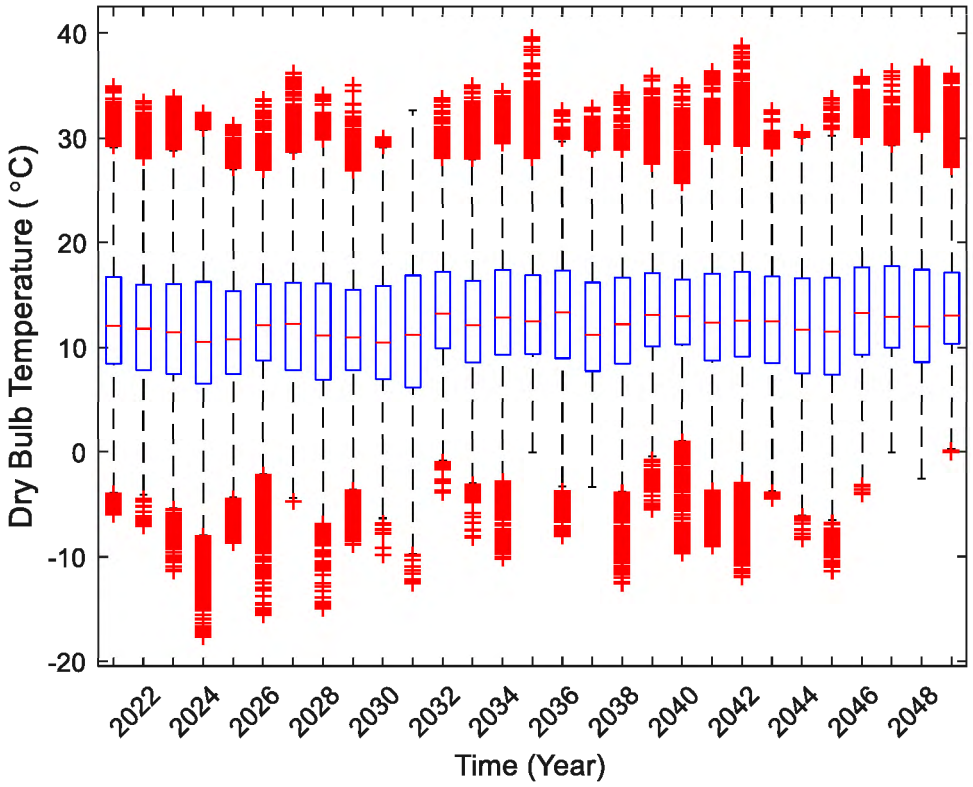

C38: Temperature box plot yearly 2021 to 2050 (Realization 3)

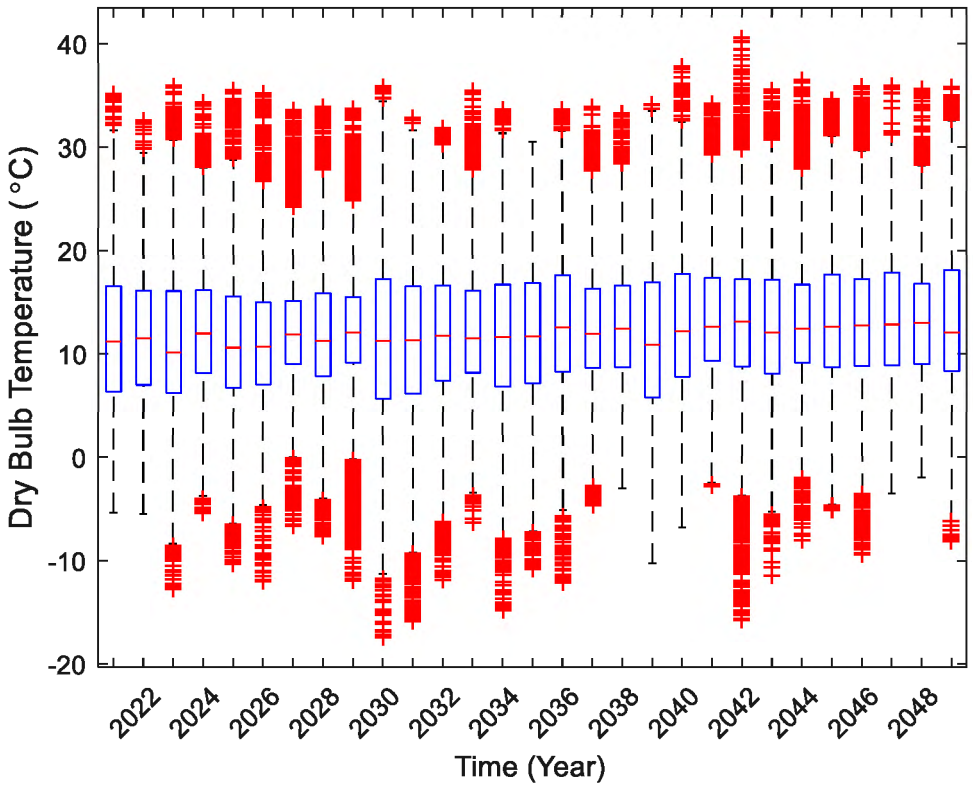

C39: Temperature box plot yearly 2021 to 2050 (Realization 4)

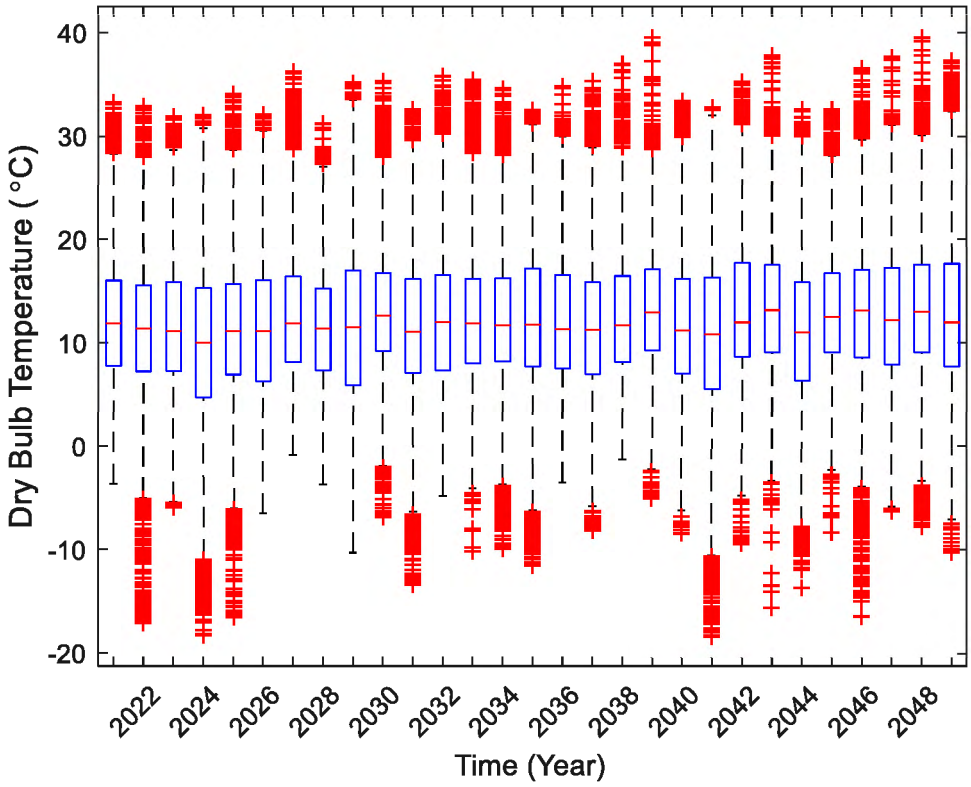

C40: Temperature box plot yearly 2021 to 2050 (Realization 5)

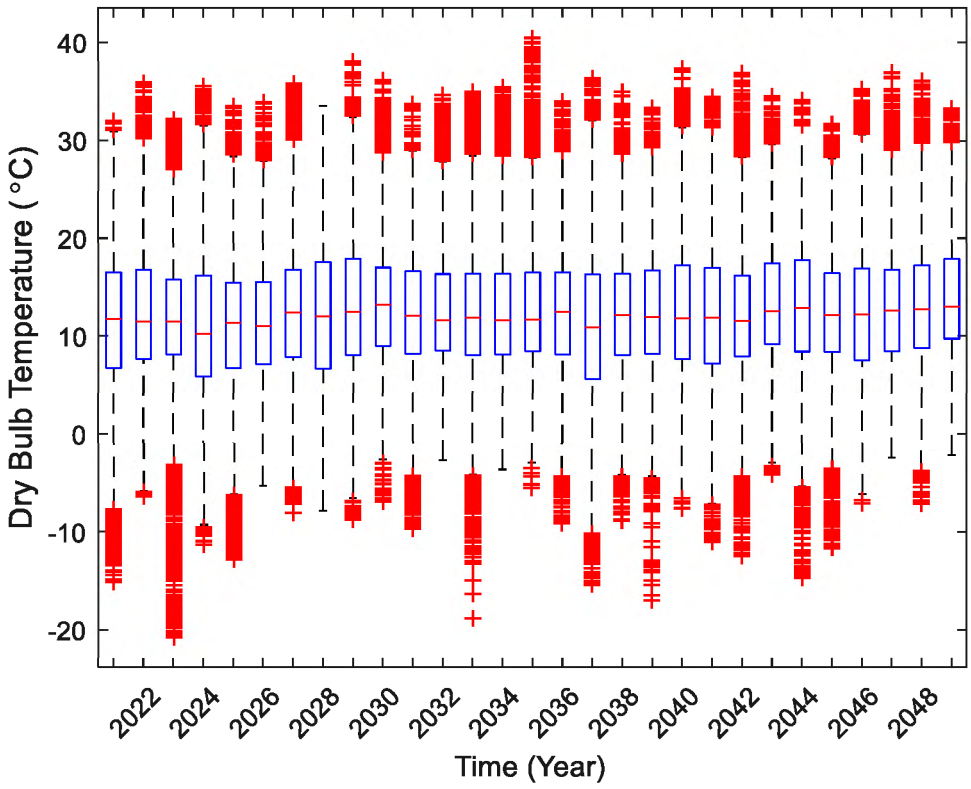

C41: Temperature box plot yearly 2021 to 2050 (Realization 6)

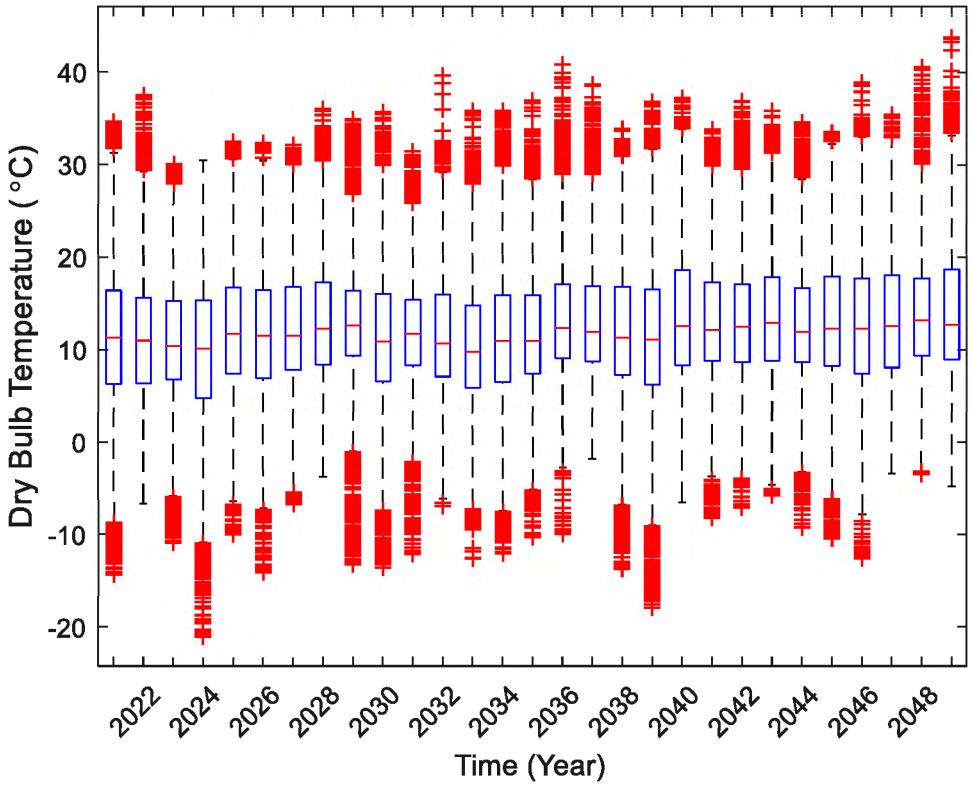

C42: Temperature box plot yearly 2021 to 2050 (Realization 7)

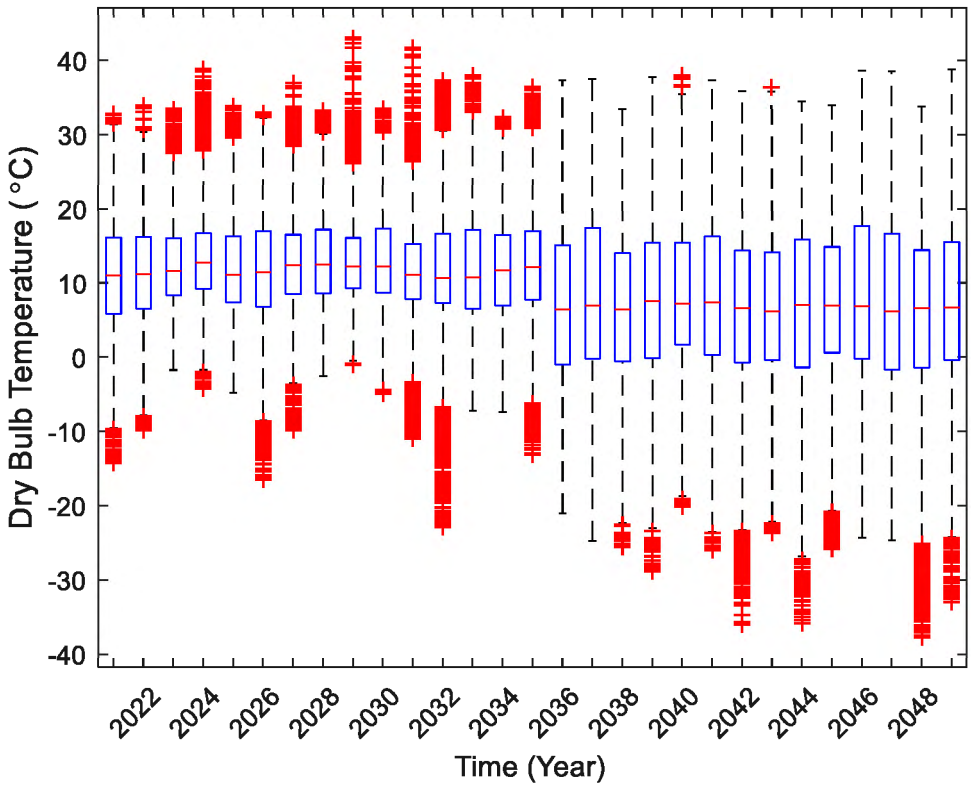

C43: Temperature box plot yearly 2021 to 2050 (Realization 8)

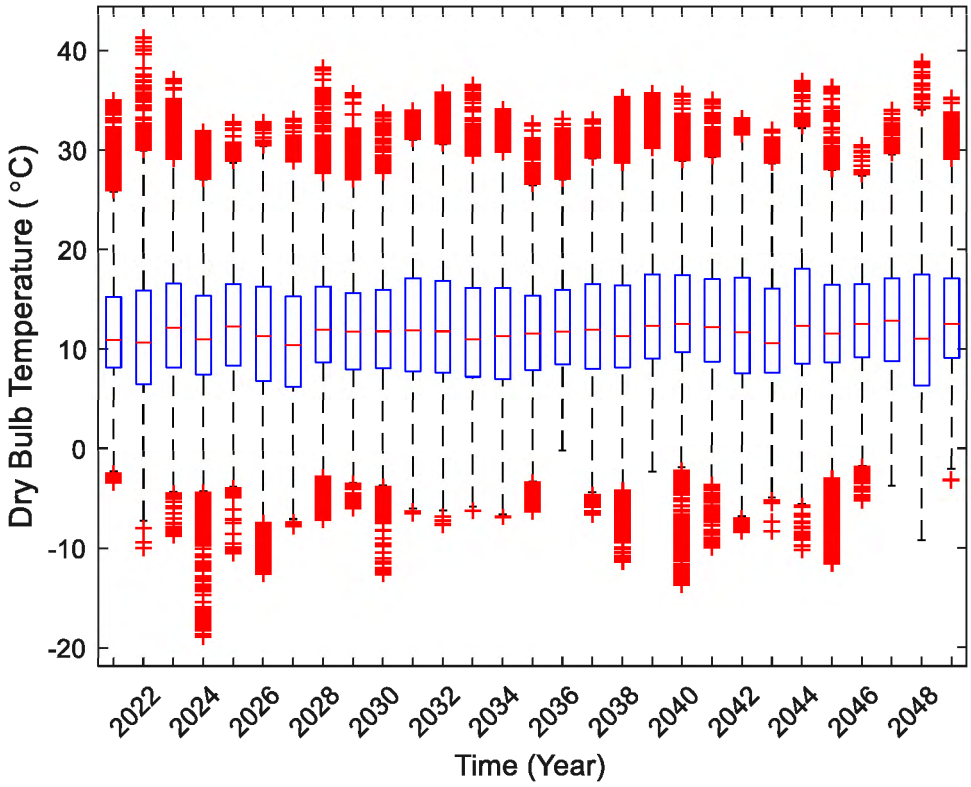

C44: Temperature box plot yearly 2021 to 2050 (Realization 9)

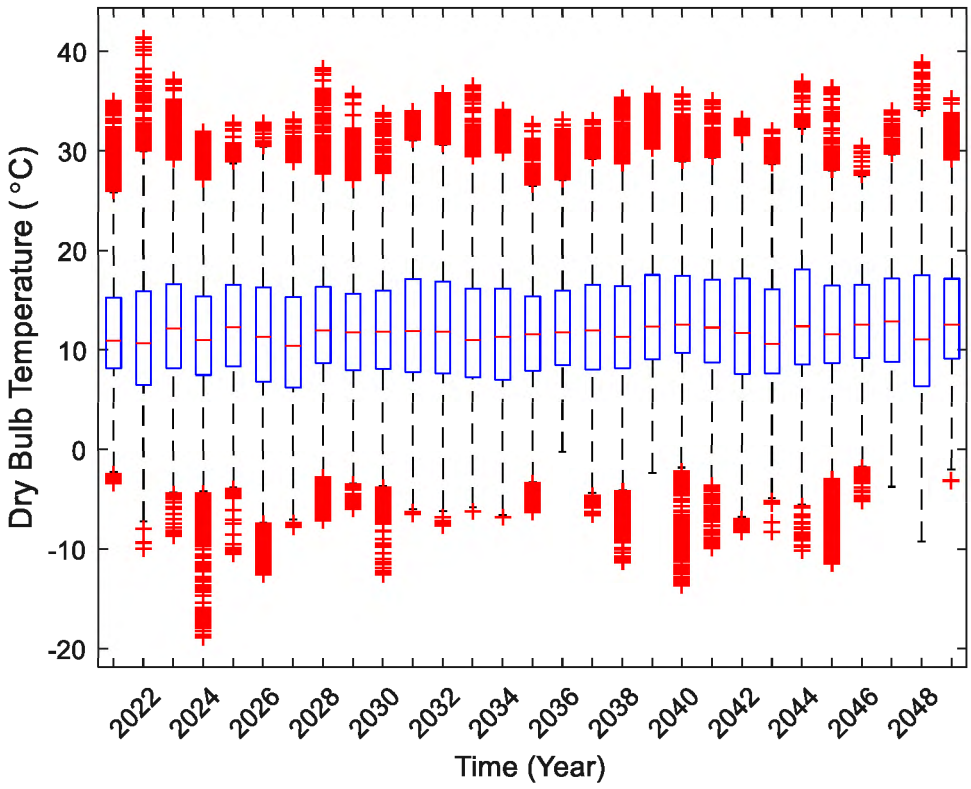

C45: Temperature box plot yearly 2021 to 2050 (Realization 10)

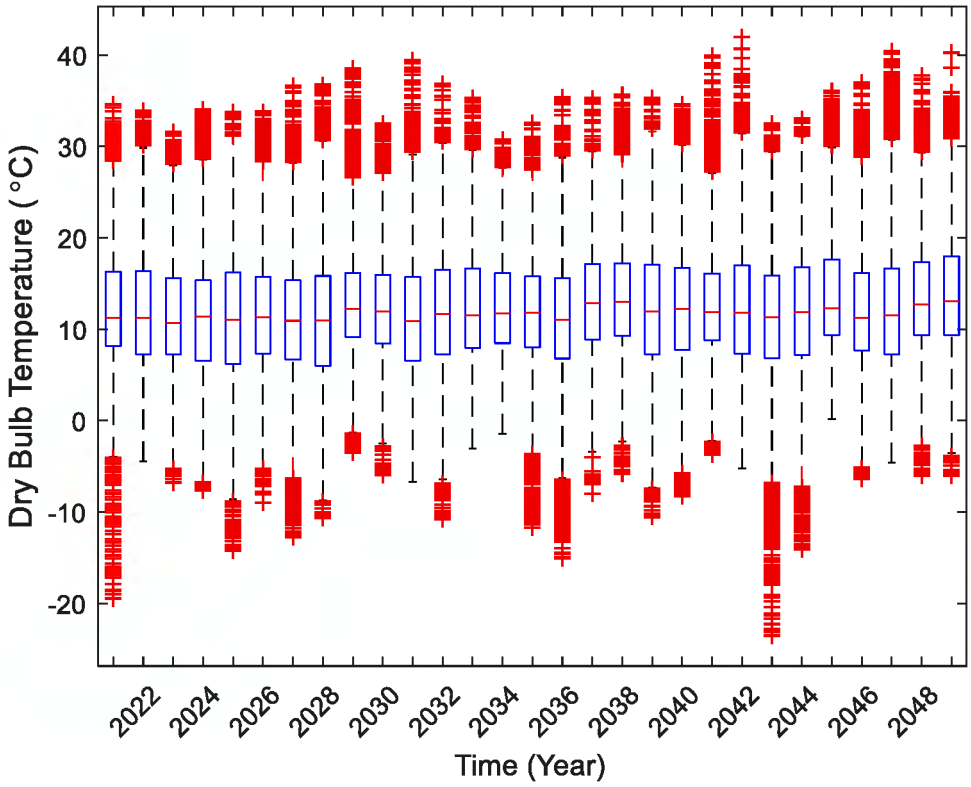

C46: Temperature box plot yearly 2021 to 2050 (Realization 11)

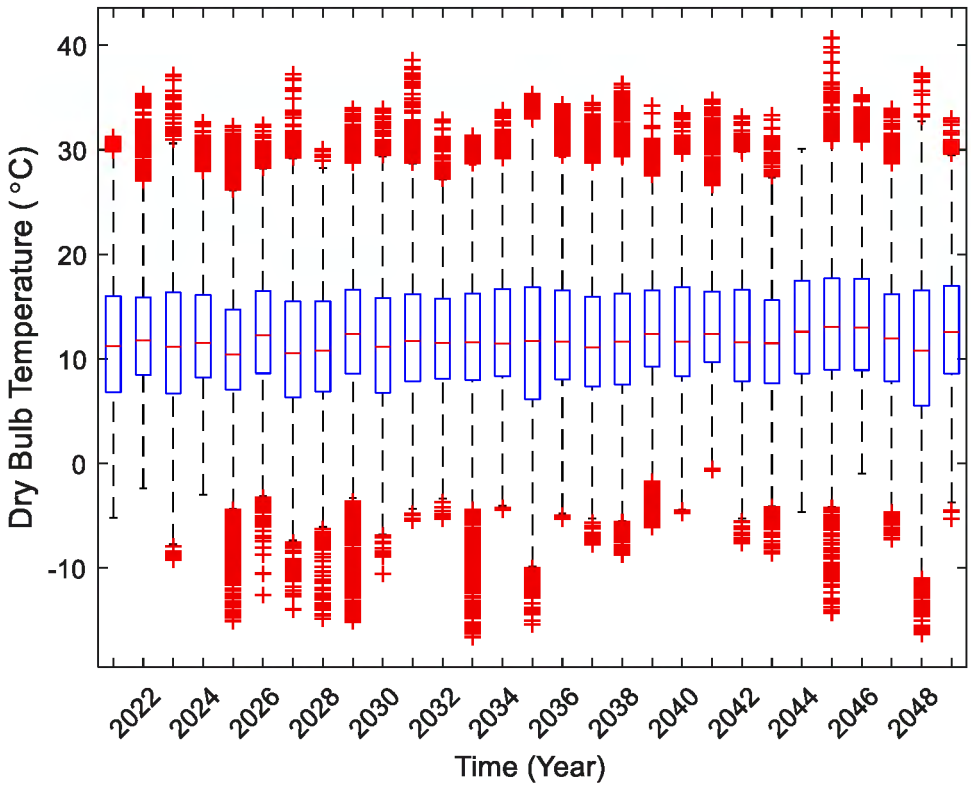

C47: Temperature box plot yearly 2021 to 2050 (Realization 12)

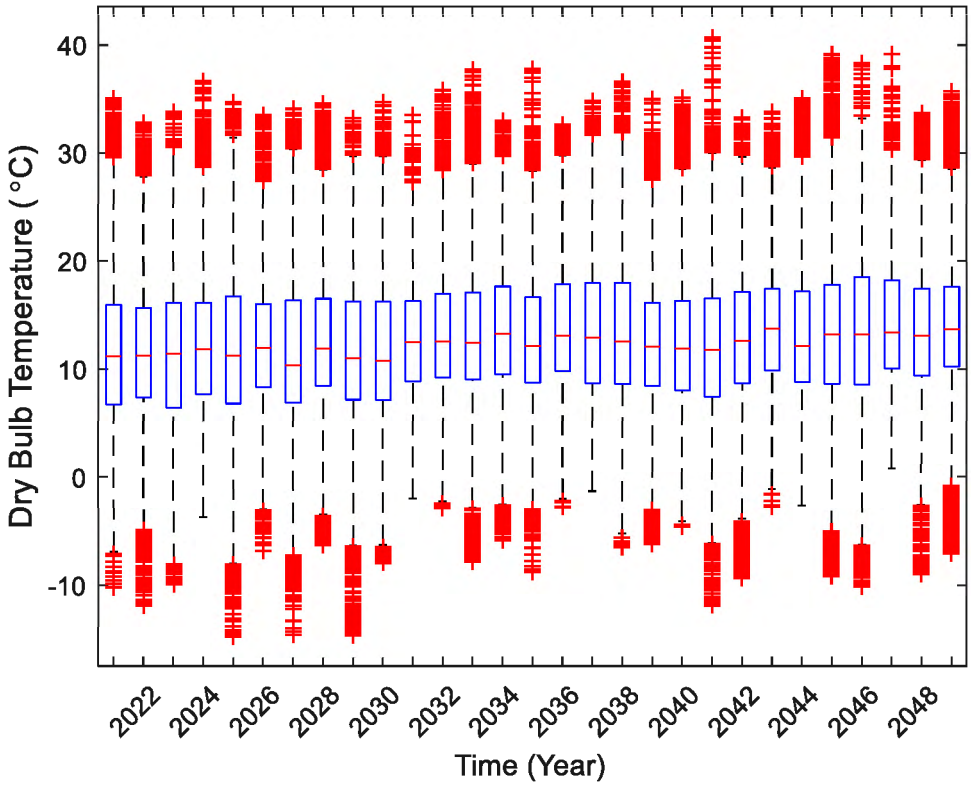

C48: Temperature box plot yearly 2021 to 2050 (Realization 13)

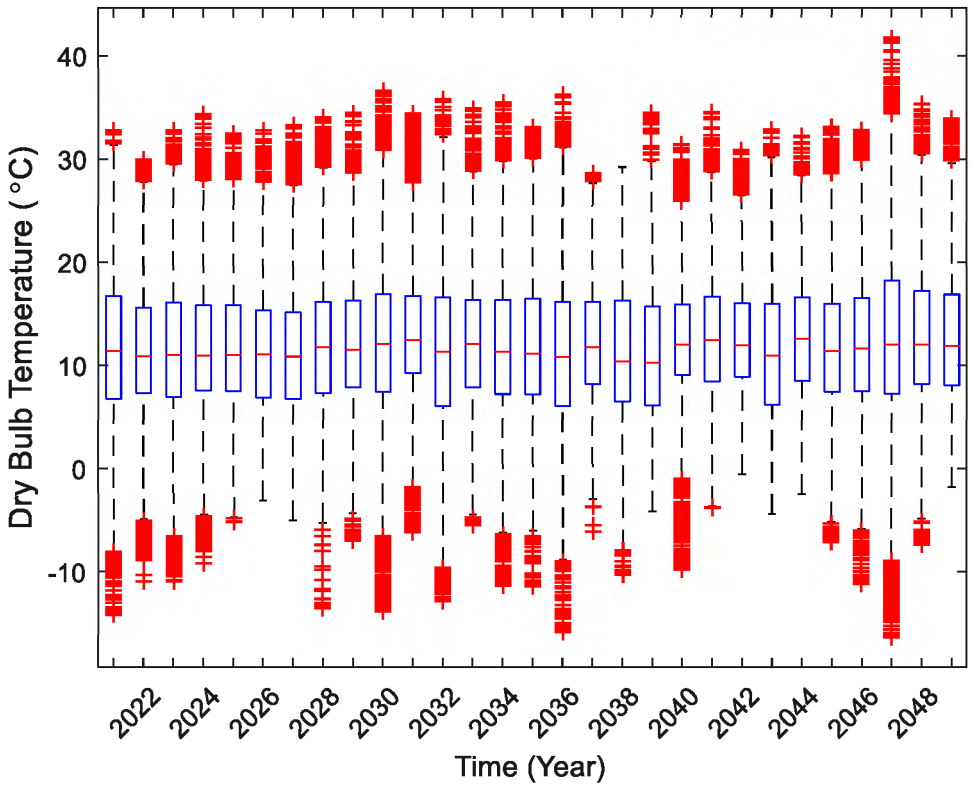

C49: Temperature box plot yearly 2021 to 2050 (Realization 14)

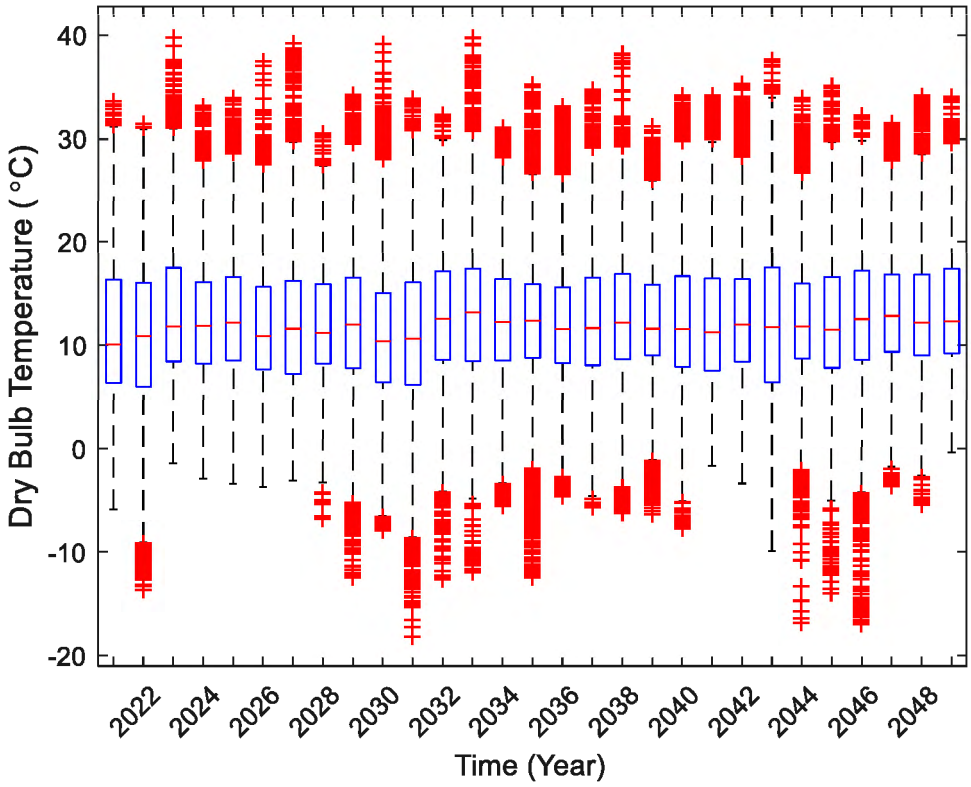

C50: Temperature box plot yearly 2021 to 2050 (Realization 15)

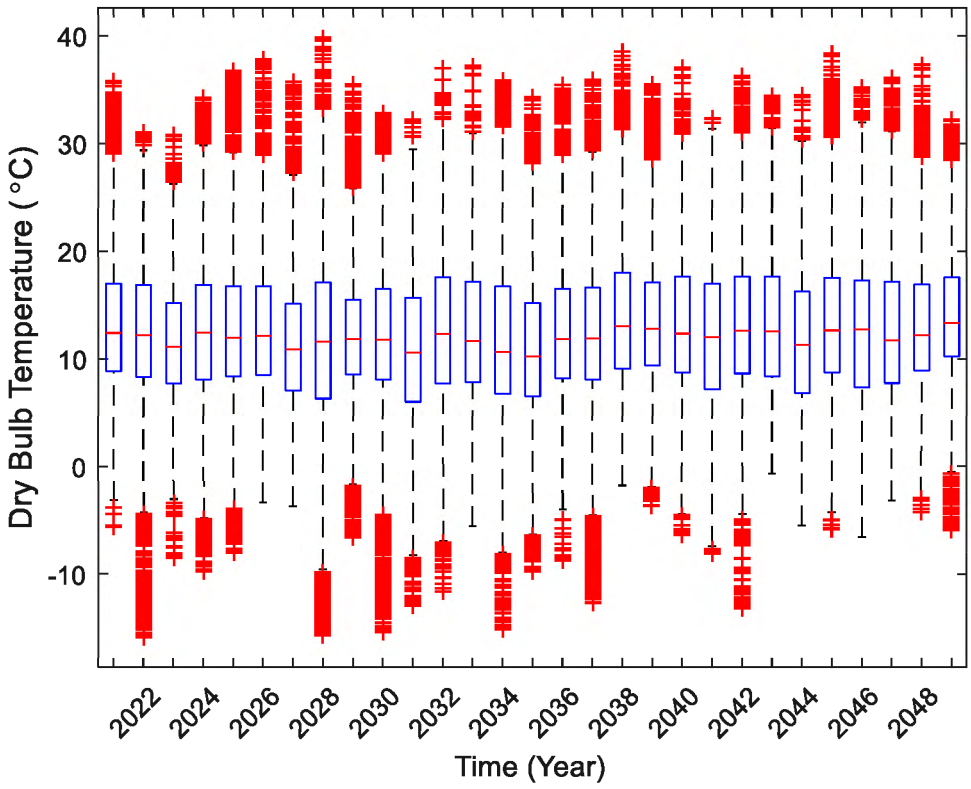

C51: Past time period relative humidity box plot for 15 realizations.

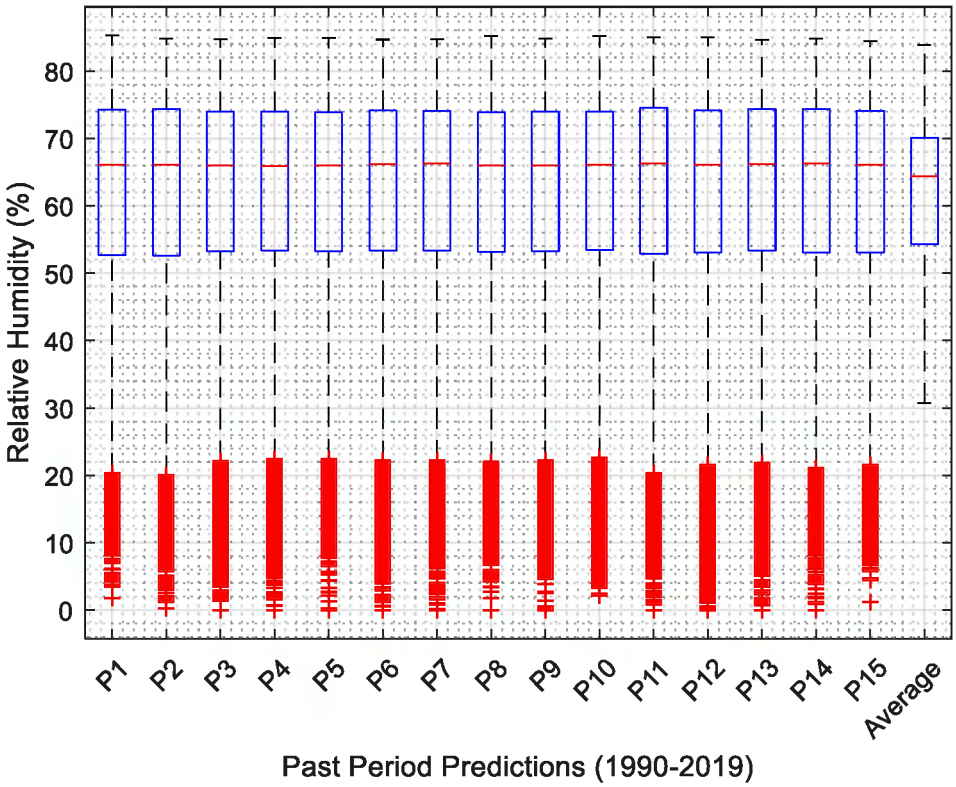

C52: Near future period relative humidity box plot for 15 realizations.

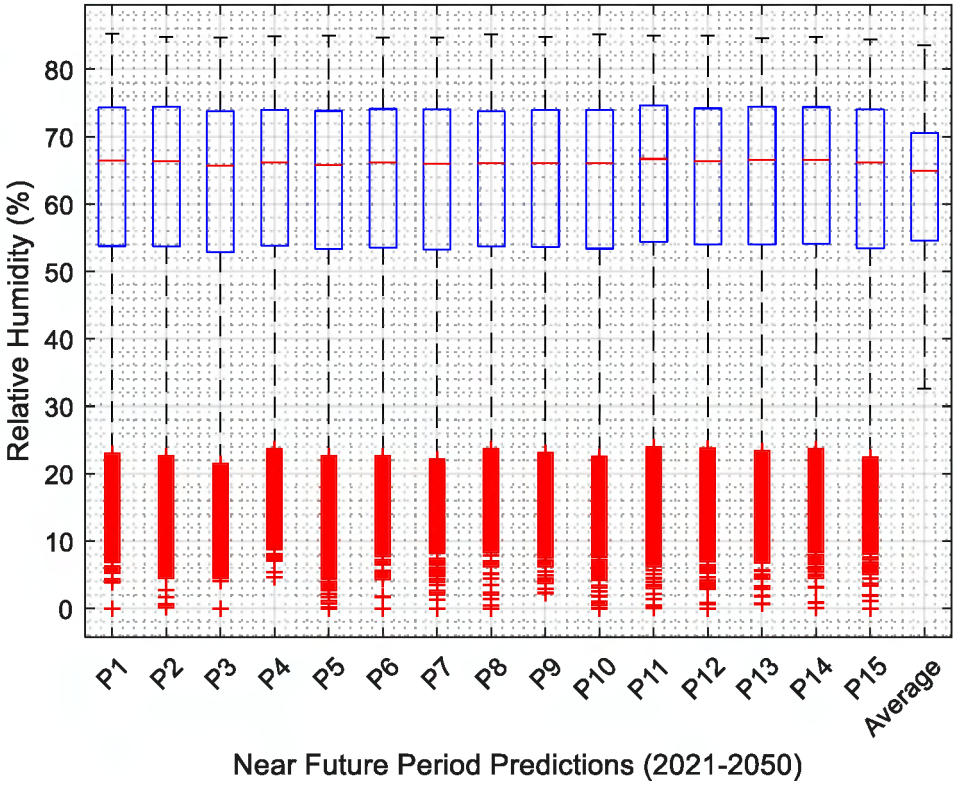

C53: Far future period relative humidity box plot for 15 realizations.

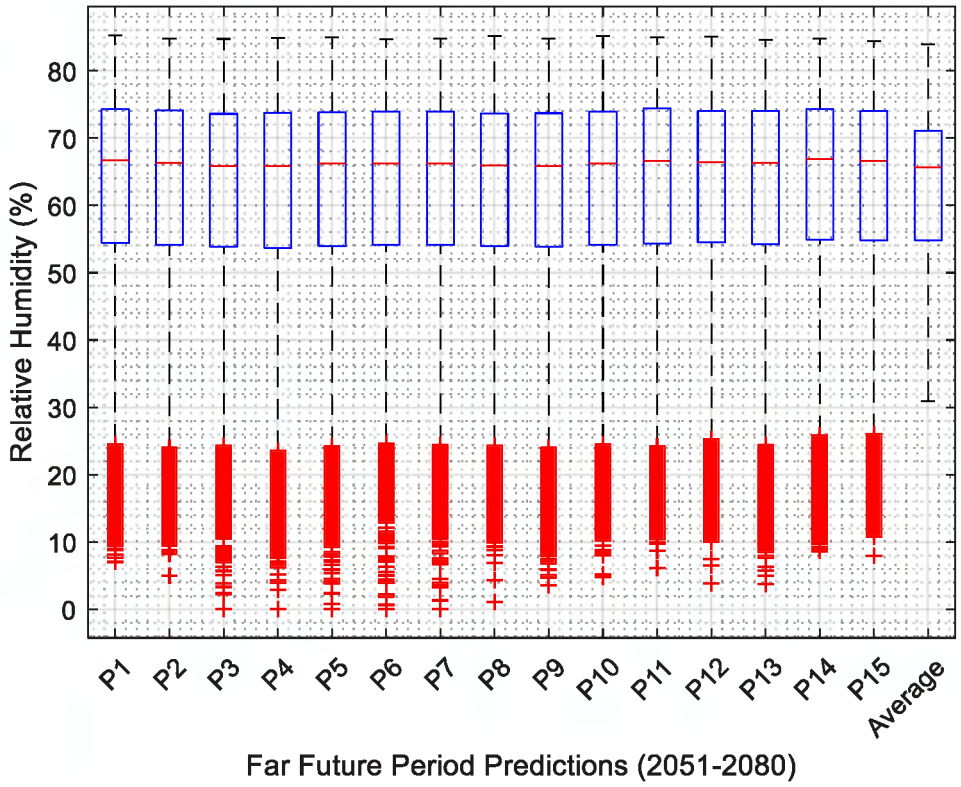

C54: Relative humidity Histogram with Kernel PDF plot for Realization 1

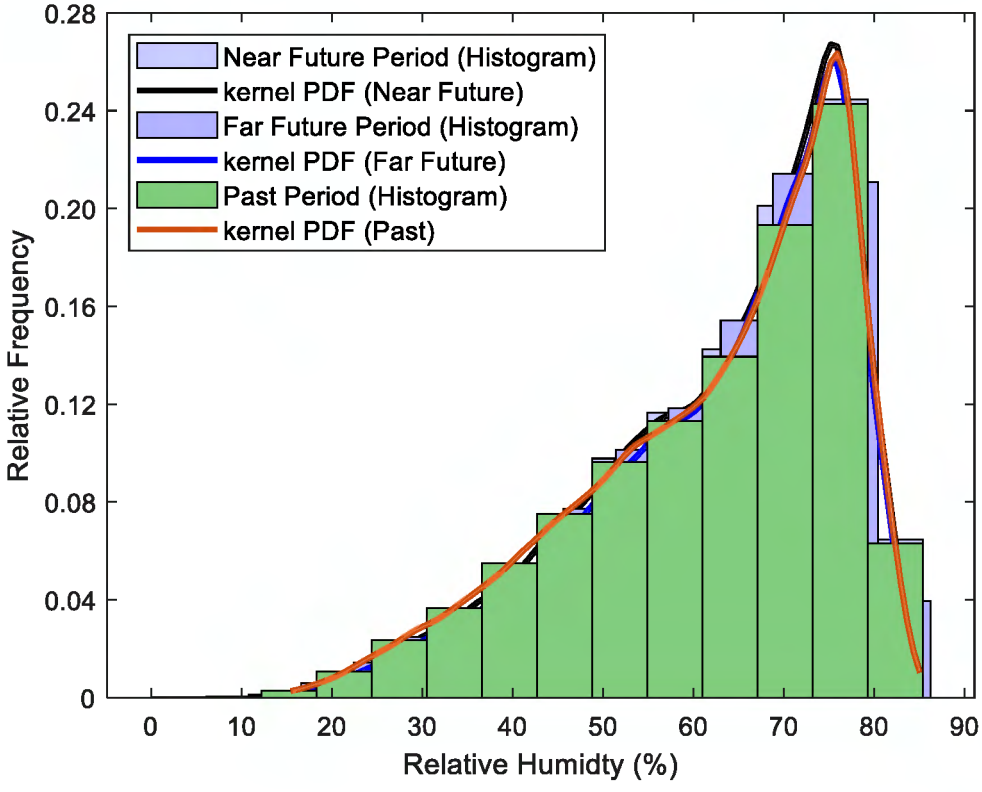

C55: Relative Humidity box plot for every five years from 1990 to 2080 (Realization1)

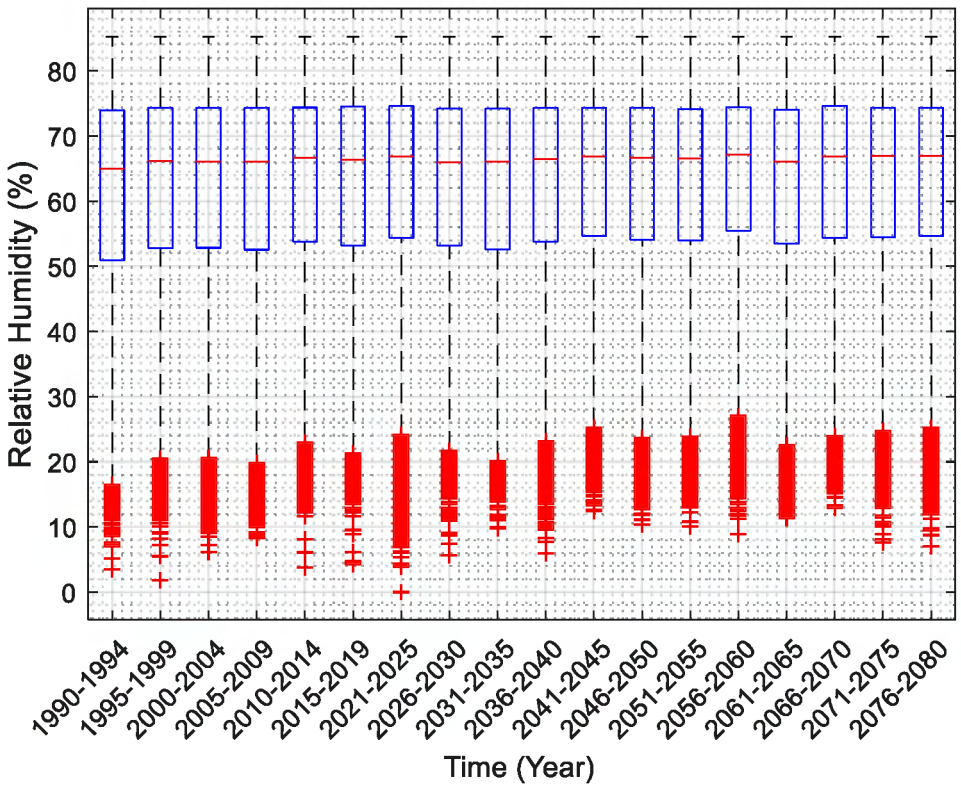

C56: Relative humidity Histogram with Kernel PDF plot for Realization 2

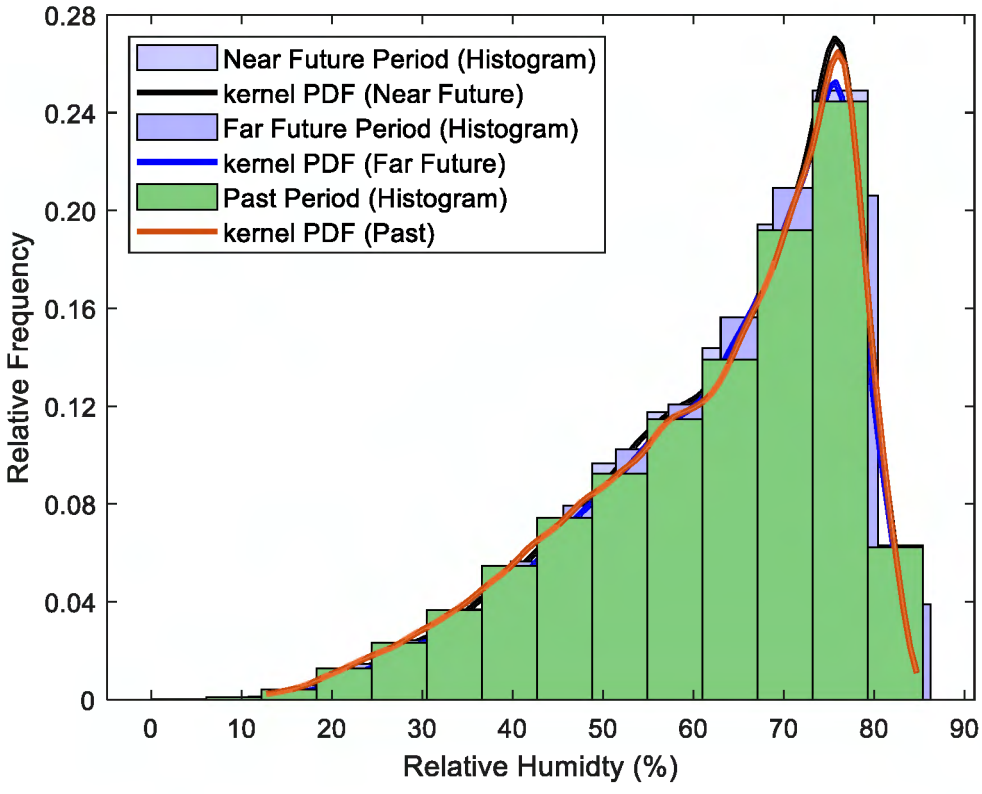

C57: Relative Humidity box plot for every five years from 1990 to 2080 (Realization2)

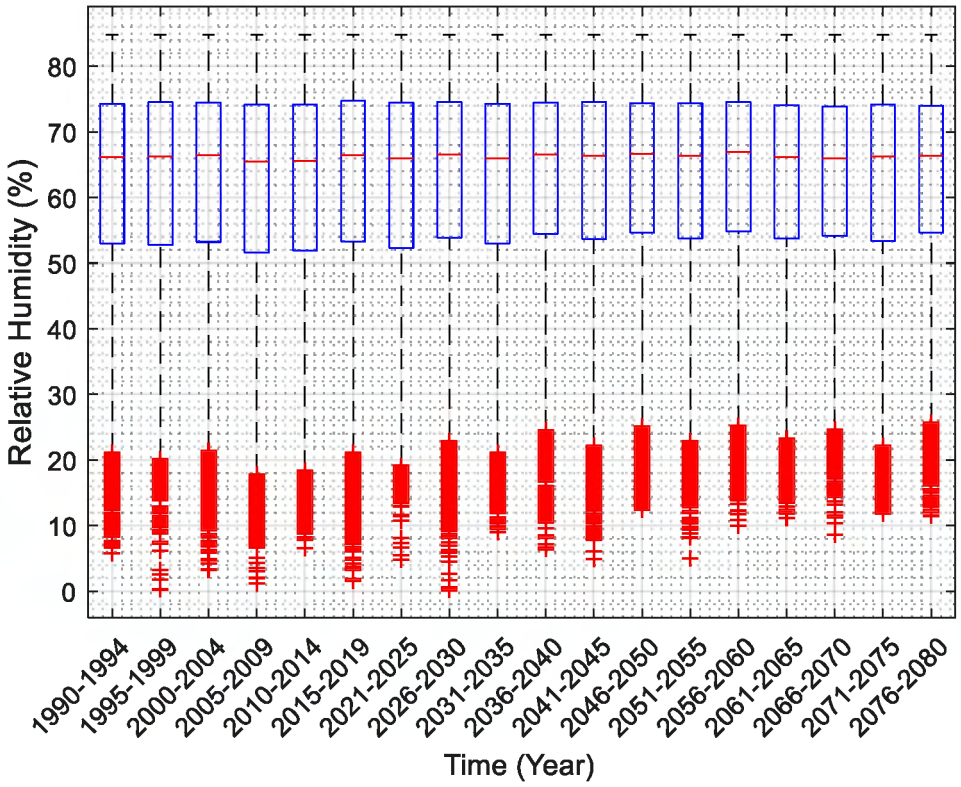

C58: Relative humidity Histogram with Kernel PDF plot for Realization 3

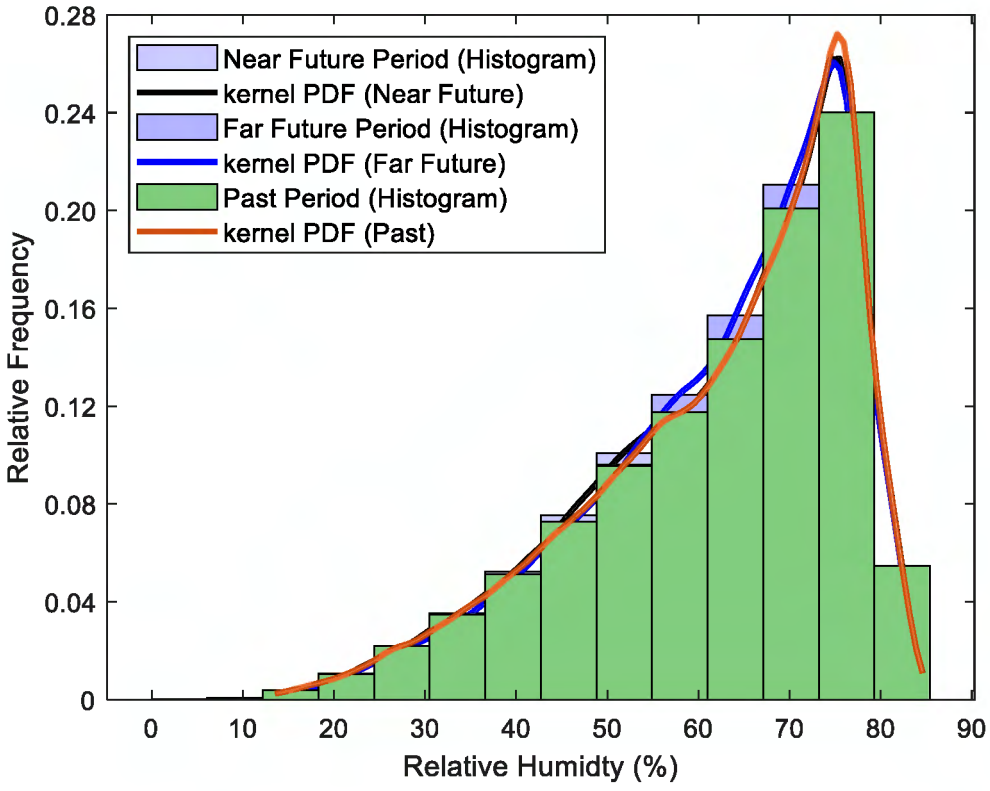

C59: Relative Humidity box plot for every five years from 1990 to 2080 (Realization3)

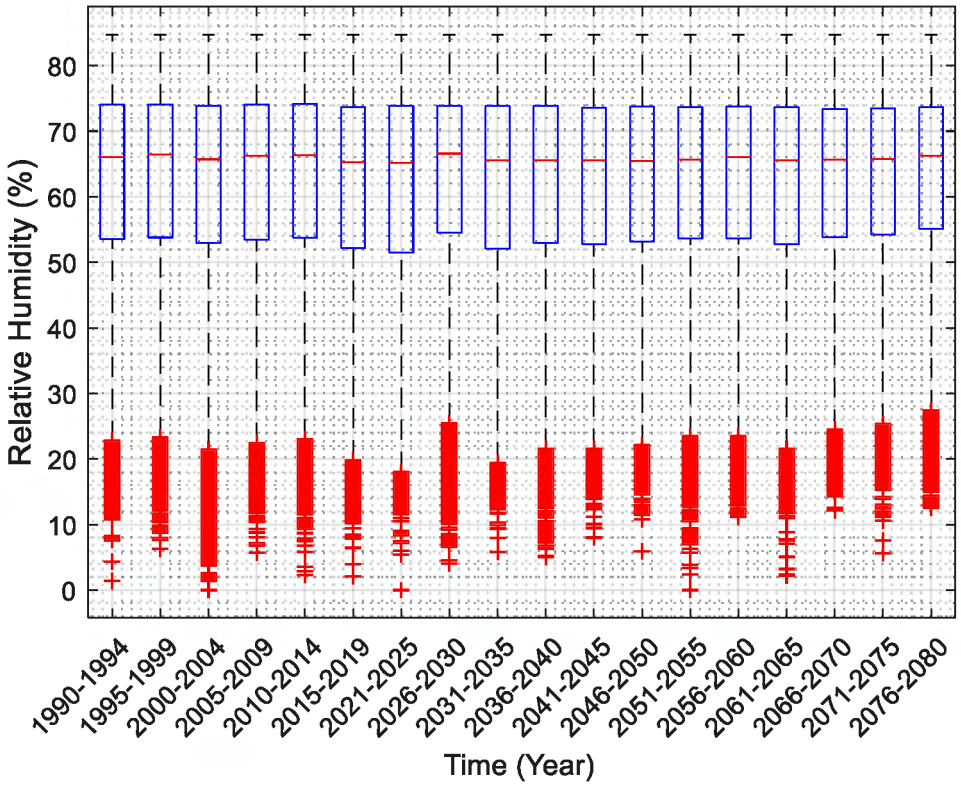

C60: Relative humidity Histogram with Kernel PDF plot for Realization 4

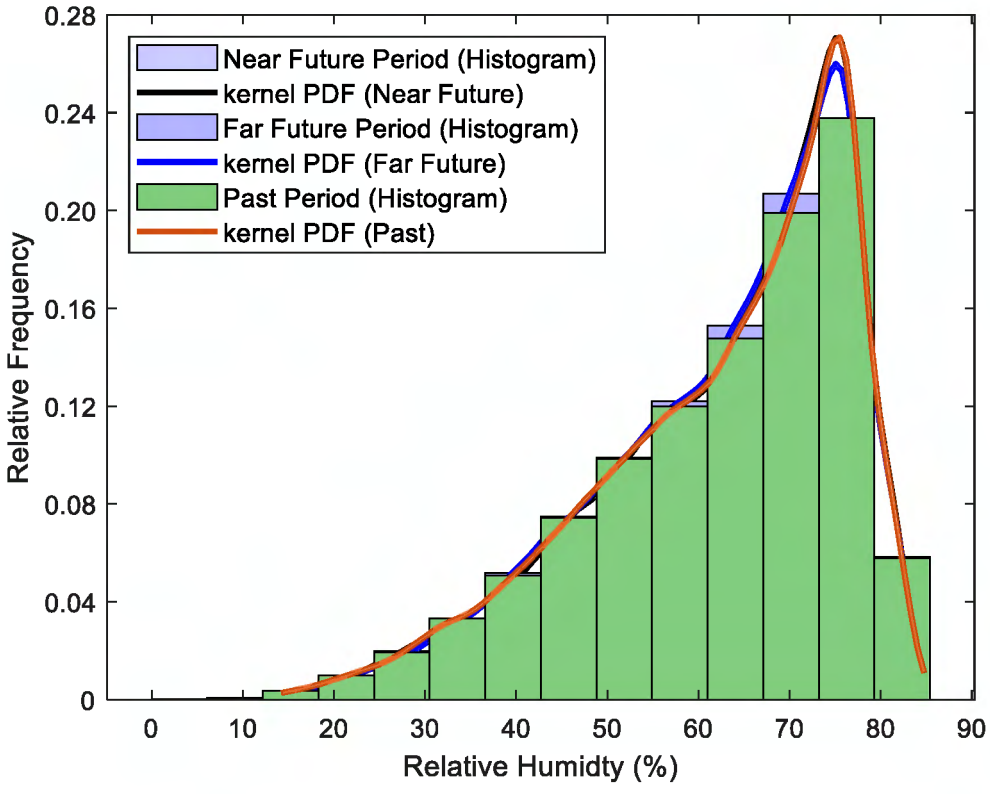

C61: Relative Humidity box plot for every five years from 1990 to 2080 (Realization4)

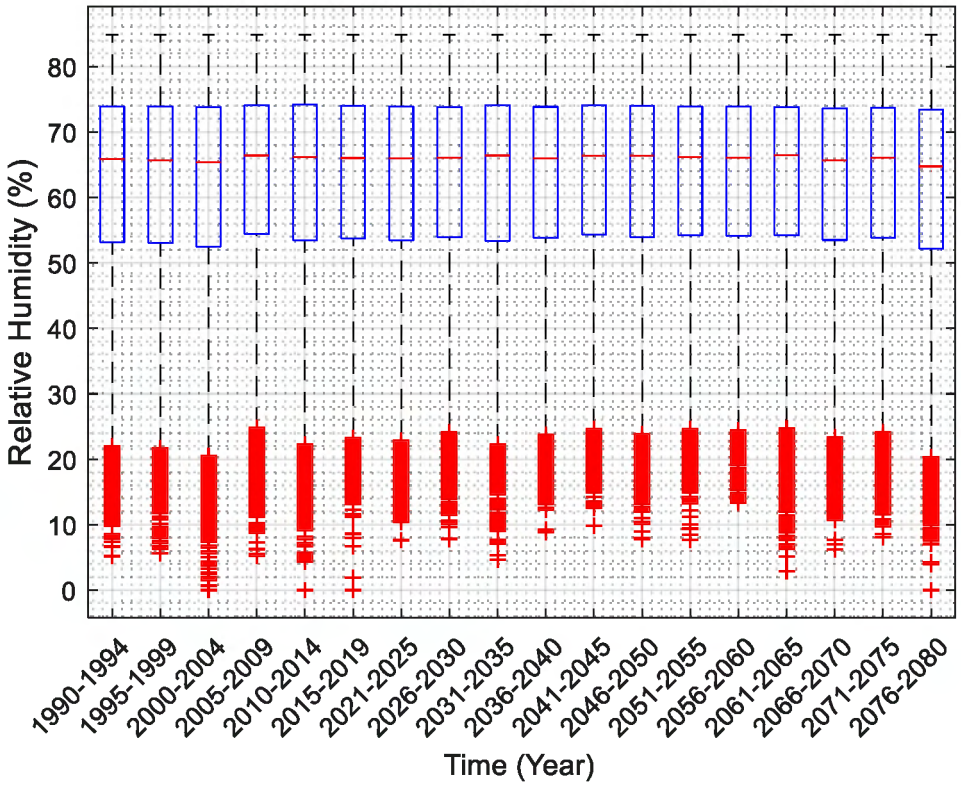

C62: Relative humidity Histogram with Kernel PDF plot for Realization 5

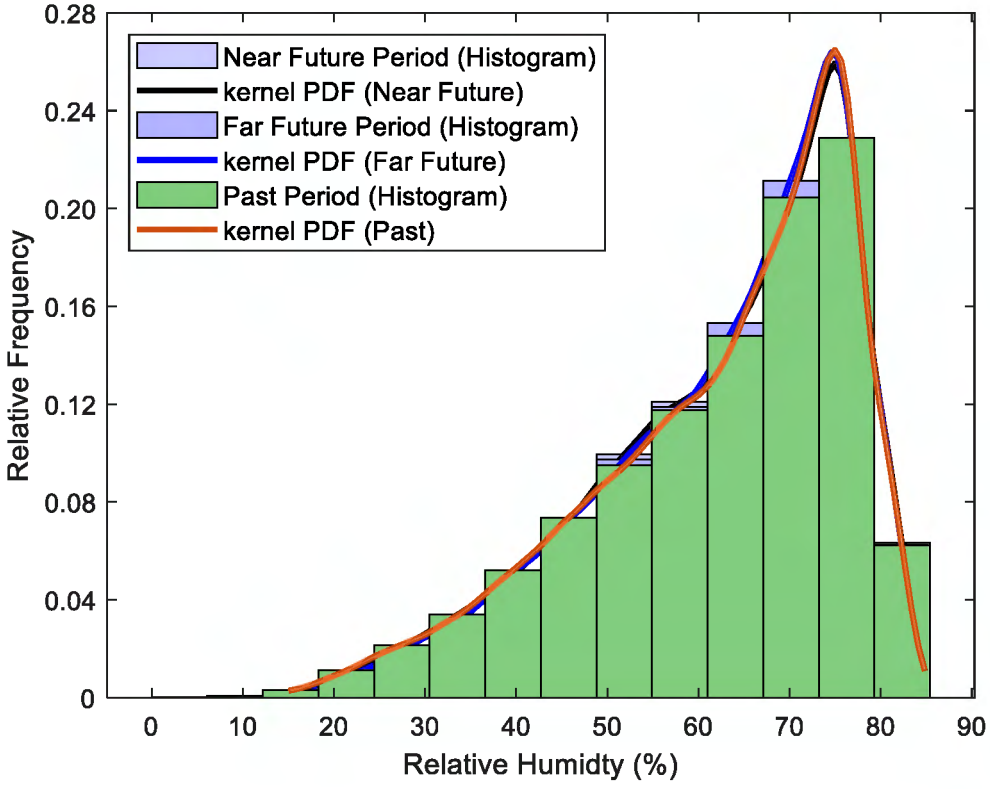

C63: Relative Humidity box plot for every five years from 1990 to 2080 (Realization5)

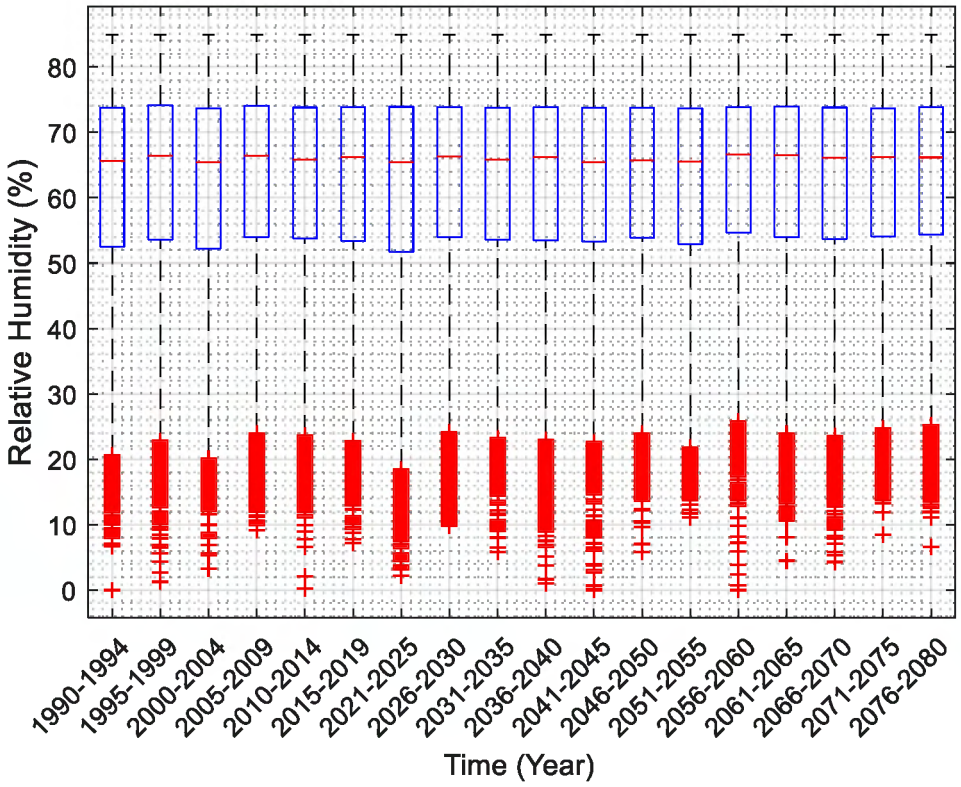

C64: Relative humidity Histogram with Kernel PDF plot for Realization 6

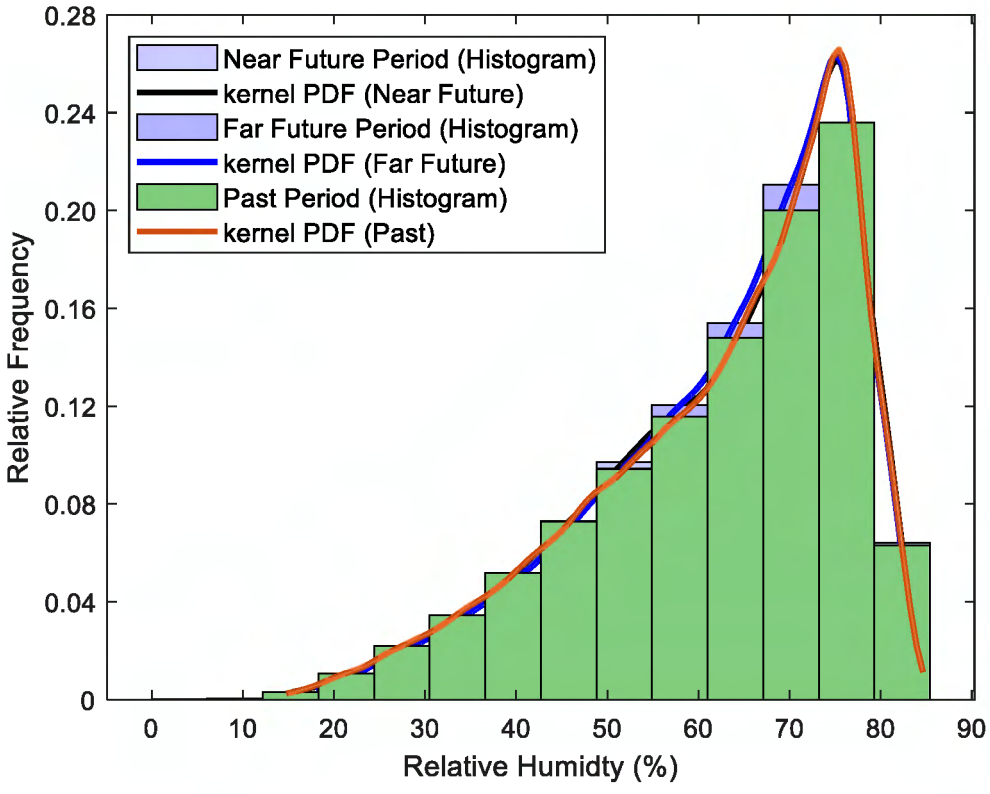

C65: Relative Humidity box plot for every five years from 1990 to 2080 (Realization6)

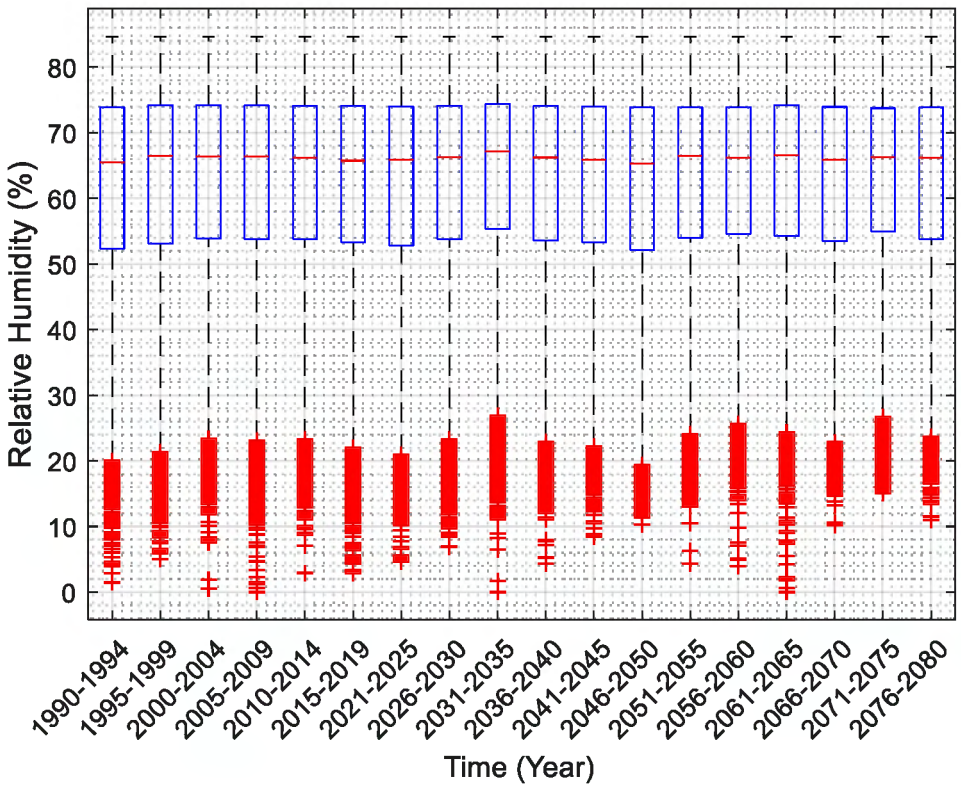

C66: Relative humidity Histogram with Kernel PDF plot for Realization 7

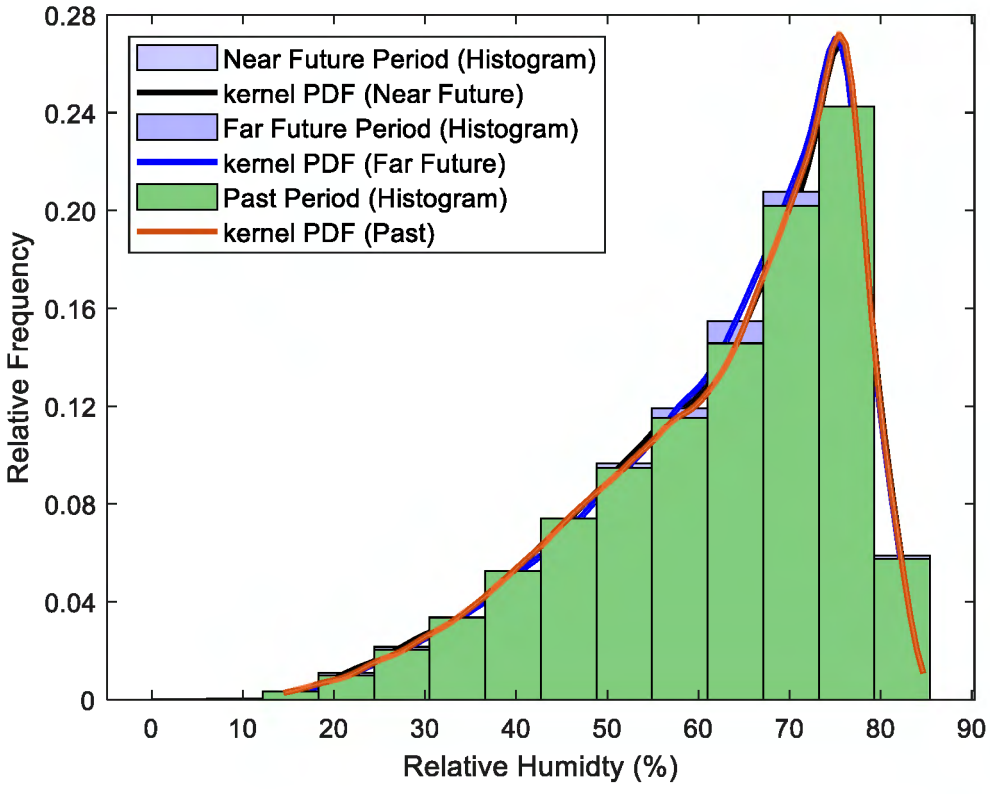

C67: Relative Humidity box plot for every five years from 1990 to 2080 (Realization7)

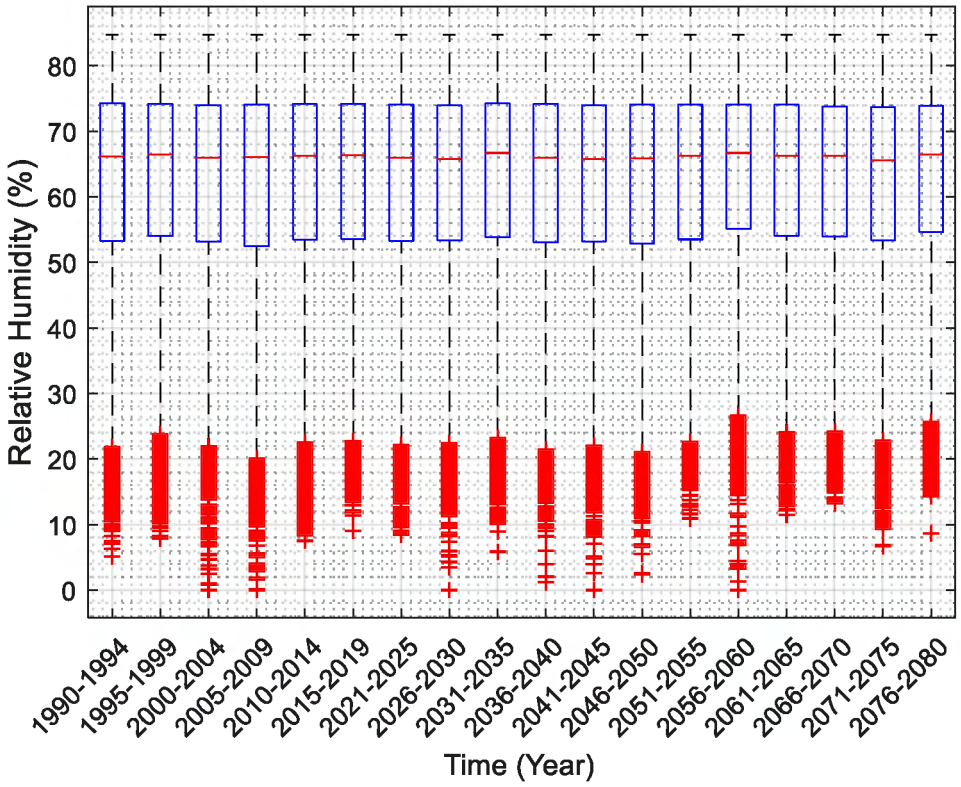

C68: Relative humidity Histogram with Kernel PDF plot for Realization 8

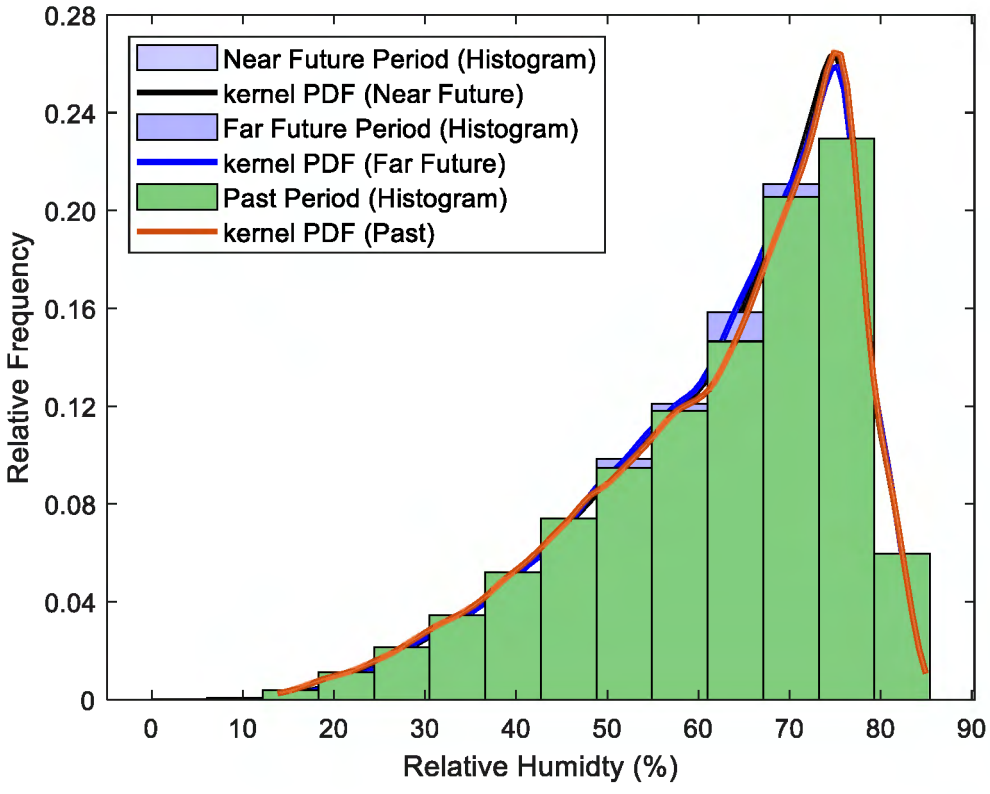

C69: Relative Humidity box plot for every five years from 1990 to 2080 (Realization8)

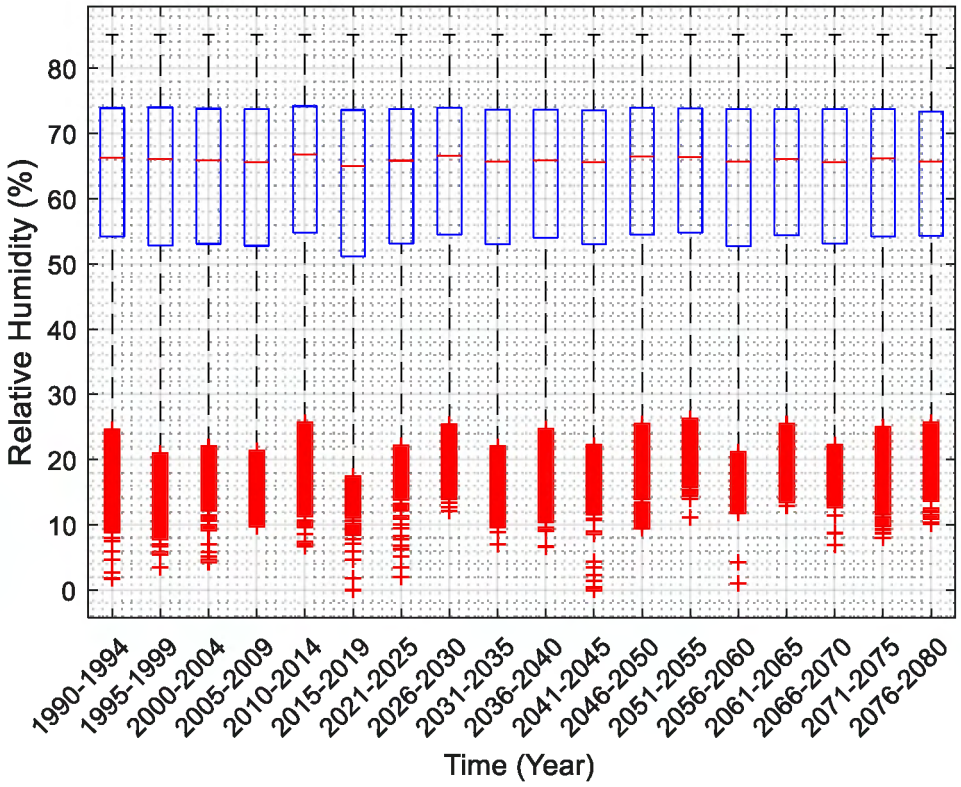

C70: Relative humidity Histogram with Kernel PDF plot for Realization 9

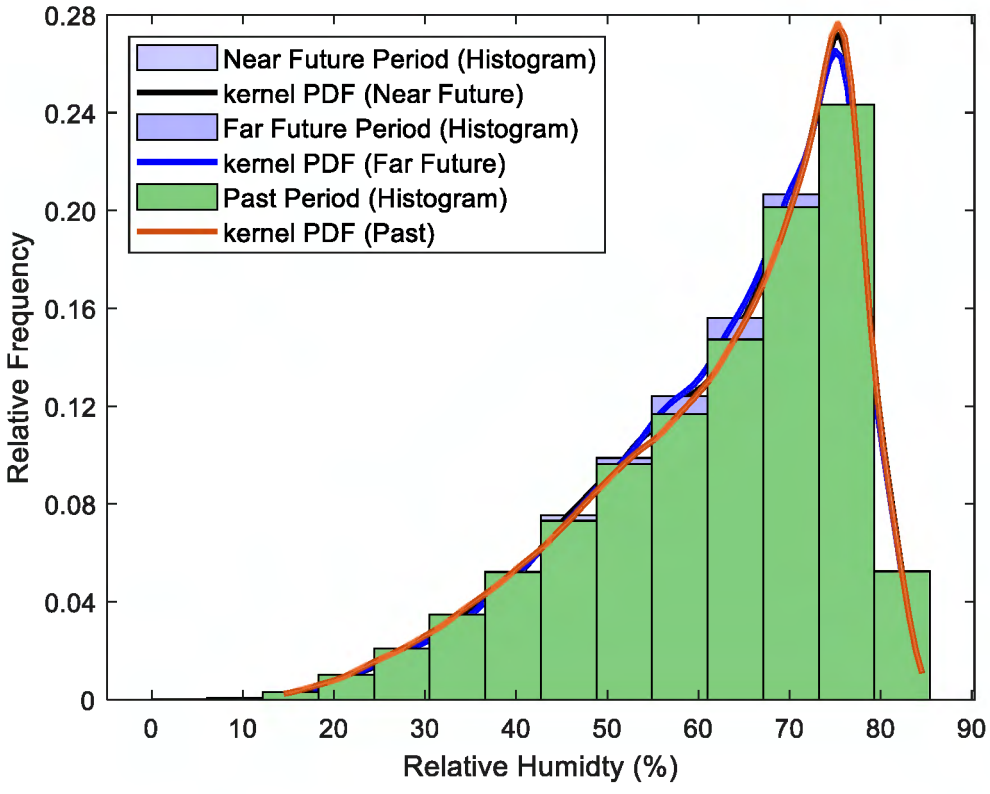

C71: Relative Humidity box plot for every five years from 1990 to 2080 (Realization9)

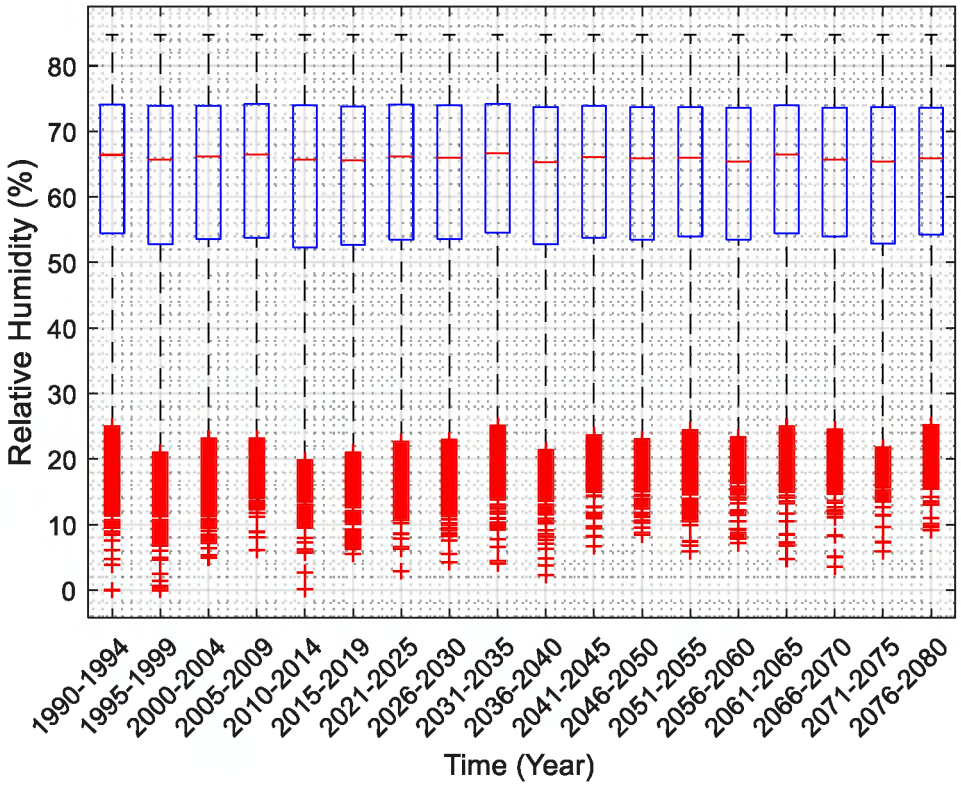

C72: Relative humidity Histogram with Kernel PDF plot for Realization 10

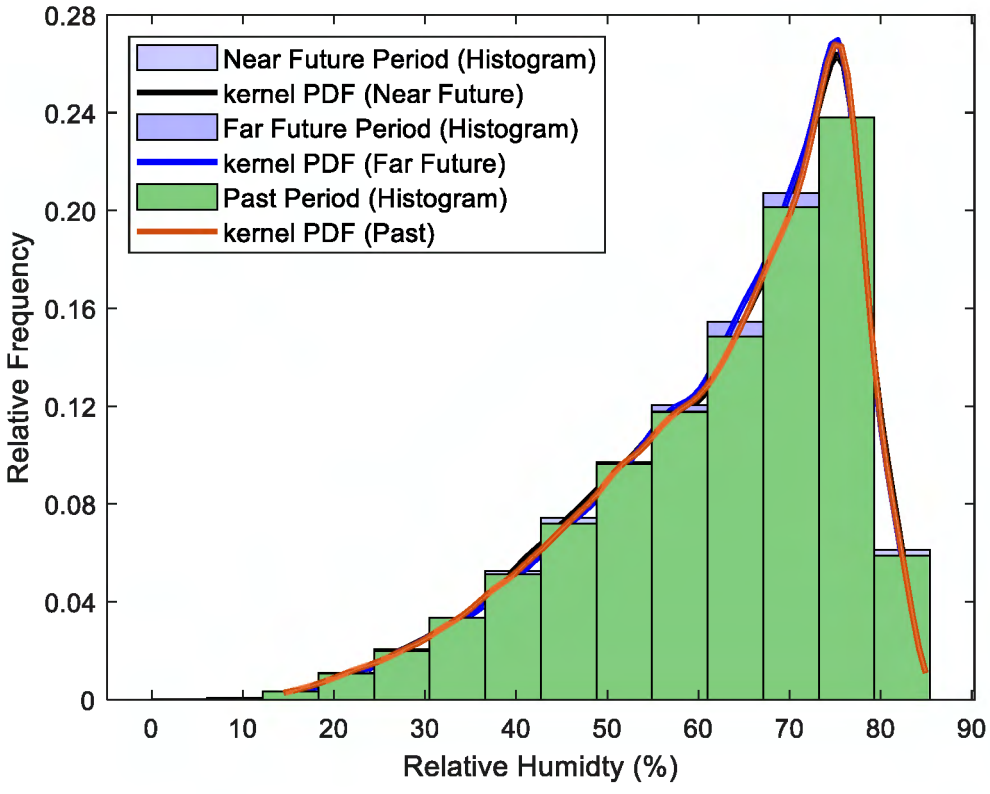

C73: Relative Humidity box plot for every five years from 1990 to 2080 (Realization10)

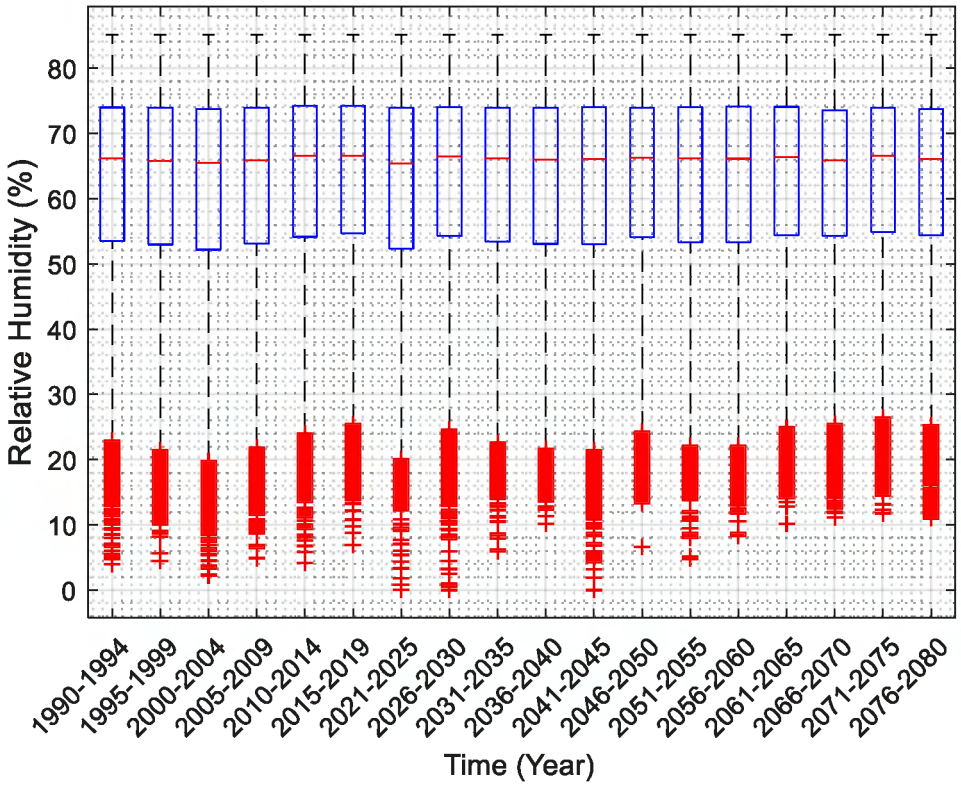

C74: Relative humidity Histogram with Kernel PDF plot for Realization 11

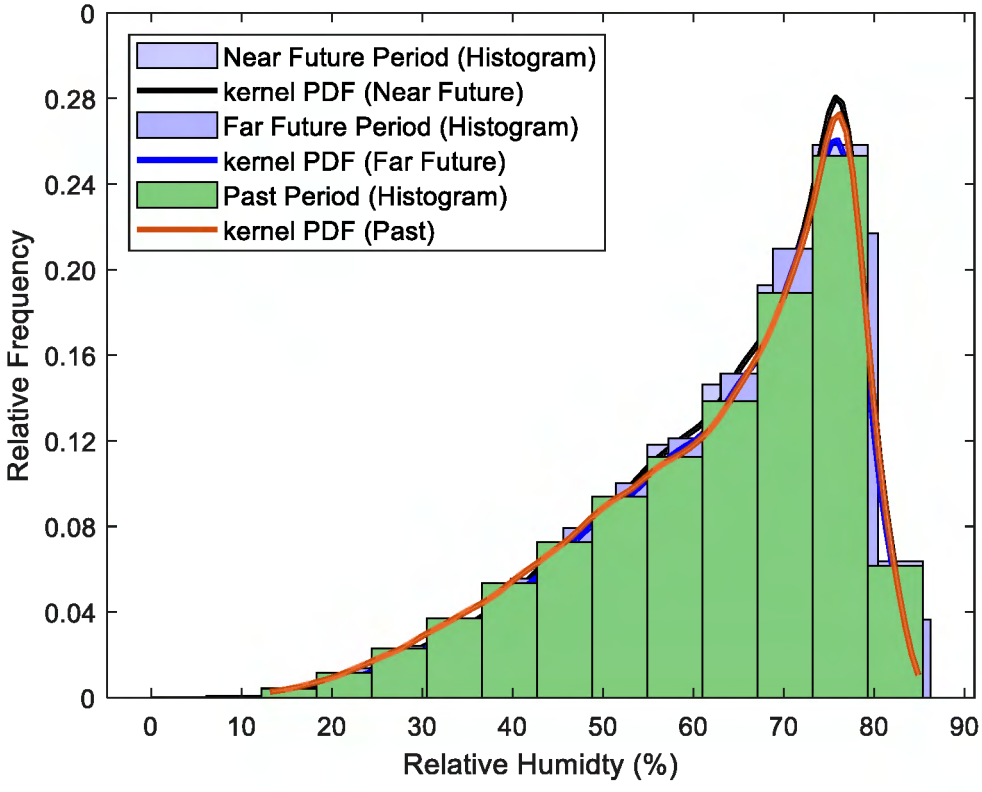

C75: Relative Humidity box plot for every five years from 1990 to 2080 (Realization11)

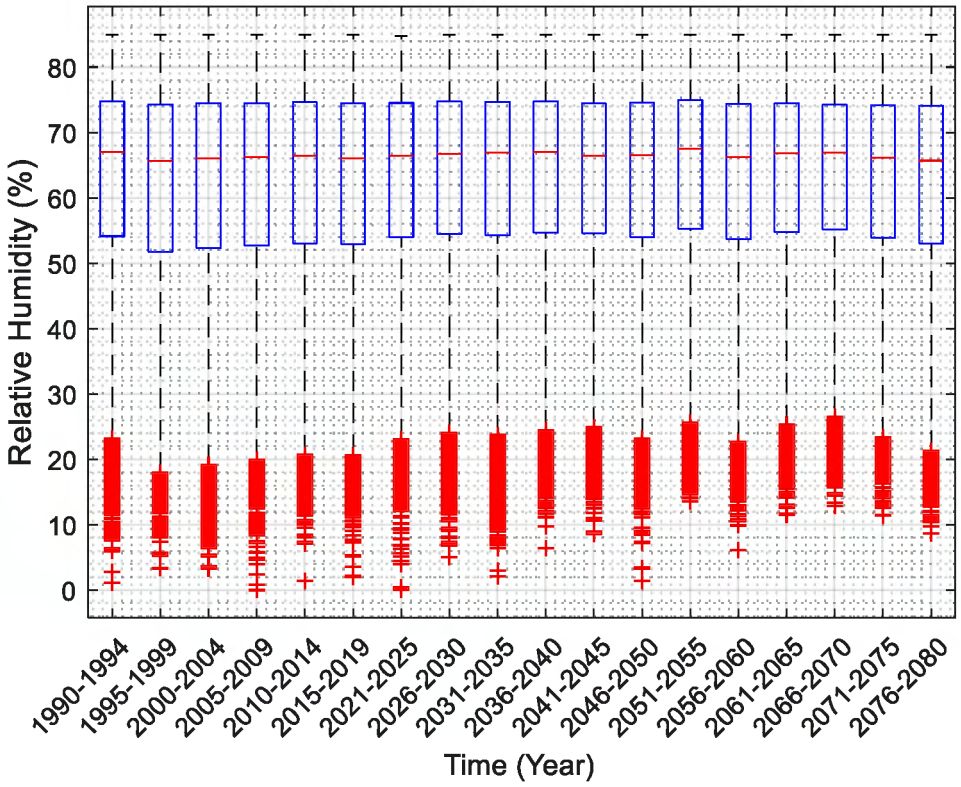

C76: Relative humidity Histogram with Kernel PDF plot for Realization 12

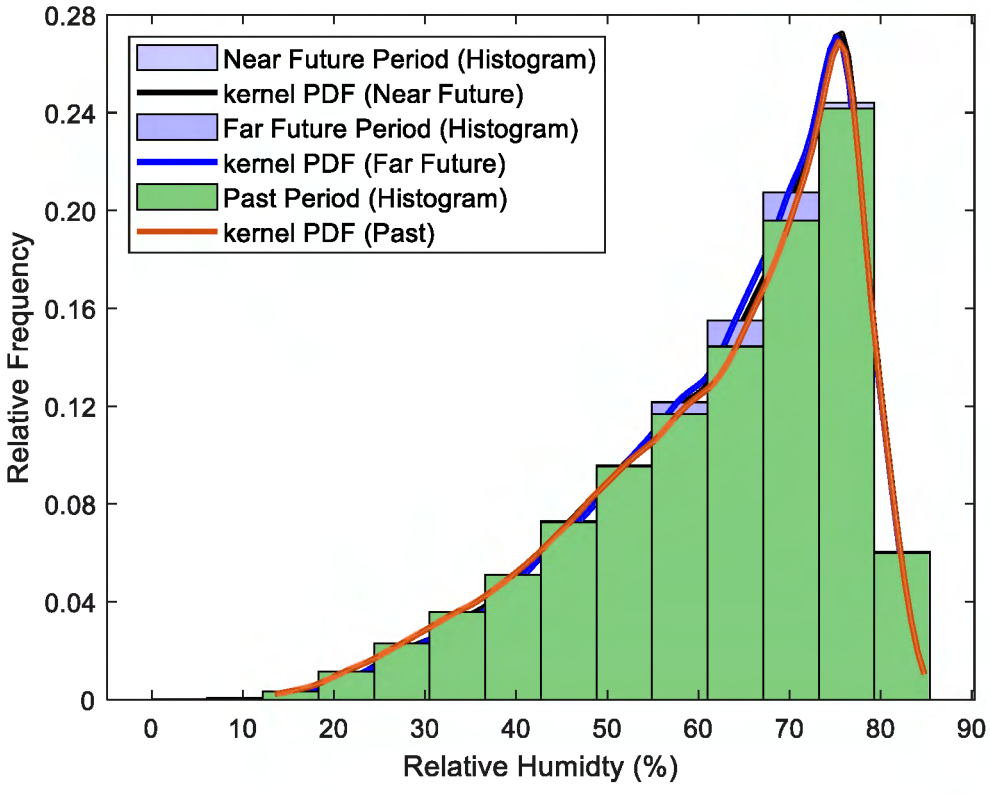

C77: Relative Humidity box plot for every five years from 1990 to 2080 (Realization12)

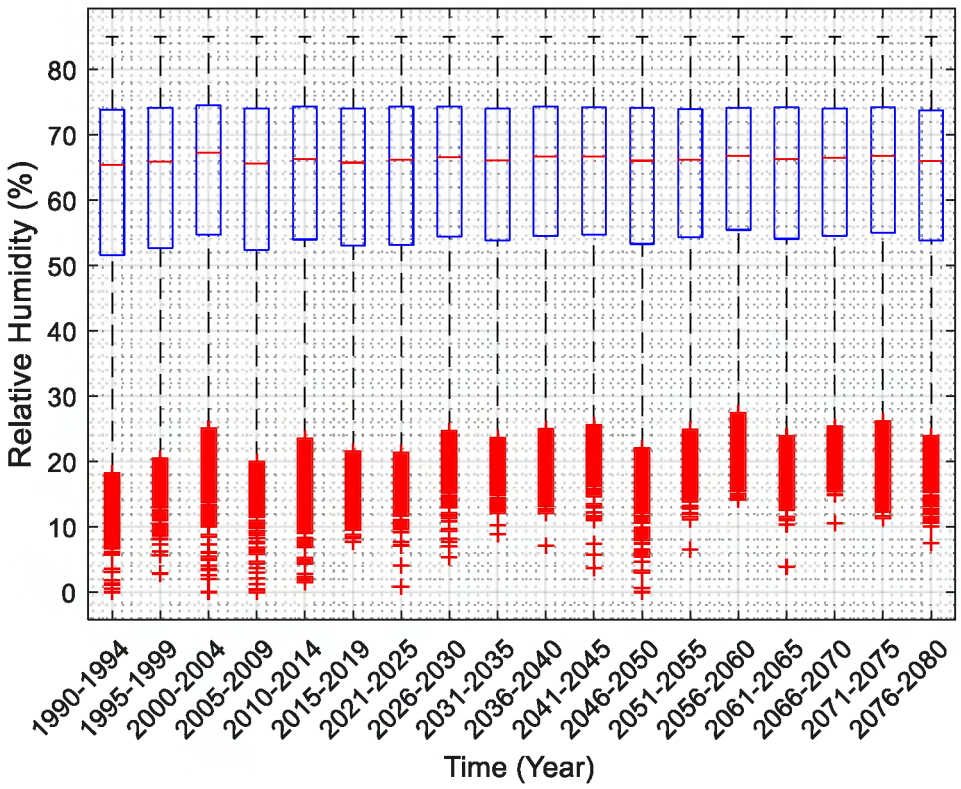

C78: Relative humidity Histogram with Kernel PDF plot for Realization 13

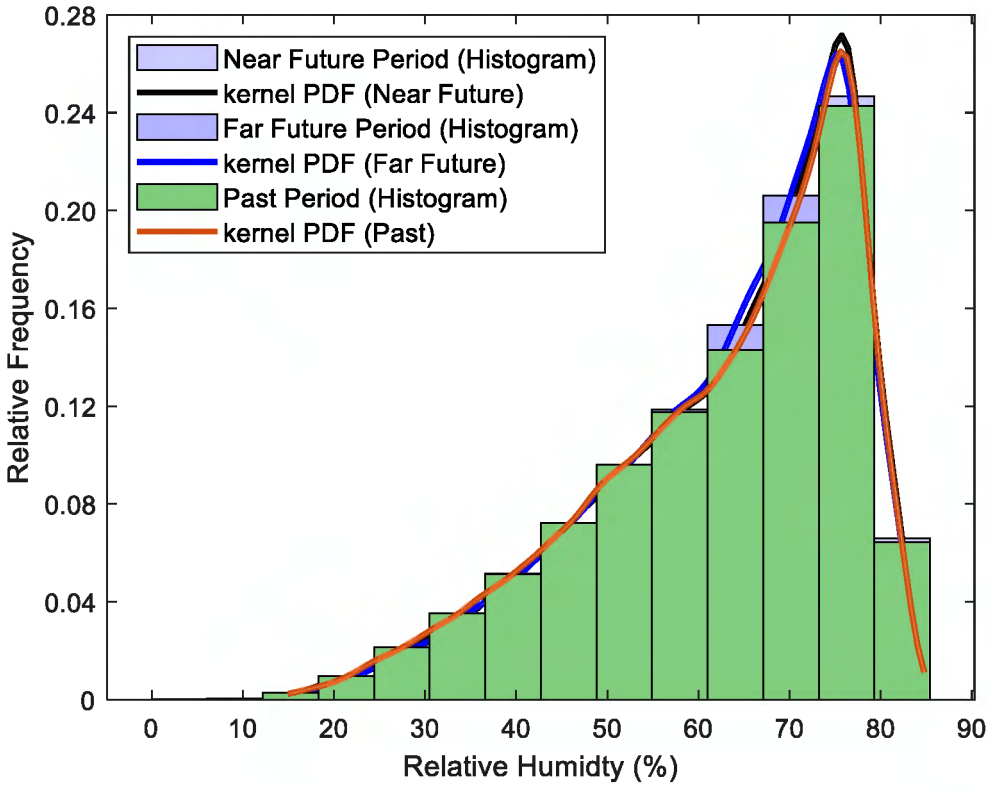

C79: Relative Humidity box plot for every five years from 1990 to 2080 (Realization13)

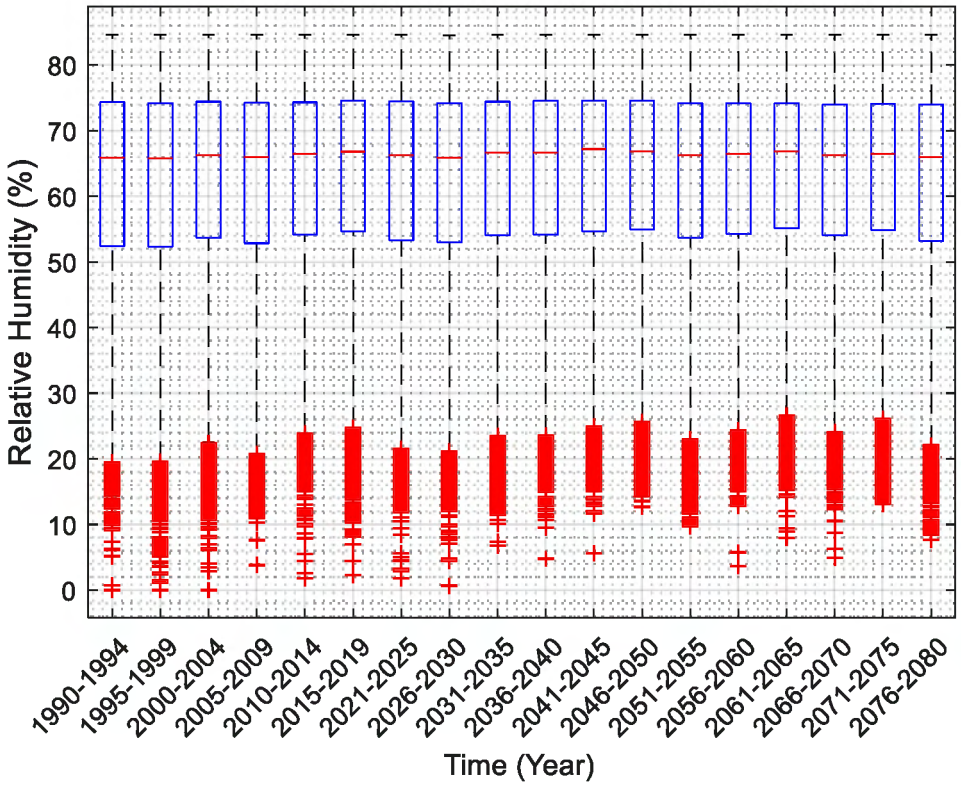

C80: Relative humidity Histogram with Kernel PDF plot for Realization 14

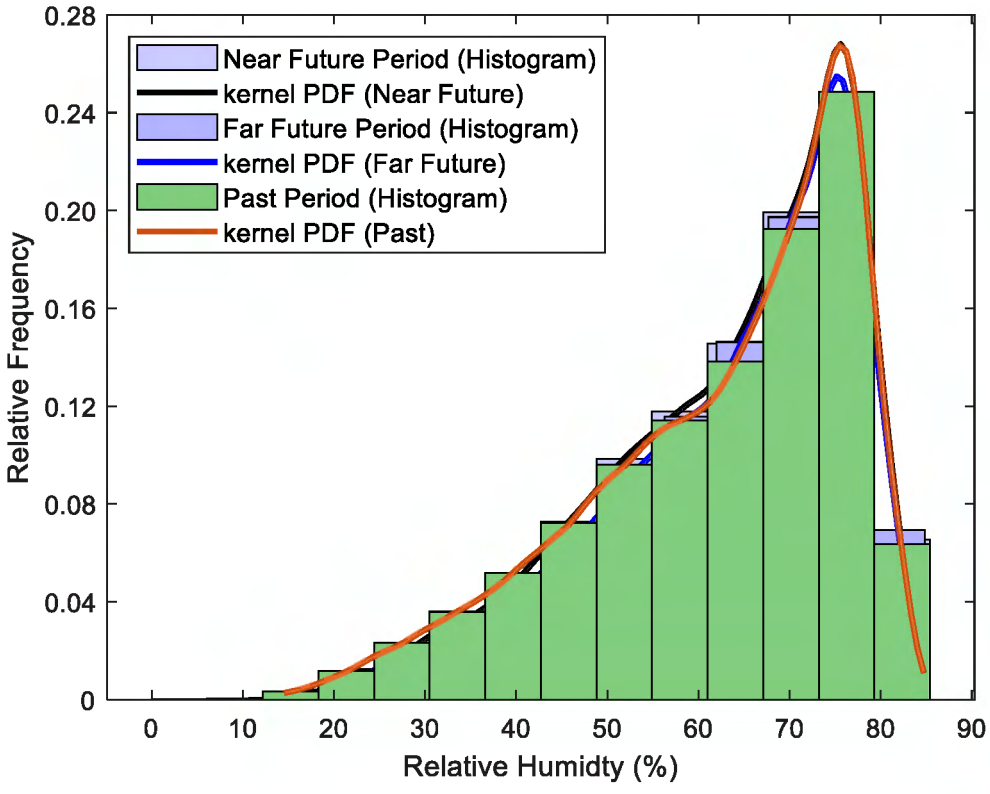

C81: Relative Humidity box plot for every five years from 1990 to 2080 (Realization14)

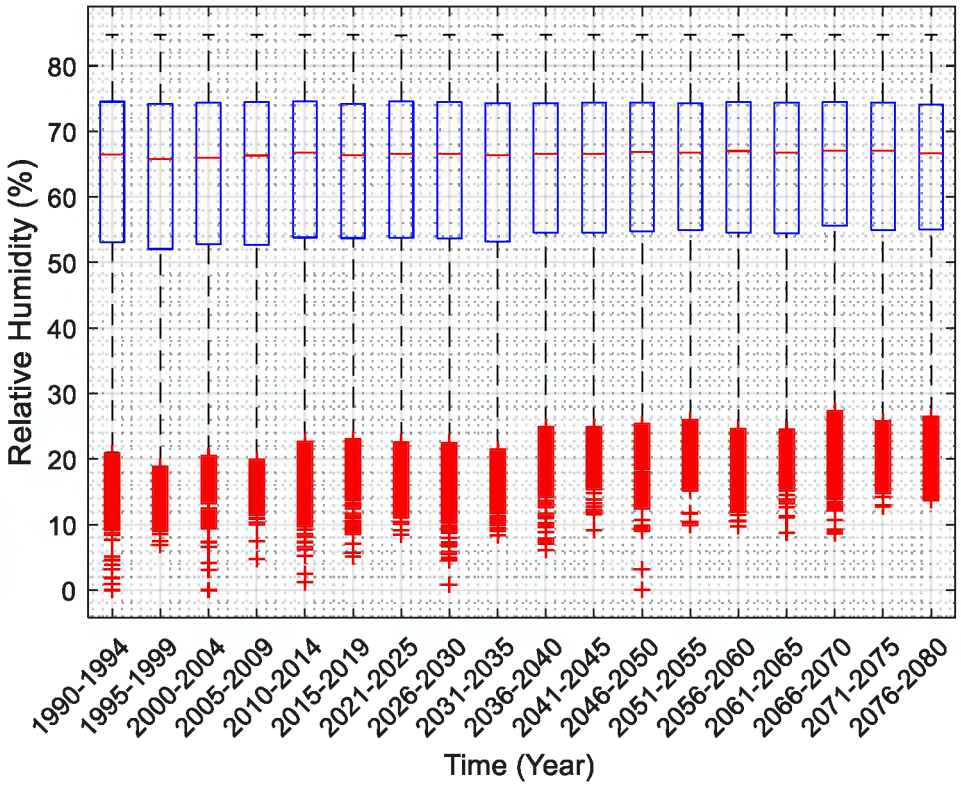

C82: Relative humidity Histogram with Kernel PDF plot for Realization 15

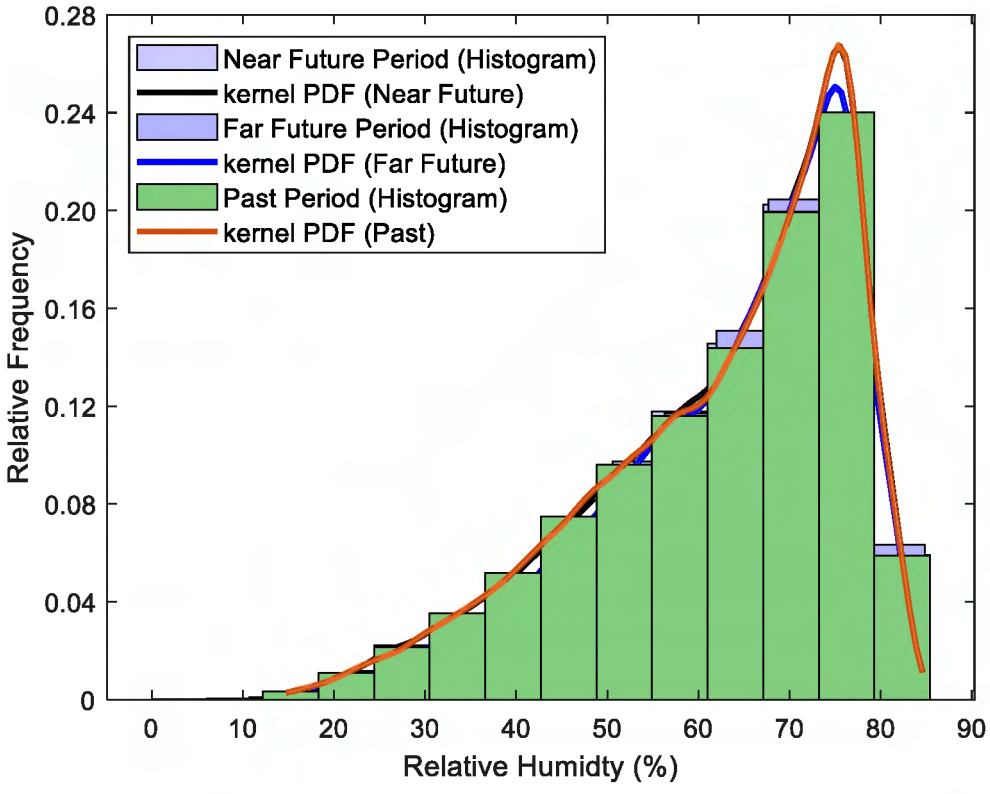

C83: Relative Humidity box plot for every five years from 1990 to 2080 (Realization15)

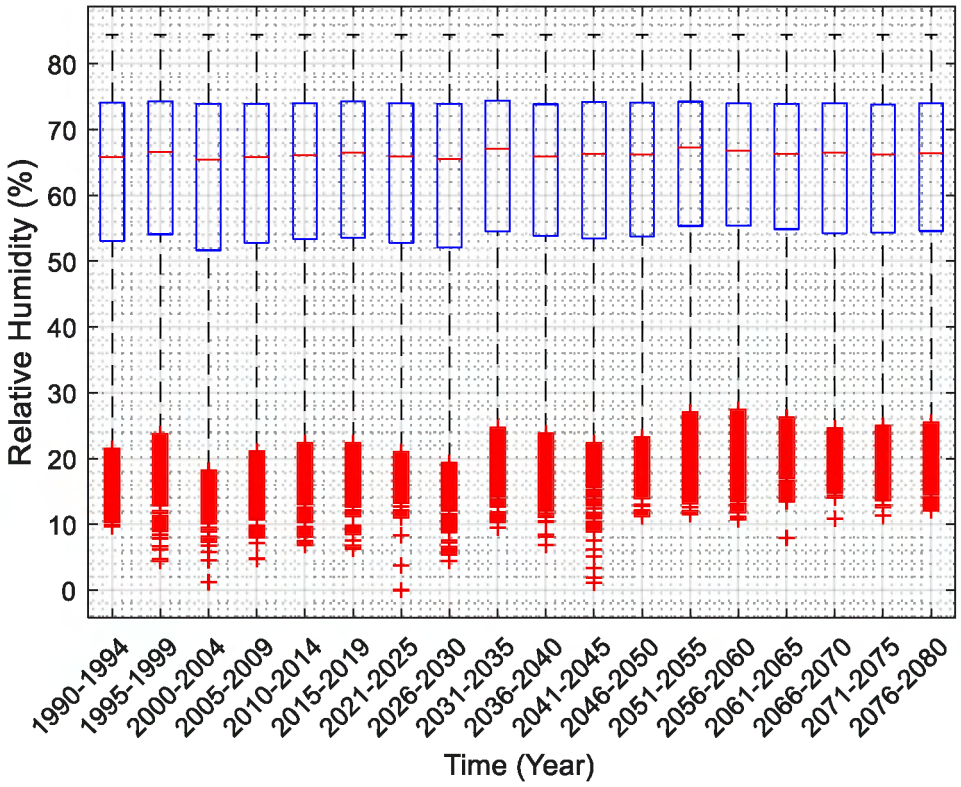

C84: Relative humidity Histogram with Kernel PDF plot (Average)

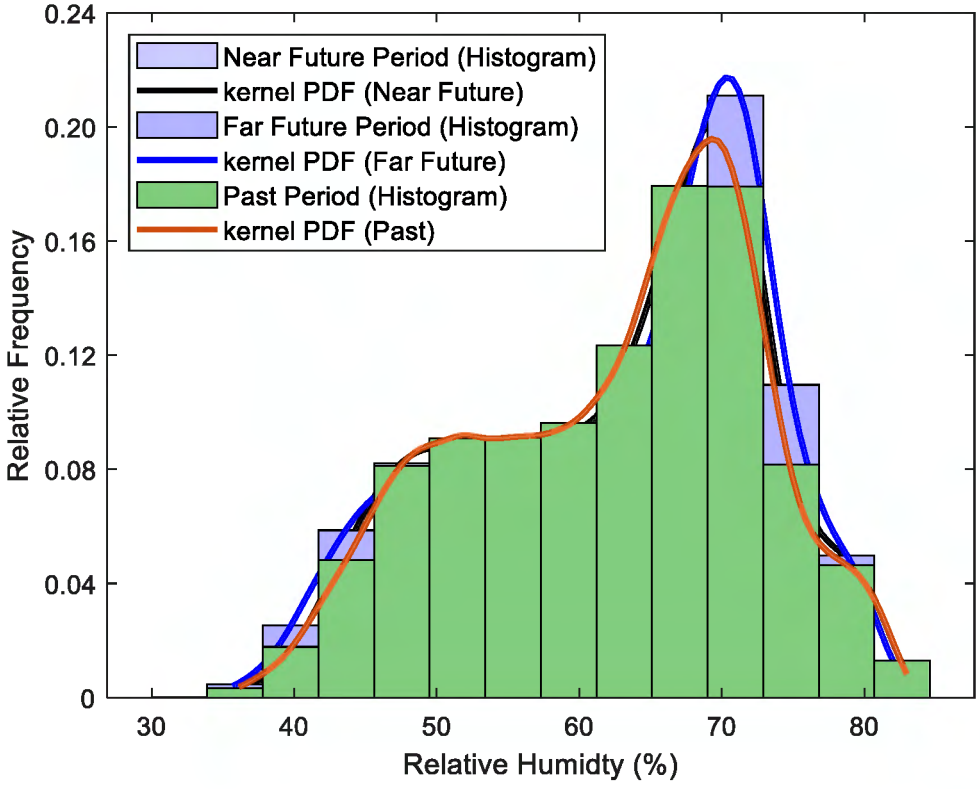

C85: Relative Humidity box plot for every five years from 1990 to 2080 (Average)

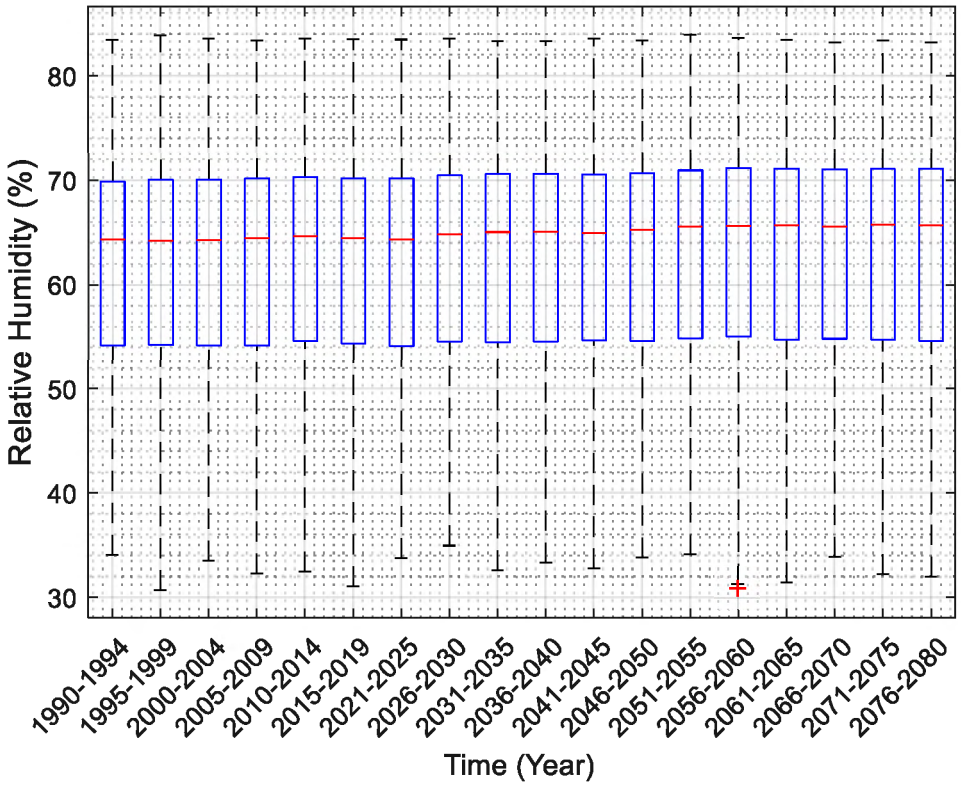

C86: Relative Humidity box plot yearly from 2021 to 2050 (Realization 1)

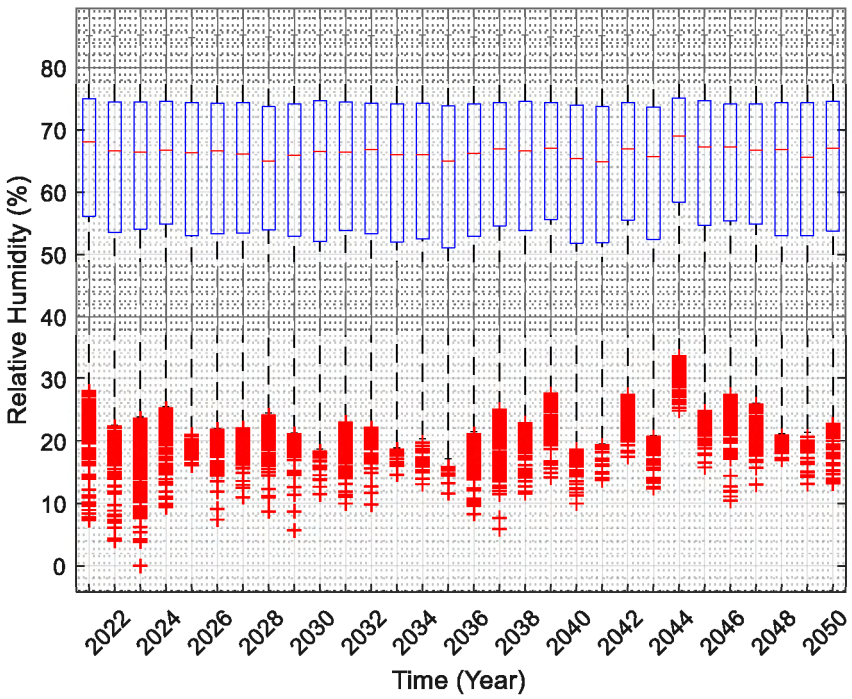

C87: Relative Humidity box plot yearly from 2021 to 2050 (Realization 2)

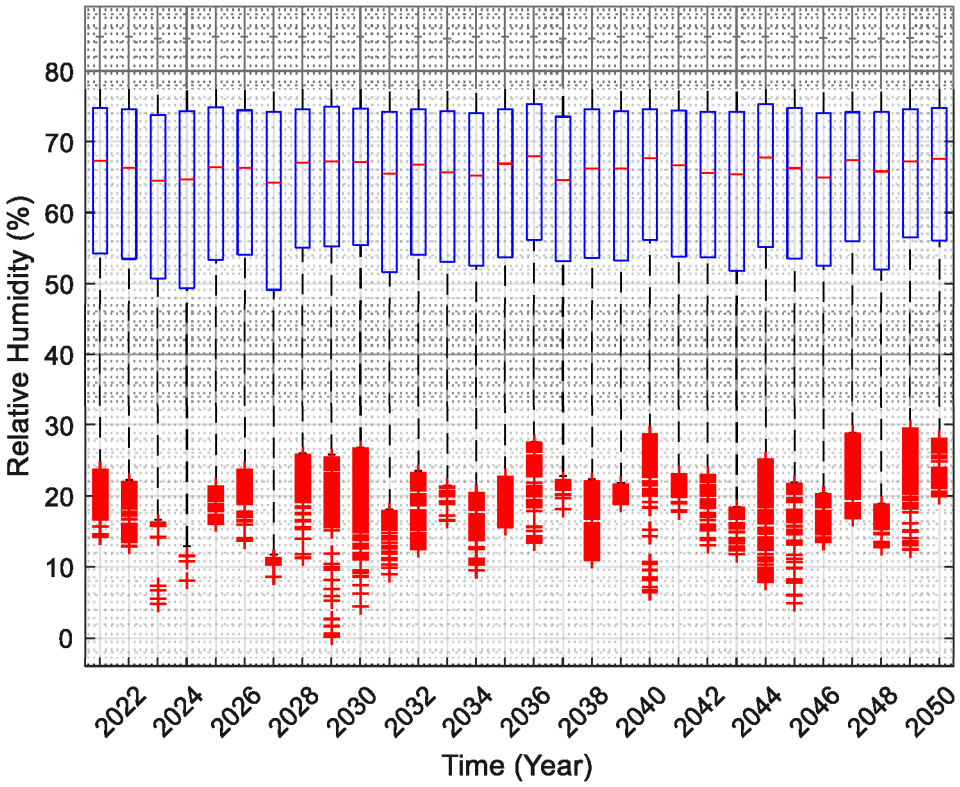

C88: Relative Humidity box plot yearly from 2021 to 2050 (Realization 3)

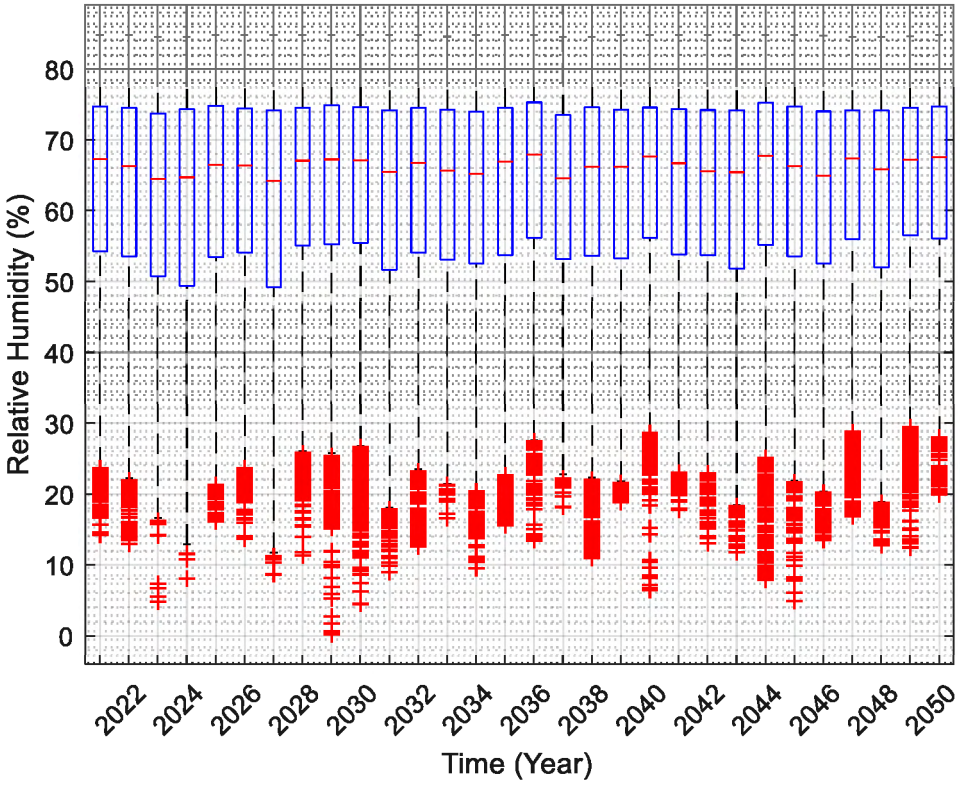

C89: Relative Humidity box plot yearly from 2021 to 2050 (Realization 4)

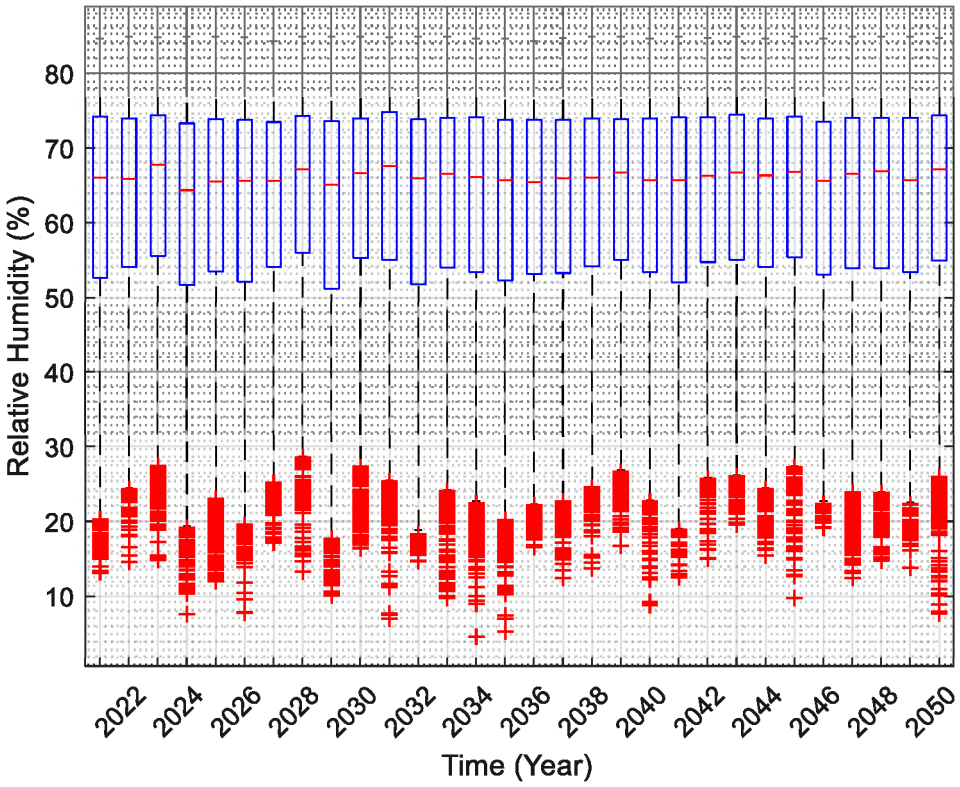

C90: Relative Humidity box plot yearly from 2021 to 2050 (Realization 5)

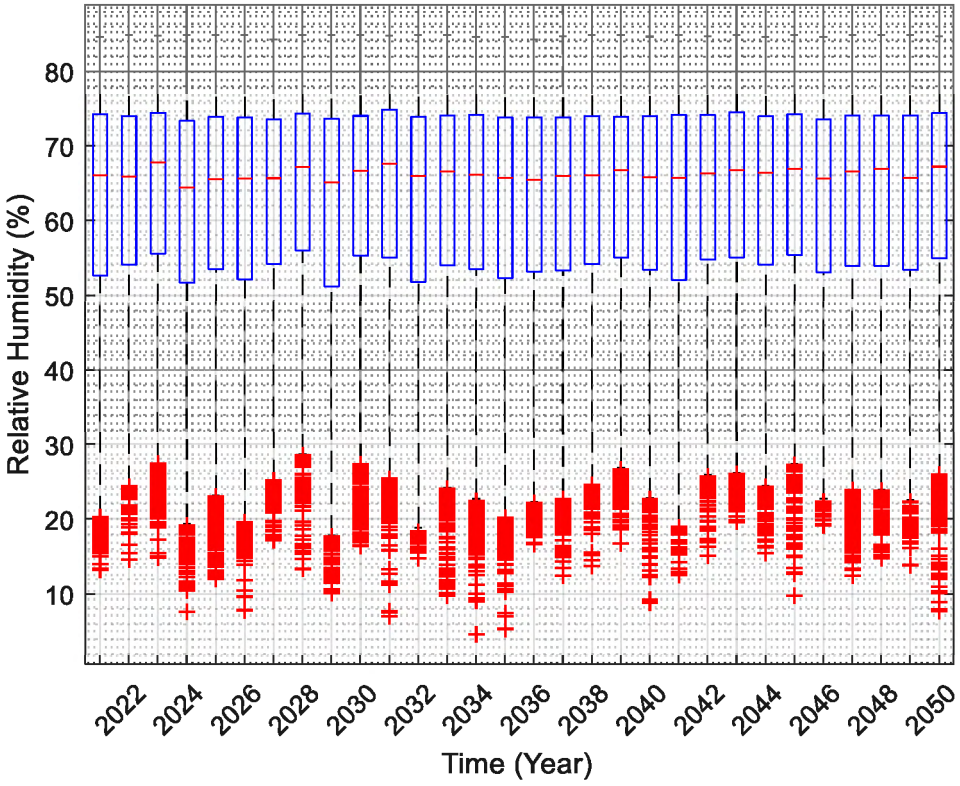

C91: Relative Humidity box plot yearly from 2021 to 2050 (Realization 6)

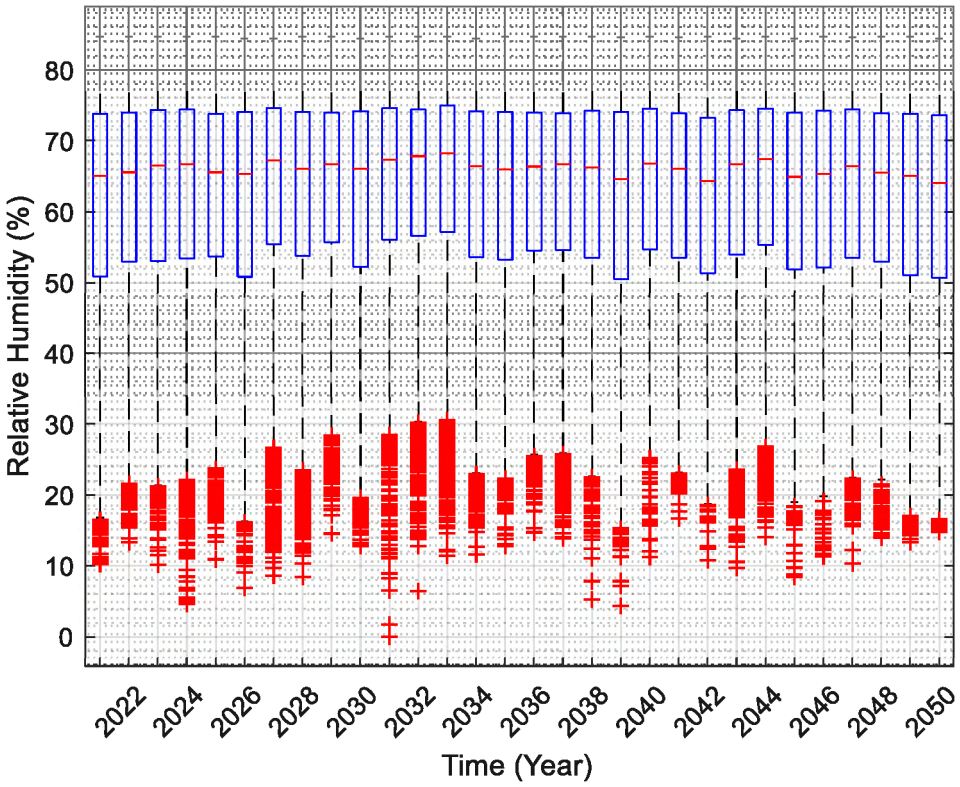

C92: Relative Humidity box plot yearly from 2021 to 2050 (Realization 7)

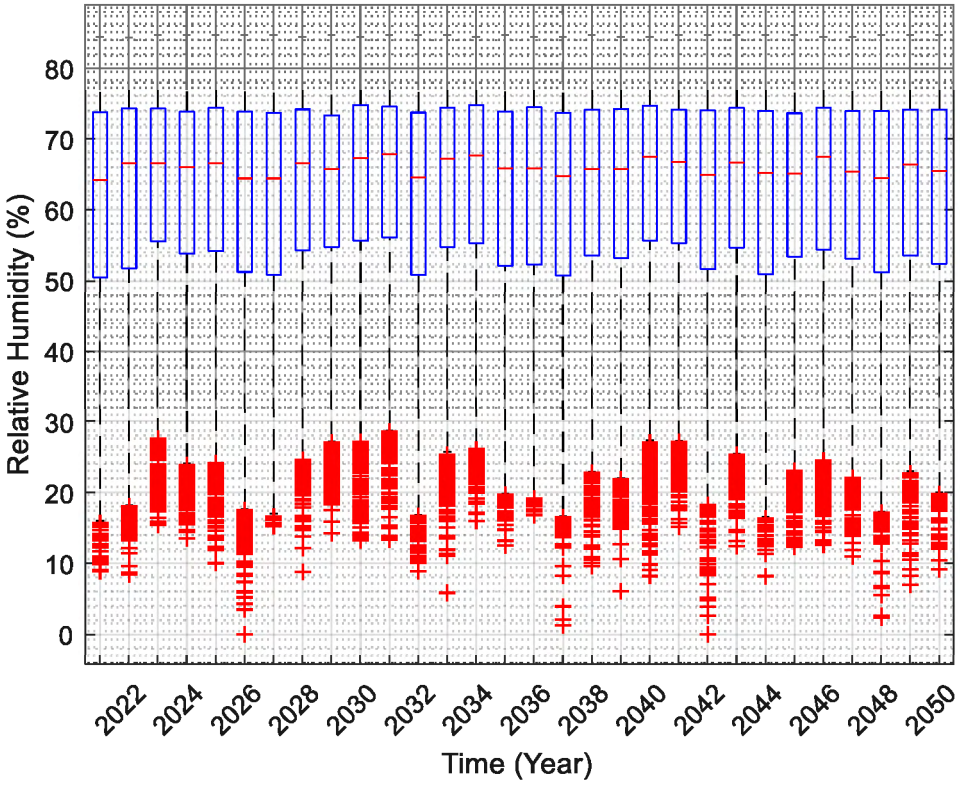

C93: Relative Humidity box plot yearly from 2021 to 2050 (Realization 8)

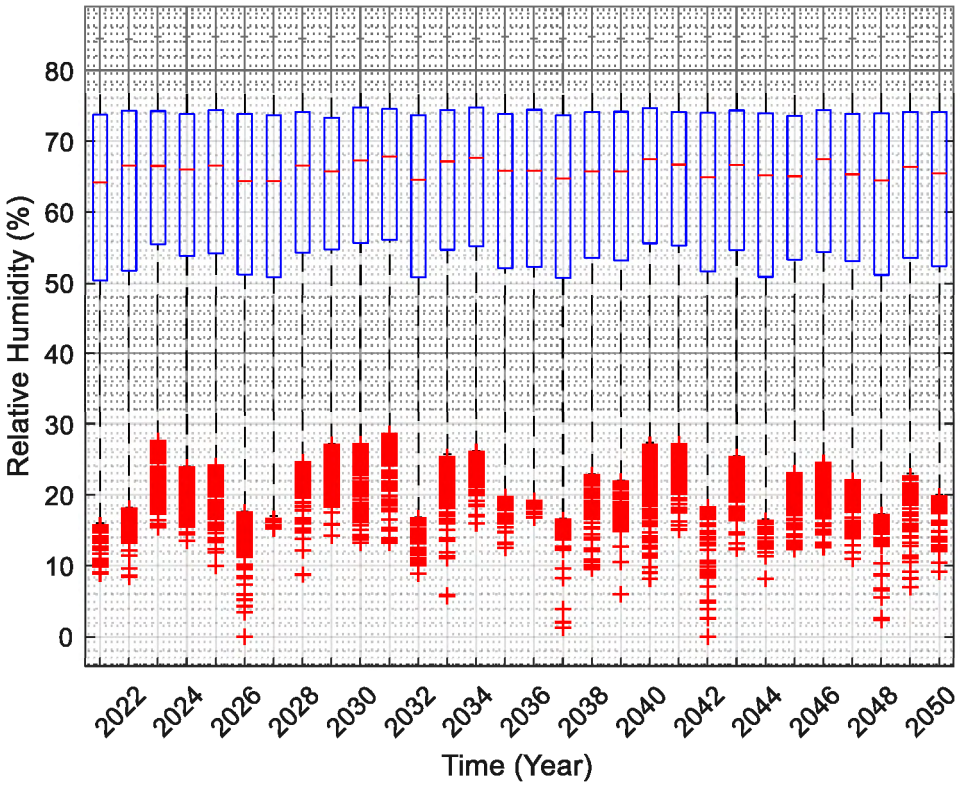

C94: Relative Humidity box plot yearly from 2021 to 2050 (Realization 9)

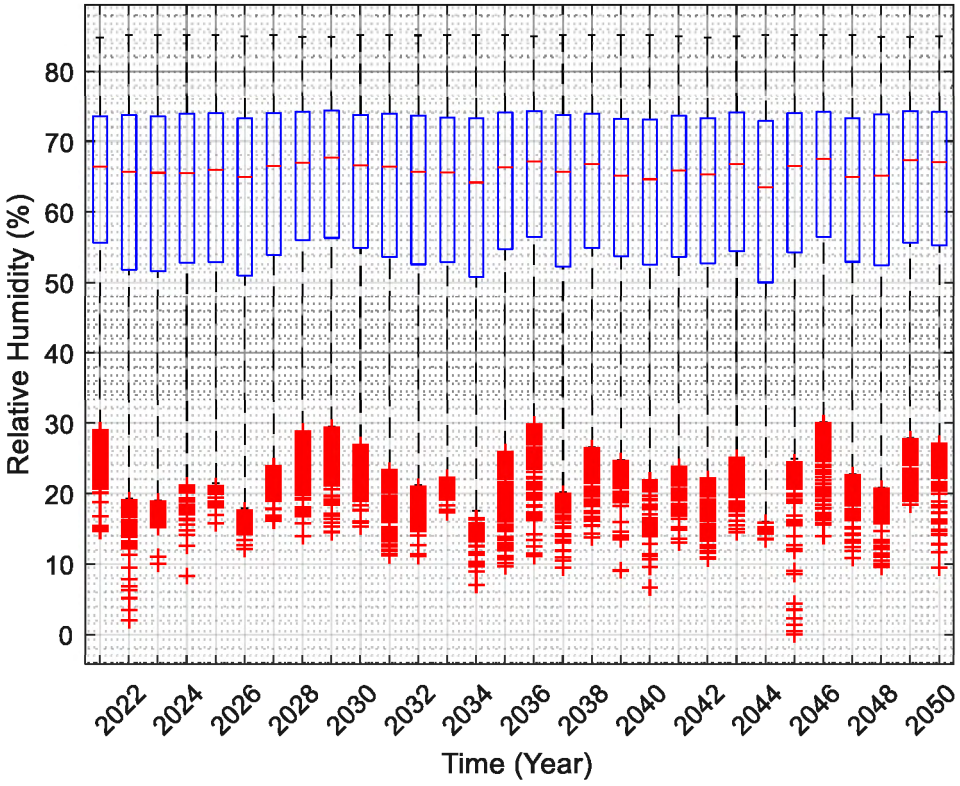

C95: Relative Humidity box plot yearly from 2021 to 2050 (Realization 10)

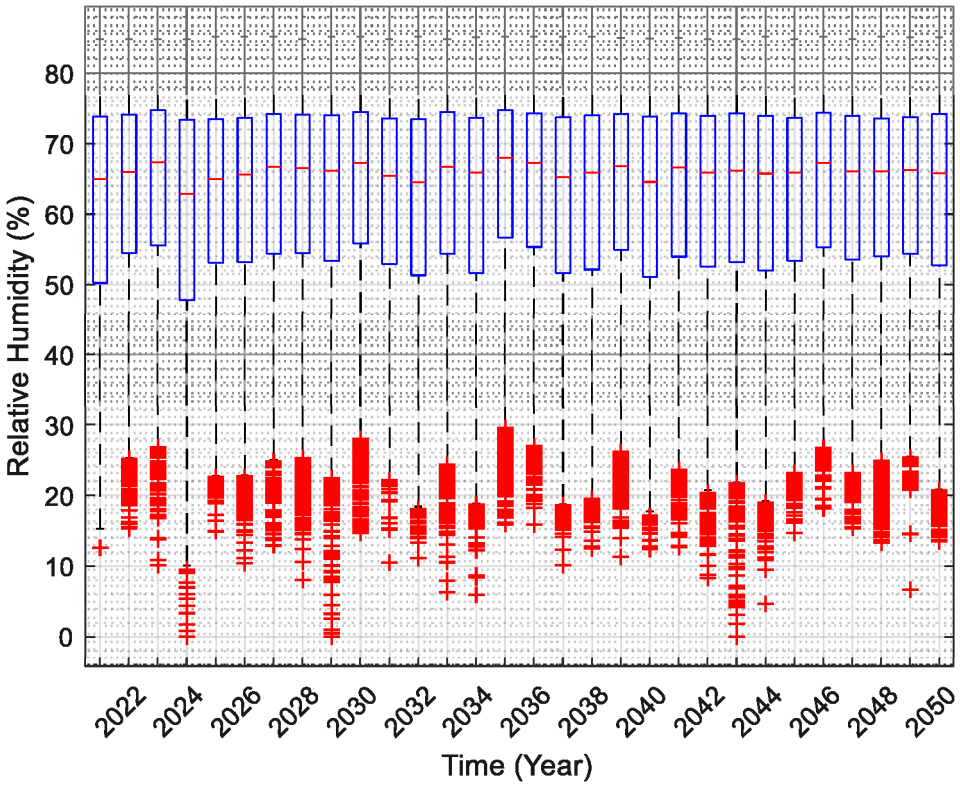

C96: Relative Humidity box plot yearly from 2021 to 2050 (Realization 11)

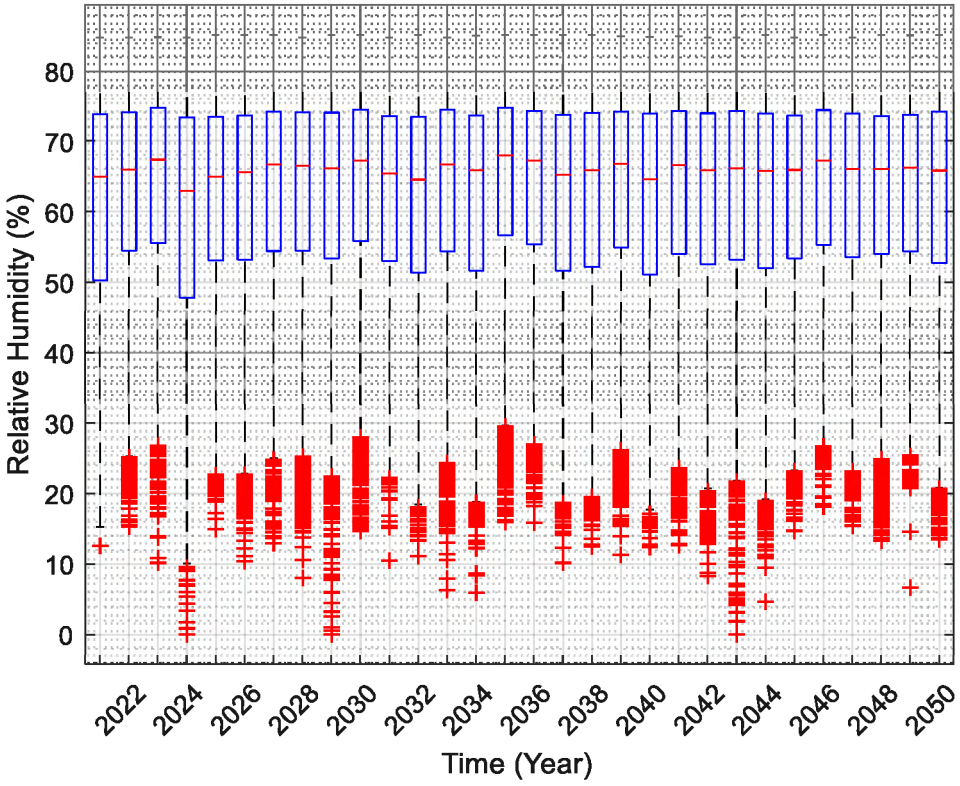

C97: Relative Humidity box plot yearly from 2021 to 2050 (Realization 12)

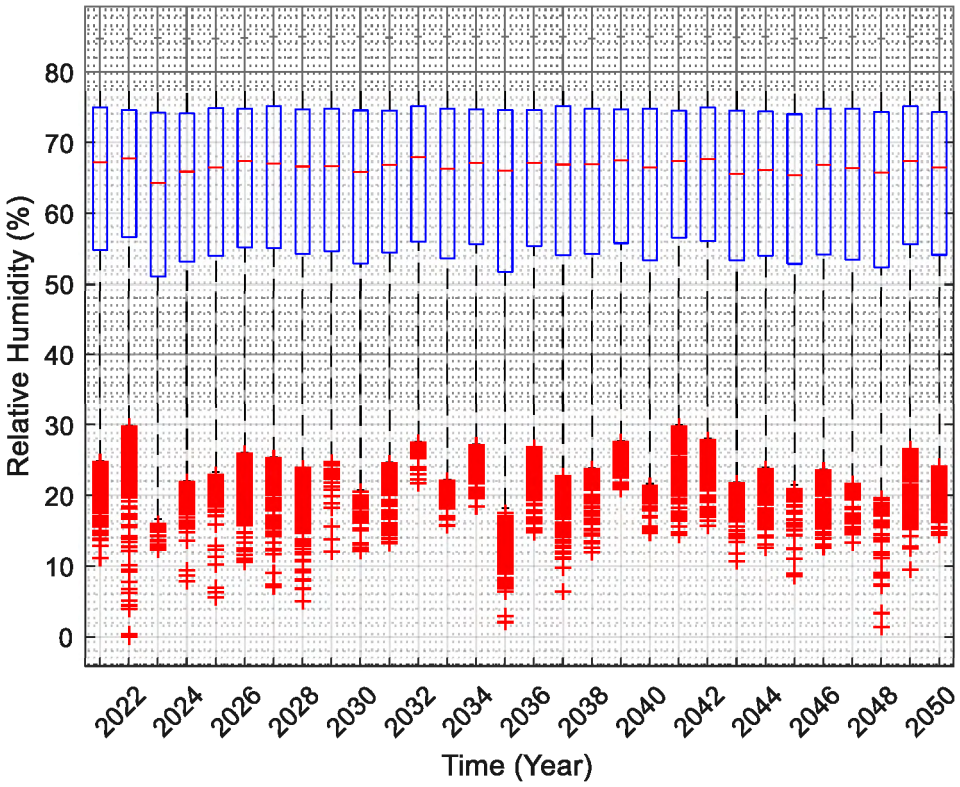

C98: Relative Humidity box plot yearly from 2021 to 2050 (Realization 13)

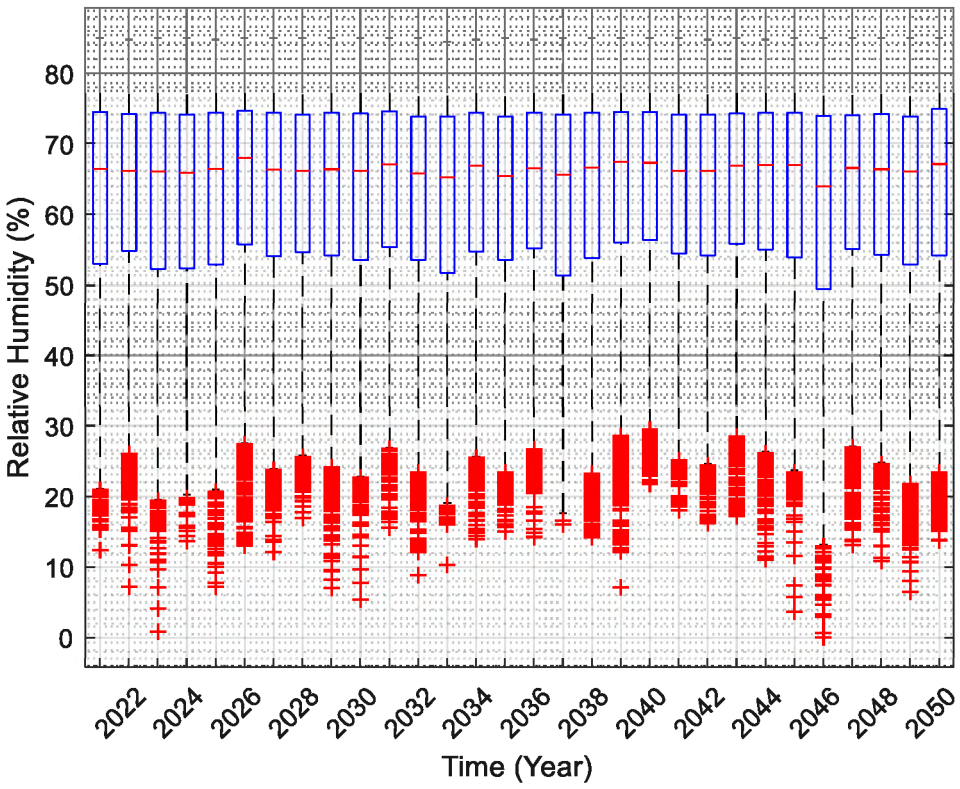

C99: Relative Humidity box plot yearly from 2021 to 2050 (Realization 14)

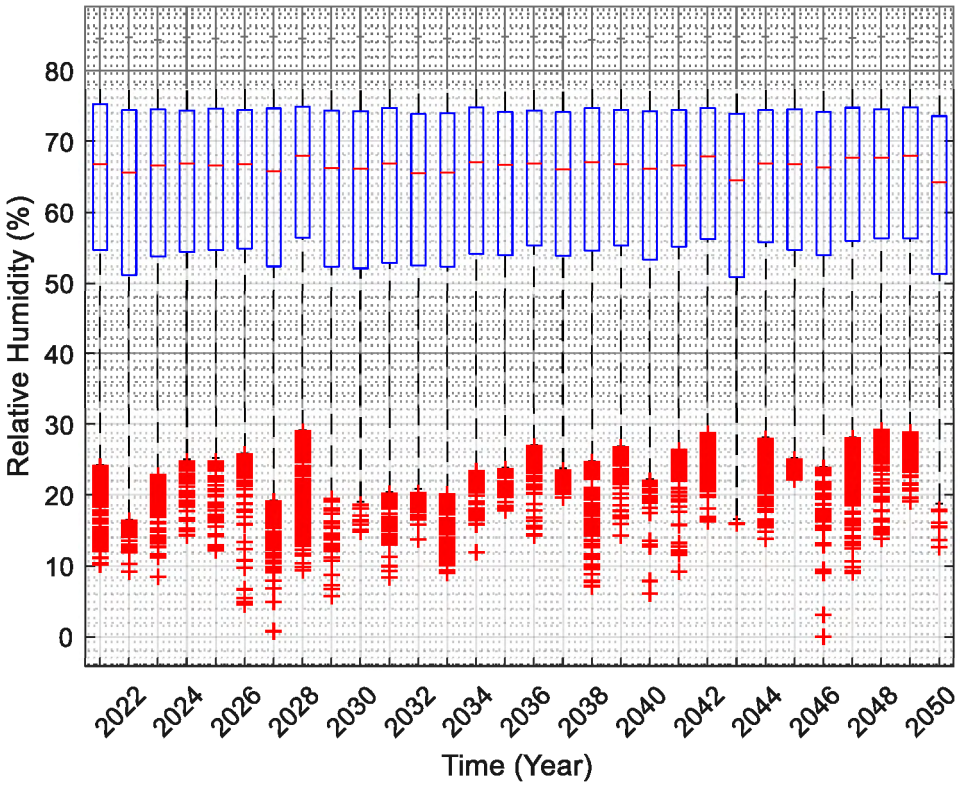

C100: Relative Humidity box plot yearly from 2021 to 2050 (Realization 15)

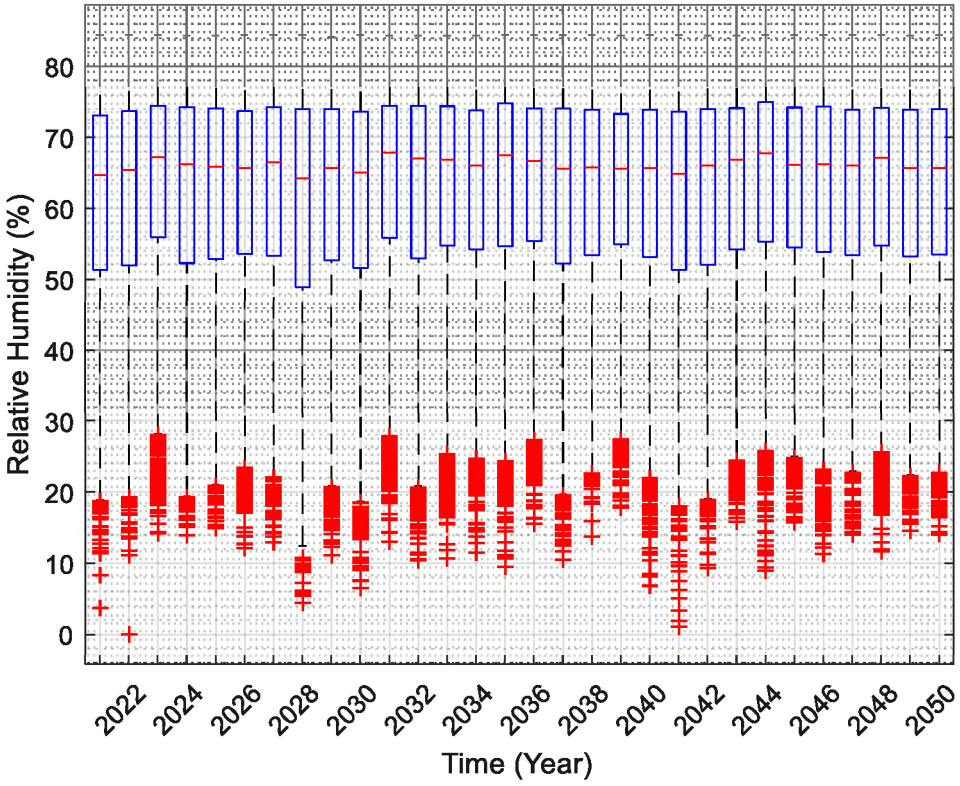

11 Appendix D

Different hygrothermal models may differ from another model based on the considered nature of physics or the number of assumptions made. One of the primary sources of discrepancies arises from boundary conditions. Defo M. (2018) has briefly discussed about hygrothermal models and boundary conditions as presented below,

Moisture Boundary Conditions on Interior surface:

$$q_{m,i} = \beta_i\left(P_{v,i} - P_{vsurf,i}\right) + \rho_v\overrightarrow{V_a} \quad (1)$$

Where,

$q_{m,i}$: Moisture flux normal to interior surface (kg/m^{2}s)

$P_{vsurf,i}$: Water vapor pressure at the indoor surface (Pa)

$P_{v,i}$: Water vapor pressure of indoor air (Pa)

β_i: Indoor film coefficient for convection (kg/m^{2}sPa or s/m)

ρ_v: Density of water vapor (kg/m^3)

V_a: Air velocity (m/s)

Moisture Boundary Conditions on Exterior surface:

$$q_{m,e} = \beta_e\left(P_{v,o} - P_{vsurf,o}\right) + \rho_v\overrightarrow{V_a} + WDR \quad (2)$$

Where:

$q_{m,e}$: Moisture flux normal to the exterior surface (kg/m^{2}s)

β_e: Outdoor surface film coefficient (kg/m^{2}sPa or s/m)

$P_{v,o}$: Vapour pressure of outdoor air (Pa)

$P_{vsurf,i}$: Vapour pressure at the exterior surface (Pa)

WDR: Wind-driven rain (mm/h or kg/m^2.s)

Heat Boundary Conditions on Outdoor Surface:

$$q_{h,e} = h_o\left(T_{e,o} - T_{s,e}\right) - \varepsilon\sigma\left({T_{s,e}}^4 - {T_{sky}}^4\right) + L_v\beta_e\left(p_{vsurf,e} - p_{v,o}\right) + L_v\rho_v V_a + q_a \quad (3)$$

$$h_o = h_c + h_r \quad (4)$$

Where

$q_{h,e}$: Total heat flow across the exterior surface (W/m^2)

h_o: Sum of convective and radiative heat transfer at the exterior surface (W/m^{2}K)

h_c: Convection heat transfer coefficient (W/m^{2}K)

h_r: Radiation heat transfer coefficient (W/m^{2}K)

$T_{e,o}$: Equivalent exterior temperature or sol-air temperature (°C)

$T_{s,e}$: Exterior wall surface temperature (°C or K)

T_{sky}: Sky temperature (K)

q_a: Sensible heat of dry air flowing into or out of the wall due to bulk air movement (W/m2)

→ Ignoring the sensible heat due to wind-driven rain the advection term (q_a) computed as (Defo M. (2018)):

$$q_a = \rho_a c_a[V_f T_{a,f} - \max\left(V_f, 0\right) x\, \Delta T_o] \quad (5)$$

In which: $\begin{cases} T_{a,f} = T_{s,e}\ if\ V_f < 0 \\ T_{a,f} = T_{e,o}\ if\ V_f > 0 \end{cases}$ *and* $\begin{cases} \Delta T_o = T_e - T_a \\ \Delta T_o = 0\ otherwise \end{cases}$

Where:

V_f: Air velocity at the air-solid interface (m/s)

T_f: Air temperature at the interface (°C)

$T_{a,o}$: Outside air temperature (°C)

Convection heat transfer coefficient

$$h_c = 5.82 + \frac{3.96V}{3.6} \; if \; V \leq 18 \; km/h \tag{6}$$

$$h_c = 7.68\left(\frac{V}{3.6}\right)^{0.75} \; if \; V > 18 \; km/h \tag{7}$$

Radiation heat transfer coefficient

The radiation heat transfer coefficient is given by:

$$h_r = \varepsilon\sigma(\bar{T} + 273.15)^3 \tag{8}$$

Where

ε: Emissivity of the wall

σ: Ste fan-Boltzmann constant

$\bar{T}$ (°C) is the average temperature between the surface temperature of the wall and the ambient air temperature:

$$\bar{T} = \frac{1}{2}\, x \left(\frac{h_c T_a + \frac{\lambda}{\Delta x_{1/2}} T + L_v(Q_{v1} - Q_{v2})}{h_c + \frac{\lambda}{\Delta x_{1/2}}} + T_a \right) \tag{9}$$

Where:

λ: Thermal conductivity (W/m.K)

T: Temperature of the internal node near the surface (°C)

T_a: Outdoor air temperature (°C)

L_v: Latent heat of evaporation of water (J/kg)

Q_{v1}: Vapour flux arriving to the surface (kg/m^{2}s)

Q_{v2}: Vapour flux leaving the surface and entering the wall (kg/m^{2}s)

Sky Temperature

$$T_{sky} = (F_1 T_a^4 + F_2 A^4)^{0.25} \quad (10)$$

$$F_1 = 1 - F_2 \quad (1)$$

$$F_2 = \left[cos\left(\frac{0.5\beta\pi}{180}\right)\right]^2 \quad (12)$$

$$A = (1 - 0.125c_I)x\ (0.0552T_a^{1.5}) + 0.125c_I T_a \quad (13)$$

Where:

Ta: Outdoor air temperature (K)

c_I: Cloudiness index

β: inclination (°)

Sol-air temperature

$$T_{e,o} = T_{a,o} + \frac{\alpha I_T}{h_o} \quad (14)$$

Where:

α: External wall surface absorption coefficient

I_T: Total irradiance (W/m^2)

External wall surface temperature

$$T_{s,e} = \frac{a_i T_e + a_{i+1} T_{i+1} + L_v\left(Q_{v,i} - Q_{v,i+1}\right) - \rho_a c_a V_f \Delta T_o}{a_i + a_{i+1}} \quad (15)$$

With: $a_i = h_e + \rho_a c_a \max(V_f, 0)$

$$a_{i+1} = \frac{\lambda_{i+1}(u_{i+1}, T_{i+1})}{\Delta x_{1/2}} - \rho_a c_a \min(V_f, 0) \quad (16)$$

$$\begin{cases} \Delta T_o = T_e - T_a \; if \; V_f > 0 \\ \Delta T_o = 0 \; otherwise \end{cases}$$

Where:

T_{i+1}: Temperature at node i+1 (°C)

$Q_{v,i}$: Vapour flux arriving at the surface (kg/m^2.s)

$Q_{v,i+1}$: Vapour flux leaving the surface and entering the wall (kg/m^2.s)

T_a: Outdoor air temperature (°C)

T_e: Sol-air temperature (°C)

$\lambda_{i+1}(u_{i+1}, T_{i+1})$: Thermal Conductivity (W/m.k) at node i+1

Total solar radiation is given by;

$$I_T = I_{d\beta} + I_{b\beta} + I_r \quad (17)$$

Where;

$I_{b\beta}$: Beam radiation

$I_{d\beta}$: Diffuse radiation

I_r: Reflected radiation

Models to calculate hourly diffused solar radiation on inclined surface are discussed by Maleki et al. (2017), as shown below. Diffuse radiation models classified as isotropic and anisotropic based on how the sky divided into regions with normal and elevated diffuse radiation intensities. For instance, the isotropic model assumes the diffuse radiation distributed uniformly throughout the sky, whereas the anisotropic model represents non-uniform distribution.

Isotropic Models

Badescu's Model:

$$I_{d\beta} = \left(\frac{3 + \cos(2\beta)}{4}\right) x\ I_d \quad (18)$$

Koronakis' Model

$$I_{d\beta} = \frac{1}{3}\left(\frac{1}{2 + cos\beta}\right) x\ I_d \quad (19)$$

Liu and Jordan's Model

$$I_{d\beta} = \left(\frac{1 + \cos\beta}{2}\right) x\ I_d \quad (2)$$

Tian's Model

$$I_{d\beta} = \left(1 - \frac{\beta}{180}\right) x\, I_d \tag{21}$$

Anisotropic Models

Bugler's Model

$$I_{d\beta} = \left(\frac{1 + cos\beta}{2}(I_d - 0.05\frac{I_{b\beta}}{cos\theta_z})\right) + 0.05 I_{b\beta} cos\theta \tag{22}$$

Temps and Coulson's Model

$$I_{d\beta} = \frac{1}{2} I_d (1 + cos\beta) P_1 P_2 \tag{23}$$

Where P_1 and P_2 represent vicinity of the sun's disc and sky radiation, which are given by;

$$P_1 = 1 + cos^2\theta(sin^3\theta_z) \tag{24}$$

$$P_2 = 1 + sin^3(\frac{\beta}{2}) \tag{25}$$

Steven and Unsworth's Model

$$I_{d\beta} = I_d \left[\left(0.51\left(\frac{cos\theta}{cos\theta_z}\right)\right) + \left(\frac{1 + cos\beta}{2}\right) - \frac{1.74}{1.26\pi}\left\{\sin\beta - \beta\frac{\pi}{180}cos\beta - \pi sin^2\frac{\beta}{2}\right\}\right] \tag{26}$$

Where, θ is incidence angle, $\theta_z$zenith angle, β tilt angle

The equations given to calculate direct beam, diffused and reflected radiation on inclined surface by Defo M. (2018) are;

$$I_d = \frac{I_{DN}}{\sin\alpha}\cos\theta \tag{27}$$

$$I_{dif} = D_{HI} x \left[\frac{1 + \cos(\frac{\beta\pi}{180})}{2}\right] \tag{28}$$

$$I_r = R_I \left[\frac{1 - \cos\left(\frac{\beta\pi}{180}\right)}{2} \right] \quad (29)$$

Where,

I_d: direct solar radiation

I_{DN}: direct normal irradiance from weather data (W/m^2)

D_{HI}: diffuse irradiance on horizontal surface

α: solar altitude (°)

$R_{I:}$ is the reflected irradiance from weather data

Heat boundary condition on interior surface:

At the indoor wall surface, heat flow includes convection, radiation, advection, and latent heat (Defo M. (2018)):

$$q_{h,in} = h_i\left(T_{e,in} - T_{s,in}\right) + \varepsilon\sigma\left(T_{s,in}^4 - T_{sky}^4\right) + L_v\beta_i\left(p_{vsurf,in} - p_{v,in}\right) + L_v p_v V_a \quad (30)$$

$$h_i = h_c + h_r \quad (31)$$

Where:

$q_{h,in}$: Total heat flow across the exterior surface (W/m^2)

h_i: Sum of convective and radiative heat transfer at the interior surface (W/m^2.k)

h_c: Indoor convection heat transfer coefficient (W/m^2.K)

h_r: Indoor radiation heat transfer coefficient (W/ m^2.K)

$T_{e,in}$: Equivalent indoor temperature or sol-air temperature (°C)

$T_{s,in}$: Indoor wall surface temperature (°C or K)

T_{sky}: Sky temperature (K)

q_a: Sensitive heat of dry air flowing into or out of the indoor wall surface due to bulk air movement (W/m^2)

Where advection term gives as:

$$q_a = \rho_a c_a [V_f T_x - \max(V_f, 0)\, x\, \Delta T_{in}] \quad (32)$$

In which: $\begin{cases} T_x = T_{s,in} if\ V_f < 0 \\ T_x = T_{e,in}\ if\ V_f > 0 \end{cases} and \begin{cases} \Delta T_{in} = -(T_{e,in} - T_{a,in}) if\ V_f < 0 \\ \Delta T_{in} = 0\ otherwise \end{cases}$

Where:

V_f: Air velocity at the solid/air interface (m/s)

T_x: Air temperature at the interface (°C)

$T_{a,in}$: Indoor air temperature (°C)

Indoor heat transfer coefficients

The default value for the convective heat transfer coefficient is set to 8 for indoor surface, whereas the radiation heat transfer coefficient is given by (Defo M. (2018));

$$h_r = \varepsilon_{in} \sigma (\bar{T}_{in} + 273.15)^3 \quad (33)$$

Where:

ε_{in}: Emissivity of the indoor wall surface

$\bar{T}_{in}$: is the average between surface temperature and the indoor air temperature

$$\bar{T}_{in} = \frac{1}{2} x \left(\frac{h_c T_{a,in} + \frac{\lambda_i}{\Delta x_{1/2}} T_i + L_v (Q_{v1} - Q_{v2})}{h_c + \frac{\lambda_i}{\Delta x_{1/2}}} + T_{a,in} \right) \quad (34)$$

Where:

λ_i: Thermal conductivity (W/m.K) of node near the surface

T_i: Temperature of the internal node near the surface (°C)

$T_{a,in}$: Indoor air temperature (°C)

L_v: Latent heat of evaporation of water (J/kg)

Q_{v1}: Vapour flux arriving to the surface (kg/m^{2}s)

Q_{v2}: Vapour flux leaving the surface (kg/m^{2}s)

Indoor equivalent temperature

$$T_{e,in} = T_{a,in} + \frac{\alpha_{in} I_{T,in}}{h_i} \quad (35)$$

$I_{T,in}$: Accounts for the short-wave that heat the inside wall and long-wave exchange with surroundings.

Indoor surface temperature

$$T_{s,in} = \frac{\alpha_i T_i + \alpha_{i+1} T_{e,in} + L_v (Q_{v,i} - Q_{v,i+1}) - \rho_a c_a V_f \Delta T_{in}}{a_i - a_{i+1}} \quad (36)$$

With:

$$a_i = \frac{\lambda_i(u_i, T_i)}{\Delta x_{1/2}} + \rho_a c_a max(V_f, 0) \quad (37)$$

Where:

T_i: Temperature at node i near the surface (°C)

$Q_{v,i}$: Vapour flux from node i to the surface (kg/m^{2}s)

$Q_{v,i+1}$: Vapour flux from or to the environment (kg/m^{2}s)

$T_{e,in}$: Effective or equivalent indoor temperature (°C)

h_i: Equivalent heat transfer coefficient (hc + hr) (W/m2K)

$\lambda_i(u_i, T_i)$: Thermal conductivity (W/m K) using u and T at node i

12 Reference

Abiodun, B., & Adedoyin, A. “A Modelling Perspective of Future Climate Change” in Letcher, T. (2nd) *Climate Change Observed Impacts on Planet Earth*. Elsevier, 2016, pp. 355-371

Andric, I., Gomesa, N., Pina, A., Ferrao, P., Fournier, J., Lacarriere, B., LeCorre, O. “Modelling the long-term effect of climate change on building heat demand: A case study on a district level” Energy and Buildings 126 (2016) 77-93

ANSI/ASHRAE Standard 160-2016. “Criteria for Moisture-Control Design Analysis in Buildings.” ISSN 1041-2336

ASHRAE (2013) “Heat, Air, and Moisture control in building assemblies-material properties” ASHRAE Handbook—Fundamentals (SI), Chapter 26

Ayala, D., & Aktas, Y. “Moisture dynamics in the masonry fabric of historic buildings subjected to wind-driven rain and flooding” Building and Environment 104 (2016) 208-220

Belcher, S., Hacker, J., & Powell, D. “Constructing design weather data for future climates” Building Services Engineering Research and Technology 26 (2005) 49-61.

Beaulieu, P. et. al. “Hygrothermal Response of Exterior Wall Systems to Climate Loading: Methodology and Interpretation of Results for Stucco, EIFS, Masonry, and Siding- Clad Wood-Frame Walls” National Research Council Canada, Ottawa, 2002

Cellura, M., Guarino, F., Longo, S., & Tumminia, G. “Climate change and the building sector: Modelling and energy implications to an office building in southern Europe” Energy for Sustainable Development 45 (2018) 46–65

Chan A. “Developing future hourly weather files for studying the impact of climate change on building energy performance in Hong Kong” Energy and Buildings 43 (2011) 2860-2868

Cox, R., Drews, M., Rode, C., & Nielsen, S. “Simple future weather files for estimating heating and cooling demand” Building and Environment 83 (2015) 104-114

Crawford, J., Venkataraman, K., & Booth, J. “Developing climate model ensembles: A comparative case study” Journal of Hydrology 568 (2019) 160-173

Defo, M. “Review of the implementation of a hygrothermal simulation model.”
National Research Council Canada, 2018

Derome, D., Kubilay, A., Defraeye, T., Blocken, B., & Carmeliet, J. “Ten questions concerning modeling of wind-driven rain in the built environment” Building and Environment 114 (2017) 495-506

De Wilde, P., and Coley, D. “The implications of a changing climate for buildings” Building and Environment 55 (2012) 1-7

Djebbar, R., Kumaran, K., Reenen, D., & Tariku, F. “ Hygrothermal Modelling of Building Envelope Retrofit Measures in Multiunit Residential and Commercial Buildings” National Research Council: Ottawa, ON, Canada, 2002; p. 187.

Environment and Climate Change Canada “Canada’s Changing Climate Report” CCCR2019

Flato, G., Marotzke, J., Abiodun, B., Braconnot, P., & Chou, C., Collins, W., Cox, P., Driouech, F., Emori, S., Eyring, V., Forest, C., Gleckler, P., Guilyardi, E., Jakob, C., Kattsov, V., Reason, C., Rummukaines, M. Evaluation of climate models. Chapter 9 in climate change 2013: the physical science basis. Contribution of Working Group I to the Fifth Assessment Report of the Intergovernmental Panel on Climate Change

Finch, G., & Straube, J. “Ventilated Wall Claddings: Review, Field Performance, and Hygrothermal Modelling” 2007, ASHRAE

Gaur, A., Lacasse, M., & Armstrong, M. “Climate Data to Undertake Hygrothermal and Whole Building Simulations Under Projected Climate Change Influences for 11 Canadian Cities” National Research Council Canada, 2019.

Ge, H., & Ye, Y. “Investigation of Ventilation Drying of Rain screen Walls in the Coastal Climate of British Columbia” 2007 ASHRAE

Guan, L. “Preparation of future weather data to study the impact of climate change on buildings” Building and Environment 44 (2009) 793-800

Guarino, F., Croce, D., Tinnirello, I., & Cellura, M. “Data fusion analysis applied to different climate change models: An application to the energy consumptions of a building office” Energy & Buildings 196 (2019) 240-254

Hansena T., Bjarløv, S., & Peuhkuri, R. “The effects of wind-driven rain on the hygrothermal conditions Behind wooden beam ends and at the interfaces between internal insulation and existing solid masonry” Energy and Buildings 196 (2019) 255-268

Hwang, R., Shih, W., Lin, T., & Huang, K. “Simplification and adjustment of the energy consumption indices of office building envelopes in response to climate change” Applied Energy 230 (2018) 460–470

Invidiata, A., & Ghisi, E. “Impact of climate change on heating and cooling energy demand in houses in Brazil” Energy and Buildings 130 (2016) 20-32

IPCC “Climate Change 2014: Synthesis report. Contribution of Working Groups I, II and III to the Fifth Assessment Report of the Intergovernmental Panel on Climate Change” IPCC, Geneva, Switzerland, 2014, 151pp

IPCC “Climate change 2007: Impacts, Adaptation, and Vulnerability. Contribution of Working Group II to the Fourth Assessment Report of the Intergovernmental Panel on Climate Change“ IPCC, Cambridge University Press, Cambridge, UK, 2007, 976pp

IPCC “Climate change 2007: Synthesis Report. Contribution of Working Groups I, II and III to the Fourth Assessment Report of the Intergovernmental Panel on Climate Change” IPCC, Geneva, Switzerland, 2007, 104pp

Jiang, A., Liu, X., Czarnecki, E., & Zhang, C. “Hourly weather data projection due to climate change for impact assessment on building and infrastructure” Sustainable Cities and Society 50 (2019) 101-688

Kikumoto, H., Ookaa, R., Arima, Y., & Yamanaka, T. “Study on the future weather data considering the global and local climate change for building energy simulation” Sustainable Cities and Society 14 (2014) 404-413

Kolio, A., Pakkala, T., Lahdensivu, J., & Kiviste, M. “Durability demands related to carbonation induced corrosion for Finnish concrete buildings in changing climate” Engineering Structure 62-63 (2014) 42-52.

Kubilay, A., Derome, D., & Carmeliet, J. “Analysis of time-resolved wind-driven rain on an array of low-rise cubic buildings using large eddy simulation and an Eulerian multiphase model” Building and Environment 114 (2017) 68-81

Kumaran, M., Lackey, J., Normandin, N., Tariku, F., Van Reenen, D. “A Thermal and Moisture Transport Property Database for Common Building and Insulating Materials” Final Report from ASHRAE Research Project 1018-RP, 2002

Künzel, H. “Simultaneous Heat and Moisture Transport in Building Components. One and two-dimensional calculation using simple parameters” Fraunhofer Institute of Building Physics, 1995

Künzel, H., Karagiozis, A., and Kehrer, M. “Assessing the benefits of cavity ventilation by hygrothermal simulation” Proceedings Building Physics Symposium, Leuven 2008, pp. 17-20

Larsen, S., Filippin, C., & Barea, G. “Impact of climate change on energy use and bioclimatic design of residential buildings in the 21st century in Argentina” Energy and Buildings 184 (2019) 216-229

Liso, K., Kvande, T., & Time, B. “Climate Adaptation Framework for Moisture-resilient Building in Norway” Energy Procedia 132 (2017) 628-633

Maleki, S., Hizam, H., and Gomes, C. “Estimation of Hourly, Daily and Monthly Global Solar Radiation on Inclined Surfaces: Models Re-Visited” Energies 134 (2017) 10

Moss, R., et al. “The next generation of scenarios for climate change research and assessment” Nature 463 (7282) (2010) 747-756

Mukhopadhyaya, P., Kumaran, M., Lackey, J., Normandin, N., van Reenen, D., & Tariku, F. “Hygrothermal properties of exterior claddings, sheathing boards, membranes and insulation materials for building envelope design” National Research Council Canada (NRCC-50287), 2007

Nik, V., Kalagasidis, A., & Kjellström, E. “Statistical methods for assessing and analyzing the building performance in respect to the future climate” Building and Environment 53 (2012) 107-118

Nik, V., Kalagasidis, A., & Kjellström, E. “Assessment of hygrothermal performance and mold growth risk in ventilated attics in respect to possible climate changes in Sweden” Building and Environment 55 (2012) 96-109

Nik, V., & Kalagasidis, A. “Impact study of the climate change on the energy performance of the building stock in Stockholm considering four climate uncertainties” Building and Environment 60 (2013) 291-304

Nijland, T., Adan, O., Van Hees, R., and Van Etten, B. “Evaluation of the effects of expected climate change on the durability of building materials with suggestions for adoption” HERON 54 (2009) 1-37

North, G., Kim, K. (2017) “Energy Balance Climate Models” Weinheim, Germany: Wiley-VCH

Orr, S., Young, M., Stelfox, D., Curran, J., & Viles, H. “Wind-driven rain and future risk to build heritage in the United Kingdom: Novel metrics for characterizing rain spells” Science of The Total Environment 640-641 (2018) 1098-1111

Pérez-Andreu, V., Aparicio-Fernández, C., Martínez-Ibernón, A., & Vivancos, J. “Impact of climate change on heating and cooling energy demand in a residential building in a Mediterranean climate” Energy 165 (2018) 63–74

Ramos, N., Delgado, J., Barreira, E., De Freitas V. “Hygrothermal properties applied in numerical simulation: Interstitial condensation analysis” Building Appraisal 5 (2009) 161-170

Robert, A., & Kummert M. “Designing net-zero energy buildings for the future climate, not for the past” Building and Environment 55 (2012) 150-158

Sandberg, P. “Building Components and Building Elements-Calculation of surface Temperature to Avoid Critical surface Humidity and Calculation of Interstitial Condensation” Draft European Standard CEN/TC89/W10N107, 1995

Sehizadeh, A., Ge, H. “Impact of future climate on the durability of typical residential wall assemblies retrofitted to the PassiveHaus for the Eastern Canada region” Building and Environment 97 (2016) 111-125

Shen, M., Chen, J., Zhuan, M., Chen, H., Xu, C., & Xiong, L. “Estimating uncertainty and its temporal variation related to global climate models in quantifying climate change impacts on hydrology” Journal of Hydrology 556 (2018) 10-24

Shen, P. “Impacts of climate change on U.S. building energy use by using downscaled hourly future weather data” Energy and Buildings 134 (2017) 61-70

Spandagos, C., & Ng, T. “Equivalent full-load hours for assessing climate change impact on building cooling and heating energy consumption in large Asian cities” Applied Energy 189 (2017) 352–368

Stanzel, P., & Kling, H. “From ENSEMBLES to CORDEX: Evolving climate change projections for Upper Danube River flow” Journal of Hydrology 563 (2018) 987-999

Straube, J., “Moisture and Materials” Building Science Press, 2006, https://www.buildingscience.com/documents/digests/bsd-138-moisture-and-materials

Tariku, F. “Whole Building Heat and Moisture Analysis” Concordia University, Montreal, Canada, 2008

Tariku, F., Cornick, S., & Lacasse, M., "Simulation of wind-driven rain effects on the performance of a stucco-clad wall" NRC Publications Archive (NRCC-4944), 2007

Tariku, F., & Iffa, E. "Empirical model for cavity ventilation and hygrothermal performance assessment of wood frame wall systems: Experimental study" Building and Environment 157 (2019) 112-126

Vereecken, E., & Roels, S. "Review of mold prediction models and their influence on mold risk evaluation" Building and Environment 51 (2012) 296-310

Wang, H.,& Chen, Q. "Impact of climate change heating and cooling energy use in buildings in the United States" Energy and Buildings 82 (2014) 428-436

Wang, L., Liu, X., & Brown, H. "Prediction of the impacts of climate change on energy consumption for a medium-size office building with two climate models" Energy and Buildings 157 (2017) 218-226

Watt, D., Sjöberg, S., & Wahlgren, P. "Hygrothermal performance of a lightweight timber wall assembly with an exterior air barrier" Energy Procedia 78 (2015) 1419-1424

Wu, X., Liu, J., Li, C., & Yin., J. "Impact of climate change on dysentery: Scientific evidences, uncertainty, modeling and projections" Science of the Total Environment 714 (2020) 136702

Zhai, Z., & Helman, J. "Implications of climate changes to building energy and design" Sustainable Cities and Society 44 (2019) 511-519